

applied sciences

Special Issue Reprint

Machine Tools, Advanced Manufacturing and Precision Manufacturing

Edited by
Abhilash Puthanveettil Madathil and Xichun Luo

mdpi.com/journal/applsci

MDPI

Machine Tools, Advanced Manufacturing and Precision Manufacturing

Machine Tools, Advanced Manufacturing and Precision Manufacturing

Guest Editors

Abhilash Puthanveettil Madathil
Xichun Luo

MDPI

Basel • Beijing • Wuhan • Barcelona • Belgrade • Novi Sad • Cluj • Manchester

Guest Editors

Abhilash Puthanveettil Madathil
National Manufacturing
Institute Scotland (NMIS)
University of Strathclyde
Paisley
UK

Xichun Luo
Design, Manufacturing and
Engineering Management
University of Strathclyde
Glasgow
UK

Editorial Office
MDPI AG
Grosspeteranlage 5
4052 Basel, Switzerland

This is a reprint of the Special Issue, published open access by the journal *Applied Sciences* (ISSN 2076-3417), freely accessible at: https://www.mdpi.com/journal/applsci/special_issues/P7NC7924OX.

For citation purposes, cite each article independently as indicated on the article page online and as indicated below:

Lastname, A.A.; Lastname, B.B. Article Title. *Journal Name* **Year**, *Volume Number*, Page Range.

ISBN 978-3-7258-8603-6 (Hbk)
ISBN 978-3-7258-8604-3 (PDF)
https://doi.org/10.3390/books978-3-7258-8604-3

Cover image courtesy of Abhilash Puthanveettil Madathil

© 2026 by the authors. Articles in this reprint are Open Access and distributed under the Creative Commons Attribution (CC BY) license. The reprint as a whole is distributed by MDPI under the terms and conditions of the Creative Commons Attribution-NonCommercial-NoDerivs (CC BY-NC-ND) license (https://creativecommons.org/licenses/by-nc-nd/4.0/).

Contents

About the Editors . . . . . **vii**

Abhilash Puthanveettil Madathil and Xichun Luo
Machine Tools, Advanced Manufacturing, and Precision Manufacturing
Reprinted from: *Appl. Sci.* **2025**, *16*, 2127, https://doi.org/10.3390/app16042127 . . . . . **1**

Cédric Leroy, Sylvain Lavernhe and Édouard Rivière-Lorphèvre
Hermite Quartic Splines for Smoothing and Sampling a Roughing Curvilinear Spiral Toolpath
Reprinted from: *Appl. Sci.* **2024**, *14*, 7492, https://doi.org/10.3390/app14177492 . . . . . **4**

Csaba Felhő and Tanuj Namboodri
Statistical Analysis of Cutting Force and Vibration in Turning X5CrNi18-10 Steel
Reprinted from: *Appl. Sci.* **2025**, *15*, 54, https://doi.org/10.3390/app15010054 . . . . . **20**

Slobodan Tabakovic, Milan Zeljkovic, Sasa Zivanovic, Alexander Budimir, Zoran Dimic and Aleksandar Kosarac
Calibration of a Hybrid Machine Tool from the Point of View of Positioning Accuracy
Reprinted from: *Appl. Sci.* **2024**, *14*, 5275, https://doi.org/10.3390/app14125275 . . . . . **38**

Jaroslaw Galkiewicz and Urszula Janus-Galkiewicz
A Machine Tool for Boring of the Diesel Engine Block Counterbore
Reprinted from: *Appl. Sci.* **2025**, *15*, 9143, https://doi.org/10.3390/app15169143 . . . . . **55**

Andrei Osan and Mihai Banica
Comparison of the Wear of Toroidal and Spherical Cutters in Milling and the Impact of Corrosion
Reprinted from: *Appl. Sci.* **2025**, *15*, 8403, https://doi.org/10.3390/app15158403 . . . . . **66**

Paschalis Charalampous
Performance Investigation of Coated Carbide Tools in Milling Procedures
Reprinted from: *Appl. Sci.* **2025**, *15*, 3765, https://doi.org/10.3390/app15073765 . . . . . **79**

Shen-Yung Lin and Chia-Jen Hsieh
Construction of a Cutting-Tool Wear Prediction Model through Ensemble Learning
Reprinted from: *Appl. Sci.* **2024**, *14*, 3811, https://doi.org/10.3390/app14093811 . . . . . **96**

Víctor Meana, Pablo Zapico, Eduardo Cuesta, Sara Giganto, Lorenzo Meana and Susana Martínez-Pellitero
Additive Manufacturing of Ceramic Reference Spheres by Stereolithography (SLA)
Reprinted from: *Appl. Sci.* **2024**, *14*, 7530, https://doi.org/10.3390/app14177530 . . . . . **125**

Angela Mirea Bellocchio, Elia Ciancio, Ludovica Ciraolo, Serena Barbera and Riccardo Nucera
Three-Dimensional Printed Attachments: Analysis of Reproduction Accuracy Compared to Traditional Attachments
Reprinted from: *Appl. Sci.* **2024**, *14*, 3837, https://doi.org/10.3390/app14093837 . . . . . **142**

Emmanouil-Marinos Mantalas, Vasileios D. Sagias, Paraskevi Zacharia and Constantinos I. Stergiou
Neuro-Fuzzy Model Evaluation for Enhanced Prediction of Mechanical Properties in AM Specimens
Reprinted from: *Appl. Sci.* **2025**, *15*, 7, https://doi.org/10.3390/app15010007 . . . . . **154**

Barbara Rivolta, Riccardo Gerosa and Davide Panzeri
Selective Laser-Melted Alloy 625: Optimization of Stress-Relieving and Aging Treatments
Reprinted from: *Appl. Sci.* **2025**, *15*, 5441, https://doi.org/10.3390/app15105441 . . . . . **174**

Miriam Pekarčíková, Marek Kliment, Jana Kronová, Peter Trebuňa and Anton Hovana
Simulation-Based Optimization of Material Supply in Automotive Production Using RTLS Data
Reprinted from: *Appl. Sci.* **2025**, *15*, 9102, https://doi.org/10.3390/app15169102 . . . . . **193**

Simion Haragâș, Roland Ninacs, Ovidiu Buiga, Lucian Tudose, Alexandru Haragâș, Ioana Monica Sas-Boca and Felicia Aurora Cristea
An Attempt to Establish a Mathematical Model for an Unconventional Worm Gear with Bearings
Reprinted from: *Appl. Sci.* **2024**, *14*, 10833, https://doi.org/10.3390/app142310833 . . . . . **211**

About the Editors

Abhilash Puthanveettil Madathil

Abhilash Puthanveettil Madathil is a researcher at the National Manufacturing Institute Scotland (NMIS), specializing in AI-driven manufacturing innovations. His research expertise lies in AI-enabled smart manufacturing, digital twins, additive manufacturing, ultra-precision, and non-traditional manufacturing processes. Previously, he worked as a Research Associate at the Centre for Precision Manufacturing (CPM), University of Strathclyde, where he successfully developed and implemented digital twin solutions for the smart manufacturing of high-value products as part of the 'SMART' EPSRC project. Abhilash holds a Ph.D. from the Indian Institute of Technology Palakkad (India). He also earned a master's degree in engineering design (First rank at the university level) from Amrita University (India). With over 30 research articles published in reputed international peer-reviewed journals (Google Scholar h-index 15), he has also published two edited books on "*Bioimplants Manufacturing*" and "*Data-driven decisions in manufacturing*". He has also contributed to several international conference publications including CIRP SI, CIRP ICME, WCMNM, Nanoman, and SPIE Photonics. Recently, his perspectives on the need for explainability in AI-enabled manufacturing systems were published in the highly reputed Nature journal *npj Advanced Manufacturing*. He recently won two best paper awards at international conferences—NanoMan 2022 in Dublin, Ireland, and ICPE 2024 in Japan. He is the Co-chair of the 3rd AIGC 2025 international conference.

Xichun Luo

Xichun Luo is a Professor of Ultra Precision Manufacturing, Director of Research of the Department of Design, Manufacturing and Engineering Management and Technical Director of the Centre for Precision Manufacturing (CPM) at the University of Strathclyde. Prof. Luo has strong research interest in fundamental studies and applied research in ultra precision machining, micro, nano, and atomic scales of manufacturing. His research revealed atomic-level machining mechanisms for semiconductor materials, Si, SiC and GaAs and ion-induced damage of diamond and developed ultra-precision freeform machining technologies. Prof. Luo won the Institution of Mechanical Engineers (IMechE) 2015 Ludwig Mond Prize for research and development of novel digital tools for micro and nanomanufacturing. He has over 240 publications, including 2 books, 4 invited book chapters, over 170 papers in highly ranked journals (Google Scholar h-index: 57), 70 conference papers, and 4 patents. Prof. Luo is an Elected Fellow of the International Society for Nanomanufacturing, the International Academy of Engineering and Technology, and the International Association of Advanced Materials. He is a member of the Scientific Committee of the European Society for Precision Engineering & Nanotechnology (euspen) and Technical Committee of the Advanced Forming Research Centre (2013-2019). He is the Secretary General of the International Academy of Engineering and Technology since 2019 and the Past-President of The Chinese Automation and Computing Society in the UK. Prof. Luo is the founding Editor-in-Chief of *High-end Manufacturing*, and Associate Editor for Proceedings of IMechE Part C: *Journal of Mechanical Engineering Science*, *Journal of Micromanufacturing*, and *Mechanical Sciences*, and an editorial board member for *Micromachines*, *Nanomanufacturing* and *Metrology*, and the *International Journal of Extreme Manufacturing*.

applied sciences

MDPI

Editorial

Machine Tools, Advanced Manufacturing, and Precision Manufacturing

Abhilash Puthanveettil Madathil [1,2] and Xichun Luo [2,*]

[1] National Manufacturing Institute Scotland (NMIS), University of Strathclyde, Paisley, Renfrew PA3 2EF, UK; abhilash.p-m@strath.ac.uk
[2] Centre for Precision Manufacturing, Design Manufacturing and Engineering Management (DMEM), University of Strathclyde, Glasgow G1 1XJ, UK
* Correspondence: xichun.luo@strath.ac.uk

Modern industries impose numerous challenges on manufacturing technologies and systems due to stringent quality requirements, the adoption of difficult-to-machine materials, high demands on miniaturization, mass customization, high productivity, and sustainability targets. Addressing these challenges requires a holistic approach that integrates advanced manufacturing processes, equipment, measurement and data-driven control methods.

In this context, this Special Issue provides a focused forum for research that advances the domains of machining processes, precision engineering, intelligent monitoring, digitalization, and additive manufacturing. It comprises thirteen articles spanning the topics: machining efficiency and toolpath planning, machine tool design and calibration, tool performance and wear prediction, additive manufacturing and post-processing, and data-enabled production logistics. Collectively, these papers emphasize improving accuracy and surface integrity while simultaneously increasing productivity and robustness through better modelling, sensing, and decision support.

In machining science and machine-tool performance, productivity improvements are pursued not only in terms of higher cutting speeds but also through smoother trajectories, improved motion consistency, and reduced non-productive time [1,2]. In addition to quality–time tradeoffs, these strategies are motivated by energy efficiency and tool-life considerations, since smoother motion profiles can reduce peak loads, vibration, and heat accumulation, thereby providing better surface integrity and dimensional consistency.

Precision is reinforced through systematic calibration, compensation, and measurement practices, highlighting the role of metrology and error management in achieving reliable micron-level performance. Recent studies highlight that accuracy is constrained by dynamic and thermally induced errors, in addition to static geometric deviations, motivating new calibration strategies that better represent real operating conditions. In parallel, advances in volumetric error modelling and prediction for multi-axis CNC systems support earlier-stage error detection and more effective compensation throughout the working volume [3,4].

Tool life and process reliability are now being treated as predictive tasks, combining sensor signals with machine learning-based approaches to anticipate degradation and maintain consistent output quality [5,6]. These approaches are particularly valuable in high-mix environments, where variability in materials, geometry, and cutting conditions makes fixed tool change intervals inefficient. By enabling condition-based maintenance and early anomaly detection, predictive tool health models can reduce scrap and downtime while supporting stable surface integrity and dimensional accuracy.

Additive manufacturing contributions have grown from just the feasibility demonstrations toward increased quality and application readiness, where property prediction, post-processing strategies, and geometric verification are essential for dependable deployment [7,8]. Accordingly, there is an increased research focus on linking process parameters to repeatable dimensional accuracy and performance, supported by metrology-driven verification that reduce uncertainties.

Finally, contributions connecting manufacturing engineering with systems-level decision-making and mechanism innovation are becoming increasingly important. For example, conceptual frameworks for operations management and Industry 4.0-oriented supply planning highlight the growing role of traceable, responsive logistics supported by data and modelling [9]. In parallel, mechanism and transmission innovations relevant to machine tools and automation continue to be explored through mathematical modelling and design-led evaluation [10].

We thank all authors for their valuable contributions, the reviewers for their rigorous assessments, and the editorial office for their support in delivering this Special Issue.

Acknowledgments: We would like to take this opportunity to thank all the authors for submitting their papers to this Special Issue, and all the reviewers for dedicating their time and helping to improve the quality of the submitted papers.

Conflicts of Interest: The authors declare no conflicts of interest.

List of Contributions:

1. Leroy, C.; Lavernhe, S.; Rivière-Lorphèvre, É. Hermite Quartic Splines for Smoothing and Sampling a Roughing Curvilinear Spiral Toolpath. *Appl. Sci.* **2024**, *14*, 7492. https://doi.org/10.3390/app14177492.
2. Felhő, C.; Namboodri, T. Statistical Analysis of Cutting Force and Vibration in Turning X5CrNi18-10 Steel. *Appl. Sci.* **2024**, *15*, 54. https://doi.org/10.3390/app15010054.
3. Tabakovic, S.; Zeljkovic, M.; Zivanovic, S.; Budimir, A.; Dimic, Z.; Kosarac, A. Calibration of a Hybrid Machine Tool from the Point of View of Positioning Accuracy. *Appl. Sci.* **2024**, *14*, 5275. https://doi.org/10.3390/app14125275.
4. Galkiewicz, J.; Janus-Galkiewicz, U. A Machine Tool for Boring of the Diesel Engine Block Counterbore. *Appl. Sci.* **2025**, *15*, 9143. https://doi.org/10.3390/app15169143.
5. Osan, A.; Banica, M. Comparison of the Wear of Toroidal and Spherical Cutters in Milling and the Impact of Corrosion. *Appl. Sci.* **2025**, *15*, 8403. https://doi.org/10.3390/app15158403.
6. Charalampous, P. Performance Investigation of Coated Carbide Tools in Milling Procedures. *Appl. Sci.* **2025**, *15*, 3765. https://doi.org/10.3390/app15073765.
7. Lin, S.Y.; Hsieh, C.J. Construction of a cutting-tool wear prediction model through ensemble learning. *Appl. Sci.* **2024**, *14*, 3811. https://doi.org/10.3390/app14093811.
8. Meana, V.; Zapico, P.; Cuesta, E.; Giganto, S.; Meana, L.; Martínez-Pellitero, S. Additive Manufacturing of Ceramic Reference Spheres by Stereolithography (SLA). *Appl. Sci.* **2024**, *14*, 7530. https://doi.org/10.3390/app14177530.
9. Bellocchio, A.M.; Ciancio, E.; Ciraolo, L.; Barbera, S.; Nucera, R. Three-Dimensional Printed Attachments: Analysis of Reproduction Accuracy Compared to Traditional Attachments. *Appl. Sci.* **2024**, *14*, 3837. https://doi.org/10.3390/app14093837.
10. Mantalas, E.M.; Sagias, V.D.; Zacharia, P.; Stergiou, C.I. Neuro-Fuzzy Model Evaluation for Enhanced Prediction of Mechanical Properties in AM Specimens. *Appl. Sci.* **2024**, *15*, 7. https://doi.org/10.3390/app15010007.
11. Rivolta, B.; Gerosa, R.; Panzeri, D. Selective Laser-Melted Alloy 625: Optimization of Stress-Relieving and Aging Treatments. *Appl. Sci.* **2025**, *15*, 5441. https://doi.org/10.3390/app15105441.
12. Pekarčíková, M.; Kliment, M.; Kronová; J; Trebuňa, P.; Hovana, A. Simulation-Based Optimization of Material Supply in Automotive Production Using RTLS Data. *Appl. Sci.* **2025**, *15*, 9102. https://doi.org/10.3390/app15169102.

13. Haragâș, S.; Ninacs, R.; Buiga, O.; Tudose, L.; Haragâș; A; Sas-Boca, I.M.; Cristea, F.A. An attempt to establish a mathematical model for an unconventional worm gear with bearings. *Appl. Sci.* **2024**, *14*, 10833. https://doi.org/10.3390/app142310833.

References

1. Busatto, M.; Caprio, L.; Cazzador, M.; Previtali, B. Compensating thermal expansion via tool path correction during fusion laser cutting of Al5754. *Int. J. Adv. Manuf. Technol.* **2025**, *141*, 4985–5004. [CrossRef]
2. Taifa, I.; Vhora, T. Cycle time reduction for productivity improvement in the manufacturing industry. *J. Ind. Eng. Manag. Stud.* **2019**, *6*, 147–164.
3. Abir, J.; Longo, S.; Morantz, P.; Shore, P. Virtual metrology frame technique for improving dynamic performance of a small size machine tool. *Precis. Eng.* **2017**, *48*, 24–31. [CrossRef]
4. Wu, H.; Li, X.; Sun, F.; Zhao, Y. A status review of volumetric positioning accuracy prediction theory and static accuracy design method for multi-axis CNC machine tools. *Int. J. Adv. Manuf. Technol.* **2022**, *122*, 2139–2159. [CrossRef]
5. Cheng, M.; Jiao, L.; Yan, P.; Jiang, H.; Wang, R.; Qiu, T.; Wang, X. Intelligent tool wear monitoring and multi-step prediction based on deep learning model. *J. Manuf. Syst.* **2022**, *62*, 286–300. [CrossRef]
6. Kim, G.; Yang, S.M.; Kim, D.M.; Kim, S.; Choi, J.G.; Ku, M.; Lim, S.; Park, H.W. Bayesian-based uncertainty-aware tool-wear prediction model in end-milling process of titanium alloy. *Appl. Soft Comput.* **2023**, *148*, 110922. [CrossRef]
7. Akbari, P.; Zamani, M.; Mostafaei, A. Machine learning prediction of mechanical properties in metal additive manufacturing. *Addit. Manuf.* **2024**, *91*, 104320. [CrossRef]
8. Laleh, M.; Sadeghi, E.; Revilla, R.I.; Chao, Q.; Haghdadi, N.; Hughes, A.E.; Xu, W.; De Graeve, I.; Qian, M.; Gibson, I.; et al. Heat treatment for metal additive manufacturing. *Progress Mater. Sci.* **2023**, *133*, 101051. [CrossRef]
9. Reyes, J.; Mula, J.; Díaz-Madroñero, M. Development of a conceptual model for lean supply chain planning in industry 4.0: Multidimensional analysis for operations management. *Prod. Plan. Control* **2023**, *34*, 1209–1224. [CrossRef]
10. Haragâș, S.; Ninacs, R.; Buiga, O.; Tudose, L.; Haragâș, A.; Sas-Boca, I.M.; Cristea, F.A. An attempt to establish a mathematical model for an unconventional worm gear with bearings. *Appl. Sci.* **2024**, *14*, 10833. [CrossRef]

Disclaimer/Publisher's Note: The statements, opinions and data contained in all publications are solely those of the individual author(s) and contributor(s) and not of MDPI and/or the editor(s). MDPI and/or the editor(s) disclaim responsibility for any injury to people or property resulting from any ideas, methods, instructions or products referred to in the content.

applied sciences

MDPI

Article

Hermite Quartic Splines for Smoothing and Sampling a Roughing Curvilinear Spiral Toolpath

Cédric Leroy [1], Sylvain Lavernhe [2] and Édouard Rivière-Lorphèvre [1,*]

[1] Machine Design and Production Engineering Lab, UMONS Research Institute for Materials Science and Engineering, University of Mons, Place du Parc 20, 7000 Mons, Belgium; cedric.leroy@umons.ac.be
[2] LURPA, ENS Paris-Saclay, Université Paris-Saclay, Avenue des Sciences 4, 91190 Gif-sur-Yvette, France; sylvain.lavernhe@ens-paris-saclay.fr
* Correspondence: edouard.rivierelorphevre@umons.ac.be

Abstract: From an industrial point of view, the milling of 2.5*D* cavities is a frequent operation, consuming time and presenting optimization potential, especially through a judicious choice of the tool trajectory. Among the different types of trajectories, some have a general spiral-like aspect and can potentially offer a reduced machining time. They are called curvilinear trajectories and are obtained by interpolation between structure curves, which are the numerical solutions of a partial differential equation. In this case, the machine tool will connect points, and the trajectory will be made up of small segments. While these trajectories exhibit all the necessary qualities on a macroscopic level for rapid tool movement, the tangential discontinuities at a microscopic scale, inherent in the discretization, significantly increase the machining time. This article proposes a method to reparameterize the structure curves of the curvilinear spiral with a set of C^2 connected Hermit quartic spline patches. This creates a smooth toolpath that can be machined at an average feedrate closer to the programmed one and will, de facto, reduce the machining time. This article shows that the proposed method increases on two representative geometries of cavities and toolpath quality indicators, and reduces the milling time from 10% to 18% as compared to the PDE curvilinear spiral generation method proposed by Bieterman and Sandström. In addition, the proposed method is suitable for any non-convex pocket, with or without island(s).

Keywords: pocket milling; roughing; curvilinear toolpath; hermite quartic spline

1. Introduction

Pocketing 2.5*D* cavities, which is common from an industrial point of view (e.g., in aeronautical structure parts or aerospace electronic crankcase), is a time-consuming operation.

As shown by [1], manufacturing costs are time dependent and typically represent, for dies and molds, 30% of the total price of a piece [2].

In this context, many studies aim to reduce the machining time. The main lines for optimization are enhancing the understanding of cutting phenomena [3–5], improving tool performance [6], selecting the best tools, defining the optimal milling parameters [7–9], and, finally, enhancing the toolpath geometry [10–12].

From this last perspective, the most common approach is to work on the tool trajectory to increase its speed. Multiple studies (e.g., [13,14]) have demonstrated that tangency discontinuities along the trajectory result in increased machining time. These discontinuities necessitate changes in the velocity vector (both in direction and magnitude) along the trajectory, which challenges the machine tool's acceleration and jerk capabilities. As these capacities are limited, the numerical control system of the machine imposes restrictions on these variations, so the tool requires additional time and distance to achieve the programmed feed rate after negotiating corners or halts along the toolpath. Therefore, it is essential to minimize such discontinuities, for which two methods exist:

- Local adjustments on classical toolpath (Zig-Zag or Contour Parallel) are employed to eliminate or to smooth out the discontinuities [15–17];
- Global strategy to build a spiral-like trajectory (or curvilinear spiral). Macroscopically, this kind of toolpath begins at a center point of the pocket and expands outward without "stop and go". The toolpath morphs progressively to the shape of the pocket boundary. Natively, curvilinear spirals (or spiral-like toolpath) have a higher degree of continuity [18–21].

Primarily, two approaches are used to build curvilinear spirals:

- Geometrical approaches such as mapping [22,23], morphing [24], or the medial axis method [19,20];
- Differential approaches using an elliptical partial differential equation (**PDE**) [21] or a level-set propagation model [18]. In those cases, curvilinear trajectories are generated through interpolation between selected structure curves, which are the solutions of the used PDE.

To determine a point on a curvilinear path, an interpolation method is needed. Bieterman et al. [21] use the intersection of a Fresnel vector (winding angle) and two discrete structure curves (Figure 1). The trajectory point is established through a linear angular interpolation between the two intersecting points (Equation (1)):

$$\rho_S(\theta_i) = \rho_{int}(\theta_i) + (\rho_{ext}(\theta_i) - \rho_{int}(\theta_i)).\frac{\theta_i}{2\pi} \ , \ \theta_i \in [0, 2\pi[\tag{1}$$

with $\rho_S(\theta_i)$, discrete polar equation of a spiral-like turn; $\rho_{ext}(\theta_i)$, discrete polar equation of the external structure curve; $\rho_{int}(\theta_i)$, discrete polar equation of the internal structure curve.

This method is effective when the cavity is sufficiently convex (i.e., without significant protrusions; mathematically, when the polar function of the pocket border is explicit). However, for pockets with more complex geometries, a partitioning task is required as proposed by [25] and illustrated in Figure 2.

Moreover, the structure curves are constructed through interpolations between a series of points calculated using finite element method software. In the context of G1 linear interpolation, the trajectory consists of numerous small segments. Although the trajectory may exhibit characteristics adapted to high feed rates on a macroscopic scale, the tangency discontinuities inherent to this method significantly increase the machining time on a smaller scale. Since 'polynomial' interpolators are not yet widely adopted in the industry, efforts are needed to smooth the toolpath and improve its degree of continuity.

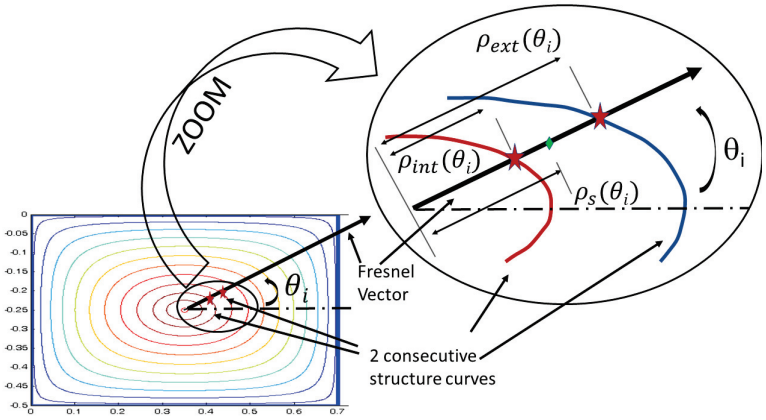


Figure 1. Interpolation between two structure curves with a Fresnel vector.

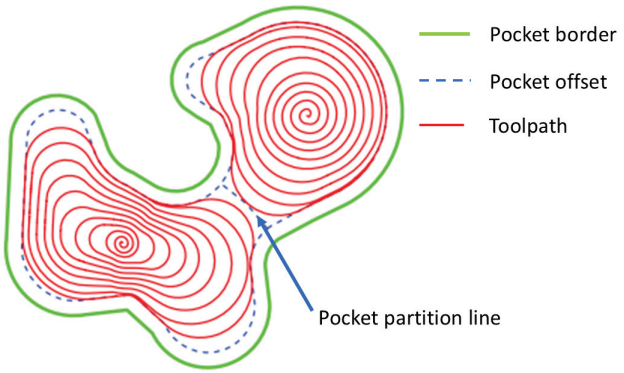


Figure 2. Partition of a pocket [25].

The simplest method to achieve this objective is the use of a Finite Impulse Response filter (**FIR**); [21] suggests a moving average technique. However, the use of such filters may result in a loss of tool position control, potentially leading to a machining in inappropriate zones. Other various studies [22,26,27] achieve three of five-axis trajectory smoothing, via B-splines or Bézier curves. Table 1 shows a summary of the methods proposed in the literature summarizing their main focuses.

Table 1. Research timeline.

Years	Authors	Main Focuses	Benefits and Limitations
<2000	Held	Generation of toolpaths on arbitrary geometry Zig-zag or parallel contour	/
2003	Bieterman [21]	Spiral toolpath PDE approach	Suitable only for globally convex pocket Not suitable for pocket with island
2004	Pateloup [28]	Corner smoothing	Local smoothing
2009	Held [29]	Spiral toolpath Geometric approach	Use of Voronoï diagrams Not suitable for island
2011	Xiong [18]	Spiral toolpath PDE approach Level set propagation	No smoothing Suitabel for pockets with island but with composite spiral
2011	Banerjee [30]	Spiral toolpath PDE approach	Only globally convex pocket Suitable for pocket with a centered island G^1 toolpath
2013	Xu [23]	Spiral toolpath Geometric approach Mapping	Not suitable for pocket with island No smoothing
2018	Held [19]	Spiral toolpath Geometric approach	Simplier to implement Polygonal spiral (G^0)
2023	Hua [27]	Curve smoothing B-Spline	Not integrated in a spiral construction

This article proposes a method to reparameterize the structure curves of the curvilinear spiral with a set of Hermit quartic spline patches C^2 connected (continuity in tangency and curvature). Analytically, the spiral-like toolpath, formed through linear combination of these curves, maintains the C^2 continuity, ensuring a smaller machining time.
Moreover, the proposed method eliminates the need of Fresnel's vector to establish the spiral parametrization, so the toolpath can be directly created without partitioning the

pocket. It allows a generalization of Bieterman's procedure for any 2.5D pocket geometries, even with non-convex geometry.

2. Methodology for Smoothing Toolpaths

Figure 3 summarizes the proposed method and the structure of the following paragraphs.

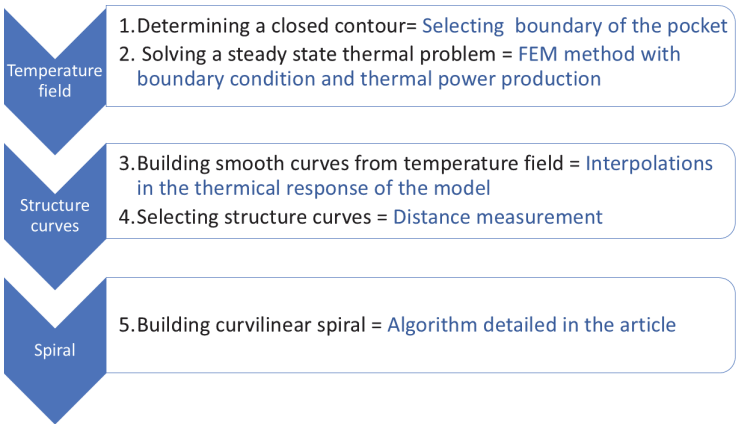


Figure 3. Structure chart of the proposed method.

2.1. Determining a Closed Contour

The first step involves establishing a closed contour to define a layer of the 2.5D pocket, which will be milled layer by layer. As the paper is focused on the roughing operation, an offset distance from the border must be accounted for regarding the radial width of the cut of the finishing pass ($D_{offset} = \frac{\phi_{tool}}{2}$).

2.2. Solving a Steady State Thermal Problem

Given their smooth nature [31], the solutions of a 2D thermal problem (i.e., isotherms) are chosen for building structure curves: a layer of the pocket is uniformly heated while the border is maintained at 0 $[K]$. The heat equation is (Equation (2)):

$$\rho c \frac{\partial T}{\partial \tau} = \vec{\nabla}(\lambda \vec{\nabla} T) + q \ , \ \partial\Omega = 0 \ [K] \tag{2}$$

with ρ, the areal density of the layer [kg/m^2]; c, the specific heat of the layer [J/(kg K)];$T(x, y)$, the temperature field on the layer [K]; τ, the time [s]; λ, the thermal conductivity of the material [W/K]; q, the areal heat source [W/m^2]; $\partial\Omega$, the border condition.

The stationary equation with $q = 1[W/m^2]$ and $\lambda = 1[W/K]$ is expressed in Equation (3) and is equivalent to Equation (4) proposed by [21]. Note that the values of q and λ do not alter the general shape of the solution temperature field but only impact the maximum temperature:

$$-\Delta T = \frac{q}{\lambda} \ , \ \partial\Omega = 0 \ [K] \tag{3}$$

$$-\Delta\phi(x, y) = 1, \partial\Omega = 0 \tag{4}$$

2.3. Building Smooth Curves from Temperature Field

Equation (3) is solved using a classical finite element method (**FEM**). Some isotherm curves from the resulting temperature field can be used to construct the spiral-like trajectory. However, due to the discretization inherent in FEM and the necessary interpolations, these curves are microscopically noisy and exhibit tangency discontinuities. To address this issue, a fitting-smoothing method is implemented.

2.3.1. Hermite Quartic Spline Interpolation

The Hermite quartic spline interpolation model (**HQS**) was presented by [32] and is a generalization of the usual Hermite cubic spline interpolation. The general form of the HQS interpolation is (Equation (5)):

$$\begin{cases} x(u) = ea_0(u)x_0 + ea_1(u)x_1 + eb_0(u)\cos(\theta_0) + eb_1(u)\cos(\theta_1) \\ y(u) = ea_0(u)y_0 + ea_1(u)y_1 + eb_0(u)\sin(\theta_0) + eb_1(u)\sin(\theta_1) \end{cases} \tag{5}$$

with $P_u = (x(u), y(u))$, the coordinates of an interpolated point; $u \in [0,1]$, the real interpolant; (x_0, y_0), the coordinates of the spline first point ($u = 0$); (x_1, y_1), the coordinates of the spline last point ($u = 1$); θ_0 and θ_1, the orientations of the tangent at the beginning and at the end, respectively; and ea_0, ea_1, eb_0, eb_1, the blending functions ("e" is for extended).

The degree of blending function equals to 4 and, thereby, 5 constraints are allowed and detailed below.

- The spline passes over two points P_0 and P_1: +2 constraints;
- The spline respects tangent orientations at the beginning and at the end: +2 constraints;
- An initial curvature C_0 is fixed: +1 constraint.

The blending functions are described with four parameters: k_0, k_1, α, β (Equation (6), Figure 4). If α and $\beta = 0$, blending functions are those of classical cubic Hermite splines.

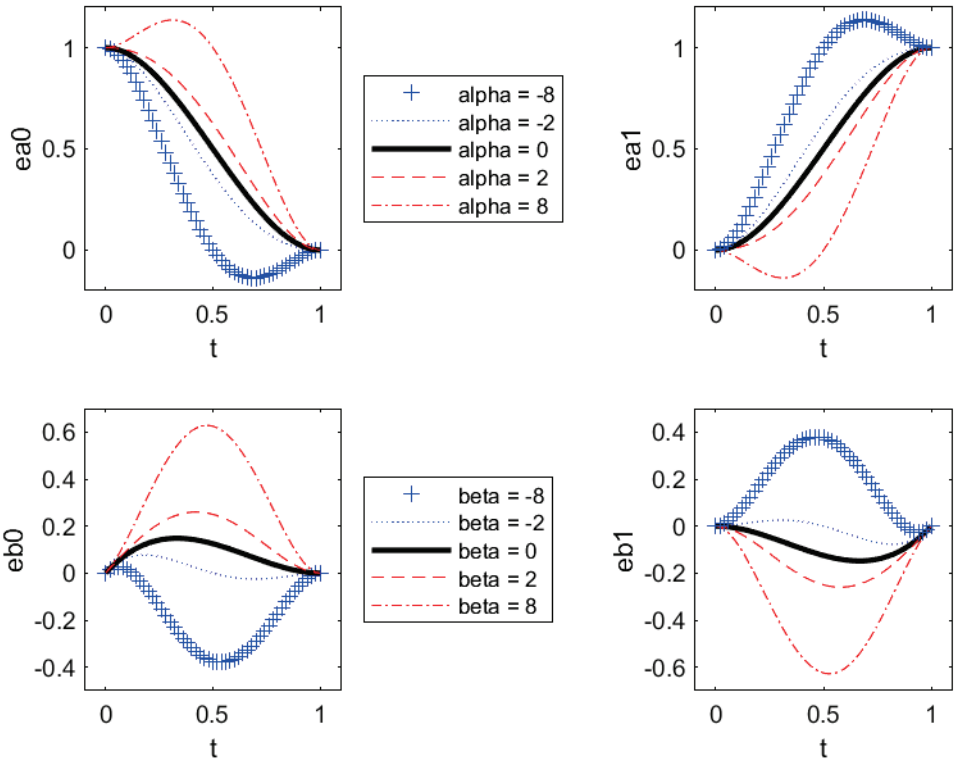


Figure 4. Representation of blending functions of Hermite quartic splines.

$$\begin{cases} ea_0(u) = 1 + (\alpha - 3)\,u^2 + 2(1-\alpha)\,u^3 + \alpha\,u^4 \\ ea_1(u) = (3-\alpha)\,u^2 + 2(\alpha-1)\,u^3 - \alpha\,u^4 \\ eb_0(u) = k_0\,\left(t + (\beta-2)\,u^2 + (1-2\beta)\,u^3 + \beta\,u^4\right) \\ eb_1(u) = k_1\,\left(-(\beta+1)\,u^2 + (2\beta+1)\,u^3 - \beta\,u^4\right) \end{cases} \quad u \in [0,1] \tag{6}$$

- k_0 and k_1 do not affect the orientation of the tangent, only the norm of the tangent vector;
- α and β are called shape parameters and allow the shape modification of blending functions.

The initial curvature (C_0) is a complex function of k_1, k_2, α and β (Equation (7)):

$$C_0 = C]_{u=0} = \left[\frac{\frac{dx}{du} \cdot \frac{d^2x}{du^2} - \frac{dy}{du} \cdot \frac{d^2y}{du^2}}{(\frac{dx}{du}^2 + \frac{dy}{du}^2)^{\frac{3}{2}}} \right]_{u=0} = f_0(k_1, k_2, \alpha, \beta) \quad (7)$$

But this expression can be analytically inverted to isolate β by the use of the Symbolic Toolbox of MatLab, for example (Equation (8)). The final curvature is obtained in the same way but for $u = 1$ in Equation (7) and is noted as $C_1 = f_1(k_0, k_1, \alpha, \beta)$:

$$\beta = f_0^{-1}(C_0, k_1, k_2, \alpha) \quad (8)$$

2.3.2. From Interpolation to Smooth Curve Decomposition

This model of interpolation, between two points, makes it possible to fit and decompose a discrete curve, in this case, an isotherm, into a small number of splines connected in tangency and curvature (named **patches**). Figure 5 explains the procedure followed.

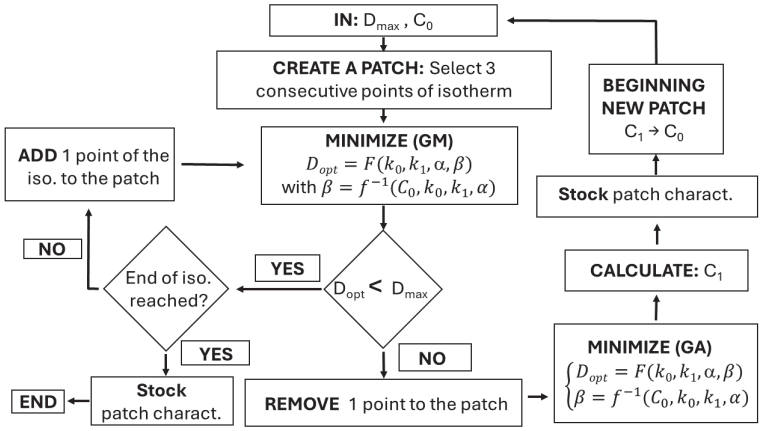


Figure 5. General algorithm of isotherm decomposition in minimum C^2 connected patches.

D_{max} is the maximum acceptable distance between the curve and patch points; C_0 represents the algebraic initial curvature of the first patch. D_{max} and C_0 are user-fixed parameters. D_{opt} is the optimized (i.e., minimized) distance between the patch points and HQ spline. **GA** is for the Genetic Algorithm method, and **GM** is for the gradient descent method. C_1 is the calculated final curvature of the patch that becomes the initial curvature of the new patch.

By using this procedure, a discrete isotherm may be split into a minimum number of Hermite quartic splines, continuous, connected in tangency and curvature (called **isoHQ**), and respecting a maximum chordal error.

2.4. Selecting Structure Curves

To select the structure curves among isotherms and to build the toolpath, isotherms are first decomposed into isoHQ and then sampled.

The analytical expression of patches, along with Equation (9), enables the computation of the curvilinear length of each patch (s_{patch}) and, consequently, the total length of an isoHQ. Using normalization (the normalized length is set to one), points can be sampled, equally spaced along an isoHQ:

$$s_{patch} = \int_0^1 \sqrt{\left(\frac{dx(u)}{du}\right)^2 + \left(\frac{dy(u)}{du}\right)^2} du \quad (9)$$

The selection of the structure curves is performed by evaluating the distance (D_{isoHQ}) between sampling points of 2 isoHQ (an external one $isoHQ_{ext}$ and an internal one

$isoHQ_{int}$) and linking it with an acceptable distance (D_{rte}) equal to the radial tool engagement. If $P_j \in isoHQ_{ext}$ and $Q_i \in isoHQ_{int}$, Equation (10) is computed:

$$D_{isoHQ} = MAX_j\{\, MIN_i[\, \sqrt{(\, P_j(x) - Q_i(x)\,)^2 + (\, P_j(y) - Q_i(y)\,)^2}\,]\,\} \quad (10)$$

- If $D_{isoHQ} < D_{rte}$, the work is restarted with a more internal $isoHQ_{int}$;
- If $D_{isoHQ} > D_{rte}$, the penultimate evaluated $isoHQ_{int}$ is chosen as the structure curve, and the loop is restarted.

Thereby, the distance between two structure curves is under control and always under D_{rte}, which guarantees machining without unmilled areas.

2.5. Building Curvilinear Spiral

To build a curvilinear spiral, a linear interpolation between points $(xiso_i(j); yiso_i(j))$ and $(xiso_{i+1}(j); yiso_{i+1}(j))$ of the same normalized curvilinear abscissa of two consecutive structure curves is achieved (Figure 6, Equation (11)):

$$\begin{cases} xs_i(j) = xiso_i(j) + \frac{j}{n}\{xiso_{i+1}(j) - xiso_i(j)\} \\ ys_i(j) = yiso_i(j) + \frac{j}{n}\{yiso_{i+1}(j) - yiso_i(j)\} \end{cases} \quad (11)$$

with $xs_i(j)$ and $ys_i(j)$, the coordinates of the point j from the turn i of the curvilinear spiral, and n, the total number of points along the isotherms.

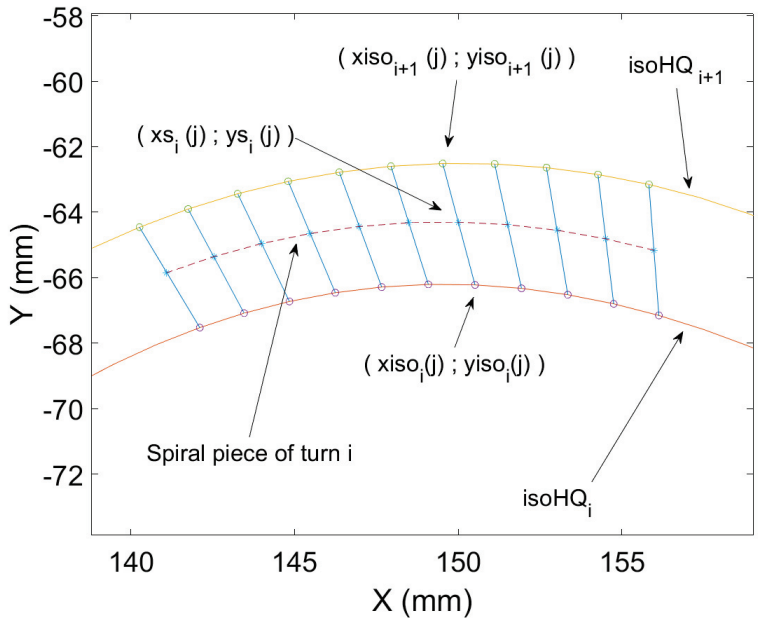


Figure 6. Building the curvilinear spiral between 2 isotherms.

3. Toolpath Quality Evaluation

As shown in many research works, notably in [13,14], discontinuities in the tangency and curvature of the toolpath geometry challenge the limited acceleration and jerk of each axis of the numerically controlled machine tool. Therefore, the average speed rate is always lower than the programmed one, and the milling time is longer than expected.

Here, a double objective is pursued: increasing the speed along the toolpath (which can reduce milling time) and mastering the position of the tool along the milling path. For the tool speed evaluation, two methods are employed:

- A local approach: VPOp.
- A global approach: Toolpath absolute curvature value.

VPOp (Velocity Profile Optimization—version 2.6) is licensed software developed by X. Beudaert and et al. [33]. Based on kinematic data and the CNC parameters of a given machine tool, it generates optimized feedrate planning that respects the capabilities of the milling center and thus predicts the actual tool speed and slowdowns for the tool. So, the modelized milling time is close to the real one. VPOp is used locally to analyze the velocity profile along two turns of the curvilinear spiral.

To analyze the entire trajectory, histograms of the toolpath absolute curvature value ($|C|$ in mm^{-1}) are used as well as 95% and 99% quantiles of $|C|$ named **Cut95** and **Cut99**. These last indicators can quickly give, unlike VPOp, the geometrical quality of a toolpath and, consequently, the possibility of NC to respect the programmed feed rate.

A comparison will be made between the "no fitted" toolpath (called **RAW**) and the fitted one with HQS method (called **HQS**). For another comparison point for milling time, a filtered toolpath is also computed, called **FIR**, and corresponding to a moving average on three points applied twenty times (this combination gives results close to the HQS method). Note that the more the filter is applied, the smoother the trajectory but the more the position control is lost. So, the FIR toolpath is absolutely not suitable to satisfy our goal.

4. Case Study 1—BIG Pocket

4.1. Fitting and Selecting Structure Curves

The 2.5D pocket given by M. Bieterman and D. Sandström [21] is considered for this work. Because it presents a large variety of tangency and curvature values, this pocket is a good test for the proposed algorithm.

With the conditions exposed in Section 2.4, a temperature field is computed using a finite element method (12.10^3 nodes). The maximum temperature is around $500[K]$. The mesh and some isotherms are shown in Figure 7. Our following analysis considers 100 of them; note that the temperature rises from the outside to the inside of the pocket.

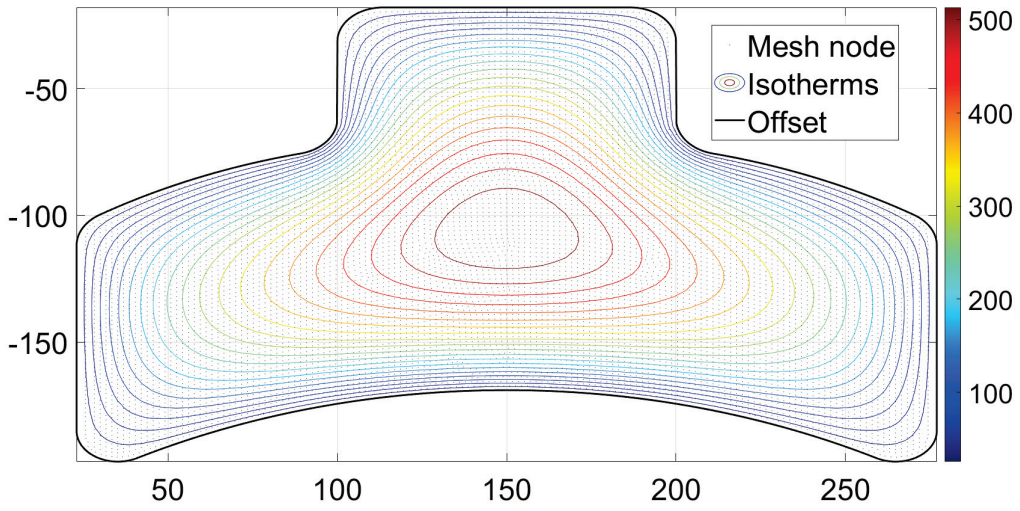


Figure 7. Mesh and isotherms on a layer of the cavity.

To fit isotherms with HQS patches, the parameter D_{chord} must be fixed. A too small value increases the number of patches, and the local smoothing is less efficient. On the other hand, a higher value may cause over-machining of the pocket's border. $D_{chord} = 0.5$ [mm] seems, in this case, to be a good compromise but remains a parameter.

At this stage of the work, our fitting method splits each discrete isotherm (composed with a maximum of about 2500 points) into a maximum of about 25 C^2 connected patches. Figure 8 shows the result of a fit along an isothermal curve. Note that the beginning of the isotherm is chosen in a low-curvature zone. So, the initial curvature of the first patch is arbitrarily fixed at 0.1 [mm^{-1}] to respect the curvature orientation. As a reminder, the first patch and the last one of each isoHQ are only C^0 connected.

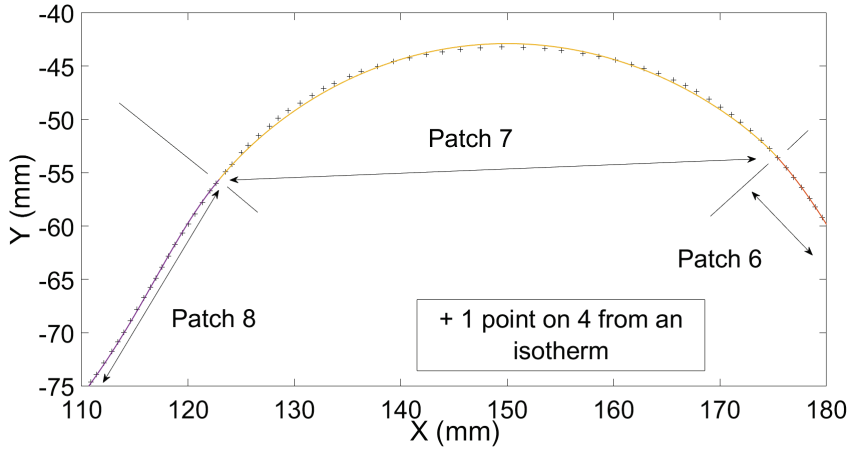


Figure 8. Local result of the Hermit quartic spline interpolation on an isothermal curve.

Now, a sample of each isotherm as described above must be performed. In total, 360 points are used to represent an isoHQ (Figure 9).

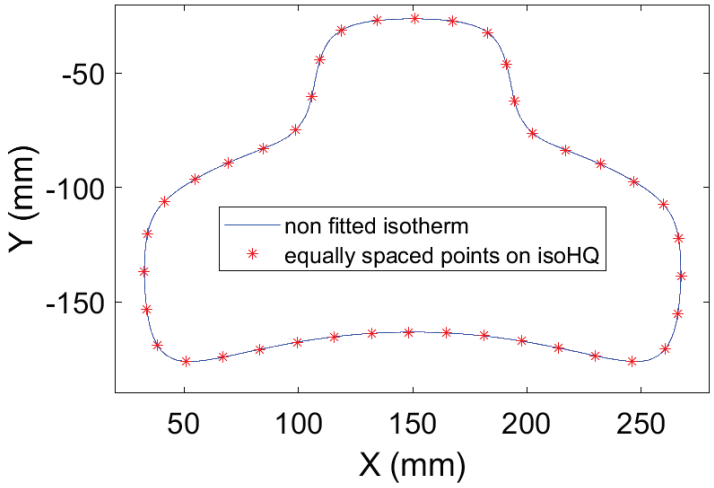
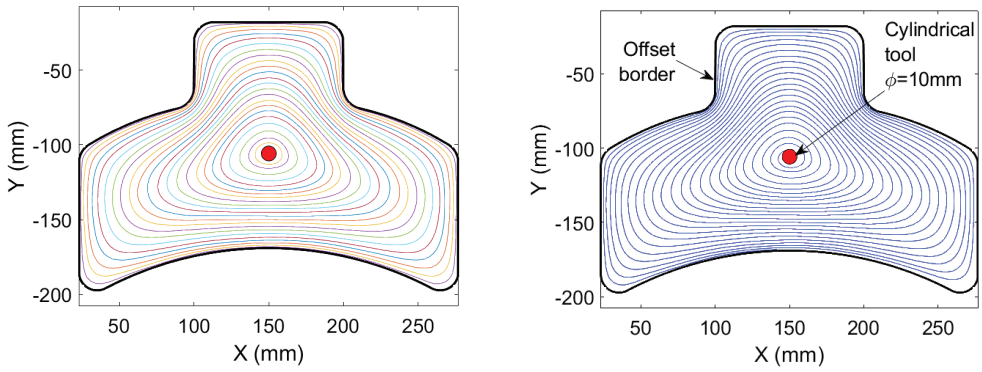


Figure 9. Result of the curvilinear sampling.

For this work, the tool diameter is fixed at 10 [mm] with a radial covering of 25%: the acceptable distance (D_{rte}) between two isotherms is 7.5 [mm]. Figure 10a shows the 23 automatically selected structure curves.



(**a**) Structure curves (**b**) Resulting curvilinear spiral

Figure 10. Structure curves and spiral-like tool path.

4.2. Building and Evaluation of Curvilinear Spiral

Finally, each revolving of curvilinear spiral is built by linear interpolation between two points of the same index (i.e., the same normalized curvilinear abscissa) of two consecutive structure curves. Figure 10b shows the curvilinear spiral built with our method.

Locally, the feedrate is simulated with VPOp. Two turns of the curvilinear spiral are chosen in three zones of the pocket (internal, intermediate, and external). The modeled machine tool is a *Mikron UCP710*. Its characteristics are reported in Table 2 [34].

Table 2. Kinematic characteristics of the Mikron UCP710 machine tool [34].

Mikron UCP710	V_{max} [m/min]	a_{max} [m/s^2]	J_{max} [m/s^3]
X_m	30	2.5	5
Y_m	30	3	5

For each zone, three fitting methods are tested (RAW = no fit, FIR = moving average, HQS = Hermite quartic spline interpolation), and the toolpath length and the milling time are collected. The average feed rate is calculated. The programmed feed rate (V_m) is fixed at 10,000 [mm/min]. Data are summarized in Table 3, and Figure 11 shows the velocity profile as a function of the curvilinear abscissa for the three intermediate toolpaths (black = RAW, blue = HQS, red = FIR). Figure 12 links the velocity profile with the positions of the tool along the curvilinear spiral turns. Slowdowns for points A, B, C, E, F, G are due to the "high" curvature of the toolpath. D and H are, in fact, the beginnings of a curvilinear spiral turn, and there, as already explained, the C^2 connectivity is lost.

Table 3. Simulated milling time for 3 fitting methods.

Toolpath Location	Fitting Method	Toolpath Length [mm]	Milling Time [s]	Δt/t [%]	$\overline{V_m}$ [mm/min]
Internal	RAW	346	19	/	1092
	FIR	345	15.5	−18	1335
	HQS	328	15.8	−17	1245
Intermediate	RAW	650	22	/	1773
	FIR	645	17	−22	2276
	HQS	635	18.5	−16	2059
External	RAW	1383	32.3	/	2569
	FIR	1358	29	−10	2810
	HQS	1398	29	−10	2892

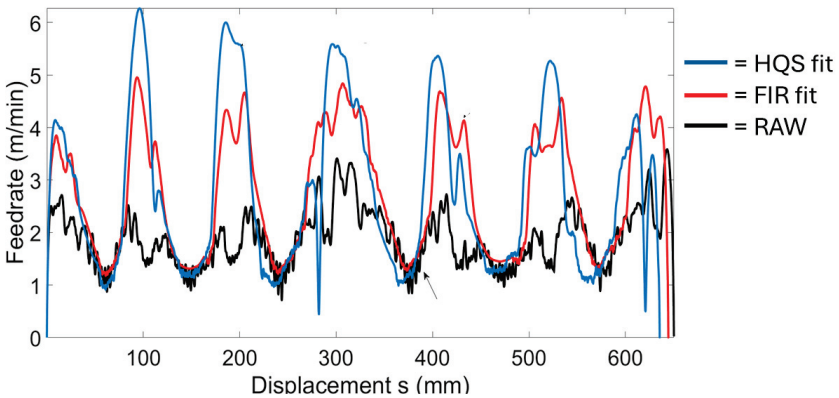


Figure 11. Velocity profile as a function of curvilinear abscissa—intermediate turns.

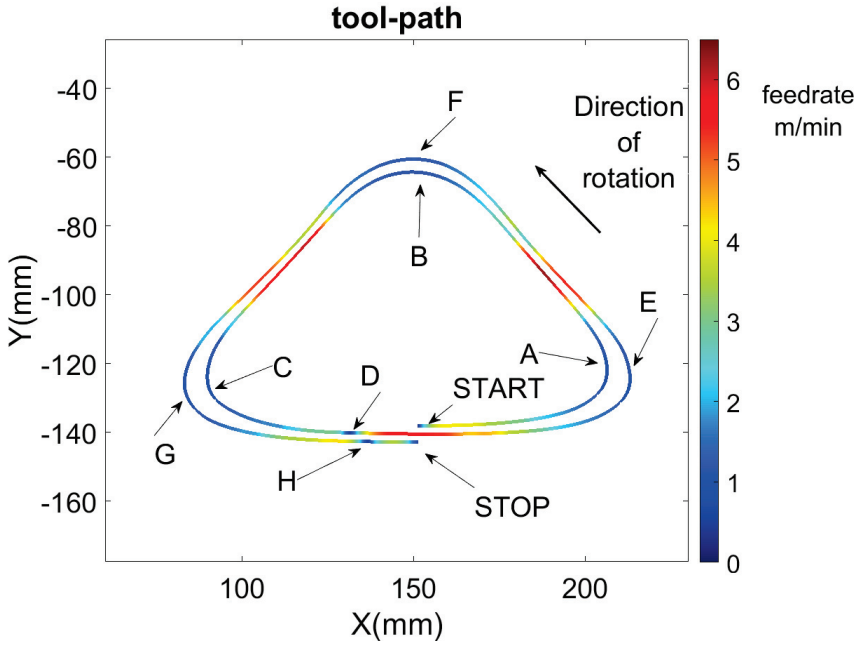


Figure 12. Positions of the feed rate slowdowns along the path (to be linked with Figure 11).

The results in Table 3 demonstrate that the method proposed in the paper, based on the reconstruction of isothermal curves with a small number of Hermite quartic spline patches, reduces the simulated milling time by 10% to 20% in each zone of the pocket, compared to the RAW toolpath. Although the FIR filter is selected for comparison, the HQS method offers an advantage: it maintains control over the distance between the RAW isotherm and the fitted one, a feature not preserved by the FIR method.

The histogram in Figure 13 and the statistical indicators in Table 4 confirm the improvement of the toolpath: small curvatures are more populated, and both Cut95 and Cut99 values are significantly lower for the HQS method. Moreover, this new method eliminates the need for a Fresnel vector to generate the toolpath. Consequently, the limitation of using the Bieterman's method exclusively for 'globally convex pockets' is no longer necessary. Therefore, the HQS method allows the creation of curvilinear toolpaths similar to those by Bieterman and Sandström but applicable to non-convex cavities as demonstrated in the second case study.

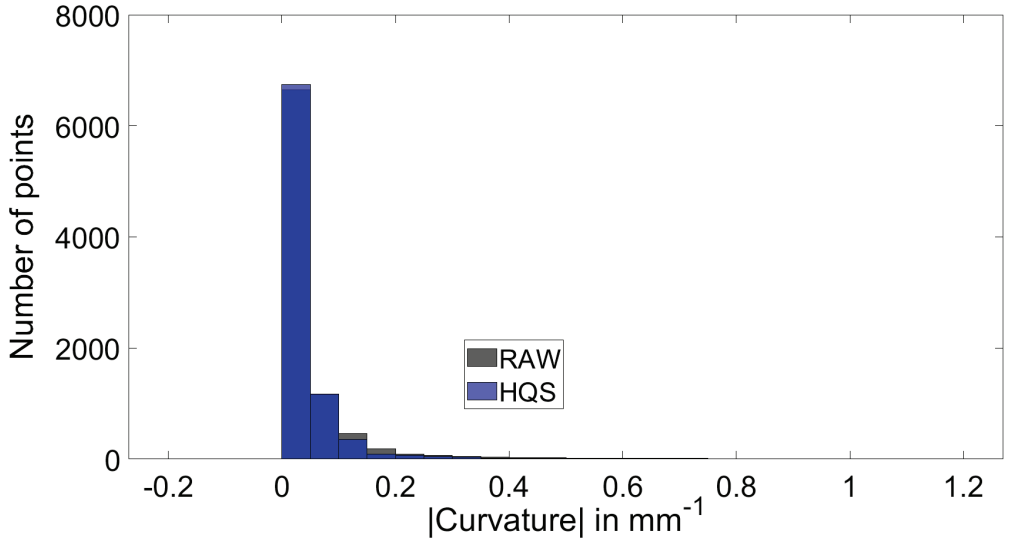


Figure 13. BIG pocket—histogram of $|Curvature|$ for RAW and HQS entire curvilinear spiral.

Table 4. BIG pocket—curvature statistical indicators of entire curvilinear spiral.

	Curvature Absolute Value (|C|, mm^{-1})	
	RAW	**HQS**
Cut95	0.24	0.14
Cut99	1.30	0.97

5. Case Study 2—HUG Pocket

The second test case is a pocket with a similar geometry to the pocket proposed by Huang [35]. The major interest of this geometry is its non-convexity: the winding angle (Fresnel's vector, a polar parametrization) approach proposed by Bieterman [21] is not functional, while the method proposed in this paper can handle such geometries. Figure 14 shows that our isotherms reconstruction method works for building a curvilinear spiral for "globally non-convex" pockets. It is built between 17 isotherms and constructed with around 6500 points. Note that the temperature field has two global maxima symmetrically disposed with the pocket axis: two beginning points for the curvilinear spiral are possible.

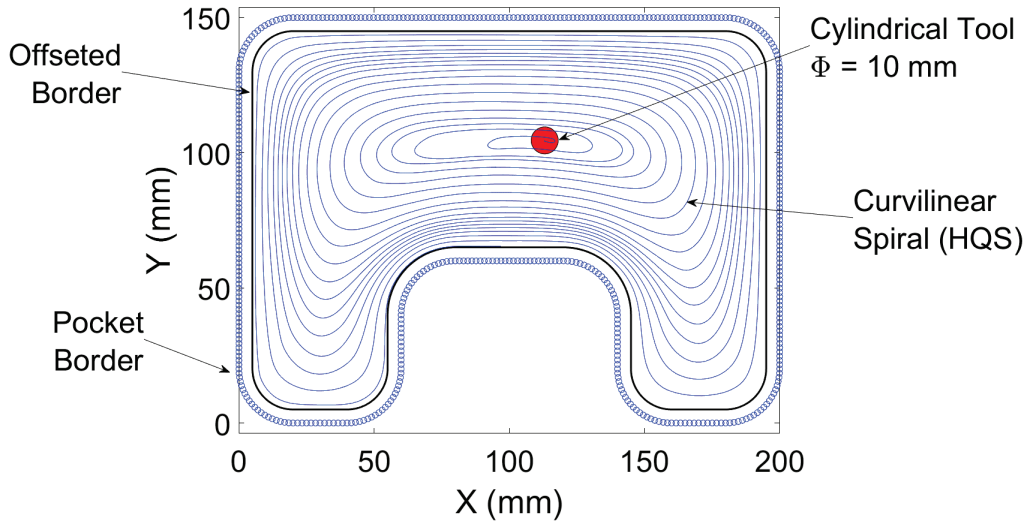


Figure 14. Entire toolpath.

Toolpath Quality Indicators

Figure 15 shows a histogram of curvature for the entire curvilinear spiral.

As mentioned earlier, the method proposed by Bieterman is unable to generate a toolpath for this pocket. The comparison will be made using only RAW and HQS structure curves (isotherms). As in the previous case, three isotherms are selected (Figure 16): external (iso3), intermediate (iso10), and internal (iso14). The histograms (Figure 17), statistical indicators (Table 5), and simulated milling time (Table 6) demonstrate the geometric improvement in the toolpath quality. In each case, the curvature distribution is more concentrated, and Cut95 and Cut99 values are significantly lower. Additionally, the simulated milling time along each isotherm decreases by approximately 20%.

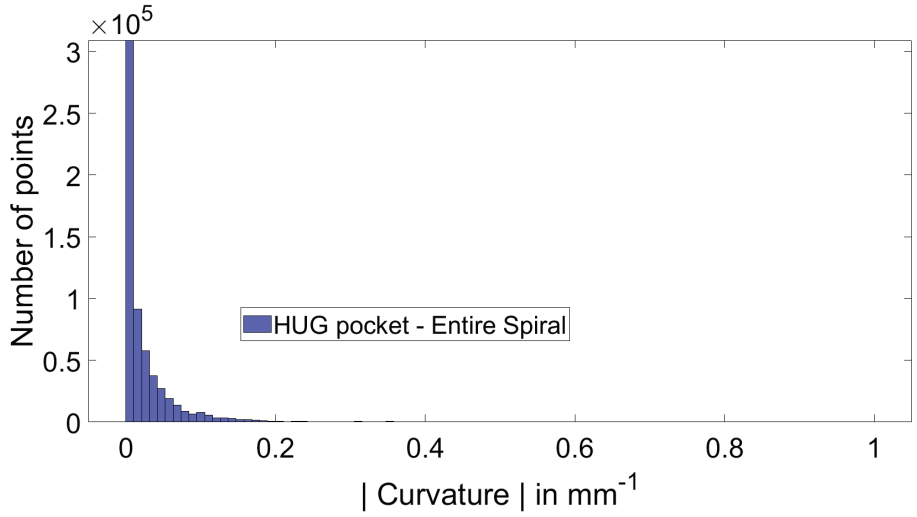


Figure 15. HUG pocket—HQS curvilinear entire spiral.

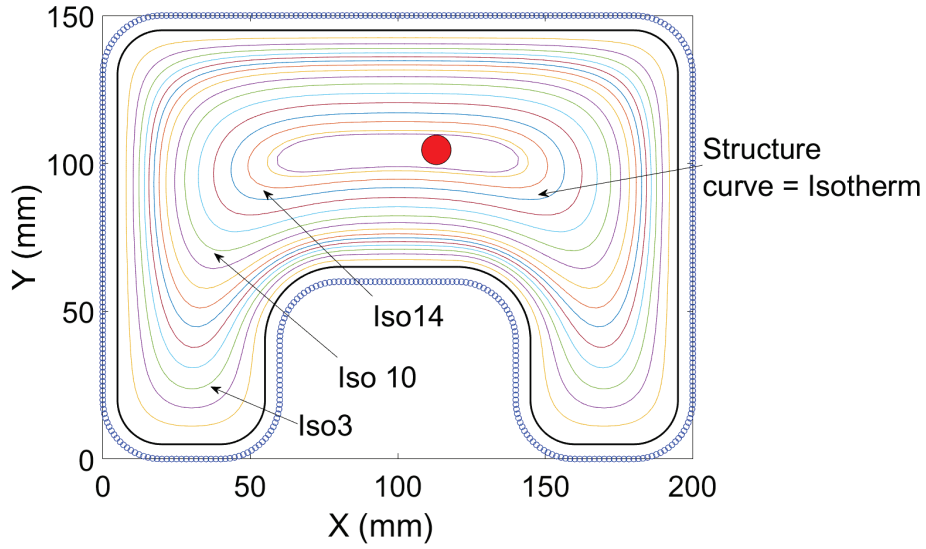


Figure 16. HUG pocket—structure curves.

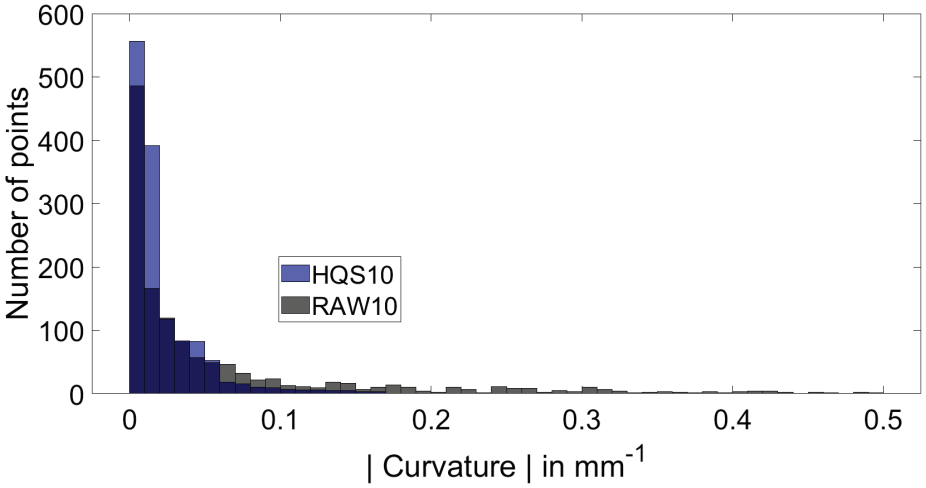


Figure 17. HUG pocket—histogram of curvature absolute value for Iso10.

Table 5. HUG pocket—curvature quality statistical indicators.

	Curvature Absolute Value (|C|, mm^{-1})					
	Entire Spiral					
Cut95	0.12					
Cut99	0.72					
	Iso3		Iso10		Iso14	
	RAW	HQS	RAW	HQS	RAW	HQS
Cut95	0.38	0.07	0.45	0.07	0.44	0.10
Cut99	1.07	0.08	1.05	0.13	1.51	0.12

Table 6. Simulated milling time comparison for 3 structure curves.

Toolpath Location	**Fitting Method**	**Milling Time [s]**	**Δt /t [%]**
Internal (Iso14)	RAW	9	/
	HQS	7.3	−19
Intermediate (Iso10)	RAW	15.2	/
	HQS	12.2	−20
External (Iso3)	RAW	22.3	/
	HQS	17	−24

6. Conclusions

This article proposes a new method to construct curvilinear spiral toolpaths from structure curves obtained by the FEM solution of PDE inspired from a thermal problem. To reduce the tangency discontinuities due to discretization, the structure curves of the spiral are rebuilt with Hermit quartic spline patches. This method performs the following:

- Models structure curves for any geometry of pockets thanks to the associated thermal model;
- Guarantees a C^2 continuity of the structure curves and enhances the continuity level of the curvilinear spiral;
- Creates a toolpath having, globally, a low curvature;
- Allows the user to define a maximum chordal error along the structure curves.

Two representative geometries of pockets are used as examples and show reductions of 10 to 18% of machining time as compared to the state of the art. The proposed method also offers a generalization to non-convex pockets as compared to methods from the literature. In the future, the goal will be the use of Hermite quartic curves directly in a numerical controller that can handle spline interpolations.

Author Contributions: Conceptualization, C.L.; methodology, C.L.; software, C.L. and S.L.; validation, C.L.; formal analysis, C.L. and É.R.-L.; investigation, C.L.; writing—original draft preparation, C.L.; writing—review and editing, C.L., S.L. and É.R.-L.; visualization, C.L.; supervision, É.R.-L.; project administration, É.R.-L.; funding acquisition, É.R.-L. All authors have read and agreed to the published version of the manuscript.

Funding: This research received no external funding.

Institutional Review Board Statement: Not applicable.

Informed Consent Statement: Not applicable.

Data Availability Statement: The data presented in this study are available on request from the corresponding author.

Acknowledgments: We wish to thank the LURPA lab from ENS Paris-Cachan for the collaboration proposition and the VPOp licensing agreement, X. Beudaert for the developed software and S. Lavernhe for its parametrization, Fl. Poulaert for the language correction of the paper.

Conflicts of Interest: The authors declare no conflicts of interest.

Glossary

Abbreviation	**Meaning**
BIG	Pocket used by Bieterman [21]
Cut95	95% quantile of absolute curvature value
Cut99	99% quantile of absolute curvature value
FEM	Finite Element Method
FIR	Finite Impulse Response = a Filtering Method
GA	Genetic Algorithm Method
GM	Gradient Descent Method
HQS	Hermite Quartic Spline interpolation
HUG	Pocket geometry used by Huang [35]
iso	Isotherm curve
isoHQ	Isotherm fitted with HQS method
PDE	Partial differential equation
RAW	No Fit used
VPOp	Velocity Profile Optimization software [33]
Nomenclature	**Meaning**
C_0	Initial curvature of a patch (mm^{-1})
C_1	Final curvature of a patch (mm^{-1})
D_{isoHQ}	Distance between 2 fitted isotherms (mm)
D_{max}	Acceptable distance between HQS spline and isotherm points (mm)
D_{offset}	Offset distance (mm)
D_{opt}	Optimized distance between patch and isotherm points (mm)
D_{rte}	Radial tool engagement (mm)
k_0, k_1, α, β	The four parameters of Hermite Quartic Spline interpolation
u	The interpolant of Hermite Quartic Splines
ea_0, ea_1, eb_0, eb_1	The four blending functions of Hermite Quartic Splines
s	Curvilinear length (mm)
ϕ_{tool}	Diameter of the tool (mm)
$\rho_S(\theta_i)$	Discrete polar equation of a spiral-like turn
$\rho_{ext}(\theta_i)$	Discrete polar equation of an external isotherm
$\rho_{int}(\theta_i)$	Discrete polar equation of an internal isotherm

References

1. Tlusty, G. *Manufacturing Process and Equipment*, 1st ed.; Pearson: Hoboken NJ, USA, 1999.
2. Altan, T.; Lilly, B.; Yen, Y.C.; Altan, T. Manufacturing of Dies and Molds. *CIRP Ann.—Manuf. Technol.* **2001**, *50*, 404–422. [CrossRef]
3. M'Saoubi, R.; Chandrasekar, S. Editorial—Special issue "The cutting of metals: Exploring phenomena at the confluence of materials and extreme mechanics". *Int. J. Mach. Tools Manuf.* **2021**, *168*, 103769. [CrossRef]
4. Zhang, D.; Zhang, X.M.; Nie, G.C.; Yang, Z.Y.; Ding, H. Characterization of material strain and thermal softening effects in the cutting process. *Int. J. Mach. Tools Manuf.* **2021**, *160*, 103672. [CrossRef]
5. Ping, Z.; Yue, X.; Shuangfeng, H.; Ailing, S.; Baoshun, L.; Xiao, Y. Experiment and simulation on the high-speed milling mechanism of aluminum alloy 7050-T7451. *Vacuum* **2020**, *182*, 109778. [CrossRef]
6. Aurich, J.C.; Kieren-Ehses, S.; Mayer, T.; Bohley, M.; Kirsch, B. An investigation of the influence of the coating on the tool lifetime and surface quality for ultra-small micro end mills with different diameters. *CIRP J. Manuf. Sci. Technol.* **2022**, *37*, 92–102. [CrossRef]
7. D'Souza, R.M. On setup level tool sequence selection for 2.5-D pocket machining. *Robot. Comput.-Integr. Manuf.* **2006**, *22*, 256–266. [CrossRef]
8. Aggarwal, S.; Xirouchakis, P. Selection of optimal cutting conditions for pocket milling using genetic algorithm. *Int. J. Adv. Manuf. Technol.* **2013**, *66*, 1943–1958. [CrossRef]
9. Wu, L.; Li, C.; Tang, Y.; Yi, Q. Multi-objective Tool Sequence Optimization in 2.5D Pocket CNC Milling for Minimizing Energy Consumption and Machining Cost. *Procedia CIRP* **2017**, *61*, 529–534. [CrossRef]
10. Bouard, M.; Pateloup, V.; Armand, P. Pocketing toolpath computation using an optimization method. *Comput.-Aided Des.* **2011**, *43*, 1099–1109. [CrossRef]
11. Patel, D.D.; Lalwani, D.I. Quantitative Comparison of Pocket Geometry and Pocket Decomposition to Obtain Improved Spiral Tool Path : A Novel Approach. *J. Manuf. Sci. Eng.* **2018**, *139*, 031020. [CrossRef]

12. Romero, P.E.; Dorado, R.; Díaz, F.A.; Rubio, E.M. Influence of Pocket Geometry and Tool Path Strategy in Pocket Milling of UNS A96063 Alloy. *Procedia Eng.* **2013**, *63*, 523–531. [CrossRef]
13. Lavernhe, S.; Tournier, C.; Lartigue, C. Kinematical performance prediction in multi-axis machining for process planning optimization. *Int. J. Adv. Manuf. Technol.* **2008**, *37*, 534–544. [CrossRef]
14. Beudaert, X.; Lavernhe, S.; Tournier, C. Feedrate interpolation with axis jerk constraints on 5-axis {NURBS} and {G1} tool path. *Int. J. Mach. Tools Manuf.* **2012**, *57*, 73–82. [CrossRef]
15. Pateloup, V.; Duc, E.; Ray, P. Bspline approximation of circle arc and straight line for pocket machining. *Comput.-Aided Des.* **2010**, *42*, 817–827. [CrossRef]
16. Altintas, Y.; Tulsyan, S. Prediction of part machining cycle times via virtual CNC. *CIRP Ann.* **2015**, *64*, 361–364. . [CrossRef]
17. Herzog, R.; Blanc, P. Optimal G2 Hermite interpolation for 3D curves. *Comput.-Aided Des.* **2019**, *117*, 102752. [CrossRef]
18. Xiong, Z.H.; Zhuang, C.G.; Ding, H. Curvilinear tool path generation for pocket machining. *Proc. Inst. Mech. Eng. Part B J. Eng. Manuf.* **2011**, *225*, 483–495. [CrossRef]
19. Held, M.; de Lorenzo, S. On the generation of spiral-like paths within planar shapes. *J. Comput. Des. Eng.* **2018**, *5*, 348–357. [CrossRef]
20. Abrahamsen, M. Spiral tool paths for high-speed machining of 2D pockets with or without islands. *J. Comput. Des. Eng.* **2019**, *6*, 105–117. [CrossRef]
21. Bieterman, M.B.; Sandstrom, D.R. A Curvilinear Tool-Path Method for Pocket Machining. *J. Manuf. Sci. Eng.* **2003**, *125*, 709–715. [CrossRef]
22. Sun, S.; Altintas, Y. A G3 continuous tool path smoothing method for 5-axis CNC machining. *CIRP J. Manuf. Sci. Technol.* **2021**, *32*, 529–549. [CrossRef]
23. Xu, J.; Sun, Y.; Zhang, X. A mapping-based spiral cutting strategy for pocket machining. *Int. J. Adv. Manuf. Technol.* **2013**, *67*, 2489–2500. [CrossRef]
24. Romero-Carrillo, P.; Torres-Jimenez, E.; Dorado, R.; Díaz-Garrido, F. Analytic construction and analysis of spiral pocketing via linear morphing. *Comput.-Aided Des.* **2015**, *69*, 1–10. [CrossRef]
25. Held, M.; Spielberger, C. Improved Spiral High-Speed Machining of Multiply-Connected Pockets. *Comput.-Aided Des. Appl.* **2014**, *11*, 346–357. [CrossRef]
26. Song, D.N.; Ma, J.W.; Zhong, Y.G.; Yao, J.J. Global smoothing of short line segment toolpaths by control-point-assigning-based geometric smoothing and FIR filtering-based motion smoothing. *Mech. Syst. Signal Process.* **2021**, *160*, 107908. [CrossRef]
27. Hua, L.; Huang, N.; Yi, B.; Zhao, Y.; Zhu, L. Global toolpath smoothing for CNC machining based on B-spline approximation with tool tip position adjustment. *Int. J. Adv. Manuf. Technol.* **2023**, *125*, 3651–3665. [CrossRef]
28. Pateloup, V.; Duc, E.; Ray, P. Corner optimization for pocket machining. *Int. J. Mach. Tools Manuf.* **2004**, *44*, 1343–1353. [CrossRef]
29. Held, M.; Spielberger, C. A smooth spiral tool path for high speed machining of 2D pockets. *Comput.-Aided Des.* **2009**, *41*, 539–550. [CrossRef]
30. Banerjee, A.; Feng, H.Y.; Bordatchev, E.V. Process planning for corner machining based on a looping tool path strategy. *Proc. Inst. Mech. Eng. Part B J. Eng. Manuf.* **2011**, *225*, 1578–1590. [CrossRef]
31. Courant, R.; Hilbert, D. *Methods of Mathematical Physics: Partial Differential Equations*; John Wiley & Sons: New York, NY, USA, 2008.
32. Xie, J.; Liu, X. The EH interpolation spline and its approximation. *Abstr. Appl. Anal.* **2014**, *2014*, 745765. [CrossRef]
33. Beudaert, X. Commande Numérique Ouverte: Interpolation Optimisée Pour L'usinage 5 Axes Grande. Ph.D. Thesis, ENS Cachan, Gif-sur-Yvette, France, 2013.
34. Grandguillaume, L.; Lavernhe, S.; Tournier, C. A tool path patching strategy around singular point in 5-axis ball-end milling. *Int. J. Prod. Res.* **2016**, *54*, 7480–7490. [CrossRef]
35. Huang, N.; Lynn, R.; Kurfess, T. Aggressive Spiral Toolpaths for Pocket Machining Based on Medial Axis Transformation. *J. Manuf. Sci. Eng.* **2017**, *139*, 051011. [CrossRef]

Disclaimer/Publisher's Note: The statements, opinions and data contained in all publications are solely those of the individual author(s) and contributor(s) and not of MDPI and/or the editor(s). MDPI and/or the editor(s) disclaim responsibility for any injury to people or property resulting from any ideas, methods, instructions or products referred to in the content.

applied sciences

MDPI

Article

Statistical Analysis of Cutting Force and Vibration in Turning X5CrNi18-10 Steel

Csaba Felhő * and Tanuj Namboodri

Institute of Manufacturing Science, University of Miskolc, 3515 Miskolc, Hungary;
tanuj.namboodri@student.uni-miskolc.hu
* Correspondence: csaba.felho@uni-miskolc.hu

Abstract: X5CrNi18-10 is a corrosion-resistant steel that has become popular in the automotive, marine, food, nuclear, and other industries. Chromium alloyed in the X5CrNi18-10 increases the material's toughness, which influences the cutting phenomena such as the cutting force and vibration. It is necessary to investigate the effect of the machining parameters on the X5CrNi18-10 turning, particularly the feed, which has significant effects on the cutting phenomena. The objective of this research is to investigate the correlation between the feed and cutting phenomena to improve the product quality, reduce machining disruptions, and optimize the parameters for a low cutting speed and vibration. Statistical analysis has shown promise in identifying the impact of variables using correlation analysis and estimated marginal means plots. This study highlights the findings of the Pearson's correlation analysis between the feed, active cutting force, and active vibration as well as the estimated marginal means plots between the machining parameters and cutting phenomena. The results indicate that there is a strong correlation between the feed and active cutting force with a coefficient of correlation of 0.688, as well as the feed and active vibration with a coefficient of correlation of 0.697. The estimated marginal means plots indicate that as the cutting speed increases, the value of the active vibration and the active force decreases.

Keywords: cutting force analysis; vibration analysis; turning process; X5CrNi18-10 steel; statistical analysis; machining dynamics; regression analysis

1. Introduction

Corrosion-resistant steels are an important group of materials with mechanical and corrosion-resistant properties, which are an essential part of the engineering industry. These steels are widely used in several industries, including automotive, marine, aerospace, medical, food, and nuclear [1]. Among these, austenitic stainless steels (ASSs) account for more than 70% of the stainless-steel groupings [2–6]. Chromium (Cr) forms a protective passivation layer in an oxidizing environment. However, the same properties make the material difficult to machine [7]. The machinability of this steel grade is affected by a high tendency to deformation strengthening, low thermal conductivity, and good ductility [8]. These issues complicate achieving a surface in the high-precision accuracy class, which is important in marine pump shafts and automotive components. X5CrNi18-10 is highly tough; therefore, it is necessary to understand the cutting conditions like the cutting force and vibration during the machining process to identify the optimal machining parameters, including the cutting speed, feed rate, and depth of cut. The cutting force helps to remove the excess material, which plays a critical role in the turning process. Analysis of the cutting

force is very important to understand the machinability of the material, especially when the material possesses properties like toughness. The cutting force can be divided into three components, as shown in Figure 1: the cutting force ($\vec{F_c}$), which is tangential, the feed force ($\vec{F_f}$), which is axial, and the radial force ($\vec{F_r}$), which is also radial. However, the effective force that is responsible for the main cutting force is called the active force ($\vec{F_a}$), which is the sum of various components of the cutting and feed forces. The passive force is the radial force, which is irrelevant because the workpiece and tool remain stationary in the direction of force. The active force ($\vec{F_a}$) or ($\vec{AF}$) in turning operation is noted by Equation (1).

$$\vec{F_a} = \sqrt{F_c^2 + F_f^2} \tag{1}$$

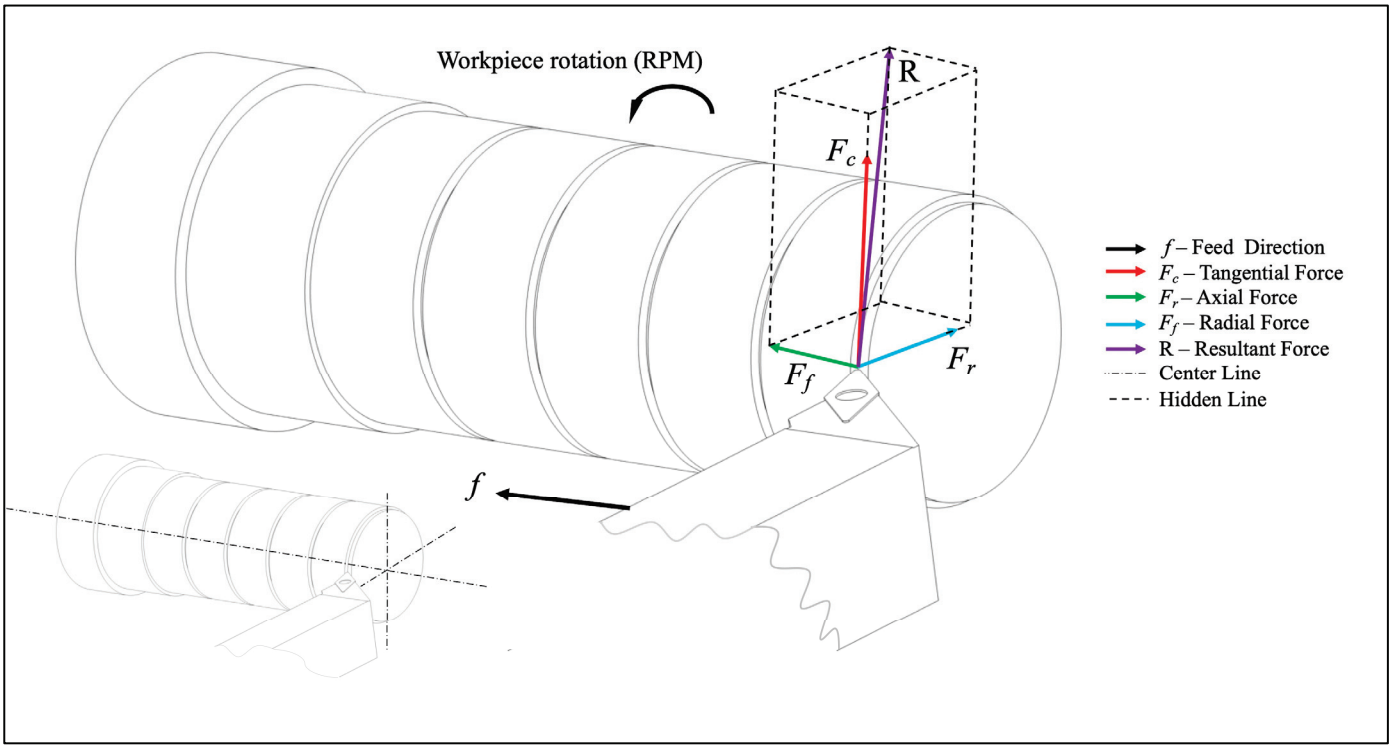


Figure 1. Direction of forces in the turning operation.

A larger cutting force generates a poor surface finish and extensive surface damage during high-speed turning [9]. Understanding cutting phenomena also requires the study of the vibration induced by the cutting force components. These vibrations have an impact on common machining processes, including turning, milling, and drilling. In an investigation, it was found that the variations in cutting force components and vibration have a direct impact on the flank wear [10]. It was concluded that vibration is a common concern in turning processes, affecting machining results, particularly tool wear [11]. Machining vibrations, often known as chatter, have several effects on the quality characteristics of the final machined product. Like the cutting force, the induced vibration can also be divided into three components: tangential (V_t), axial (V_a), and radial (V_r) vibrations; however, the effective vibration, which is responsible for affecting the quality parameters, is tangential and radial. The effective vibration (V_e) or (AV_b) can be defined by Equation (2), as follows. The effective vibration is the sum of tangential (V_t) and radial (V_r). The study [12] calculated the component's RMS values and found that the vibration RMS values are much smaller in

the axial direction because the tool is moving in the axial direction; so, the vibration values can be neglected in the axial [13].

$$V_e = \sqrt{V_t^2 + V_r^2} \quad (2)$$

Several researchers [14–19] have studied vibration and its effect on the quality parameters of the machined surface, mainly the surface roughness. Cutting forces and vibration are the result of the machining parameters; proper selection of these parameters can lower the value of cutting forces and vibration during the machining, which affects the quality parameters of the machined surface, mainly the surface roughness. Optimal cutting parameters, including the cutting speed, feed rate, and depth of cut, are crucial for improving the machinability and extending the tool life. The feed rate significantly affects the signal characteristics of cutting forces and vibrations, with a specific frequency band most sensitive to these changes [20]. Increasing the feed rate increases the cutting forces, while the cutting force decreases with increasing speed [21]. Monitoring the cutting phenomenon improves productivity, increases the tool life, and avoids disruption in machining; several scholars [17,22–26] have used various methodologies to investigate the correlations between the machining parameters, cutting forces, and vibration. However, no significant conclusion has been drawn that highlights the relationship between the feed rate, cutting forces, and vibration.

As a result, understanding the effects of cutting phenomena like cutting forces and vibration in X5CrNi18-10 steel grade is important to avoid failures in manufacturing processes, particularly those involving machining. This research aims to study the correlation between the feed, cutting forces, and vibration in the turning of X5CrNi18-10 steel grade using a piezoelectric dynamometer and MPU6050 sensor, and to check the validity of the regression model, analysis of variance (ANOVA) is used. Additionally, this research highlights the effect of machining parameters—the feed, cutting speed, and depth of cut on the cutting forces and vibration using estimated marginal means plots.

2. Materials and Methods

The test material for this study is steel X5CrNi18-10; it is an austenitic chrome nickel steel. Nickel is an austenitic-forming element that expands the austenite region in Fe alloys. Although chromium belongs to ferrite-forming elements, with a suitable concentration of Cr and Ni, these steels have an austenitic structure at room temperature [27]. The chemical composition with a weight percentage of X5CrNi18-10 (1.4301), according to EN10088-2, is provided in Table 1.

Table 1. Chemical composition of steel X5CrNi18-10 (1.4301): EN10088-2 (weight%) [28].

C	Si	Mn	Ni	P	S	Cr	N
≤0.07	≤1	≤2	8–10.5	≤0.045	≤0.015	17.5–19.5	≤0.11

Figure 2 highlights the diameter of the workpiece. The specimen was divided into five equal surfaces of 30 mm length, each with a gap of 4 mm between the surfaces and a 5 mm depth, creating a groove parting the surfaces. These surfaces were divided to experiment with the different machining parameters where the feed, depth of cut, and cutting speed were varied according to the design of the experiments. The vibration and cutting forces data were recorded on each surface. Initially, the specimen was a 50 mm cylinder. Four specimens were used in the experiment, providing a total of twenty surfaces; however, only eighteen surfaces were used in the experiment, per the design of the experiment.

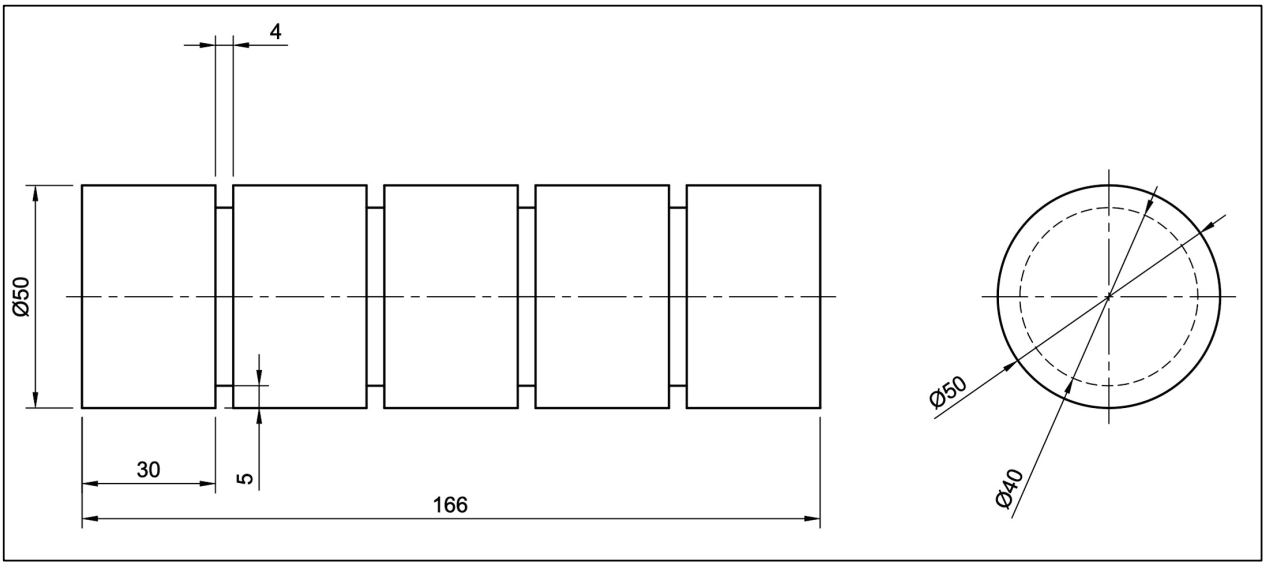


Figure 2. Drawing of workpiece specimen.

The tool used in the experiment was the DDJNL2525M15 from Seco Tools, Björnbacksvägen, Sweden [29], shown in Figure 3. The tool's shank is 25 mm in height (H) and breadth (B), providing stability while turning. The rotary holder version given is R for right-handed operation. The turning inserts have a basic shape known as D, which relates to a 55° insert angle. The tool's overall length L1 is 150 mm, ensuring sufficient reach during operations, and the clamping system is labelled as D, indicating the method used to secure the insert. The angle of attack of the holder is defined as J at 93°, which influences the tool's alignment during the cut. In addition, the cutting edge of the cutting insert is 15 mm. The specification of the tool is presented in Table 2.

Table 2. DDJNL2525M15 tool description [29].

Shank Height (H)	Shank Width (B)	Rotary Holder Version	Turning Inserts Basic Shape	Total Length (L1)	F	Clamping System	Angle of Attack Holder	Edge Length
25 mm	25 mm	R (right)	D 55°	M 15 mm	32 mm	D	J 93°	15 mm

A Seco Tools DNMG150604-MF1 insert was used during all the experiments; the insert specifications are provided in Figure 3. The insert size and form are denoted by DN 1506, which denotes a specific geometric arrangement suited for a variety of turning operations. It is made of carbide with a PVD coating, which improves the wear resistance and cutting performance. The insert is labelled neutral in terms of hand orientation, which means it can be used in both left- and right-handed applications. The cutting-edge length is 15.5 mm, providing a large cutting surface for material removal. The insert's thickness is 6.35 mm, ensuring endurance and strength during cutting operations. The corner radius is 0.4 mm, which affects the finishing quality and lowers the cutting forces.

The finish turn OD turning operation was carried out to obtain experimental data in the wet condition. The HAAS ST-20 Y series machine from Leoben, Austria, was used to conduct all the experiments, as shown in Figure 4a; this machine is a Y-axis CNC turning center, with a max capacity of 298 × 572 mm, 63.5 mm bar, 533 mm swing, ± 50.8 mm Y-axis travel, 20 hp vector drive, 4000 rpm, A2–6 spindle, 210 mm chuck, and a 12-station BMT 65 turret. This machine is suitable for larger workpieces and for complex operations [30]. The coolant used during the experiment was a 5% emulsion of CIKS HKF 420 type oil. It was necessary to use this coolant to achieve the best results.

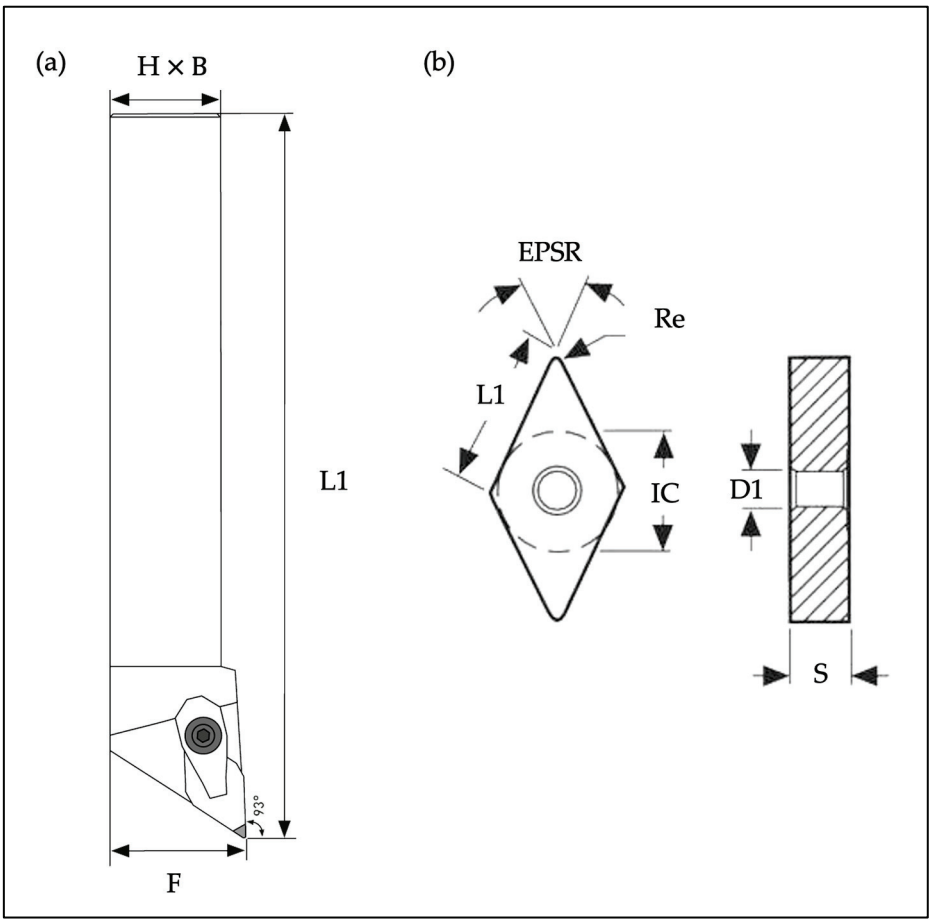


Figure 3. (**a**) Tool description; (**b**) insert specification [29].

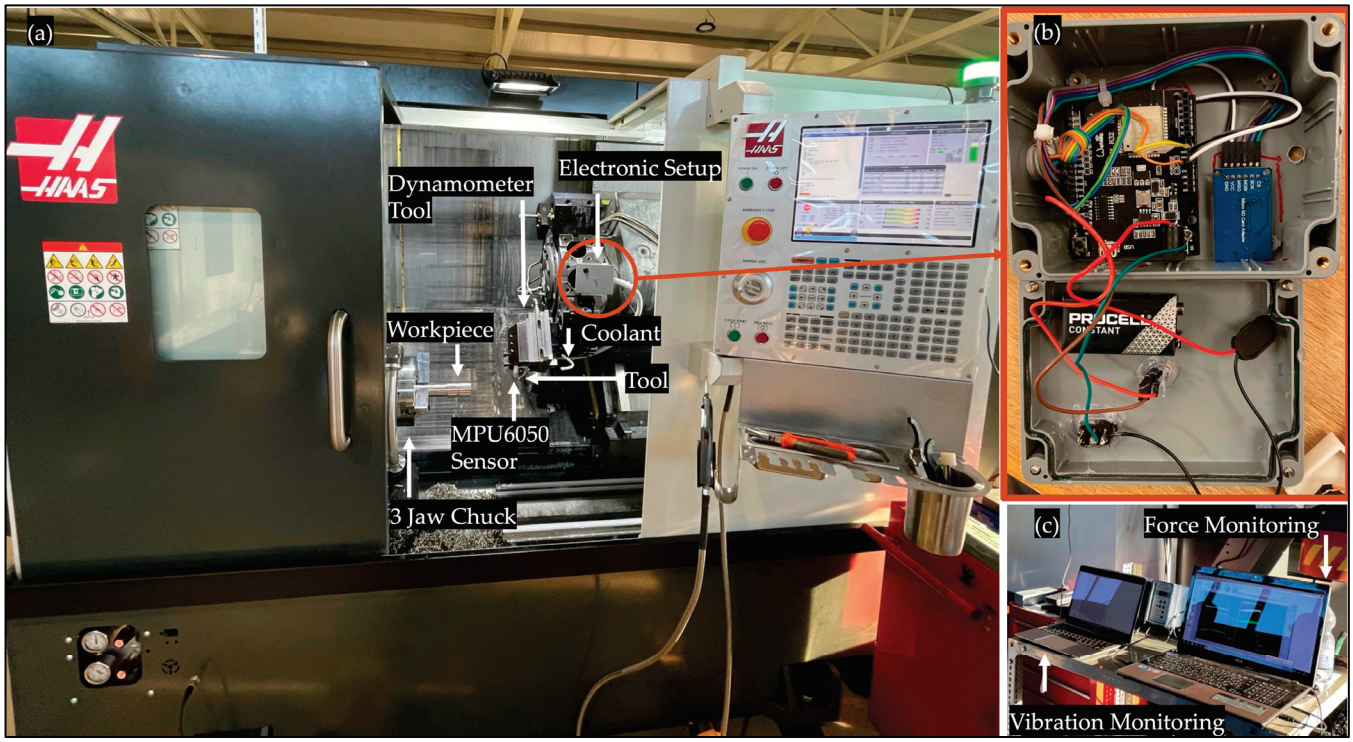


Figure 4. (**a**) HAAS ST-20 Y CNC machine; (**b**) electronic setup; (**c**) real-time monitoring vibration and cutting forces.

Figure 4b represents the device developed to measure the vibration signals during the turning operation. Two monitors were used in the experiment, one for monitoring the vibration signals and another for monitoring the cutting forces. The vibration signal measurement device was fabricated using a 3D printer and milling on the plastic box, and the sensor case was printed to prevent it from chips and coolant lubricant used during the machining operation. A wire casing was provided so that the chips falling during operation did not interrupt the measurement. A switch and LED were included in the developed device so that after all the initialization and checkup, when the LED switch turned on and emitted the green light, it showed that everything was working, and the vibration signals were saved in the attached SD card. The sensor was attached to the tool with the clip to collect the vibrational data, as shown in Figure 5a,b. The electronic setup box was screwed on the tool holder; the setup allowed the electronic box to be stationary concerning the movement of the tool, which provided an uninterrupted connection to the experiment. The direction of the sensor with respect to the tool direction was the same as the dynamometer direction, where Y is radial, X is tangential, and Z is axial. The cutting force components were measured using a three-component piezoelectric dynamometer from Kistler Corporation 9257-A from Kistler AG, Winterthur, Switzerland, Figure 5a,b.

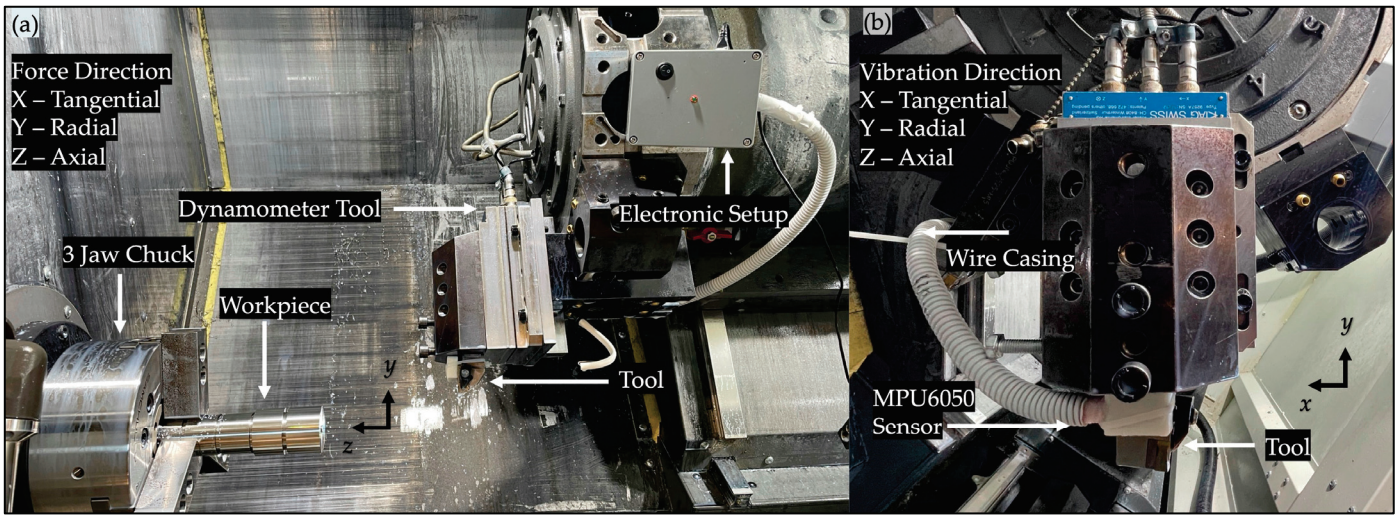


Figure 5. (**a**) Experimental setup. (**b**) Vibration sensor and dynamometer setup.

The dynamometer output was amplified using a charge meter Kistler Corporation Model 5015A for three force components, i.e., Fx, Fy, Fz, which was connected to the National Instruments Compact DAQ-9171 from NI Hungary Kft., Debrecen, Hungary. It is a four-channel data acquisition unit (USB). The amplified signals from the charge amplifier are supplied into the data acquisition system, where they are transformed into digital output, which is then transferred to the computer. The setup allowed for the installation of a dynamometer between the tool holder of the CNC lathe and the tool without interacting with other parts. The three cutting force components were measured, as seen in Figure 5a. The tool, dynamometer, and sensor position are defined in Figure 5a and 5b, respectively, and the monitor allows the validation of the data during the process; to avoid any error, it is recommended to visualize the real-time data. This configuration allowed the experiment to be conducted cleanly and without errors.

The experiments were designed based on Taguchi's orthogonal array (OA). In this setup, the depth of cut was examined at two levels, 0.5 mm, and 1 mm, the cutting speed was examined at three levels, at 150, 200, and 300 m/min, and the feed rate was also varied at three levels, 0.08, 0.16, and 0.24 mm/r. According to Taguchi's rules, the selection of a

suitable orthogonal array depends on the total number of degrees of freedom (DOF) of the processing parameters, the total DOF for the experiment is 5, and the selected OA should consist of at least as many degrees of freedom. The L_{18} array provided sufficient variation to analyze these factors. Table 3 represents Taguchi's orthogonal array, designed systematically to investigate the influence of various machining parameters on the performance outcomes.

Table 3. Taguchi's orthogonal array L_{18}.

No.	Depth of Cut (a_p) mm	Cutting Speed (V_c) m/min	Feed Rate (f) mm/rev
1	0.5	150	0.08
2	0.5	150	0.16
3	0.5	150	0.24
4	0.5	200	0.08
5	0.5	200	0.16
6	0.5	200	0.24
7	0.5	300	0.08
8	0.5	300	0.16
9	0.5	300	0.24
10	1	150	0.08
11	1	150	0.16
12	1	150	0.24
13	1	200	0.08
14	1	200	0.16
15	1	200	0.24
16	1	300	0.08
17	1	300	0.16
18	1	300	0.24

3. Results

The vibration and cutting forces were measured in each experiment to understand the relationship and behavior of the machining parameters on each other.

3.1. Vibration Analysis

The vibrational data were collected through the electronic setup; as mentioned in the experimental setup, the data were saved in "[dot] csv" format with order time (ms). The selected range of the accelerometer has a full-scale ±2 g, a sensitivity of 16,384 LSB/g, and a sampling data rate of 1 kHz. Acceleration in the X direction (AccX) (m/s^2) is tangential acceleration, acceleration in the Y direction (AccY) (m/s^2) is radial acceleration, the acceleration in the Z direction is axial, and it was kept at zero intentionally because of the movement of the tool in the Z direction. The active vibration consists of the X and Y components. After the collection of data, Origin Pro 2024b academic licensed software was used to process the data and analyze the signals during the machining process. The raw or unfiltered data from the sensor, where the vibrational signals in are terms of acceleration in the X direction and acceleration in the Y direction, were computed, and the magnitude was taken. Figure 6 represents the magnitude of the tangential and radial acceleration. The active vibration (AV_b) is the sum of the tangential and radial acceleration, as mentioned in Equation (2).

The data were separated according to the surface to calculate the relation between the vibration and the machining parameters. EX in Figures 6 and 7 means the experiment number. The change in feed values is defined by three colors: dark blue, where the value of the feed is 0.08 mm/rev, pink, with a feed rate of 0.16 mm/rev, and sky blue, with a feed rate of 0.24 mm/rev. The cutting speed in Figures 6 and 7 is also represented by three

colors, dark grey with V_c—150 m/min, Light grey with V_c—200 m/min, and orange with V_c—300 m/min. These colors help to visualize the effect of the machining parameters on the vibration and cutting forces.

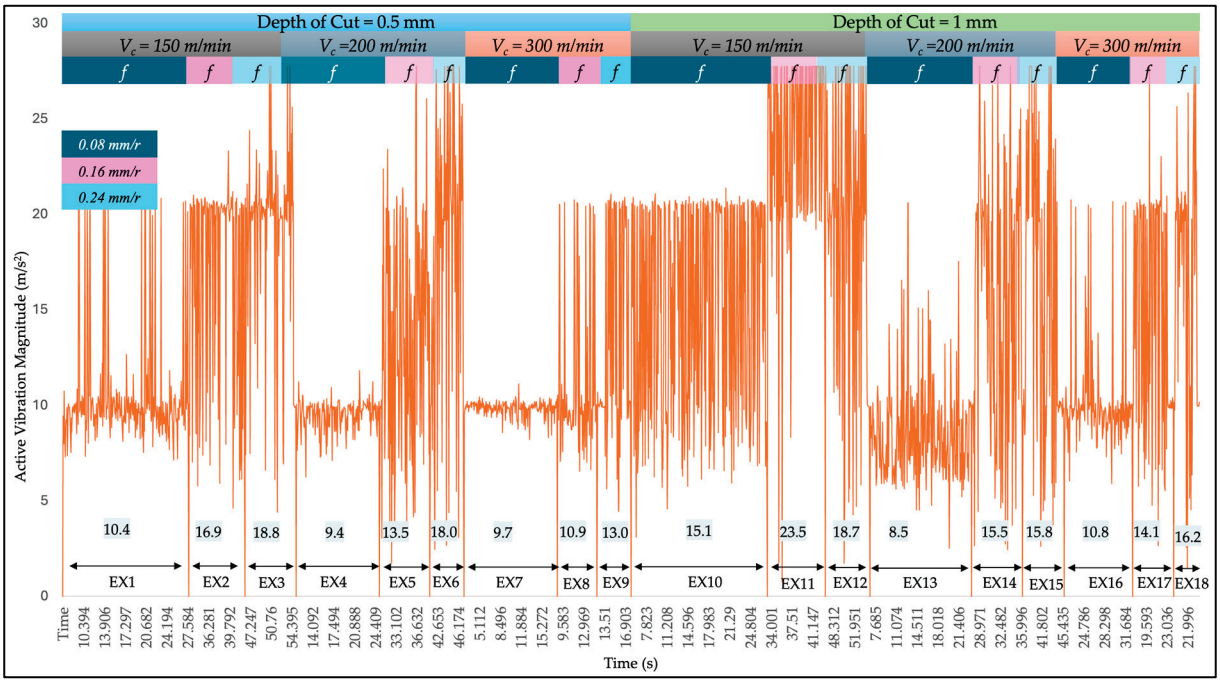


Figure 6. The magnitude of active vibration with time for each experiment.

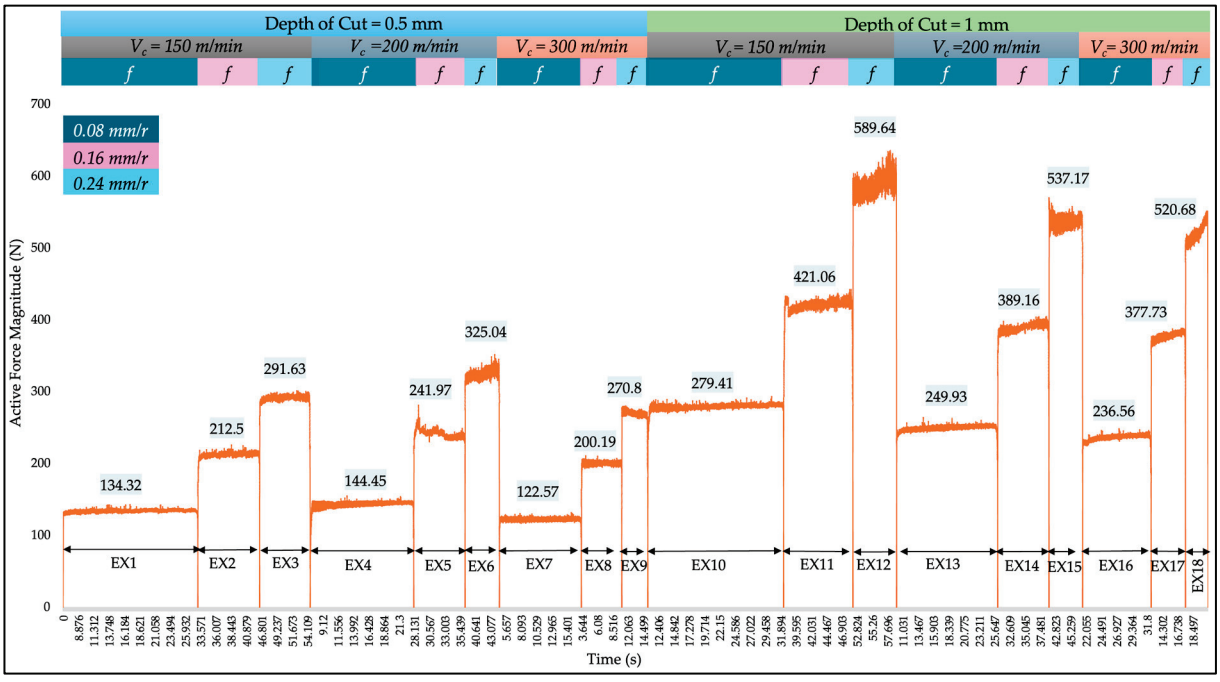


Figure 7. Magnitude of active force with time for each experiment with changes in machining parameters.

It can be visualized from Figure 6 that the total no. of experiments was eighteen, and active vibration RMS is computed for each experiment. The horizontal axis represents the time in seconds. Figure 6 displays the depth of cut on the top, the cutting speed below it, and the feed rate used for each experiment.

Figure 6 can be used to analyze the effect of vibration in each experiment with a change in parameter. It can be analyzed from Figure 6 that, during each used machining parameter,

the value of the active vibration RMS is low, high, or medium. The vibration analysis represents that with an increase in the feed rate, the vibration during the machining process also increases.

It can be concluded from Figure 6 that, with a lower feed rate (f)—0.08 mm/rev, V_c—200 m/min and 300 m/min, and a_p—0.5 mm and 1 mm, less vibration can be achieved in the turning of X5CrNi18-10. The lowest value of the active vibration RMS can be seen in EX13 with DOC (a_p)—1 mm, V_c—200 m/min, and f—0.08 mm/rev, but the signal peaks are high in that period; however, in EX4, with DOC (a_p)—0.5 mm, V_c—200 m/min, and f—0.08 mm/rev, there are better results with a low active vibration RMS value and low peaks.

The highest value of the active vibration RMS can be seen in EX11 with DOC (a_p)—1 mm, V_c—150 m/min, and f—0.16. EX12 also shows the high peaks of vibration with high variation, which suggests that these machining parameters DOC (a_p)—1 mm, V_c—150 m/min, and f—0.24 mm/rev, will impact the quality of the product and tool [10,11]. The other active vibration magnitude values are highlighted in Figure 6 and Table 4.

Table 4. Machining parameters and results for correlation analysis.

Exp. No.	DOC (a_p) mm	V_c m/min	f mm/rev	AV_b RMS m/s^2	AF RMS N
1	0.5	150	0.08	10.96	134.32
2	0.5	150	0.16	17.83	212.53
3	0.5	150	0.24	19.56	291.63
4	0.5	200	0.08	9.56	144.45
5	0.5	200	0.16	14.87	241.97
6	0.5	200	0.24	19.61	325.04
7	0.5	300	0.08	9.84	122.57
8	0.5	300	0.16	11.82	200.19
9	0.5	300	0.24	14.53	270.8
10	1	150	0.08	16.11	279.41
11	1	150	0.16	24.24	421.06
12	1	150	0.24	20.22	589.64
13	1	200	0.08	8.95	249.93
14	1	200	0.16	17.1	389.16
15	1	200	0.24	17.68	537.17
16	1	300	0.08	10.51	236.56
17	1	300	0.16	15.66	377.73
18	1	300	0.24	17.46	520.68

3.2. Force Analysis

The force data were collected through a three-component piezoelectric dynamometer from the Kistler Corporation electronic setup; as mentioned in the experimental setup, the data were saved in "[dot] txt" format with the order time (s); the force in the X direction F(x), (N), is a tangential force, which is also the called the cutting force ($\vec{F_c}$), the force in Y direction F(y), (N), is the radial force, which is also called the passive force ($\vec{F_r}$), and the force in the Z direction is axial F(z), which is also called the feed force ($\vec{F_f}$), in N. The active cutting force is the sum of the tangential and axial force; so, the force in the Y direction was kept at zero intentionally, because the tool is stationary in Y, and the force value is very low in comparison with the other forces and can be ignored.

Figure 7 represents the active force magnitude with the machining parameters for each experiment; it can be visualized from Figure 7, that the active cutting force RMS value is smaller in EX7 with DOC (a_p)—0.5 mm, V_c—200 m/min, and f—0.08 mm/rev, and it can be concluded from the vibration analysis that EX7 also has one of the least active

vibration RMS values. With DOC (a_p)—0.5 mm and f—0.08 mm/rev active force RMS having lower value with all cutting speeds, it can be concluded that these parameters are favorable to achieving a low cutting force value and preventing the machined product from deformation. Further, it can be also visualized that the value of the active cutting force decreases as the cutting speed increases.

In EX12, the active cutting forces reached their maximum value with DOC (a_p) 1 mm, V_c—150 m/min, and f—0.24 mm/rev. Similarly, the vibration value was high in EX12. It can also be analyzed from Figure 7 that, with an increase in the feed rate, the active cutting force value also increases. With DOC (a_p)—1mm, the value of the active cutting force RMS significantly increased, which can be understood by MRR. During the turning of X5CrNi18-10 steel, a deep cut is not recommended, as it can impact the quality of the machined product.

The other active force magnitude values can be visualized in Table 4 and Figure 7. Figures 6 and 7 can be compared, and the best machining parameters can be optimized with the comparison, where the vibration is low and the cutting force value is low, which will reduce chatter during the turning operation, and a good quality product can be produced.

3.3. Standard Deviation Results

The standard deviation was calculated for the magnitude of cutting forces data and the vibration data using MATLAB_R2023a academic license. The standard deviation is calculated using Equation (3), where s—sample standard deviation, EX1 represents experiment number 1, n—number of elements in the sample, x_i—each data point, and $\bar{x}$—mean of the dataset [31].

$$std(EX1) = \sqrt{\frac{1}{n-1}\sum_{i=1}^{n}\ (x_i - \bar{x})^2} \tag{3}$$

The two datasets have nearly close standard deviation values, which suggests that the amount of variability or spread in each dataset is the same, even though the datasets are different in terms of their values or distributions. Experiment 1, for both force and vibrations, has a low standard deviation indicating more consistent sampling with less fluctuation. The standard deviation between the force and vibration data is shown in Figure 8.

In Experiment 12, the force has a high standard deviation compared to the vibration, suggesting greater variability. In Experiments No. 3, 5, 8, and 17, the values are closer for both the force and vibration, suggesting that the variability is similar for both the cutting force and vibration. It is important to assess the consistency and variability during each test.

3.4. Statistical Analysis

Statistical analysis consists of the correlation of the results between the feed, active vibration RMS values, and active cutting force RMS values. In addition, the analysis of variance checks the validity of the model. The linear regression line graph between the feed, active vibration RMS, and active force RMS is shown to provide insights. To conclude the effect of the machining parameter on the active vibration and active force, an estimated marginal means plot is drawn.

Table 4 represents the calculated data of the active cutting force RMS and the active vibration RMS data for correlation with the machining parameters, feed rate (f), depth of cut (a_p), and cutting speed (V_c). To understand the relationship between the variables, Pearson correlation analysis was studied, where the correlation coefficient lies between -1 and 1. In the case of the coefficient of relation, $r > 0$ shows a positive correlation between the

two variables, the value of r is near +1 means the correlation is a strong positive correlation, and when the value is near 0, it shows the correlation is weak. If r < 0, there is a negative correlation between the variables, which shows that changing the value of the variable will not have a direct effect on the other.

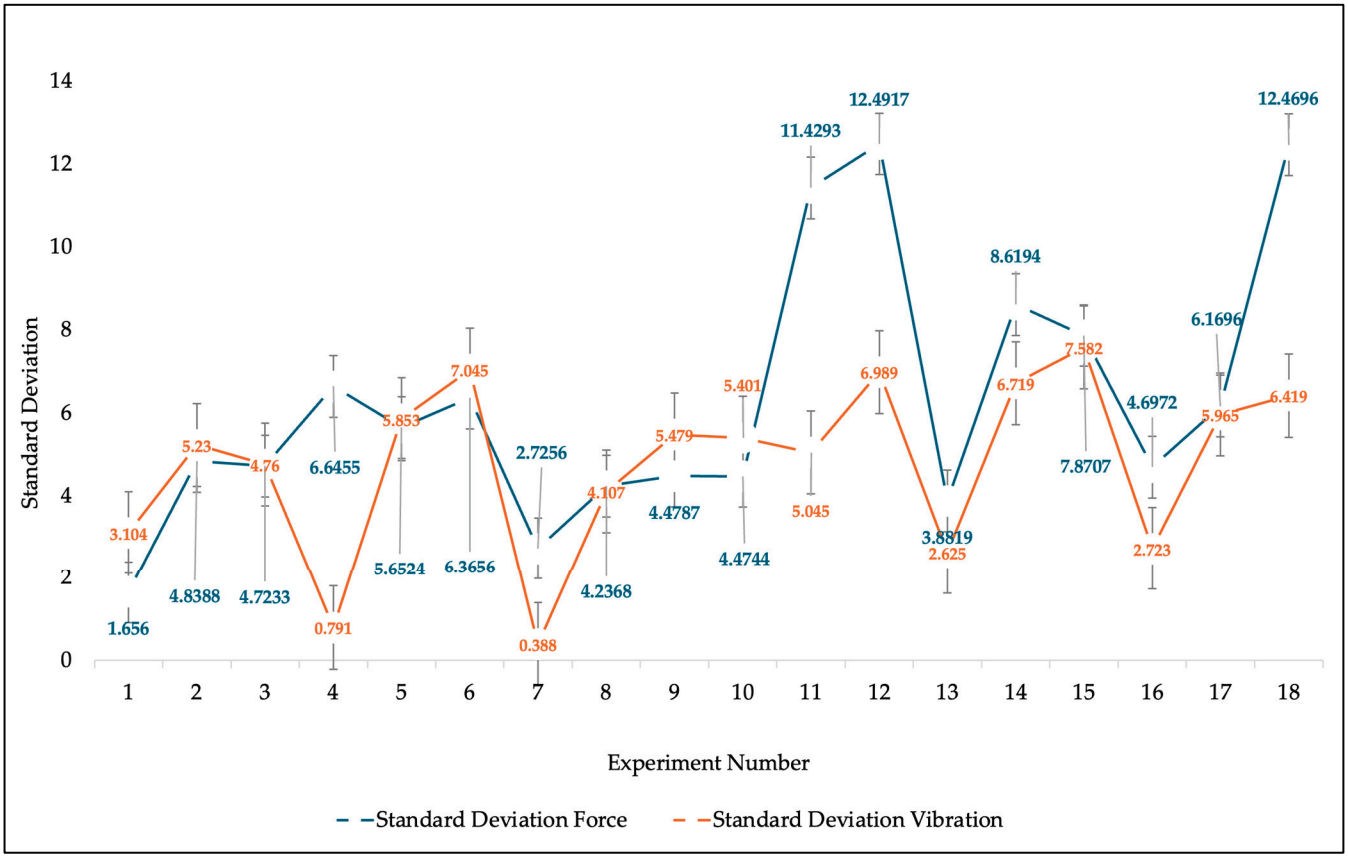


Figure 8. The standard deviation of active cutting force magnitude and active vibration magnitude.

3.4.1. Correlation Analysis Between Feed Rate, AV_b RMS, and AF RMS

The Pearson correlation analysis between three main key variables of the study, feed, active force RMS, and active vibration RMS, is represented in Table 5.

Table 5. Correlation analysis feed, active force RMS and active vibration RMS.

Correlations Variables	Feed Rate (*f*)	Active Vibration RMS (AV_b RMS)	Active Force RMS (AF RMS)
Feed Rate (*f*)	1	0.697 **	0.688 **
Active Vibration RMS (AV_b RMS)	0.697 **	1	0.699 **
Active Force RMS (AF_RMS)	0.688 **	0.699 **	1

** Correlation is significant at the 0.01 level (2-tailed).

The correlation coefficient between the feed rate and active force RMS is 0.688, indicating a very strong positive linear relationship which suggests that increasing the feed rate also influences the increase in the active force, and there is less than 1% probability that this observed correlation is due to random variation.

The correlation between the feed and active vibration RMS also suggests a strong positive linear relationship with a correlation coefficient of 0.697; as the feed rate increases,

the active vibration RMS also increases. The correlation coefficient between the active force RMS and active vibration RMS is 0.699, which is statistically significant at the 0.01 level, suggesting that a higher active force influences a higher active vibration.

3.4.2. ANOVA Results Between the Feed Rate and AF RMS

According to the experimental results in Table 4, the first-order regression model of active force RMS as a function of feed was developed at a 95% of confidence level, as shown in Figure 9. The Equation (4), is given by

$$y = 80.09 + 1420x. \quad (4)$$

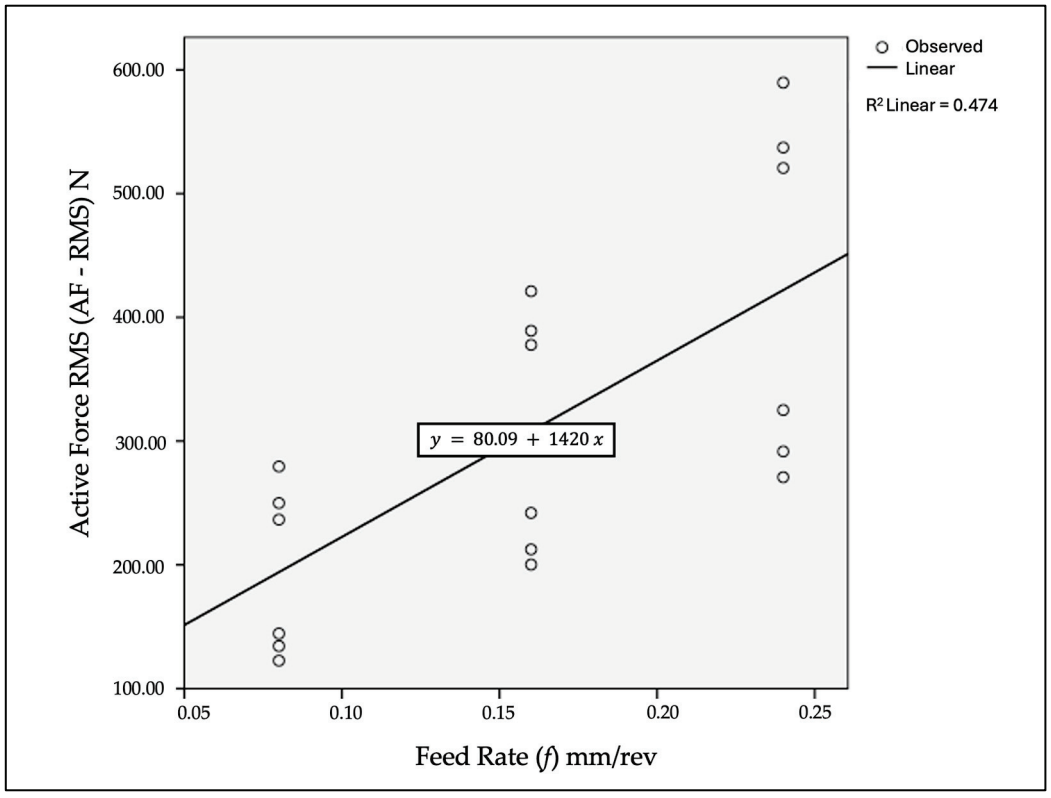


Figure 9. Linear regression line graph between feed rate and active force RMS.

Figure 9 represents the linear regression line graph between the feed and active force, where the circles represent observed values. In Equation (4), y represents one variable, and x represents the other variable, the Equation, $y = ax + b$, where a is the slope and b is the y-intercept, can be used to predict y based on the observed level of x, which highlights the impact of one variable on another. In Equation (3), x is the feed, and y is the active force RMS; with R^2 = 48.6%, y is the active force RMS in [N], and the feed is in [mm/r]. The analysis of variance (ANOVA) is represented in Table 6. The model is found to be statistically significant with a *p*-value (probability of significance) less than 0.05, in this case, 0.002. [a] Dependent Variable—active force RMS; [b] predictors—(constant), feed rate; "df" is degrees of freedom, which shows the number of independent variables in the model. The analysis of variance (ANOVA) of regression was evaluated to check the validity of the model.

Table 6. ANOVA of feed and active force RMS.

ANOVA [a]						
Model		**Sum of Squares**	**df**	**Mean Square**	**F**	**Sig.**
1	Regression	155,888.17	1	155,888.167	14.41	0.002 [b]
	Residual	173,046.81	16	10,815.426		
	Total	328,934.98	17			

[a] Dependent variable: active force RMS (AF RMS), [b] predictors: (constant), feed rate (*f*) mm/rev.

3.4.3. ANOVA Results Between Feed Rate and AV_b RMS

The first-order regression model for active vibration RMS as a function of feed rate, as shown in Figure 10, is given by Equation (5).

$$y = 8.17 + 44.93x \quad (5)$$

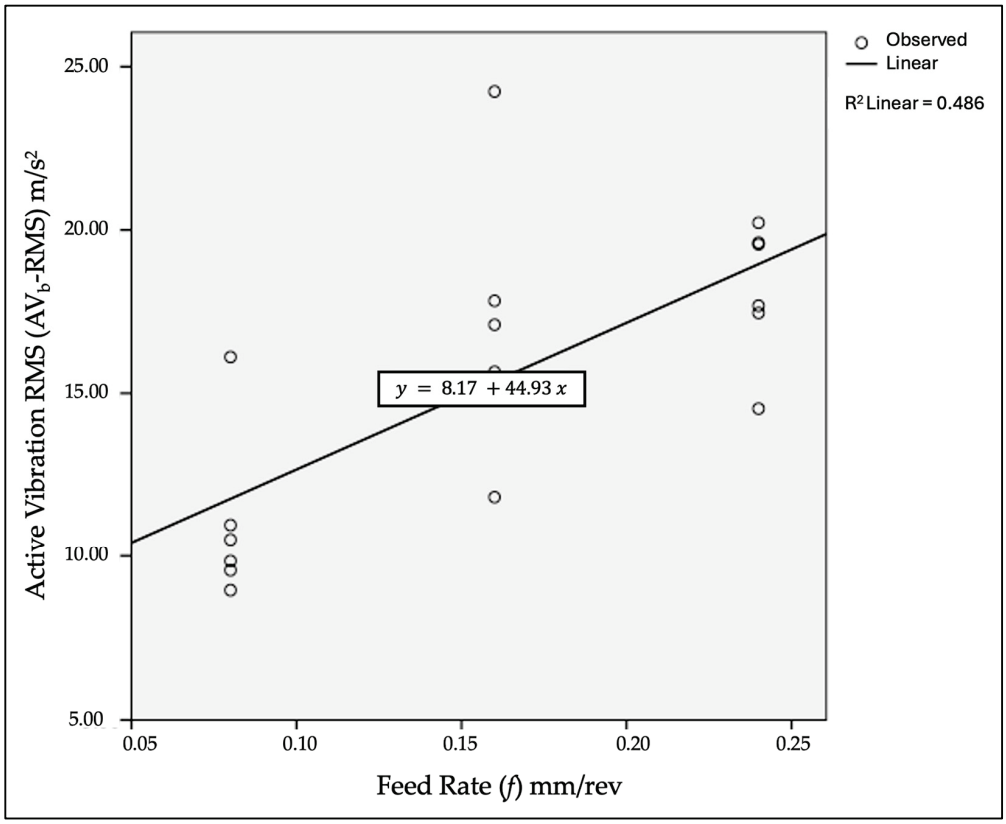


Figure 10. Linear regression line graph between feed rate and active vibration RMS.

With R^2 = 47.4, the statistical significance of the model is studied by ANOVA, as shown in Table 7. The probability of significance is less than 0.05, and the exact *p*-value is 0.001, which is statistically significant or of high significance. [a] Dependent variable—active vibration RMS, [b] predictors—(constant), feed rate. The value of R^2 is acceptable in both cases. Figure 9 represents the linear regression line graph between the feed and active force, where the circles represent observed values.

Figure 11 represents the main effect plots, which are also called estimated marginal means plots, which are used to analyze the effect of three machining parameters (feed rate, depth of cut, and cutting speed) with active vibration (AV_b). Figure 11a represents the plot between the feed and active vibration RMS. It highlights that the higher feed rate increases the vibration from 0.08 mm/rev to 0.16 mm/rev, with a moderate increase by increasing

the feed from 0.16 mm/rev to 0.24 mm/rev. The effect of the depth of cut also shows a significant increase, influencing the vibration, as shown in Figure 11b. The cutting speed shows a decrease, which implies that by increasing the cutting speed, the vibration in the machining can be reduced, which can be seen in Figure 11c.

Table 7. ANOVA of feed and active vibration RMS.

ANOVA [a]						
Model		**Sum of Squares**	**df**	**Mean Square**	**F**	**Sig.**
1	Regression	155.016	1	155.016	15.1	0.001 [b]
	Residual	164.275	16	10.267		
	Total	319.291	17			

[a] Dependent variable: active vibration RMS (AV_b RMS), [b] predictors: (constant), feed rate (f).

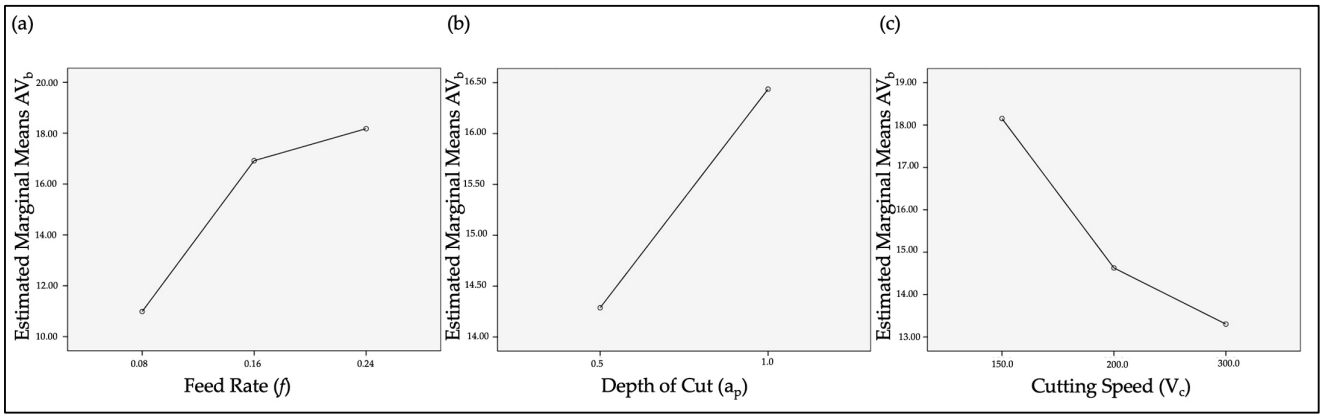


Figure 11. Main effect plot between AV_b RMS and machining parameters, (**a**) feed and AV_b, (**b**) depth of cut and AV_b, and (**c**) cutting speed and AV_b.

The active force (AF) RMS and machining parameters also show significant results, as shown in Figure 12. The result implies that with an increase in the feed rate, the magnitude of the cutting forces also increases, as shown in Figure 12c, which is expected due to the material removal. The AF RMS also increases with the depth of cut, which can be seen in Figure 12b. The cutting speed shows different results with an increase in the cutting speed, and the AF RMS values decrease, which can also be seen in the force analysis sections; this suggests that by increasing the cutting speed, the cutting forces values will be low, and they will have less effect on the quality indicators of the final machined product.

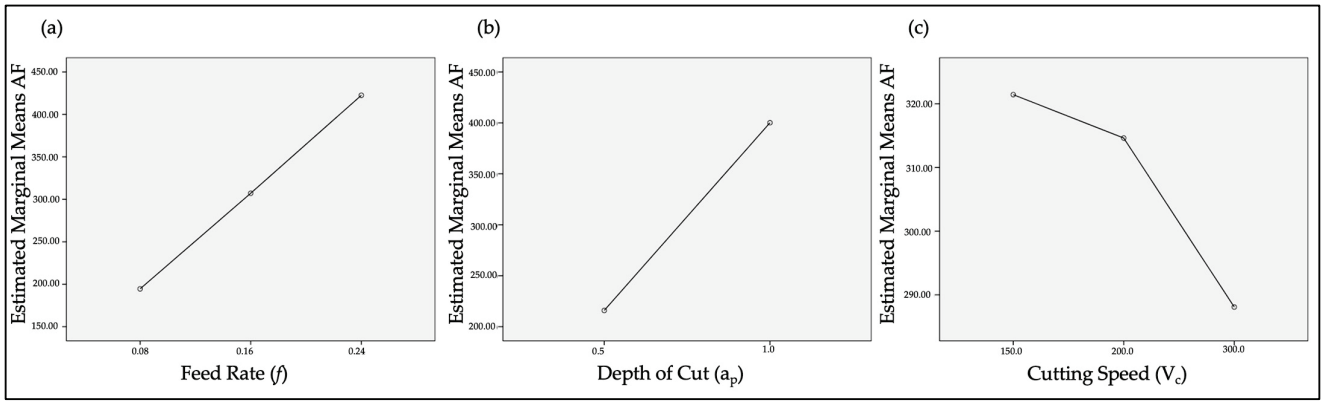


Figure 12. Main effect plot between AF RMS and machining parameters, (**a**) feed and AF, (**b**) depth of cut and AF, and (**c**) cutting speed and AF.

4. Discussion

We need to understand the correlation between the machining parameters, particularly the feed and its effect on cutting phenomena (cutting force and vibration), which affects the quality of the machined products in terms of the surface integrity shape. The research demonstrates the computed active vibration RMS, the active force RMS, and the correlation analysis between the variables.

The active vibration RMS results are presented in Table 4 and Figure 6. The results highlight that changes in the machining parameters, feed, depth of cut, and cutting speed, influence the vibration peaks and RMS value. The low feed rate, f—0.08 mm/rev, with different cutting speeds and depths of cut, as shown in Figure 6, suggests favorable results. To achieve better results, DOC—0.5 mm is suggested. The cutting speed also influences the value of the active vibration RMS; as the cutting speed is increased, the AV_b RMS value decreases, i.e., vibration impacts during machining can be reduced at a higher speed. EX13, with V_c—200 m/min, f—0.08 mm/rev, and DOC—1 mm, has less vibration magnitude during the whole experiment; however, the vibration peaks are high in comparison to EX1, EX4, and EX7 with the same feed. As the feed rate is increased, the magnitude of vibration increases. To achieve less vibration during the turning of X5CrNi18-10, the feed should be kept low, the cutting speed should be high, and the depth of cut should be low.

The active cutting force results are presented in Table 4 and Figure 6; the cutting force analysis also suggests similar results. It is visualized in Figure 6 that increasing the feed rate results in higher cutting forces, which impacts the shape deformation, poor surface finish, and tool wear. It is recommended to keep a low feed rate to achieve better quality products. EX7, with V_c—300 m/min, f—0.08 mm/rev, and DOC—0.5 mm, shows the lowest active cutting force value of 122.57 N during the whole experiment. In EX12, the highest magnitude of AF RMS was observed for V_c—150 m/min, f—0.24 mm/rev, and DOC—1 mm; to achieve better results, these parameters should not be considered. To have less impact of the cutting forces on the quality of the product, the feed should be kept low, with a low depth of cut and cutting speed.

The standard deviation results between the cutting force and vibration data suggest that the amount of variability in each dataset is the same. EX3, 5, 8, and 17 show that the values of both the force and vibration are closer, suggesting consistency during each test.

The correlation analysis between the feed and AV_b RMS suggests that there is a 69.7% correlation between the variables. The correlation analysis between the feed and AF RMS suggests that there is a 68.8% correlation between the variables. There is a 99% probability that a real relationship exists between each variable, and it is not random. The ANOVA results for the feed and AF RMS show a significant p-value of 0.002, which is less than 0.05, suggesting that the model is highly significant. Similarly, the ANOVA results for the feed and AV_b RMS show a significant p-value of 0.001, which also suggests that the model is highly significant, and a real relationship exists between the variables.

The main effects plot analysis between three machining parameters and AV_b RMS and AF RMS shows that the increase in the feed rate influences the vibration, which can also be observed in the correlation results. With the increase in DOC, the active vibration magnitude also increases. However, the cutting speed has different effects; to lower the vibration, the cutting speed must be kept high. The increase in the feed rate also influences the active cutting force, which is also noticeable in the correlation results. When the depth of cut increases, the AF RMS also increases, which can be understood by the material removal rate. However, with increasing cutting speed, the AF RMS decreases; to achieve a low AF RMS, the cutting speed must be kept high.

5. Conclusions

The research aimed to understand the effects of machining parameters on cutting phenomena like cutting forces and vibration in the turning of X5CrNi18-10 steel grade to avoid failures during the manufacturing process, and the following conclusions can be drawn from the study.

- The active vibration magnitude results suggest that to achieve low vibration, the feed rate must be kept low; according to the results, a feed rate of 0.08 mm/rev shows less vibration with different cutting speeds and DOC, and as the feed rate is increased, the magnitude of the vibration and vibration peaks also increases.
- Good results are obtained from EX4, with DOC (a_p)—0.5 mm, V_c—200 m/min, and *f*—0.08 mm/rev, with low active vibration RMS value and low peaks.
- A low feed rate results in a low magnitude of the active cutting force, and as the feed rate increases, the magnitude of the AF RMS also increases.
- The best results are obtained during EX7, with DOC (a_p)—0.5 mm, V_c—300 m/min, and *f*—0.08 mm/rev. It shows the lowest values of the active cutting force RMS during the whole experiment, with a small increase in the active vibration RMS. To achieve better results in force, these parameters should be considered.
- The correlation analysis between the feed and AV_b RMS suggests that there is a 69.7% correlation between the variables. The ANOVA results for the feed and AV_b RMS show a significant *p*-value of 0.001, which also suggests that the model is highly significant, and a real relationship exists between the variables.
- The correlation analysis between the feed and AF RMS suggests that there is a 68.8% correlation between the variables. The ANOVA results for the feed and AF RMS show a significant *p*-value of 0.002, which is less than 0.05, suggesting that the model is highly significant.
- The marginal estimated means plot shows that increasing the depth of cut also increases the AF RMS, which can be understood by MRR. However, with increasing cutting speed, the AF RMS decreases; to achieve a low AF RMS, the cutting speed must be kept high.

These findings can be used to improve manufacturing efficiency and predictive maintenance and to build more vibration-resistant tools for machining conditions, specifically in automobile and marine industries where X5CrNi18-10 steel grade is used.

Author Contributions: Conceptualization, C.F. and T.N.; methodology, C.F. and T.N.; software, T.N.; validation, C.F.; formal analysis, C.F. and T.N.; investigation, C.F. and T.N.; resources, C.F. and T.N.; data curation, T.N.; writing—original draft preparation, T.N.; writing—review and editing, C.F.; visualization, C.F.; supervision, C.F.; project administration, C.F.; funding acquisition, C.F. All authors have read and agreed to the published version of the manuscript.

Funding: This research was supported by project No. 2020-1.2.3-EUREKA-2022-00025 "Deep Learning Based Process Monitoring for Complex Machining Tasks—DeepProMach", which was realized with financial help of the National Research Development and Innovation Fund of the Ministry of Culture and Innovation of Hungary.

Institutional Review Board Statement: Not applicable.

Informed Consent Statement: Not applicable.

Data Availability Statement: The original contributions presented in the study are included in the article, further inquiries can be directed to the corresponding author.

Acknowledgments: Sincere thanks to University of Miskolc, Hungary, Faculty of Mechanical Engineering and Informatics, Institute of Manufacturing Science, for providing the academic support and

to Interstop Kft., Miskolc, Hungary, for providing the necessary resources and technical assistance that contributed significantly to this research.

Conflicts of Interest: The authors declare no conflicts of interest.

References

1. Kónya, G.; Takács, J.; Miskolczi, I.; Kovács, Z.F. Investigation of the Effects of Machining Parameters on Cutting Conditions during Orthogonal Turning of Austenite Stainless Steel. *Prod. Eng. Arch.* **2024**, *30*, 86–93. [CrossRef]
2. Labuda, W.; Starosta, R. Estimation of the Influence of Burnishing Parameters on X5CrNi18-10 Steel. In *Proceedings of the Solid-State Phenomena*; Trans Tech Publications Ltd.: Stafa-Zurich, Switzerland, 2010; Volume 165, pp. 300–305.
3. Labuda, W. The influence of cutting inserts geometric on surface roughness of steel applied to sea water pump shafts. *J. KONES Powertrain Transp.* **2015**, *22*, 133–140. [CrossRef]
4. Labuda, W.; Charchalis, A. Influence of Reduced Cutting Speed Values on Operator Safety and Cutting Tool Life in the Processes of Manufacturing and Regeneration of Marine Machinery Parts. *J. KONBiN* **2022**, *52*, 1–26. [CrossRef]
5. Labuda, W. Finishing treatment of marine pump shafts made of x5crni18-10 steel. *J. KONES Powertrain Transp.* **2018**, *25*, 215–222. [CrossRef]
6. Kantoríková, E. An Influence of Nitrogen Corrosion on Microstructural and Mechanical Features of the X5CrNi18-10 Steel. *Arch. Foundry Eng.* **2024**, *2024*, 69–75. [CrossRef]
7. Paro, J.; Ènninen, H.H.; Kauppinen, V. Tool Wear and Machinability of X5CrMnN 18-18 Stainless Steels. *J. Mech. Work. Technol.* **2001**, *119*, 14–20.
8. Labuda, W. The Influence of Cutting Parameters on Surface Topography During Turning Marine Pump Shafts. *J. KONES* **2019**, *26*, 141–148. [CrossRef]
9. Pawade, R.S.; Joshi, S.S.; Brahmankar, P.K.; Rahman, M. An Investigation of Cutting Forces and Surface Damage in High-Speed Turning of Inconel 718. *J. Mater. Process Technol.* **2007**, *192–193*, 139–146. [CrossRef]
10. Aslan, A. Optimization and Analysis of Process Parameters for Flank Wear, Cutting Forces and Vibration in Turning of AISI 5140: A Comprehensive Study. *Measurement* **2020**, *163*, 107959. [CrossRef]
11. Prasad, B.S.; Babu, M.P. Correlation between Vibration Amplitude and Tool Wear in Turning: Numerical and Experimental Analysis. *Eng. Sci. Technol. Int. J.* **2017**, *20*, 197–211. [CrossRef]
12. Namboodri, T.; Felhő, C. Correlation Analysis Between Components of Force and Vibration in Turning of 11SMn30 Steel. *Cut. Tools Technol. Syst.* **2024**, *101*, 39–50. [CrossRef]
13. Felhő, C.; Namboodri, T. ANOVA and Correlation Analysis of Feed, Cutting Forces and Tool Vibration in 11SMn30 Steel Turning. *Mater. Res. Proc.* **2024**, *46*, 184–191. [CrossRef]
14. Savella, F.B.; Pereira, V.W.S.; Shiki, S.B.; Ventura, C.E.H.; Antonialli, A.I.S. Analysis of the Effect of Part Geometry and Cutting Parameters over Tool Vibration and Surface Integrity on Hard Turning. *Int. J. Adv. Manuf. Technol.* **2022**, *122*, 4065–4077. [CrossRef]
15. Marinkovic, D.; Antic, A.; Knezev, M.; Mladjenovic, C.; Zivkovic, A. The influence of the cutting parameters on the surface roughness and vibration signal in the turning process. *MM Sci. J.* **2024**, *2024*, 7539–7544. [CrossRef]
16. Yu, Q.; Li, S.; Zhang, X.; Shao, M. Experimental Study on Correlation between Turning Temperature Rise and Turning Vibration in Dry Turning on Aluminum Alloy. *Int. J. Adv. Manuf. Technol.* **2019**, *103*, 453–469. [CrossRef]
17. Bai, W.; Sun, R.; Gao, Y.; Leopold, J. Analysis and Modeling of Force in Orthogonal Elliptical Vibration Cutting. *Int. J. Adv. Manuf. Technol.* **2016**, *83*, 1025–1036. [CrossRef]
18. Rowe, J.; Langrand, C.; Debuchy, R. Case Study of Vibration in a Mobile Milling Machine. *Vibro Eng. Procedia* **2023**, *49*, 30–37. [CrossRef]
19. Yue, C.; Gao, H.; Liu, X.; Liang, S.Y.; Wang, L. A Review of Chatter Vibration Research in Milling. *Chin. J. Aeronaut.* **2019**, *32*, 215–242. [CrossRef]
20. Dimla, D.E. The Impact of Cutting Conditions on Cutting Forces and Vibration Signals in Turning with Plane Face Geometry Inserts. *J. Mater. Process. Technol.* **2004**, *155–156*, 1708–1715. [CrossRef]
21. Şeker, U.; Kurt, A.; Çiftçi, I. The Effect of Feed Rate on the Cutting Forces When Machining with Linear Motion. *J. Mater. Process. Technol.* **2004**, *146*, 403–407. [CrossRef]
22. Ma, C.; Shamoto, E.; Moriwaki, T.; Wang, L. Study of Machining Accuracy in Ultrasonic Elliptical Vibration Cutting. *Int. J. Mach. Tools Manuf.* **2004**, *44*, 1305–1310. [CrossRef]
23. Xia, S.; Yin, Z.; Huang, C.; Guo, Y.; Zhang, C. Characteristics of Elliptical Vibration-Assisted Cutting with Variations in Tilt Angle of Elliptical Locus. *Micromachines* **2023**, *14*, 1426. [CrossRef]
24. Hanief, M.; Wani, M.F.; Charoo, M.S. Modeling and Prediction of Cutting Forces during the Turning of Red Brass (C23000) Using ANN and Regression Analysis. *Eng. Sci. Technol. Int. J.* **2017**, *20*, 1220–1226. [CrossRef]

25. Guzeev, V.; Deryabin, I.; Ardashev, D. Mathematical models of cutting forces in turning operations. *Mach. Sci.* **2023**, 36–45. [CrossRef]
26. Dorlin, T.; Fromentin, G.; Costes, J.P. Analysis and Modelling of the Contact Radius Effect on the Cutting Forces in Cylindrical and Face Turning of Ti_6Al_4V Titanium Alloy. *Procedia CIRP* **2015**, *31*, 185–190. [CrossRef]
27. Krajewski, S.J.; Gutsche, W.; Urbanowicz, K. Analysis of X5CrNi18-10 (AISI 304) Steel Susceptibility to Hot Cracking in Welded Joints Based on Determining the Range of High-Temperature Brittleness and the Nil-Strength Temperature. *Metals* **2023**, *13*, 1633. [CrossRef]
28. EU Steel and Alloy Grades Number 2024. Available online: https://www.steelnumber.com/ (accessed on 5 November 2024).
29. Seco Tools. Available online: https://www.secotools.com/article (accessed on 9 November 2024).
30. HAAS CNC. Available online: https://www.haascnc.com/ (accessed on 9 November 2024).
31. MATLAB. Available online: https://www.mathworks.com/ (accessed on 20 November 2024).

Disclaimer/Publisher's Note: The statements, opinions and data contained in all publications are solely those of the individual author(s) and contributor(s) and not of MDPI and/or the editor(s). MDPI and/or the editor(s) disclaim responsibility for any injury to people or property resulting from any ideas, methods, instructions or products referred to in the content.

applied sciences

MDPI

Article

Calibration of a Hybrid Machine Tool from the Point of View of Positioning Accuracy

Slobodan Tabakovic [1], Milan Zeljkovic [1,*], Sasa Zivanovic [2], Alexander Budimir [1], Zoran Dimic [3] and Aleksandar Kosarac [4]

[1] Faculty of Technical Sciences, University of Novi Sad, Trg D. Obradovica 6, 21000 Novi Sad, Serbia; tabak@uns.ac.rs (S.T.)
[2] Faculty of Mechanical Engineering, University of Belgrade, Kraljice Marije 16, 11120 Belgrade, Serbia; szivanovic@mas.bg.ac.rs
[3] Research and Development Institute Lola Ltd., Kneza Viseslava 70A, 11030 Belgrade, Serbia; zoran.dimic@li.rs
[4] Faculty of Mechanical Engineering, University of East Sarajevo, 71123 Istocno Sarajevo, Bosnia and Herzegovina; aleksandar.kosarac@ues.rs.ba
* Correspondence: milanz@uns.ac.rs

Abstract: The development of machine tools in the last twenty years includes, among other things, the application of mechanisms with a non-linear kinematic structure as the mechanical basis of machines. This results in significant improvements in kinematic characteristics and problems related to non-linear dependencies of the accuracy of the drive elements and the realization of movement in the machine's external coordinates. The paper presents an approach to machine tool calibration based on the original O-X glide mechanism based on the ISO 230-4 standard with the mono- and bi-directional compensation of systematic errors and adaptation to the specifics of the mechanism's kinematics. A machine tool prototype was designed and built for the research presented in the paper. The obtained results indicate the possibility of applying the existing recommendations and standards for testing the accuracy of machine tools with the need to correct the methodology by using linear and non-linear kinematic structures in machine tools.

Keywords: machine tools; calibration; hybrid kinematic; O-X glide

1. Introduction

The development and improvement of machine tools since the mid-1950s has included research on improving the kinematic structure, components, and subsystems. This ensures the fulfillment of market requirements, which implies more accurate and efficient machining and the application of higher cutting speeds while reducing processing errors.

An important role in the creation of foundations for the maximum use of existing tools and the development of new machine tools is played by tests of inaccuracies that arise during exploitation and the definition of calibration procedures. Research has shown twenty-one errors in machine tools with three numerically controlled axes with a linear kinematic structure [1]. However, it should be emphasized that there is no unequivocal systematization and definition of machine tool errors in the literature. The systematization of machine tool errors is most often performed according to their sources [2]:

(1) Geometric (geometric/kinematic);
(2) Kinematic;
(3) Due to static load;
(4) Due to heat load;
(5) Due to dynamic movement;
(6) Control system (interpretation of the movement path, signal delay, etc.).

Determining errors and compensating their values (machine calibration) represent important research areas that affect the development of machine tools. Schwenke et al.

presented an overview of the measurement of quasi-static kinematic errors [3]; a very similar, modernized view has been given elsewhere [4]. W. Gao et al. presented an overview of the most modern measurement methods, mathematical models, and compensation strategies for calibrating machine tools [5]. The basics of error compensation and available methods for measuring machine tool geometric errors are summarized and updated in [3]. In Refs. [1,6], the techniques were proposed and are based on artifacts. This research enables the control of machine tool error mapping and calibration by compensating them. A methodology for quantitatively evaluating the success of machine tool calibration methods was proposed by Bringmann et al. [7].

Improvement of the mechanical concept of machine tools in the previous period included applying non-linear kinematic structures (parallel and hybrid mechanisms) to improve the machines' exploitation characteristics. Therefore, research was initiated into the accuracy and calibration of such machine tools. The first paper on the accuracy of these machines analyzes the accuracy of mechanisms based on the Stewart platform or other types of parallel mechanisms, in which external sensors were used to measure the position and orientation of the final end-effectors. A kinematic model was used to evaluate the influence of parallel manipulator mechanism errors relative to the final end-effector's positioning accuracy. The paper [8] proposed a new method of identifying mechanism errors for a 3-PUU parallel mechanism. It is based on the inverse kinematics model and volumetric error measurement techniques using a 3D laser ball bar device. The experimental results combined with the optimization technique can determine the errors of the mechanism of the tested machine, i.e., the structural symmetry errors of the rods and joints. This method can help machine tool manufacturers to determine the basic length parameters (rod lengths) and fine-tune the kinematics (by determining the position of joints or rods) in the assembly phase.

Based on the results obtained from research on the impact of parallel kinematic structure on mechanical properties, the first commercial solutions of machine tools with parallel kinematics appeared at the end of the twentieth century. That solution enabled significant improvements in stiffness, accuracy, and movement dynamics. With the implementation of the new kinematic concept, it was observed that the application of parallel mechanisms in the development of machine tools, in addition to several advantages [9], also has certain disadvantages [10,11] that determine the area of their application (dimensions and shape of the workspace and specific control structure).

In order to make maximum use of the advantages of serial and parallel mechanisms and to reduce the impact of their shortcomings, hybrid, serial–parallel mechanisms have been used in the development of machine tools for many years. In this way, a good compromise solution that has proven to be applicable to the production of machine tools, manipulation systems, and industrial robots is provided. Examples of successful applications of hybrid mechanisms [12] include Tricept [13], Execon [13], Ecospeed [14], Geodetic Hexapod [15], and George V [16].

In machine tools with serial kinematics, the kinematic relationship between the executive part of the machine and the moving elements is linear. Therefore, we can call them machine tools with linear kinematics. In contrast, the kinematic relationships of machine tools with parallel or hybrid kinematics are significantly more complex and not linear, which is why they can be called machine tools with nonlinear kinematics [17].

In current research on the characteristics of machine tools with linear and non-linear (parallel and hybrid) kinematics, problems related to the accuracy of the machines [18], as well as the possibilities of their calibration [19], are often considered. Calibrating machine tools ensures maximum utilization of the machine's mechanical and control systems. The calibration of machine tools is a process that is carried out periodically in order to verify and improve the characteristics of machine tools [5]. This process is carried out to reduce or eliminate errors due to thermal, static, dynamic loads, and control system errors.

Calibration of linear axes of machine tools includes the following:

- Testing the positioning accuracy of the complete machine;

- Identification of systematic and random errors;
- Their removal or numerical compensation in the control system of the machine tool.

The fundamental problem of applying this procedure to machine tools with parallel or hybrid kinematics is the need to recalculate the errors on the internal coordinates of the machine defined by the nonlinear kinematics of the mechanism, even when defining the calibration parameters, and the test parameters (movement method, movement speed, stopping time) that are not explicitly defined by the standard adapt to the appropriate mechanism and its characteristics.

This paper presents part of the research conducted to determine the influence of machine tool calibration with an O-X glide kinematic structure on the positioning accuracy of the moving platform. The research was conducted to enable the compensation of errors through the calibration process by applying standardized techniques for identifying errors in the mechanical structure. In the paper, research was carried out according to the ISO 230-4 [20] standard, in static conditions, on a machine tool prototype that was made for research. In contrast, the standard parameters for which no selection recommendation was varied in a range corresponding to the exploitation values for a specific kinematic machine configuration. The results were processed according to the kinematic differences between the mechanical structure of machines with linear and non-linear kinematics. The calibration was carried out using the mono- and bi-directional compensation of systematic errors obtained by measuring accuracy.

2. Materials and Methods

2.1. Kinematic Structure of the O-X Glide Mechanism

The kinematic structure of the O-X glide mechanism is based on a planar parallel mechanism that moves translationally in the direction of one serial axis, which ensures the formation of a three-dimensional working space.

The planar parallel mechanism is ingeniously constructed with a dual kinematic structure. This innovative design realizes two different arrangements of the supporting elements, forming "O" and "X" configurations with different shapes and dimensions of working space. The dual structure of the mechanism results in two kinematic configurations with different stiffness.

Inverse and Direct Kinematics

The essential characteristics of mechanisms with parallel kinematics are represented by a mathematically relatively simple solution of inverse and complex solutions of direct kinematics. The planar parallel mechanism, which is the basis of the O-X glide mechanism due to its plane structure and simple conception, has analytically solvable kinematic solutions in both geometric configurations (extended "O" and crossed "X" configuration). Figure 1a shows the arrangement of vectors on the kinematic model of the parallel mechanism in extended configuration; Figure 1b shows this in crossed configuration.

Figure 1 shows the crossed (Figure 1a) and extended (Figure 1b) configurations of the realized version of the planar O-X glide mechanism. The vectors that determine the position and orientation of the mechanism elements are shown in the X-Z plane, as performed on the machine prototype. The following symbols were used to denote vectors [21]:

- P—position of the moving platform expressed in external coordinates of the mechanism (x_P, z_P);
- r_{P1} and r_{P2}—vectors of moving platform, which defines the orientation of platform and distance between the end of rods and position of point P (P_1 and P_2);
- r_{R1}, r_{R2}—vectors of the positions of reference points of the particular sliders (R_1 and R_2);
- r_{u1}, r_{u2}—vectors of the slide of the parallel mechanism in relation to the axis reference point, internal coordinates of the mechanism;
- l_1, l_2—vectors of rods of constant length;
- d—distance between sliders.

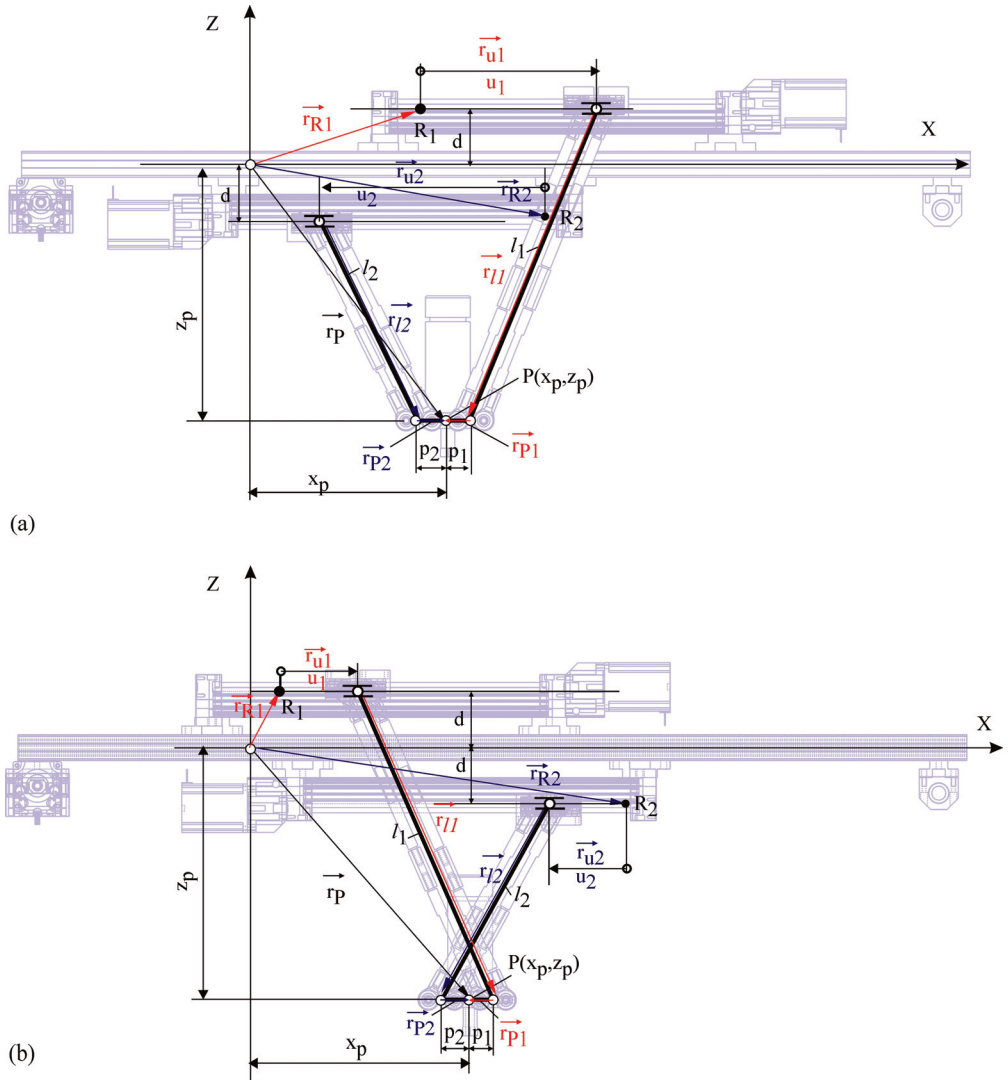


Figure 1. Kinematic model of the O-X glide parallel mechanism.

Based on Figure 1, the vector equations of the vector polygon can be set. These equations express the position vector of the moving platform as a function of the internal coordinates of the individual sliders.

$$\vec{r_P} = \vec{r_{ref1}} + \vec{r_{u1}} + \vec{r_{l1}} + \vec{r_{p1}} = \vec{r_{ref1}} + \vec{r_{u1}} + \vec{r_{l1}} + \vec{r_{p1}} \tag{1}$$

Expressed in coordinates:

$$\left\{\begin{matrix} x_P \\ z_P \end{matrix}\right\} = \left\{\begin{matrix} x_{ref1} \\ d \end{matrix}\right\} + \left\{\begin{matrix} u_1 \\ 0 \end{matrix}\right\} + \left\{\begin{matrix} l_{1x} \\ l_{1z} \end{matrix}\right\} + \left\{\begin{matrix} -p_1 \\ 0 \end{matrix}\right\} = \left\{\begin{matrix} x_{ref2} \\ d \end{matrix}\right\} + \left\{\begin{matrix} u_2 \\ 0 \end{matrix}\right\} + \left\{\begin{matrix} l_{2x} \\ l_{2z} \end{matrix}\right\} + \left\{\begin{matrix} -p_2 \\ 0 \end{matrix}\right\} \tag{2}$$

They obtain unique solutions by converting the components of vector l from the previous expressions and including them in the expressions that express the length of the rods through vector components d.

$$\begin{matrix} {l_1}^2 = {l_{1x}}^2 + {l_{1z}}^2 \\ {l_2}^2 = {l_{2x}}^2 + {l_{2z}}^2 \end{matrix} \tag{3}$$

Based on the previous expressions, the equations of inverse kinematics can be described in the mechanism's sprung (O) and crossed (X) kinematic configuration.

For the sprung configuration of the mechanism "O":

$$\begin{gathered} u_1 = x_p - x_{R1} + p_1 + \sqrt{l_1^2 - (z_p - d)^2} \\ u_2 = -x_p + x_{R2} + p_2 + \sqrt{l_2^2 - (z_p + d)^2} \\ s_3 = y_p \end{gathered} \tag{4}$$

For cross mechanism configuration "X":

$$\begin{gathered} u_1 = x_p - x_{R1} + p_1 - \sqrt{l_1^2 - (z_p - d)^2} \\ u_2 = -x_p + x_{R2} + p_2 - \sqrt{l_2^2 - (z_p + d)^2} \\ u_3 = y_p \end{gathered} \tag{5}$$

Upon closer examination, we find that the expressions we have derived are structurally identical, with the only difference being the sign in front of the square root. This square root is a key component, representing the basic relationship between the internal and external coordinates of the mechanism, which is essential for configuring the control system.

The expression can generally describe the solution of direct kinematics:

$$P(x_P, y_P, z_P) = \mathrm{f}(s_1, s_2, s_3) \tag{6}$$

By transforming the previous expressions, it is determined on the basis of Equations (4) and (5) and the following expression is obtained:

$$t_3 x_p + t_4 z_p + t_5 = 0 \tag{7}$$

based on which, we derive x_p as

$$x_p = t_6 + t_7 \cdot z_p \tag{8}$$

z is obtained by inserting expression x_p into Equation (5):

$$t_8 z_p^2 + t_9 z_p + t_{10} = 0 \tag{9}$$

After the substitutions are introduced in the previous expressions, we derive

$$\begin{gathered} t_1 = x_{R1} - p_1 + u_1, \\ t_2 = x_{R2} + p_2 - u_2, \\ t_3 = 2t_2 - 2t_1,\ t_4 = -4d, \\ t_5 = t_1^2 - t_2^2 - l_1^2 + l_2^2,\ t_6 = -(t_5/t_3), \\ t_7 = -(t_4/t_3),\ t_8 = 1 + t_7^2, \\ t_9 = 2(t_6 - t_1) \cdot t_7 - 2d, \\ t_{10} = (t_6 - t_1)^2 + d^2 - l_1^2. \end{gathered} \tag{10}$$

Based on the previous equations, the following expressions are obtained:

$$\begin{gathered} z_p = \frac{-t_9 - \sqrt{t_9^2 - 4t_8 t_{10}}}{2t_8} \\ x_p = t_6 + t_7 \cdot z_p \end{gathered} \tag{11}$$

The obtained expressions were used to configure the control system of the machine tool prototype based on the O-X glide mechanism.

2.2. Realized Prototype

The supporting structure of the machine tool prototype based on the O-X mechanism is made of aluminum profiles with adjustments that allow the installation of IGUS linear axis sub-assemblies with NEMA 19 step motors. The moving platform is made of aluminum and designed in accordance with the schedule of mechanical loads that occur during processing. The connection elements between the platform and the linear axes are realized

in the form of adjustable rods made of structural steel. Figure 2 shows the appearance of the realized prototype.

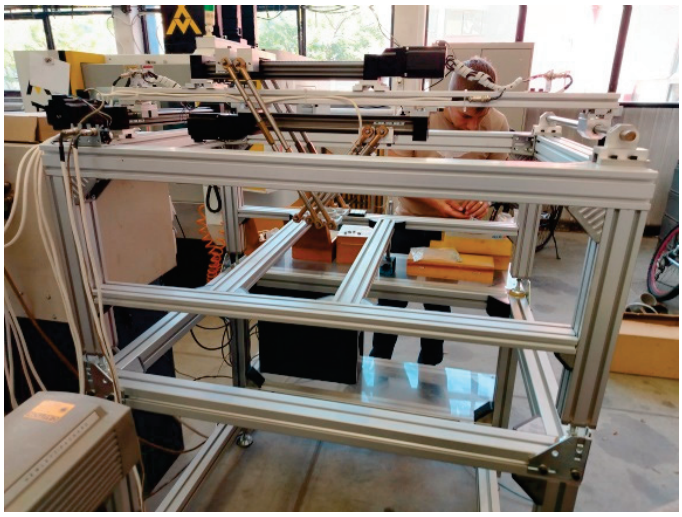


Figure 2. Realized prototype.

For prototyping and testing the influence of the calibration process of individual internal axes on positioning accuracy in external coordinates, a control system based on a PC with LinuxCNC open architecture control system, which enables control of machines with a non-linear kinematic structure, was used (Figure 3).

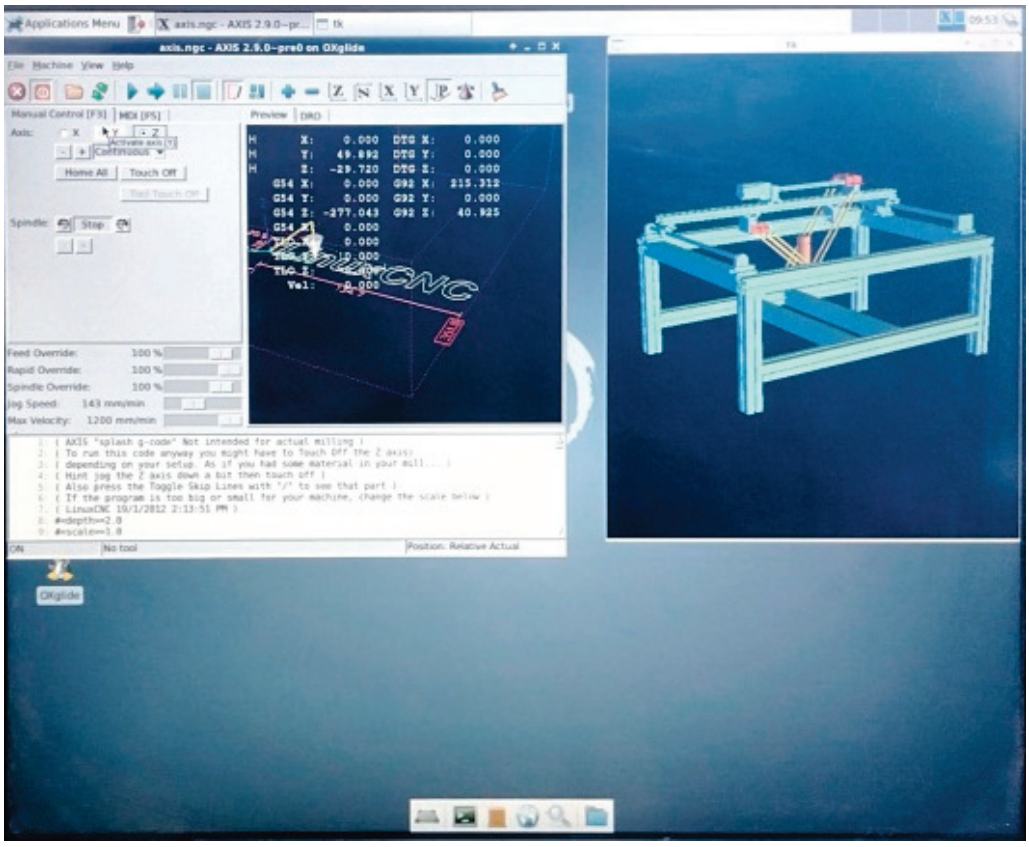


Figure 3. PC-based control system.

2.3. Positioning Accuracy Test and Applications in Machine Tool Calibration

The positioning accuracy test procedure, which is necessary for the condition analysis and calibration of machine tools, is defined by numerous standards and recommendations. ISO 230-2 [22], VDI/DGQ 3441 [23], ANSI B5.54 [24], JIS 6333 [25], and others are currently used. All procedures involve the exposure of machine elements to programmed movement along the measured axis while simultaneously measuring the achieved displacement with the machine's measuring system and reference based on instrumentation, including a laser interferometer with a compensator for environmental conditions. In this way, it is possible to compare the values measured on the machine and forward them to the machine's control system with reference values.

The conducted research is based on the procedure defined by the ISO 230-2 standard with compensation for environmental conditions. The procedure includes placing the laser measuring head (1), interferometer (2), retroreflector (3), acquisitional device (4), compensator of external conditions (5), external condition measuring device (6), sensor of temperature of machine elements (7), and computer analyzing data (8), according to the scheme shown in Figure 4.

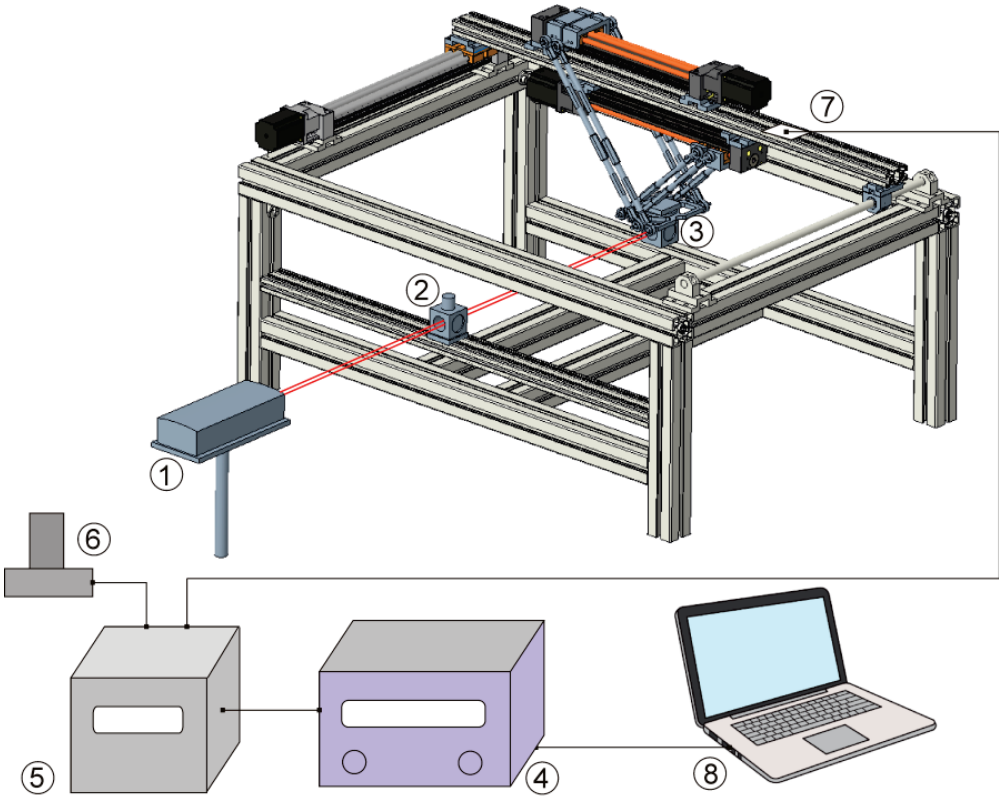


Figure 4. Positioning accuracy test procedure.

The procedure for testing the positioning accuracy of machine tools implies that the machine is programmed to perform an incremental movement along the measured axis in an automated cycle. Stopping the movement is conducted with a pause at the appropriate points according to the standard's requirements (in the positive and negative direction of movement from the start to the end programmed point). Realization of the test procedure gives the values of x_i. The results are presented tabularly and in the form of a diagram. According to the standard, the processing of measurement results includes the calculation of the following statistical quantities. These are reversal error at a position in point "i" (B_i), reversal error of an axis (B), unidirectional positioning repeatability of an axis (R), unidirectional systematic positioning error of an axis (E_+ and E_-), bi-directional systematic positioning error of an axis (E), mean bi-directional positioning error of an axis

(M), unidirectional positioning error of an axis (A_+ and A_-), and bi-directional positioning error of an axis (A).

The obtained results can be displayed as a standardized diagram showing the mean and individual deviation values from the programmed position, which enables the axis to be calibrated.

The analysis of the obtained results in the form of tables and diagrams enables the calibration of individual machine tool axes by introducing predictive error values at individual machine locations.

Calibrating machine tools with non-linear kinematics represents an additional challenge since the error is measured experimentally and expressed in external machine coordinates (the position of the executive body of the machine in the MCS coordinate system). Compensation values are entered in internal coordinates (in individual axis coordinates). Bearing in mind that movement in the direction of the X axis is realized by constant movement in the direction of the u_1 and u_2 axes and the direction of the Z axis in opposite directions at the same speed, the compensation value is determined for each point of movement according to the expression obtained by forming the first differential of the equation for internal coordinates. This gives expressions for the errors at specific points u_{1i} and u_{2i}, corresponding to the measurement points x_{pi} and z_{pi}:

$$\Delta u_{1i} = \Delta x_p + \frac{z_{pi} - d}{\sqrt{{l_p}^2 - (z_{pi} - d)^2}} \Delta z_p \tag{12}$$

$$\Delta u_{2i} = -\Delta x_p + \frac{z_{pi} - d}{\sqrt{{l_p}^2 - (z_{pi} - d)^2}} \Delta z_p \tag{13}$$

2.4. LinuxCNC and the Machine Calibration Methodology

The control system of the realized prototype is based on PC architecture and applies a modified kernel of the Linux operating system adapted for calculations of interpolation functions in real-time (real-time Linux) kernel and LinuxCNC 2.9.2 Debian 12 Bookworm RTAI management software. This type of control system was chosen for the prototype because of the open-source license, the possibility of defining non-linear kinematics, and the possibility of compensating systematic errors according to several criteria. The use of LinuxCNC primarily refers to the possibility of compensating for the backlash of the ballscrew spindle and systematic positioning errors according to the unidirectional and bidirectional methods. Error correction is realized by creating a file that introduces compensations for the indicated coordinates of the axis position (internal coordinates, i.e., slider position) in the machine coordinate system, eliminating systematic errors caused by the geometry of the spindle, guides, and assembly of machine elements.

There are two procedures for calibrating the measuring system: unidirectional, which enables the systematic errors at a certain point to be approximately brought to zero; and bidirectional, which enables separate calibration of the measuring system for movement in the positive and negative directions. The unidirectional method is used to adjust machine tools of low- and medium-accuracy classes. The bidirectional method, an additional function in most control systems, adjusts precision machine tools and coordinates measuring machines.

Table 1 shows the layout of the parameter file for bidirectional error compensation. The first column of the file represents the coordinates of the internal axis in the machine's coordinate system. In contrast, the other two represent the compensation values of the points when moving in the positive and negative directions. Position coordinates, as well as compensation values, are given in the table in millimeters. During calibration, it is possible to choose whether the compensations are specified as a compensation value or a real coordinate value for a given position.

Table 1. Values of bidirectional error compensation.

Position	Compensation in + Direction	Compensation in − Direction
14.98487	0.14448	0.12976
33.98487	0.11437	0.10103
52.98487	0.10706	0.09394
71.98487	0.07692	0.06408
90.98487	0.06960	0.05900
109.98487	0.05155	0.03921
128.98487	0.05041	0.03854
147.98487	0.02685	0.01830
166.98487	0.02138	−0.00761
185.98487	−0.00636	−0.01888
204.98487	0.00225	−0.00121

3. Test Results

3.1. Presentation of Tests and Results

Calibration of the prototype O-X glide machine tool was realized using measuring equipment for laser interferometry manufactured by HP (laser head 5500 C, display 5505 A, interferometer 10565 B retroreflector 10550 B, and compensator of external conditions 2044 A). Figure 5 shows the setup of the measuring equipment on the machine prototype during measurement, where (1) denotes the laser measuring head, (2) indicates the interferometer, and (3) signifies the retroreflector.

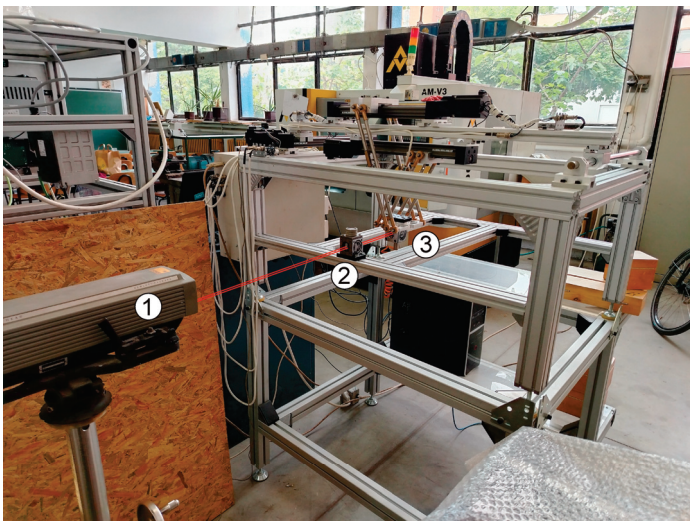


Figure 5. Realization of measurement.

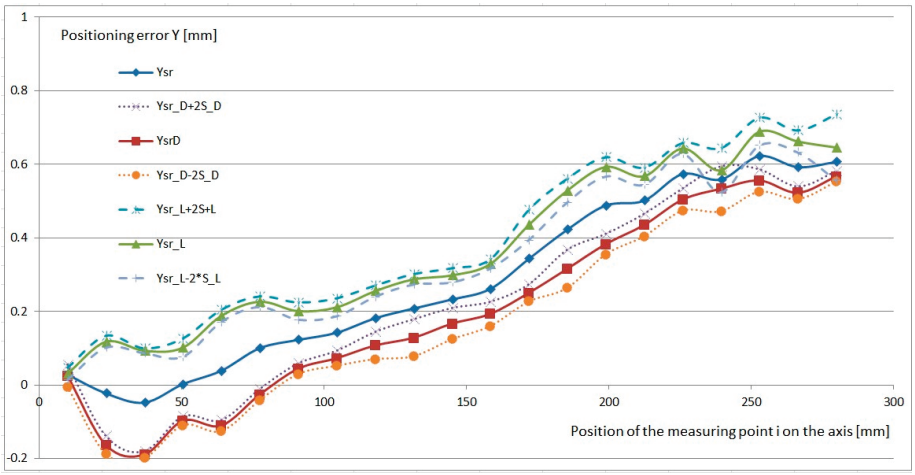
Data acquisition and processing were implemented using the Matlab r2024a programming environment, which included an application for compensating environmental conditions, calculating errors, and generating graphics created for research purposes.

Testing and calibration of the hybrid machine tool was carried out in three stages:

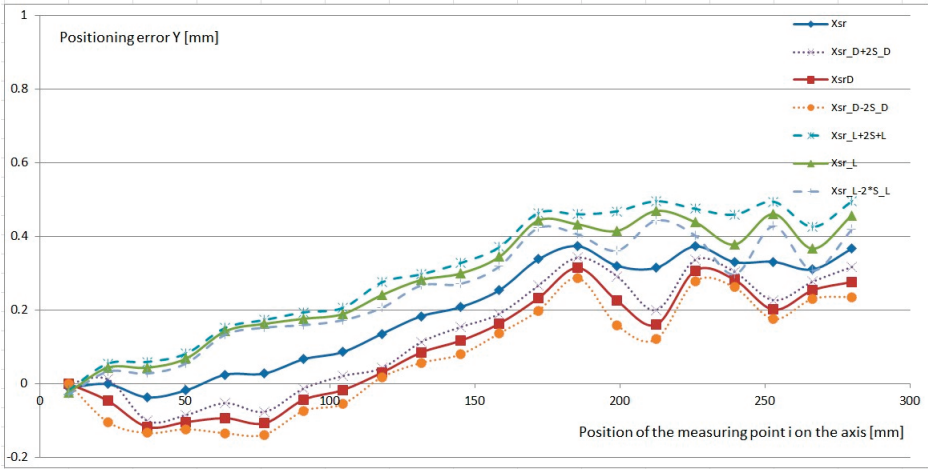
- Testing the machine in an uncompensated state for all three external axes. After that, the characteristic error sizes were calculated, and graphs were created for all three axes;
- Defining compensation values for the unidirectional compensation method, creating compensation files for all three internal axes. After compensating for the errors, the machine was tested after calibration;
- Defining compensation parameters for movement in the positive and negative direction for all three axes (bidirectional compensations).

For the Y axis (serial axis), compensation values were expressed directly from the measurement results, while for X and Z (plane parallel mechanism segments), compensation parameters were calculated for each point according to Expression (11).

Figure 6a,b show graphs for the initial state and bidirectional error compensation for the Y axis.



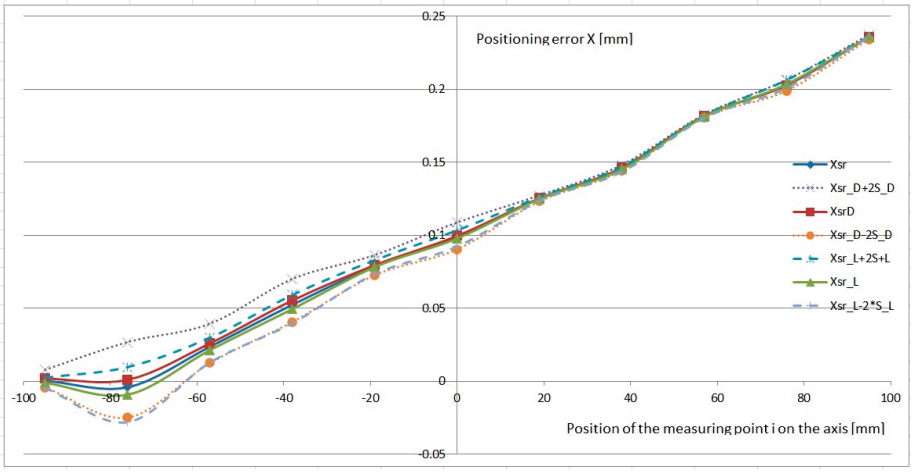
(**a**)



(**b**)

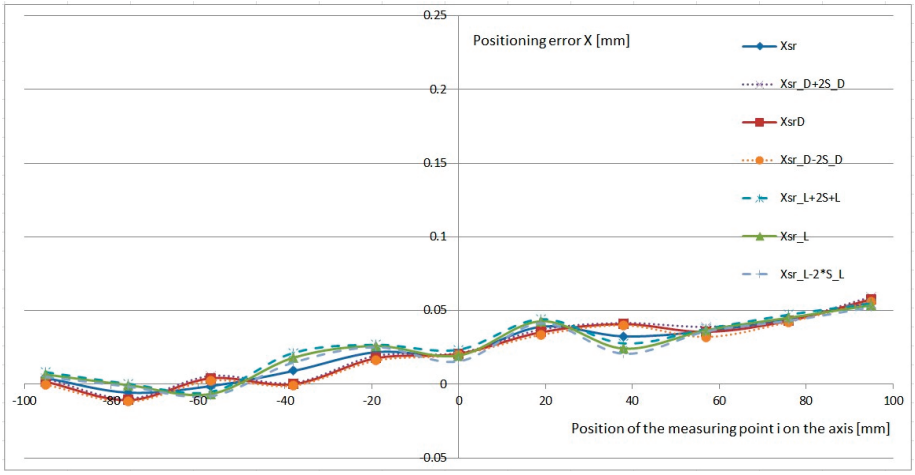
Figure 6. Initial condition (**a**) and test results after error compensation (**b**) for Y axis.

Figure 7a,b show the graphs for the initial state and bidirectional error compensation for the X axis.



(**a**)

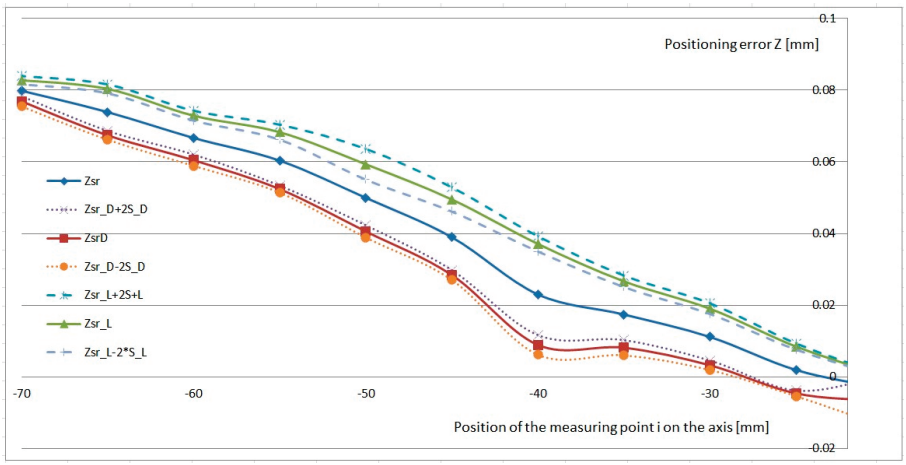
Figure 7. *Cont.*



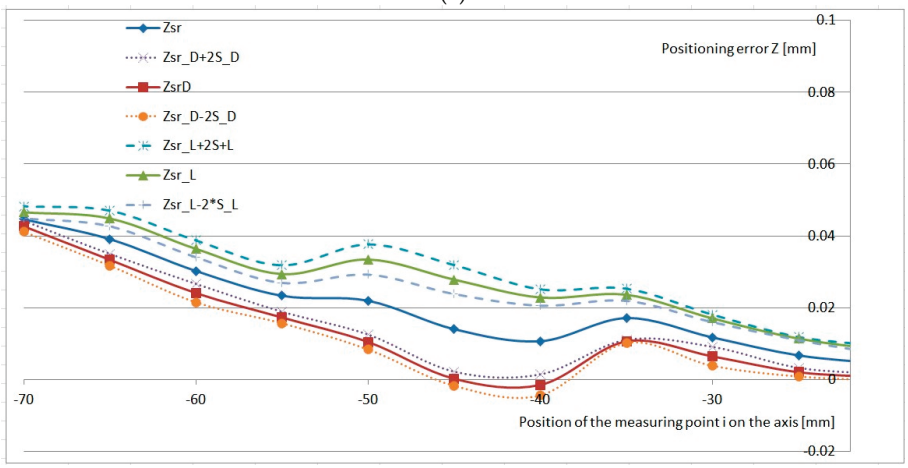
(**b**)

Figure 7. Initial state (**a**) and test results after error compensation (**b**) for the X axis.

Figure 8a,b show graphs for the initial state and bidirectional error compensation for the Z axis.



(**a**)



(**b**)

Figure 8. Initial state (**a**) and test results after error compensation (**b**) for the Z axis.

The presentation of numerical values of characteristic quantities before the compensation process as well as after unidirectional and bidirectional calibration is shown in Table 2.

Table 2. Results of the calibration process of the O-X glide mechanism.

Axis	Stage of Analyzing	B [mm]	R [mm]	E [mm]	M [mm]	A [mm]
X	Initial state	0.01658	0.05487	0.245	0.23984	0.265148
	Unidirectional calibration	0.0116	0.04464	0.1059	0.08746	0.11996
	Bidirectional calibration	0.01014	0.02226	0.06842	0.06131	0.07114
Y	Initial state	0.02371	0.389342	0.87764	0.6703	0.93336
	Unidirectional calibration	0.010784	0.37486	0.81262	0.54364	0.85545
	Bidirectional calibration	0.00492	0.32972	0.58622	0.41036	0.63381
Z	Initial state	−0.01384	0.03363	0.08956	0.08302	0.09754
	Unidirectional calibration	−0.00588	0.03306	0.0656	0.0489	0.0681
	Bidirectional calibration	−0.0039	0.02768	0.04806	0.04025	0.05266

3.2. Measurement Uncertainty of Positioning Accuracy Measurement

Following the ISO 230 standard, analysis of the test conditions and used measuring equipment was performed for the conducted tests, and in accordance with the ISO 230-9:2005 [26] standard, the measurement uncertainty was presented. Measuring equipment is set to meet all manufacturer's regulations and minimize unwanted sources of errors such as misalignment error, Brayan error (generalized Abbe error), dead path error, etc.

During the measurement, the laboratory temperature was in the range of 23 °C ± 1 °C. The measurement time did not last longer than 15 min for an individual axis. The instruments were not previously calibrated, so the uncertainty values provided by the equipment manufacturer were used. The instrument was aligned within 1 mm of the axis under test by aligning the return beam of the laser beam. The repeatability of the setting was in increments of 50 mm, and the deflection gradients were a maximum of 50 µm/m. The environmental variation error was taken from recommendations [27]. The laser interferometer was positioned so that the path error could be minimized. Table 1 shows the obtained uncertainty values for the farthest measurement point for all axes. The laser measurement system used includes automatic compensation of the environment and the coefficient of expansion. $u_{M,Device}$ and $u_{E,Device}$ were considered zero. For steel, a thermal expansion coefficient of α = 0.012 µm/mm °C was used, and the uncertainty range was set to $\Delta\alpha$ = 0.002 µm/mm °C, following ISO recommendations.

For testing, a helium–neon laser interferometer with automatic Zeeman-split two-frequency output, model number HP 5500C, was used. Table 3 presents the influential parameters of measurement uncertainty for the equipment used.

Table 3. Table of influential parameters of measurement uncertainty.

Device—u_D	X Axis	Z Axis	Y Axis	Units
L—measurement length	200	70	270	mm
a—accuracy	3.4	3.4	3.4	ppm
$u_{accuracy}$	0.1963	0.0687	0.2650	µm
Wavelength stability	0.04	0.04	0.04	ppm
$u_{wavelength}$	0.0023	0.0008	0.0031	µm
$u_{device.estimate}$	0.1986	0.0695	0.2681	µm
r—resolution	0.1	0.1	0.1	µm
$u_{resolution}$	0.0289	0.0289	0.0289	µm
u_D	0.2007	0.0753	0.2697	µm
Misalignment—u_M				
Misalignment	1	1	1	mm
γ—angle	0.2865	0.8185	0.2122	°
ΔL_m—misalignment	2.5000	7.1432	1.8519	µm
u_M	0.7217	2.0621	0.5346	µm

Table 3. *Cont.*

Device—u_D	X Axis	Z Axis	Y Axis	Units
Temperature—u_T				
Standard uncertainty of sensor	0.7	0.7	0.7	°C
$u(\Theta)_{calculated}$	0.2021	0.2021	0.2021	°C
$u_{M.Machine\ tool}$	0.4850	0.1697	0.6547	µm
$u_{M.Device}$	0	0	0	µm
T_M—Machine temperature	24	24	24	°C
ΔT	4	4	4	°C
$u(\alpha)$	0.0006	0.0006	0.0006	µm/mm°C
$u_{E.Machine\ tool}$	0.4619	0.1617	0.6235	µm
$u_{E.Device}$	0	0	0	µm
u_T	0.6697	0.2344	0.9041	µm
Environmental Variation—u_{EVE}				
E_{VE}—drift	1	1	1	µm
u_{EVE}	0.2887	0.2887	0.2887	µm
Repeatability of the Setup—u_S				
O_{ABBE}	50	50	50	mm
D_{angle}	50	50	50	µm/m
ΔL_S	3.5355	3.5355	3.5355	µm
u_S	1.0206	1.0206	1.0206	µm
At the Measuring Length—u_P				
u_P	1.4610	2.3319	1.5169	µm

Uncertainty parameters were also determined based on the measurement length. The obtained values are presented in Table 4.

Table 4. Uncertainty values of the measurement parameters.

Measurement Parameters	X Axis	Z Axis	Y Axis	Units
n—number of cycles	5	5	5	-
U(R+, R−)	1.15	1.15	1.15	µm
U(B)	4.12	4.12	4.12	µm
U(R)	4.27	4.27	4.27	µm
U(E, E+, E−)	2.88	4.64	2.99	µm
U(M) [n = 10]	2.87	4.63	2.98	µm
U(A)	3.33	3.59	3.35	µm

All values of measurement uncertainties for the observed measurements are within the limits defined by the standard.

4. Discussion

By analyzing the obtained results, the construction and exploitation characteristics of the prototype, the efficiency of the calibration process in the specific case, and the applicability of the adopted calibration methodology to machines with non-linear kinematics can be seen.

Analysis of test graphs during the initial measurement (without calibration) and after compensating errors on all three axes indicate that the Y axis of the machine tool prototype has a significant contribution of random error in the measurement. This can be explained by the construction solution of the prototype, which includes the traversal Y axis with the drive sub-assembly on one side of the gantry. Therefore, the calibration effects are the least pronounced for this axis, and the error value is the highest. The remaining two spatial axes (X and Z) created by the parallel mechanism performed very well from the point of view of random errors, bearing in mind that the prototype has an open steering coupling.

As in the case of serial mechanisms, the test indicates the necessity of calibrating machine tools with non-linear kinematics. This is indicated by the reduction values of the two-way system error along the axis (E) and the two-way positioning error along the axis (A). The results are shown in Table 5.

Table 5. Analysis of the success of the O-X glide mechanism calibration process.

Axis	Stage of Analyzing	E [mm]	Error Reduction [%]	A [mm]	Error Reduction [%]
X	Initial state	0.245		0.265148	
	Unidirectional calibration	0.1059	56.77	0.11996	54.75
	Bidirectional calibration	0.06842	72.07	0.07114	73.17
Y	Initial state	0.87764		0.93336	
	Unidirectional calibration	0.81262	7.40	0.85545	8.34
	Bidirectional calibration	0.58622	33.20	0.63381	32.09
Z	Initial state	0.08956		0.09754	
	Unidirectional calibration	0.0656	26.75	0.0681	30.18
	Bidirectional calibration	0.04806	46.33	0.05266	46.01

The obtained results indicate the efficiency of the process of calibrating machine tools as well as the possibilities realized by the application of unidirectional and bidirectional calibration for all examined axes.

Calibrating machine tools with non-linear kinematics implies the process of defining compensation values, which includes the conversion of external coordinates into internal coordinates, as well as calculating the contribution of the internal axis to the error that occurs at the top of the tool during movement. This process includes the application of expressions determined by the inverse kinematics of the mechanism and the modification of the calibration procedure following the specifics of the specific type of mechanism. In all calibration stages, measurements of current positioning accuracy values according to ISO 230 were performed three times. Control measurements showed that only two measurements (before and after the introduction of compensations) were needed to achieve the full effects of the process. This confirms the hypothesis that the calibration process of machine tools with non-linear kinematics can be realized with the same efficiency level as for machines with a linear kinematic structure.

During positioning accuracy measurements, as per ISO 230-2, the platform's speed was constant. Since the measurements were made on a machine tool with non-linear kinematics, the slide speeds were not linearly related to the platform speed, resulting in variable slide speeds during the measurement. This variable speed can affect the resulting compensation factors. During this positioning accuracy check procedure, of the two machine axes that are created with a parallel mechanism (X and Z), the X axis behaved kinematically identically or at least very similarly to the movements that are performed when checking the accuracy of machine tools with linear kinematics, since in this case the two sliders move at the same constant speed as the platform moves. On the other hand, the influence of the movement of the platform along the Z axis at constant speed on the sliders is non-linear, and different speeds and accelerations occur. This is the cause of the appearance of an additional error in the total positioning error along the mentioned axis. As a result, the calibration process had less efficiency (less error reduction). Further tests should include the influence of differences in kinematic and dynamic movement parameters on the mechanical components of mechanisms and include those results in defining compensatory parameters. Additionally, a more profound observation of such influences (observing uneven movements when measuring and measuring two or more axes) should include tests with circular interpolation using the so-called Ballbar device.

5. Conclusions

Improvements in machine tools in the 21st century are carried out in several directions. One of the most important is improving their mechanical structure through the search for solutions that are adaptable to specific application areas. By applying reconfigurable building principles and non-linear kinematic forms, solutions are realized where, in addition to an adjustable workspace, variable kinematic and dynamic characteristics of machine tools are obtained with a whole series of advantages and disadvantages compared to machine tools with serial kinematics. In such conditions, the analysis of the accuracy of the realized movements and the definition of the methodology of its determination following the valid standards represents an essential step towards a unique process of calibrating machines that considers the differences in the kinematic structure. Testing the accuracy of positioning and calibration of the hybrid machine tool described in the paper is a step in this direction. It represents an introduction to the formation of a unique methodology for testing the volumetric accuracy of machine tools, which takes into account the machine tool's kinematic characteristics, in addition to the components' characteristics.

Based on the obtained results, it can be concluded that the application of bidirectional error compensation on all three external axes of the O-X slide of the machine tool provides the complete elimination of discrete damage to the lead screw spindle and sliders as well as the gap in the nut. By analyzing the systematic errors that occur with machine tools, applying this error compensation method eliminates the need to decompose errors into individual errors and eliminate them with discrete values.

Positioning accuracy results obtained after the calibration process fully correspond to machine tools with open-loop control and applied stepper motors. They can even be considered very good, except for the Y axis, where the error is somewhat more significant due to construction reasons (on one side of the gantry is the driving element, and on the other is the sliding, driven element).

The research conducted on the results presented in the discussion indicates the influence of the stopping time, the feedrate movement speed, and the movement method during measurement. The standards determine all these influential parameters but without recommendations on when and how to choose them according to the machines' kinematic structure, purpose, and working conditions, which directly impact the calibration process. In addition, the results of such research create prerequisites for the application of Edge computing technologies to compensate for errors in real time, which is a continuation of the presented research.

Author Contributions: Conceptualization, S.T.; methodology, S.T., M.Z. and S.Z.; software, S.T.; validation, M.Z. and A.B.; investigation, S.T. and S.Z.; resources, S.T.; writing—original draft preparation, S.T.; writing—review and editing, Z.D. and S.Z.; visualization, A.K., S.T. and S.Z.; supervision, M.Z. All authors have read and agreed to the published version of the manuscript.

Funding: This research has been supported by the Ministry of Science, Technological Development and Innovation through projects "Scientific and Artistic Research Work of Researchers in Teaching and Associate Positions at the Faculty of Technical Sciences, University of Novi Sad", grant number 451-03-65/2024-03/200156, "Integrated research in macro, micro, and nano mechanical engineering", grant number 451-03-65/2024-03/200105 and "Research project of the Institute Lola Ltd.", grant number 451-03-66/2024-03/200066.

Institutional Review Board Statement: Not applicable.

Informed Consent Statement: Not applicable.

Data Availability Statement: The data presented in this study are available in the article.

Acknowledgments: We appreciate the anonymous reviewers' and editorial team members' suggestions and comments. Thanks for the support of the fund projects mentioned above.

Conflicts of Interest: Author Zoran Dimic was employed by the company Research and Development Institute Lola Ltd. The remaining authors declare that the research was conducted in the absence of any commercial or financial relationships that could be construed as a potential conflict of interest. Research and Development Institute Lola Ltd. used nonprofit founding for this research supported by the Ministry of Science, Technological Development and Innovation Republic of Serbia. The funder was not involved in the study design, collection, analysis, interpretation of data, the writing of this article or the decision to submit it for publication.

References

1. Bringmann, B.; Küng, A.; Knapp, W. A Measuring Artefact for true 3D Machine Testing and Calibration. *CIRP Ann.* **2005**, *54*, 471–474. [CrossRef]
2. Sun, T.; Wang, W.; Chen, Z.; Zhu, Y.; Xu, K.; Wu, H.; Sang, Z.; Lu, K.; Yang, H. Positioning Errors Measurement of CNC Machine Tools Based on J-DBB Method. *Appl. Sci.* **2021**, *11*, 11770. [CrossRef]
3. Schwenke, H.; Knapp, W.; Haitjema, H.; Weckenmann, A.; Schmitt, R.; Delbressine, F. Geometric error measurement and compensation of machines—An update. *CIRP Ann.* **2008**, *57*, 660–675. [CrossRef]
4. Ibaraki, S.; Knapp, W. Indirect Measurement of Volumetric Accuracy for Three-Axis and Five-Axis Machine Tools: A Review. *Int. J. Autom. Technol.* **2012**, *6*, 110–124. [CrossRef]
5. Gao, W.; Ibaraki, S.; Donmez, M.A.; Kono, D.; Mayer, J.R.R.; Chen, Y.-L.; Szipka, K.; Archenti, A.; Linares, J.-M.; Suzuki, N. Machine tool calibration: Measurement, modeling, and compensation of machine tool errors. *Int. J. Mach. Tools Manuf.* **2023**, *187*, 104017. [CrossRef]
6. Zhu, S.; Ding, G.; Qin, S.; Lei, J.; Zhuang, L.; Yan, K. Integrated geometric error modeling, identification and compensation of CNC machine tools. *Int. J. Mach. Tools Manuf.* **2012**, *52*, 24–29. [CrossRef]
7. Bringmann, B.; Besuchet, J.P.; Rohr, L. Systematic evaluation of calibration methods. *CIRP Ann.* **2008**, *57*, 529–532. [CrossRef]
8. Ke, J.-D.; Wang, Y.-J.; Tsai, J.-C. Kinematic error model of a 3-PUU parallel mechanism for translational motion. *Measurement* **2022**, *202*, 111853. [CrossRef]
9. Kelaiaia, R.; Chemori, A.; Brahmia, A.; Kerboua, A.; Zaatri, A.; Company, O. Optimal dimensional design of parallel manipulators with an illustrative case study: A review. *Mech. Mach. Theory* **2023**, *188*, 105390. [CrossRef]
10. Pandilov, Z. Dominant types of errors at parallel kinematics machine tools. *FME Trans.* **2017**, *45*, 491–495. [CrossRef]
11. Wen, K.; Gosselin, C.M. Forward Kinematic Analysis of Kinematically Redundant Hybrid Parallel Robots. *J. Mech. Robot.* **2020**, *12*, 061008. [CrossRef]
12. Fang, H.; Tang, T.; He, Z.; Liu, Y.; Zhang, J. A novel hybrid machine tool integrating a symmetrical redundantly actuated parallel mechanism: Design, kinematics, prototype and experiment. *Mech. Mach. Theory* **2022**, *176*, 105013. [CrossRef]
13. Russo, M.; Zhang, D.; Liu, X.-J.; Xie, Z. A review of parallel kinematic machine tools: Design, modeling, and applications. *Int. J. Mach. Tools Manuf.* **2024**, *196*, 104118. [CrossRef]
14. Pateloup, S.; Chanal, H.; Duc, E. Process definition of preformed part machining for taking benefit of parallel kinematic machine tool kinematic performances. *Int. J. Adv. Manuf. Technol.* **2012**, *58*, 869–883. [CrossRef]
15. Gabrovšek, B.; Novak, T.; Povh, J.; Rupnik Poklukar, D.; Žerovnik, J. Multiple Hungarian Method for k-Assignment Problem. *Mathematics* **2020**, *8*, 2050. [CrossRef]
16. Antonov, A.; Fomin, A.; Glazunov, V.; Kiselev, S.; Carbone, G. Inverse and forward kinematics and workspace analysis of a novel 5-DOF (3T2R) parallel–serial (hybrid) manipulator. *Int. J. Adv. Robot. Syst.* **2021**, *18*, 1729881421992963. [CrossRef]
17. Karimi, D.; Nategh, M.J. Kinematic nonlinearity analysis in hexapod machine tools: Symmetry and regional accuracy of workspace. *Mech. Mach. Theory* **2014**, *71*, 115–125. [CrossRef]
18. Song, J.; Mou, J.-I.; King, C. Parallel Kinematic Machine Positioning Accuracy Assessment and Improvement. *J. Manuf. Process.* **2000**, *2*, 48–58. [CrossRef]
19. Luo, Y.; Gao, J.; Zhang, L.; Chen, D.; Chen, X. Kinematic calibration of a symmetric parallel kinematic machine using sensitivity-based iterative planning. *Precis. Eng.* **2022**, *77*, 164–178. [CrossRef]
20. *ISO 230-4*; Test Code for Machine Tools—Part 4: Circular Tests for Numerically Controlled Machine Tools. Industrial Automation Systems and Integration. ISO: Geneva, Switzerland, 2022.
21. Zivanovic, S.; Tabakovic, S.; Zeljkovic, M.; Dimic, Z. Modelling and analysis of machine tool with parallel-serial kinematics based on O-X glide mechanism. *J. Braz. Soc. Mech. Sci. Eng.* **2021**, *43*, 456. [CrossRef]
22. *ISO 230-2*; Test Code for Machine Tools—Part 2: Determination of Accuracy and Repeatability of Positioning of Numerically Controlled Axes. Industrial Automation Systems and Integration. ISO: Geneva, Switzerland, 2014.
23. *DIN-VDI/DGQ 3441*; Statistische Pruefung der Arbeits- und Positionsgenauigkeit von Werkzeugmaschinen. VDI: Düsseldorf, Germany, 1977.
24. *B5.54-2005(R2020)*; Methods for Performance Evaluation of Computer Numerically Controlled Machining Centers. ASME: New York, NY, USA, 2005.
25. *JIS B 6333:1986*; Test Code for Performance and Accuracy of Numerically Controlled Knee Type Vertical Milling Machines. JSA: Tokyo, Japan, 1986.

26. *ISO 230-9*; Test Code for Machine Tools—Part 9: Estimation of Measurement Uncertainty for Machine Tool Tests According to Series ISO 230, Basic Equations. ISO: Geneva, Switzerland, 2005.
27. Quan, L.; Zhao, W. Uncertainty analysis of motion accuracy on single-axis feed drive systems. *Adv. Mech. Eng.* **2024**, *16*, 16878132231222790. [CrossRef]

Disclaimer/Publisher's Note: The statements, opinions and data contained in all publications are solely those of the individual author(s) and contributor(s) and not of MDPI and/or the editor(s). MDPI and/or the editor(s) disclaim responsibility for any injury to people or property resulting from any ideas, methods, instructions or products referred to in the content.

applied sciences

MDPI

Communication

A Machine Tool for Boring of the Diesel Engine Block Counterbore

Jaroslaw Galkiewicz * and Urszula Janus-Galkiewicz

Faculty of Mechatronics and Mechanical Engineering, Kielce University of Technology, Aleja Tysiaclecia Panstwa Polskiego 7, 25-314 Kielce, Poland; ujanus@tu.kielce.pl
* Correspondence: jgalka@tu.kielce.pl

Featured Application

The article presents a new device for in situ boring a worn or damaged counterbore in the diesel engine block to mount the cylinder liner flange.

Abstract

This paper presents the design and operating principle of a mechanical device for machining a cylinder liner flange seat in a diesel engine damaged due to cavitation or wear. Mounted on the engine block, the device allows the removal of damaged material and the formation of an undercut for the installation of repair rings. The gear ratios used allow for manual driving of the device. The device allows engine repair without the need for disassembly, which provides significant economic benefits by shortening repair time, reducing repair costs, and extending engine life, which is also important for environmental protection.

Keywords: diesel engine; engine block counterbore; cavitation; engine wear

1. Introduction

The cylinder liners of diesel engines are subject to wear by many mechanisms. The most obvious is the abrasive wear resulting from the relative movement of the piston to the cylinder [1,2]. Fuel combustion produces high temperatures that have a wide-ranging impact on the cylinder liner and engine block. The increase in temperature causes changes in the properties of the lubricating oil. Firstly, it affects the viscosity of the oil. It also causes carbonization of the lubricating oil. As a result, temperature has a very negative effect on the friction coefficient, indirectly causing increased wear on the surface of the cylinder liner due to changes in the tribological properties of the surface [3] and its shape through deformation of the cylinder liner [4]. An increase in temperature also generates thermal stresses [5], which become particularly significant when combined with mechanical deformations. The heated gases generated as a result of combustion also cause accelerated erosion of the cylinder surface. Pressure changes cause vibrations, a jump in circumferential stresses, and changes in the cylinder dimensions [6,7]. The analyses show that the greatest effect of combined thermal and mechanical stresses is observed in the upper part of the cylinder liner.

In the case of wet cylinder liners, the outer wall is in direct contact with the coolant. Geometric changes due to the rapid increase in pressure and temperature cause vibrations in the surrounding coolant. Vapor-filled spaces appear. This phenomenon is called cavitation. The returning fluid damages the metal surface it hits. This process, repeated during engine operation, ultimately leads to pitting, which involves the ejection of small lens-shaped

metal fragments from the surface of the cylinder. This phenomenon is most noticeable in the central cylinder [8].

The described extreme conditions can cause an engine-block crack. The high price of the new block causes the replacement of such an element to be the last resort. Usually, when the crack is detected early enough, the first choice is welding; however, if the crack grows too much, the only remedy is replacement of the part.

In the upper cylinder section, repeated pressure spiking to very high values and cyclical thermal stresses lead to cyclical cylinder deformation and significant loading of the cylinder seat surface in the engine block [9–11]. Importantly, the cylinder deformation is non-uniform, generating an oval shape. This causes areas in the upper part of the engine block to be characterized by accelerated wear of the cylinder seat. Contaminants and coolant entering this space cause coolant leaks, accelerated erosion of the engine block, and movement of the cylinder liner, which in turn leads to engine overheating and a drop in efficiency. An engine block damaged in this way is not suitable for further operation. In the case of damaged cylindrical liners damaged by the described mechanisms, the best solution is usually to replace them, although in the case of minor damage it is even possible to repair the damage. Unfortunately, if the engine block is damaged, alternatives include replacing them with new ones, which is very expensive, or machining the damaged surfaces and using repair rings, which is a much cheaper operation and, given environmental concerns, highly desirable (Figure 1).

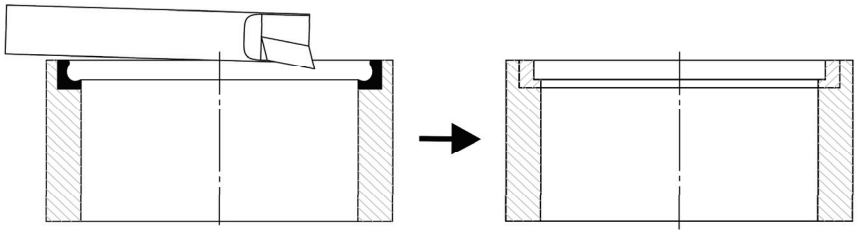


Figure 1. Schematic diagram of the processing of a worn socket.

Unfortunately, the operation of machining a seat in an engine block is very complicated due to the tools used. The most expensive solution is to use a CNC machine, such as the Rottler Cylinder Boring CNC machining center. In this case, the machining costs include the cost of operating the machine and disassembling the engine. The block is large, heavy, difficult to disassemble and, therefore, expensive to disassemble for machining or replacement. That is why the seat-boring operation should be performed without disassembling the engine using a dedicated tool. There are portable machines available in the industry that allow you to machine holes in the engine block, but they are usually expensive (for example, Monaco Tool 52050, Kent-Moore PT-2050-D Porta-Matic Counterbore Basic Kit).

This article presents a device that allows the creation of a counterbore for the installation of the repair bush, allowing the reinstallation of the cylinder liners so that the engine operates properly. The device is universal, relatively cheap, and can be easily adapted to any engine type. Most importantly, it does not require complete engine disassembly, reducing costs and repair time.

2. Materials and Methods

All non-standardized threaded components of the device are made of hardened and tempered 40HM/1.7225/42CRMO4 steel (CELSA Huta Ostrowiec, Ostrowiec Świętokrzyski, Poland). Selected steel has, first of all, high hardness, which guarantees an acceptable life span of threads. Other non-standardized elements are made of C45 steel (ArcelorMittal Poland S.A., Dąbrowa Górnicza, Poland) to reduce the cost of the device. Figure 2 shows the device's construction. It consists of a gear enabling the synchronization of the rotation of the cutting

tool with the feed, a telescopic body generating the tool feed, and a base attached to the engine by means of screws screwed into the head bolt holes. Figure 2 presents both sides of the device. The overall dimensions of the device are, approximately, diameter 215 mm, and height 337 mm.

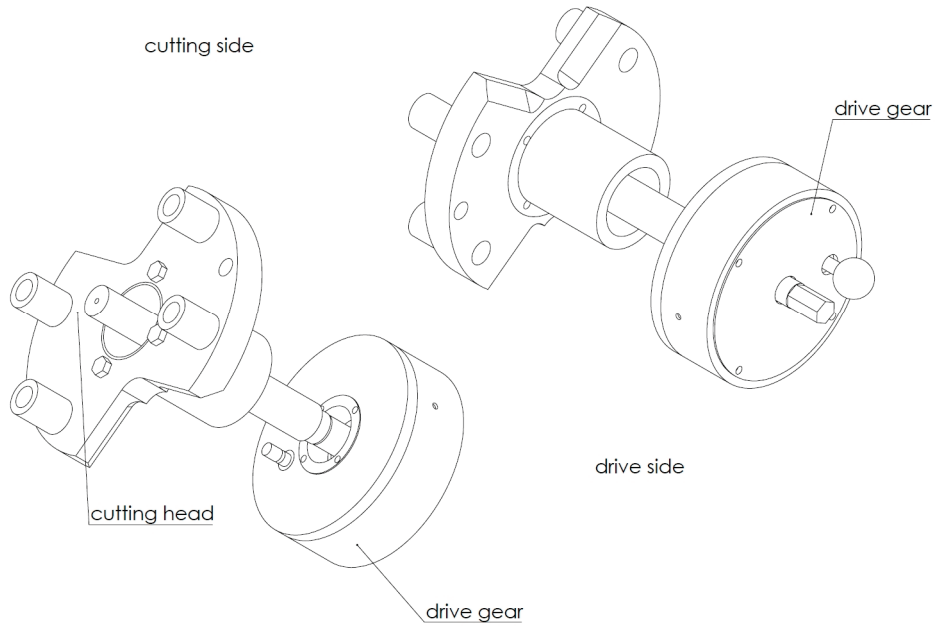
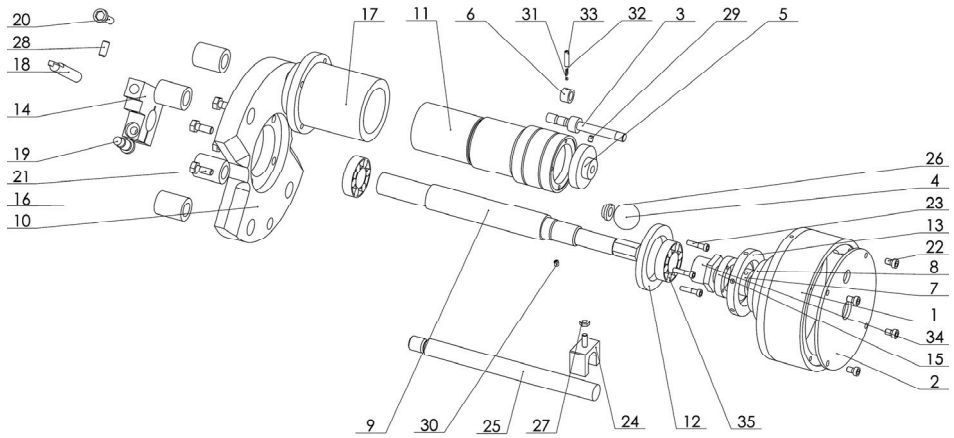


Figure 2. Main components of the device.

Figure 3 shows an exploded view of the device, revealing its internal structure and all components. Part numbers referenced in subsequent descriptions are based on Figure 3.



1 gear transmission body
2 transmission cover
3 shaft lever
4 handle
5 gear z = 32
6 sliding bearing 1
7 gear z = 28
8 gear z = 50
9 main shaft
10 plate (base)
11 body
12 retaining ring 1
13 retaining ring 2
14 head
15 nut
16 spacer
17 sleeve
18 cutting tool
19 adjusting screw
20 clamp screw
21 bolt M8x20
22 bolt M6x10
23 bolt M5x23
24 fork
25 stabilizer (rod)
26 sliding bearing 2
27 nut M6
28 set screw M8x18
29 set screw M5x7.5
30 set screw M5x6
31 ball 3mm
32 spring 3x1x8
33 set screw M5x20
34 locking nut
35 bearing 6005

Figure 3. Exploded view.

The main element of the device is shaft 9. The length of the shaft is 337 mm, while the largest diameter is 30 mm. On one end, it is terminated with a hexagon, allowing the drive to be applied. The hexagon's across-corners size is 20 mm. On the opposite end of the shaft, head 14 with the cutting tool is mounted. Figure 4 shows the assembly of the shaft and a cutting head within the bearing housing. The shaft is rigidly connected to the gear, whose body, when rotated, forces the feed of the cutting tool.

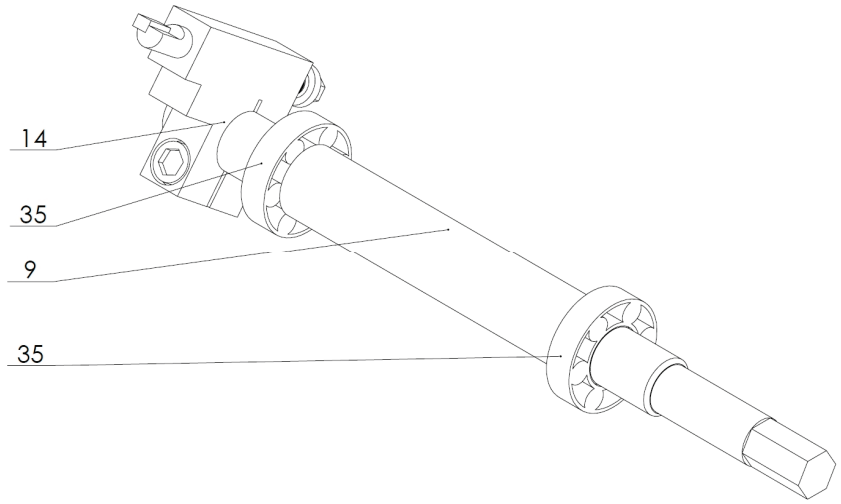


Figure 4. Shaft with bearings and cutting head.

The head 14 is clamped to shaft 9 by means of a screw M8 20. The thickness of the cutting head in the presented model is 20 mm; however, it can be adjusted to the size of the cutting tool. Its design allows one to determine the diameter of the hole that is being machined. The cutting tool 18 is pulled out of the socket to the appropriate size by means of an adjustment screw 19. After the position of the cutting tool is determined, it is fixed by means of a screw 28 (Figure 5).

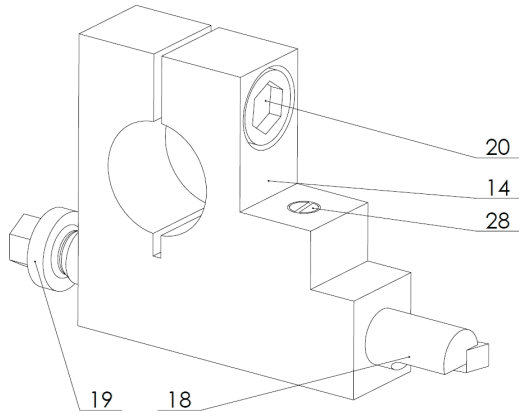


Figure 5. Cutting head.

The shaft 9 is mounted inside body 11 via two bearings 35. Figure 6 presents the shaft placed inside the body of the device with the bearings drawn in red.

The bearing on the cutting side is a sliding bearing, while the bearing on the hexagon side is locked from axial movement while maintaining the appropriate clearances (Figure 7). Both bearings are deep-groove ball bearings of the 6005 type. This bearing, together with the shaft and the upper part of the telescopic body, moves in the axial direction. The outer ring of the bearing is locked with a nut 15 screwed into the body 11, while the inner ring of the bearing is locked with a hexagonal head nut 34 screwed onto the threaded part of the shaft 9.

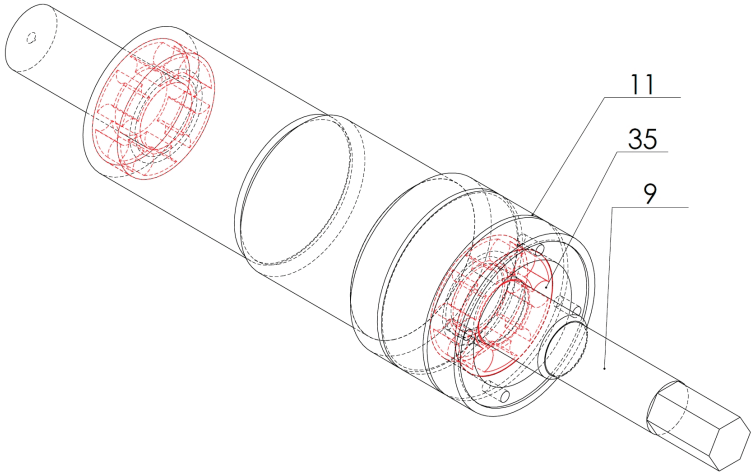


Figure 6. Location of the bearings (red elements) in the body.

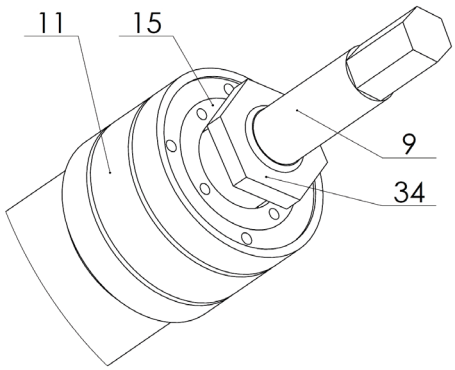


Figure 7. Bearing lock.

Gear transmission body 1 is attached to the front of the device body 11 by means of a gear wheel 8 (z = 50) attached to the body 11 with screws M5x23 23 (Figure 8). Above the gear wheel 8 there is a gear wheel 7 (z = 28). Together with the gear wheel 5 (z = 32) and the gear wheel (z = 10) cut in shaft lever 3, they constitute a drive chain that connects the rotational movement of the shaft with its feed. All gears are made with a 1.5 mm module.

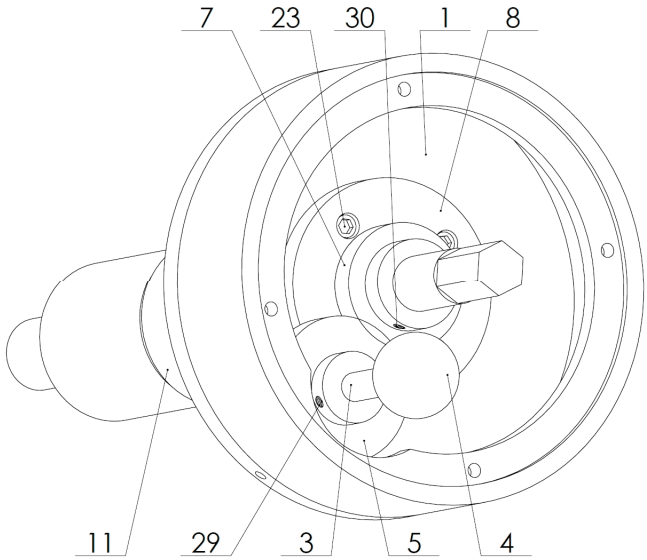


Figure 8. The interior of the gear train.

The gear can be disconnected to set the knife position by moving the shaft lever 3 terminated with a ball handle 4. The position of shaft 3 is controlled by a ball 31 placed in the appropriate lever channel by means of a spring 32. Pulling the ball handle up disengages the gears, allowing the shaft with the cutting head to rotate freely. The ball 31 of diameter 3 mm and the spring 32 are closed in the channel of body 1. The shaft 3 is mounted in the body with the brass bushings 26 and 6 and fits with an H7 tolerance (Figure 9).

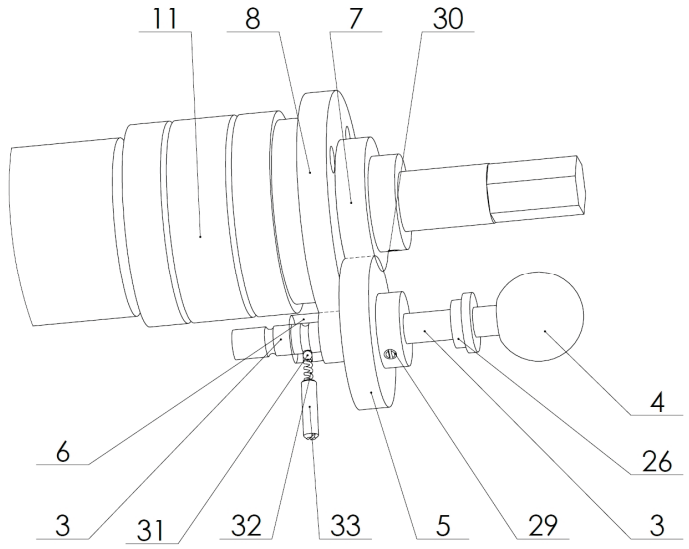


Figure 9. Drive of the cutting tool.

The body is telescopic. Sleeve 17 is screwed to element 11. The length of the sleeve is 105 mm and the overall diameter is 95 mm. The length of element 11 is 185 mm and the diameter is 68 mm. The two parts can be moved relative to each other using a thread M60x1, thus adjusting the depth of the material being removed, and then locked in place using rings 12 and 13 (Figure 10).

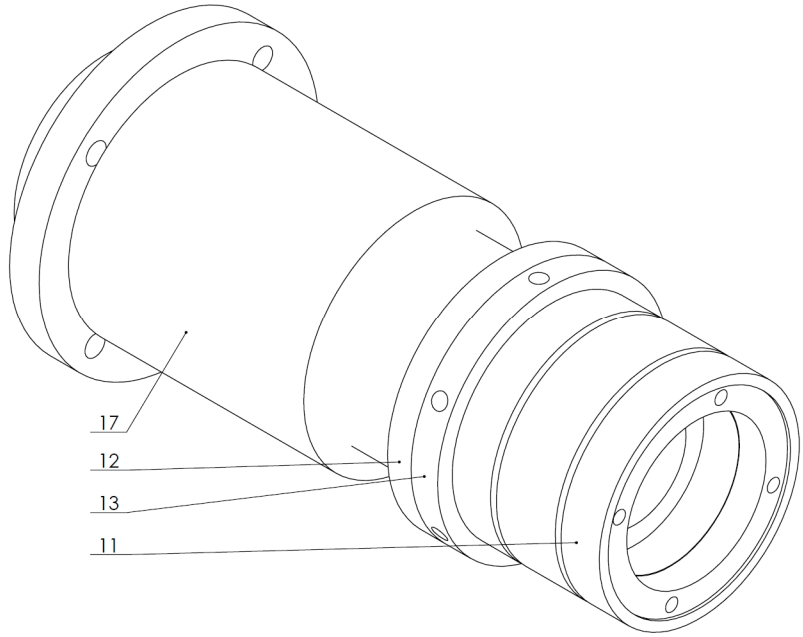


Figure 10. The body of the device.

A plate 10 is attached to the inner sleeve of body 17. The unusual shape of the plate is due to the need to provide access for the measuring tool to the surface being machined. The thickness of the plate is 25 mm, and the external diameter is 215 mm. Figure 11 shows

the optional spacer sleeves 16. The bolts pass through the holes in the base and spacer sleeves, securing the entire device to the engine block using the head bolt holes.

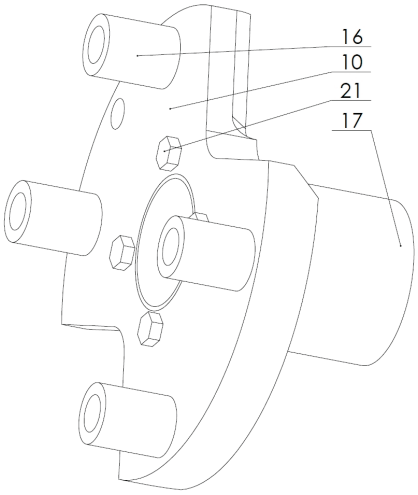


Figure 11. Base of the device.

The relative movement of both body parts (11 and 17) is locked by a rod 25 (Figure 12) screwed into the base 10. A fork 24 is screwed into gear body 1. Its position is locked by a 27 nut. The shape of the fork locks rod 25, preventing rotation of inner body 11 relative to outer body 17 at any setting of their relative axial position.

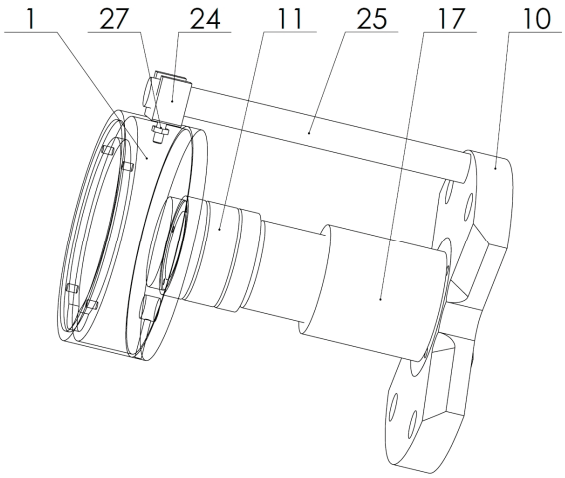


Figure 12. Body position lock.

The device can be applied to engines made by MAN, SCANIA, or DAF. Only the part 10 plate (base) requires modification to accommodate the position of the head bolt holes.

To mount the device coaxially with the hole axis, one of two methods can be used. The locating dowels or pins for the head that are present in the engine block deck can be utilized, or an additional, extra-designed cylinder that is mounted on an undamaged surface of the block. Neither method depends on type of engine.

3. Results

In the case of manual drive, it is proposed to use a crank with a length of l = 0.25 m. Assuming the operator force F = 250 N, the torque at the input (1) [12] is obtained:

$$T_{in} = Fl = 250\ \text{N} \cdot 0.25\ \text{m}\ = 62.5\ \text{Nm} \quad (1)$$

Assuming a low rotational speed of the manual attack equal to n_{in} = 10 rpm, the input power is equal to (2):

$$P_{in} = \frac{T_{in} \cdot n_{in}}{9550} = \frac{62.5 \text{ Nm} \cdot 10 \text{ rpm}}{9550} = 0.065 \text{ kW} \quad (2)$$

Assuming the efficiency of the gear transmission η_g = 0.99 [13], the rolling bearings η_b = 0.995 [12] and the efficiency of the metric thread η_t = 0.1 [14], the general efficiency of the system is obtained using Formula (3). Low thread efficiency (η_t = 0.1) reflects a conservative estimate for unlubricated sliding contact in high-load applications [14]:

$$\eta = \eta_g^2 \cdot \eta_b^3 \cdot \eta_t = 0.99^2 \cdot 0.995^3 \cdot 0.1 = 0.097 \quad (3)$$

The overall efficiency allows the power at the output shaft of the device (4) to be determined:

$$P_{out} = \frac{P_{in}}{\eta} = 0.065 \frac{\text{kW}}{0.097} = 0.006 \text{ kW} \quad (4)$$

The drive system of the device consists of a gear train. The first pair consists of gears 7 and 5, and the second pair consists of shaft 3 and gear 8. All gears are made with a 1.5 mm module. The intermediate gear ratios are (5) and (6):

$$i_1 = \frac{z_5}{z_7} = \frac{32}{28} = 1.14 \quad (5)$$

$$i_2 = \frac{z_8}{z_3} = \frac{50}{10} = 5 \quad (6)$$

This gives a total gear ratio of i = 5.71 and an output speed of n_{out} = 1.75 rpm.

The rotating shaft with the tool causes the body in which it is mounted to rotate at a speed 5.71 times slower. The body's rotation, in turn, causes it to move axially according to the thread pitch, relative to the second part of the body, which is fixed (Figure 13). The thread pitch cut in the body is 1 mm, resulting in one rotation of the shaft producing a feed of f = 0.175 mm.

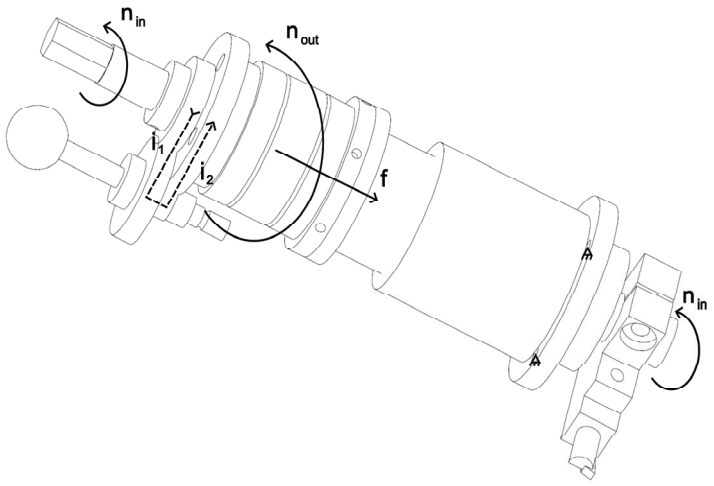


Figure 13. Principle of operation of the device.

The specific cutting resistance [15] for cast iron was assumed to be k_c = 1400 MPa. The cutting force [16], assuming that the width of the cutting layer (cut depth) is a_p = 2 mm, is (7):

$$F_c = k_c \cdot a_p \cdot f = 1400 \text{ MPa} \cdot 2 \text{ mm} \cdot 0.175 \text{ mm} = 490 \text{ N} \quad (7)$$

The calculated cutting force of 490 N assumes a uniform feed and material hardness. In practice, tool wear, misalignment, or material inhomogeneity can cause deviations of up to ±15%. If the cutting force is too high, the simplest solution is to decrease the cutting layer or change the total gear ratio, which decreases the feed but is harder to obtain because the new gears have to be applied.

The output torque is (8):

$$T_{out} = 9550 \cdot \frac{P_{out}}{n_{out}} = 9550 \cdot \frac{0.006 \text{ kW}}{1.75 \text{ rpm}} = 34.5 \text{ Nm} \quad (8)$$

With a cylinder diameter of d_c = 130 mm, this allows for a maximum cutting force of (9):

$$F_{max} = \frac{2T_{out}}{d_c} = \frac{2 \cdot 34.5 \text{ Nm}}{0.130 \text{ m}} = 530.5 \text{ N} \quad (9)$$

This value is significantly higher than the required cutting force.

4. Discussion

The presented device is capable of machining a damaged cylinder head socket in an engine block, and mounts directly on the engine block, eliminating the need for disassembly. Mounting uses screws, spacer sleeves, and head mounting holes, which offers an advantage over electromagnetic mounting in that it does not require additional procedures to maintain the alignment of the device and the machined bore. The device is relatively simple in design and does not require additional drive. The rotational movement of the cutting tool is coupled with its axial movement. This is an important advantage as one drive realizes both the main motion of the cutting tool and the feed. The presented calculations prove that a manual drive is completely sufficient for the socket machining operation. However, the calculations used the properties of Meehanite cast iron. For materials with higher specific cutting resistance, reducing the feed rate is necessary to maintain the cutting force at a level that allows manual operation. This can be easily achieved by changing the overall gear ratio. The sum of the teeth in the first gear stage is 60. This means that by shifting the profile, we can change the gear ratio from 1.14 to 5. As a result, the maximum cutting force almost doubles to 2320 N. The total cost of the device does not exceed $2500, which is competitive compared to other solutions whose prices are $10,000 or more. The cost of the device is based on a prototype. It can be reduced by using cheaper materials and an optimized design, but this will require an in-depth analysis of its performance, strength, and durability. The device extends the life of high-pressure diesel engines, resulting in an improved economic performance during their use. The potential impact on the environmental aspects of engine operation is also important. Instead of using a new engine block, which requires a lot of energy and cast iron to produce, a simple, quick operation is performed that does not require disassembling the entire engine and replacing components that do not fit the new engine block, such as bolts, gaskets, etc., which reduces costs. Replacing an engine block can range from $2000 to $15,000, and can take several weeks, while machining the holes in the block costs around $600 to $700 and takes 1–1.5 h for one hole.

The idea of designing the device emerged at the beginning of the 2020s, as the number of problems with the holes in the cylinder blocks increased noticeably.

During the COVID pandemic, difficult access to service centers prevented timely inspections and potential repairs. Undetected or detected, but unrepaired, damage to the holes in the cylinder blocks progresses slowly. Although they do not immediately disable the engine, they gradually reduce its operating parameters until a critical point occurs, beyond which continued operation threatens complete destruction of the engine. According to [17], engine block damage is the most common cause of engine failure.

Furthermore, block damage is classified as very serious, disabling the engine (level 8/10) with a moderate possibility of detection (level 5/10). This situation has led to a significant increase in reported damage of this type, which was already very common, and necessitated the development of a device capable of repairing such defects.

Author Contributions: Conceptualization, J.G. and U.J.-G.; formal analysis, J.G.; investigation, U.J.-G.; resources, J.G.; writing—original draft preparation, J.G.; writing—review and editing, J.G. and U.J.-G.; visualization, J.G. and U.J.-G.; supervision, J.G.; project administration, U.J.-G.; funding acquisition, U.J.-G. All authors have read and agreed to the published version of the manuscript.

Funding: This research did not receive external funding.

Data Availability Statement: Device blueprints are available on demand, and details of patent protection are available at the Patent Office of the Republic of Poland under claim number P.451549.

Acknowledgments: The project expenses were covered only by the authors. No AI tools have been used at any stage of the project and preparation of the article.

Conflicts of Interest: The authors declare no conflicts of interest.

Abbreviations

The following abbreviations are used in this manuscript:

η	Efficiency (index: g—transmission, b—bearings, t—thread)
a_p	Cutting depth
CNC	Computer Numerical Control
d_c	Cylinder diameter
f	Feed
F	Force
F_c	Cutting force
i	Speed ratio
k_c	Specific cutting resistance
l	Crank length
n	Rotational speed (index: in—input, out—output)
P	Power (index: in—input, out—output)
T	Torque (index: in—input, out—output)
z	Number of teeth

References

1. Musmar, S.A.; Alrousan, A.; Tlili, I. Effect of cylinder-liner rotation on wear rate: An experimental study. *Heliyon* **2019**, *5*, e02065. [CrossRef] [PubMed]
2. Zabala, B.; Igartua, A.; Fernández, X.; Priestner, C.; Ofner, H.; Knaus, O.; Abramczuk, M.; Tribotte, P.; Girot, F.; Roman, E.; et al. Friction and wear of a piston ring/cylinder liner at the top dead centre: Experimental study and modelling. *Tribol. Int.* **2017**, *106*, 23–33. [CrossRef]
3. Du, C.; Sheng, C.; Liang, X.; Rao, X.; Guo, Z. Effects of Temperature on the Tribological Properties of Cylinder-Liner Piston Ring Lubricated with Different Oils. *Lubricants* **2023**, *11*, 115. [CrossRef]
4. Serdecki, W.; Krzymień, P. The effect of changes in cylinder liner geometry on the operation of piston compression ring. *Tech. Trans.* **2012**, *8*, 285–294.
5. Velugula, R.; Ioganathan, B.T.; Varadhaiyengar, L.; Asvathanarayanan, R.; Mittal, M. An Analysis of Mechanical and Thermal Stresses, Temperature and Displacement within the Transparent Cylinder and Piston Top of a Small Direct-Injection Spark-Ignition Optical Engine. *Energies* **2023**, *16*, 7400. [CrossRef]
6. Korczewski, Z. Identyfikacja uszkodzeń tulei cylindrowych okrętowego tłokowego silnika spalinowego w eksploatacji. *Zesz. Nauk. Akad. Mar. Wojennej* **2007**, *2*, 59–72.
7. Li, G.; Gu, F.; Wang, T.; You, J.; Ball, A. Investigation into the Vibrational Responses of Cylinder Liners in an IC Engine Fueled with Biodiesel. *Appl. Sci.* **2017**, *7*, 717. [CrossRef]

8. Bako, S.; Nasir, A.; Ige, B.; Musa, N. Cavitational deterioration of Diesel power plant cylinder liner. *J. Mech. Energy Eng.* **2020**, *4*, 239–246. [CrossRef]
9. Bao, Y.; Lei, J.; Li, W.; Deng, W.; Deng, X.; Xu, Y.; Song, G.; Dai, G. Research on thermal deformation of cylinder bore with orthogonal experiment method of aluminum alloy cylinder block in diesel engine. *Appl. Therm. Eng.* **2024**, *245*, 122772. [CrossRef]
10. Fujimoto, H.; Yoshihara, Y. Measurement of cylinder bore deformation during actual operating engines. *SAE Tech. Pap. Ser.* **1991**, *100*, 16–24.
11. Selmani, E.; Delprete, C.; Bisha, A. *Simulation of the Cylinder Bore Distortion and Effect on the Sealing*; Springer Nature Applied Sciences: Berlin/Heidelberg, Germany, 2019; Volume 1, p. 314.
12. Kurmaz, L.; Kurmaz, O. *Podstawy Konstruowania Węzłów i Części Maszyn Podręcznik Konstruowania*, 5th ed.; Stanisław Adamczak, K., Ed.; Wydawnictwo Politechniki Swietokrzyskiej: Kielce, Poland, 2011.
13. Jiang, W. *Analysis and Design of Machine Elements*; John Wiley & Sons Singapore Pte. Ltd.: Singapore, 2019.
14. Ristivojevic, M.; Dimic, A.; Kolarevic, N. The influence of thread screw parameters on the efficiency of threaded joints. *Tribol. Mater.* **2023**, *2*, 20–31. [CrossRef]
15. Karpuschewski, B.; Kundrák, J.; Varga, G.; Deszpoth, I.; Borysenko, D. Determination of specific cutting force components and exponents when applying high feed rates. *Procedia CIRP* **2018**, *77*, 30–33. [CrossRef]
16. Stachurski, W. Cutting forces during longitudinal turning process of ti-6al-4v eli alloy. Theoretical and experimental values. *J. Mech. Energy Eng.* **2018**, *2*, 201–206. [CrossRef]
17. Deulgaonkar, V.R.; Ingolikar, N.; Borkar, A. Failure analysis of diesel engine piston in transport utility vehicles. *Eng. Fail. Anal.* **2021**, *120*, 105008. [CrossRef]

Disclaimer/Publisher's Note: The statements, opinions and data contained in all publications are solely those of the individual author(s) and contributor(s) and not of MDPI and/or the editor(s). MDPI and/or the editor(s) disclaim responsibility for any injury to people or property resulting from any ideas, methods, instructions or products referred to in the content.

applied sciences

MDPI

Article

Comparison of the Wear of Toroidal and Spherical Cutters in Milling and the Impact of Corrosion

Andrei Osan and Mihai Banica *

Department of Engineering and Management of Technology, North University Center of Baia Mare, Technical University of Cluj-Napoca, 430083 Baia Mare, Romania; andrei.osan@imtech.utcluj.ro
* Correspondence: mihai.banica@imtech.utcluj.ro

Abstract

In this study, the tool axis inclination angle with respect to the surface normal is used to compare the wear of spherical and toroidal milling cutters. Five different surface types were machined in this investigation using three toroidal and three spherical milling cutters at inclination angles of 15°, 35°, and 55°. Each cutter processed 45 surfaces, nine of each type. The MM1-200 microscope was used to monitor tool wear under a microscope after the surfaces had been machined. A comparison diagram and microscopic pictures of tool wear in relation to the wear surface are presented in the paper. Additionally, it contrasts the tool edge's state at the conclusion of machining with its state following five years of storage, during which time the tool was subjected to environmental influences.

Keywords: tilt angle; tool; wear; toroidal milling; spherical milling; corrosion; processing

1. Introduction

Tool wear is a common phenomenon in the machining process, which directly affects machining accuracy, quality, efficiency, and economic efficiency. Monitoring tool wear can enhance finishing process efficiency, reduce machining costs, and yield positive economic benefits.

Most publications in the field discuss the experimental analysis of the wear mechanism on the ball end milling cutter [1]. In their work, Koshy et al. [2] experimentally performed the machining of hardened 1.2379 (X1655CrCoMo12) steel (58 HRC) using a spherical cutter to identify tool durability and appropriate machining parameters, based on the analysis of edge wear patterns. They concluded that the cutting, adhesion, and positioning mechanisms are all responsible for tool wear [2].

Tool wear is a continuous process and influences the dynamics of machining. Increasing cutting speed leads to increased abrasive wear, which becomes as dominant as chemical wear [3]. The increase in wear on the edge causes an intense increase in frictional forces, which leads to an increase in cutting force [4].

Extreme machining conditions that generate high temperatures at the interface between the tool and the workpiece can significantly accelerate tool wear [5]. The intensity of tool wear, in addition to its direct influence on the surface processing time, also influences the roughness of the machined surface [6–11]. A few specialized studies have established the relationship between cutting regimes and tool wear in relation to changes in surface quality [12–18], but those publications have not mentioned the production area with the applicability of toroidal milling cutters and spherical cutters.

Francisco argues that regular milling puts a lot of pressure on the tooth and the protective layer of the tool, so the cemented carbide and the coppering layer must be chosen carefully, because poor resistance can destroy the edges of the tool. The coating almost perfectly holds the processed material from sticking, but its durability to wear and adhesion to the base can be improved by adjustments to the machining strategy [19].

A very important factor in the process of milling a complex surface with a ball end milling cutter is the selection of the machining strategy and the angle of inclination [20].

These parameters have a significant impact on machining time, surface quality, and tool wear [21]. According to the findings in [22], the inclination angle of the machined surface, $\alpha = 0$, should be avoided, because in this case, the cutting speed is equal to 0.

Schulz and Hock [23] used ball end mills at different tilt angles to study tool durability and quality of machined parts and concluded that machining at a tool tilt in the range of 10–20° is the optimal machining for fast milling in the mold manufacturing industry [23]. Tomas and Stepanka argue that tool geometry has a significant influence on the processing of CFRP materials. This study focused on investigating the effect of tool angle of action on wear, cutting forces, roughness of the machined edge, and delamination in non-contiguous milling of CFRP laminates [24].

Tool wear is commonly associated with mechanical processes that contribute to the gradual degradation of the tool; however, the influence of chemical factors should not be overlooked. Corrosive effects play a significant role in determining a tool steel's resistance to corrosion-related wear. Over time, and depending on environmental conditions, virtually all metals are subject to corrosion to varying degrees.

Tool steels are a large group of non-alloy and alloy steels that are used in the formation of various materials in engineering, their most important feature being their durability. It is intended that the material from which the tool is made has a good resistance to wear, considering all the processes and stages that a tool goes through with various factors, including physicochemical factors. In most cases, the wear process is due to several factors combined. For example, mechanical wear is often accompanied by corrosive wear, resulting in what is referred to as mechanical–corrosive wear [25–27].

It is important to identify the elementary processes of tool wear, as this allows for a better prediction of the service life of the tool, as well as making their service life more efficient [27]. The evolution of the wear of the ball end mill is divided into three stages these being the initial stage, the intermediate wear stage, and the late wear stage. In the intermediate wear phase, the reworked layer becomes smoother, which increases the contact area and reduces the pressure on the surface, thus reducing the wear rate, mainly due to the formation of crescent-shaped pits. In the advanced wear stage, the quality of the powder of the ball end cutter deteriorates rapidly, generating pronounced burs at the margins, which significantly accelerate wear. At this stage, profile breakage, fragment detachment, and micro-cracking occur, leading to tool failure [28]. I agree with what the author says above, but is there not an intermediate stage before late wear?

The visible effects of wear can be damage to the edge surface of the tool and changes in the shape of its geometry, and these cause qualitative changes in the characteristics of the machined surface over time. As a result, the life of the tool is negatively affected by the intensity of the working conditions, but also by the corrosion of the working environment [26].

It is important to monitor tool wear and keep tools in good condition to avoid non-compliant surface processing. Wear is caused by both thermal and mechanical forces, which can be mitigated by operating with proper operating parameters and with the proper trajectory to spread wear along the entire length of the edge.

While each tool will eventually have some sort of wear, the effects can be delayed by paying close attention to the cutting speed, feed on the tooth, and the angle of inclination of the tool's axis relative to what is normal on the surface. Once tool wear occurs, the protective corrosion-resistant layer is removed, exposing the worn area to further corrosion.

This paper addresses a detailed scientific analysis of milling tool wear, focusing on the comparison between three toroidal milling cutters and three spherical milling cutters used in machining a total of 45 complex surfaces with each tool. To ensure a rigorous and replicable evaluation, the machining regimes (feed rate, depth of cut, and feed) were kept constant, varying only in the angle of inclination of the tool. This variable parameter makes it possible to isolate the influence of tool geometry and angle of inclination on wear, making it easier to determine its minimum and maximum values. The main objective of the study is to quantify and compare the wear values for the two types of milling cutters, highlighting the differences in their performance and durability under surface processing conditions with complex geometries.

In addition, the paper extends the investigation into the long-term effects of corrosion on the analyzed tools. Based on the measurements made five years ago, following initial processing, new measurements will be made on the worn surfaces of the tools, which in the meantime have been exposed exclusively to ambient conditions without being reused. This stage of the study aims to evaluate corrosion-induced changes. The choice of the five-year period for storage, although seemingly arbitrary, reflects a realistic range in which corrosion can significantly affect worn surfaces and in which special tools, stored for future applications, could be reused. The results of this analysis will provide essential information on the impact of corrosion on the functional integrity of tools and the feasibility of their reuse.

This study contributes to optimizing tool selection by application and developing maintenance and storage strategies, reducing the costs associated with premature tool replacement and improving the sustainability of manufacturing processes. Through the combined approach of wear and corrosion, the work provides an integrated perspective on tool durability, with practical implications for the manufacturing industry.

2. Experimental Data

In the experimental phase, tool wear was monitored with the tool axis inclination angle—relative to the surface normal—used as the variable parameter.

To investigate the surface type effect, five types of surfaces were machined, with 27 pieces per type.

The test specimens are classified into five categories based on their physical characteristics. Experimentally, the processing of flat surfaces, the processing of spherical-convex surfaces, the processing of spherical-concave surfaces, the processing of cylindrical-convex surfaces, and the processing of cylindrical-concave surfaces will be carried out as illustrated in Figure 1.

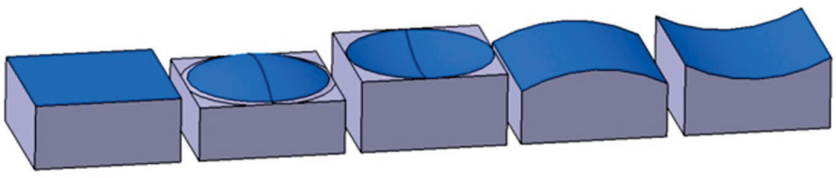


Figure 1. 3D shape of the 5 types of surfaces.

Each specimen has a width of 40 mm, a length of 40 mm, and a thickness of 20 mm, and is made of C45 carbon steel. To guarantee consistency in the data analysis, the same

materials were used for this investigation. Only the tool inclination angle was changed for each type of tool; the cutting parameters remained the same.

The flat specimen (SPLN) is a surface on which a straight line can be applied perfectly in all directions; it retains its lateral dimensions, and as a result of processing, only its height changes.

The spherical-concave surface (SFCV) is located in the upper part of the plate, symmetrically aligned with all four sides at the center of the square. The distance between the flat surface at its highest point is 5 mm, and the SFCV has a diameter of Ø85 mm.

The spherical-convex surface (SFCX) is represented by a recess in the upper part of the plate; this is positioned in the center of the plate, representing the distance of 5 mm from the maximum spherical recesses to the flat surface. The convex spherical shape has a diameter of Ø85 mm.

The cylindrical-concave surface (CICV) has a cylindrical height along the plate with a diameter of Ø85 mm and a maximum height of 5 mm.

The cylindrical-convex surface (CICX) is represented by a vertically positioned cylinder section with a depth of 5 mm, and its diameter is Ø85 mm.

The numerical control center used is the OKUMA MU-400VA, a 5-axis machine tool. The two cutting tools used are: the JHP780160E2R400.0Z4-M64 toroidal milling cutter and the JS534160D1B.0Z4-NXT ball milling cutter.

The toroidal milling cutter or corner milling cutter has a diameter of Ø16 with a maximum cutting depth of 32 mm. Its radius at the corner is 4 mm with four teeth. This cutter is shown in Figure 2.

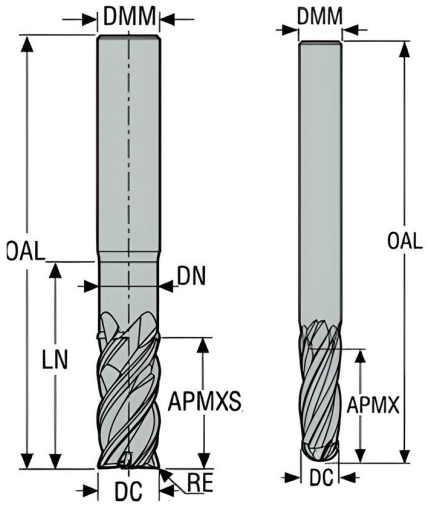


Figure 2. Graphical representation of the two milling cutters.

The ball milling cutter has a diameter of Ø16 with a maximum cutting depth of 48 mm. Its radius at the corner is 8 mm with four teeth. This cutter is shown in Figure 2.

A total of three toroidal cutters and three spherical cutters were provided, analyzing the wear of the tool according to the angle at which it is used, so each tool will be used for only one type of inclination.

As a result, each tool will process nine types of surfaces with different geometries, totaling a number of 45 surfaces processed at the same angle, these being the totality of the processes carried out with one cutter, this number of surfaces being generated following the application of the Taguchi method. Table 1 shows the surfaces processed with the toroidal tools according to the angle, Table 2 shows the surfaces processed with the spherical cutters according to the angle of inclination, and Figure 3 shows the processed specimens.

Table 1. Structure of a toroidal milling machine.

Type of Cutter	Tilt Angle	Types of Surfaces	Total Processed Surfaces
Milling Cutter toroidal 1	15°	9 flat surfaces 9 concave cylindrical surfaces 9 convex cylindrical surfaces 9 concave spherical surfaces 9 convex spherical surfaces	45 surfaces
Milling Cutter toroidal 2	35°	9 flat surfaces 9 concave cylindrical surfaces 9 convex cylindrical surfaces 9 concave spherical surfaces 9 convex spherical surfaces	45 surfaces
Milling Cutter toroidal 3	55°	9 flat surfaces 9 concave cylindrical surfaces 9 convex cylindrical surfaces 9 concave spherical surfaces 9 convex spherical surfaces	45 surfaces

Table 2. Structure of ball milling machine machining.

Type of Cutter	Tilt Angle	Types of Surfaces	Total Processed Surfaces
Ball Cutter 1	15°	9 flat surfaces 9 concave cylindrical surfaces 9 convex cylindrical surfaces 9 concave spherical surfaces 9 convex spherical surfaces	45 surfaces
Ball Cutter 2	35°	9 flat surfaces 9 concave cylindrical surfaces 9 convex cylindrical surfaces 9 concave spherical surfaces 9 convex spherical surfaces	45 surfaces
Ball Cutter 3	55°	9 flat surfaces 9 concave cylindrical surfaces 9 convex cylindrical surfaces 9 concave spherical surfaces 9 convex spherical surfaces	45 surfaces

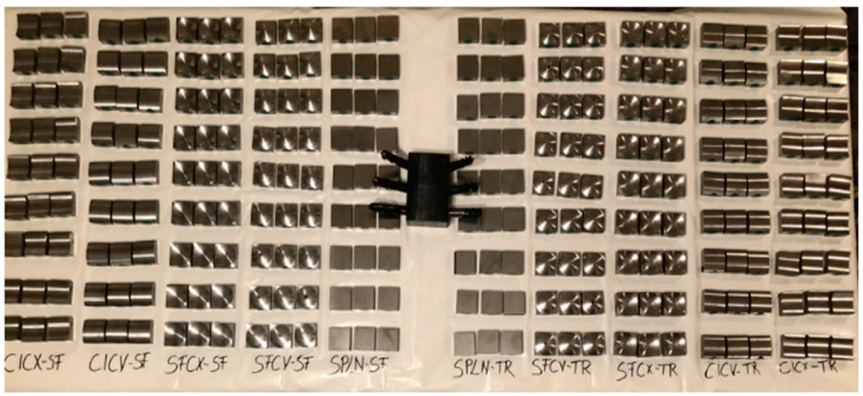


Figure 3. Parts machined with the 6 milling cutters.

For a more precise measurement and a higher quality image, the MM1-200 microscope from Garant (Saint-François-de-la-Rivière-du-Sud, QC, Canada) was used, in the Faculty of

Engineering within the North University Center in Baia Mare, illustrated in Figure 4. This is an easy-to-use, high-resolution color camera and an easy-to-use multi-touch workshop PC measuring microscope with intuitive M3 measurement software version 4, Garant. The microscope software aids in measurements and ensures their correctness by mentioning the same calibration across both measurement periods.



Figure 4. Microscope MM1-200.

Since the microscope lacks a built-in clamping device that can be tilted to the desired angles, we designed a simple device capable of positioning and holding the tool fixed at the desired angle, namely 15°, 35°, and 55°. It has a precisely machined, angled hole that fits the cutter shank diameter and a flat surface that can be placed on the microscope table. An illustration of the cutter clamp is provided in Figure 5.

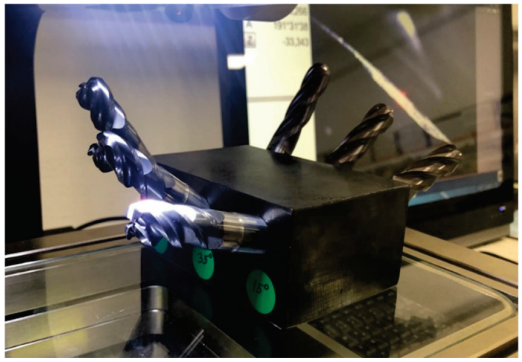


Figure 5. Positioning the tool for measuring edge wear.

3. Experimental Results

Each type of damage will progress or occur in a variety of ways, depending on the milling conditions. As stated in ISO 8688 [29], wear-related damage should be used to evaluate a tool's durability.

After processing the five types of surfaces at an angle of inclination of 15°, the resulting tool wear is shown in Figure 6a for the toroidal cutter and Figure 6b for the spherical cutter.

For the spherical cutter, the maximum edge wear length is 4.365 mm, with a maximum width of 0.136 mm, resulting in a total wear area of 0.2716 mm^2.

With a maximum length of 2.933 mm and a maximum width of 0.226 mm, the toroidal cutter exhibits wear on the edge, with a wear surface area of 0.27127 mm^2.

In this case, the values are very close, with an insignificant advantage on the side of the toroidal cutter.



Figure 6. Comparison of spherical and toroidal tool wear after machining at 15° angle. (**a**). Toroidal milling; (**b**). Spherical milling.

Referring to the processing of the five types of surfaces, with a constant angle of inclination of 35°, the tool wear situation is as follows.

Figure 7a shows the wear of the toroidal tool, which has a maximum length of 2.65 mm and a maximum width of 0.402 mm with an area of 0.44564 mm^2.

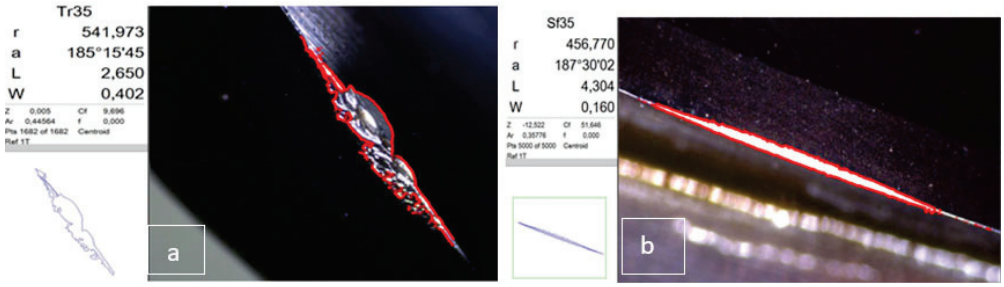


Figure 7. Comparison of spherical and toroidal tool wear during machining at 35° angle. (**a**). Toroidal milling; (**b**). Spherical milling.

Figure 7b shows the wear of the ball tool, having a length of 4.304 mm and a maximum width of 0.16 mm, with the total wear area being 0.35776 mm^2.

In this case, the toroidal cutter achieves 0.08788 mm^2 more wear on the tool edge than the ball milling cutter.

Surface processing at the 55° tool tilt angle results in tool edge wear, as shown in Figure 8. Figure 8b shows the wear of the spherical cutter with a maximum length of 4.463 mm and a maximum width of 0.194 mm, resulting in a wear area of 1.194 mm^2. In Figure 8a, the wear of the toroidal cutter is shown as having a maximum length of 2.932 mm and a maximum width of 0.255 mm, resulting in a wear area of 0.48123 mm^2.

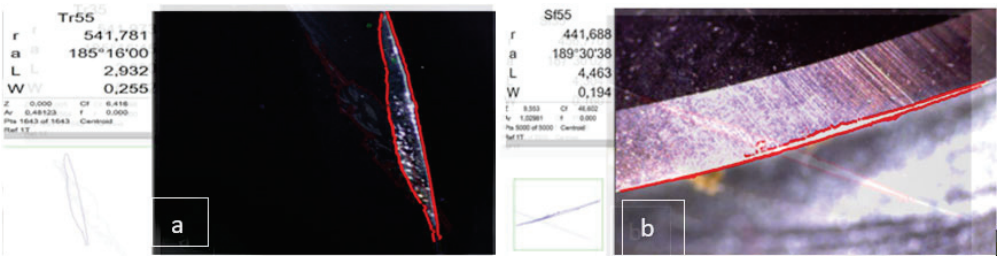


Figure 8. Comparison of spherical and toroidal tool wear during machining at an angle of 55°. (**a**). Toroidal milling; (**b**). Spherical milling.

High tool wear at a 55° tilt angle, as shown in Figure 9, is the combined result of increased cutting forces, uneven stress distribution, excessive heat generation, and suboptimal chip evacuation dynamics. These conditions amplify the abrasive and thermal wear mechanisms.

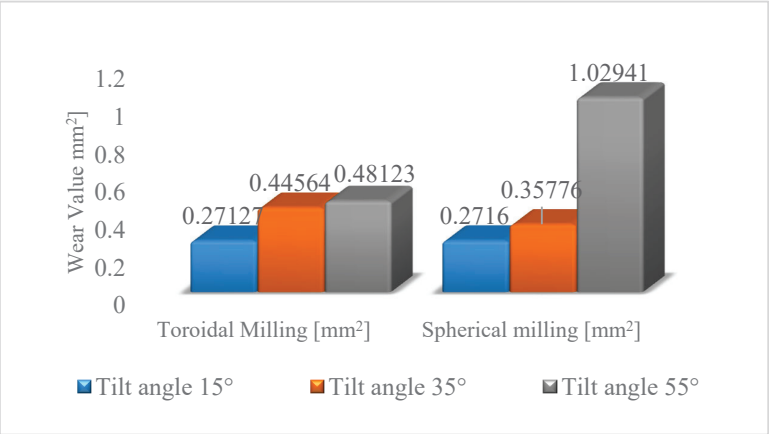


Figure 9. Graphical representation of comparative wear values between toroidal and ball milling cutters.

At a tilt angle of 55 degrees, the axial component of the cutting force increases significantly when compared to smaller angles (e.g., 15° or 35°). This results in greater pressure on the cutting edge, amplifying abrasive wear and the risk of microcracking. Additionally, at 55 degrees, the contact between the tool and the workpiece becomes more concentrated on a portion of the cutting edge, leading to localized wear. This is accentuated by the angle that does not optimize the uniform distribution of chips, unlike smaller angles, which can facilitate more efficient chip evacuation.

The spherical cutters show, on average, 38% more wear than the toroidal cutters when the wear surfaces of the two cutter types are compared. Concentrated contact, high temperatures, ineffective chip evacuation, and stronger vibrations are all blamed for this increased wear.

Toroidal cutters achieve a better balance of cutting forces (tangential, radial, and axial components) due to their larger tool–workpiece contact distribution and corner radius. This equilibrium minimizes sidewall wear and chipping by lowering the chance of vibration and focused stress.

Spherical cutters, due to the point (or linear, depending on the depth of cut) contact of the spherical edge with the workpiece, increase the axial component of the force at large angles. This leads to greater pressure on the cutting edge, amplifying abrasive wear and the risk of microcracking. Studies show that spherical cutters can generate 15–25% higher cutting forces in the axial direction compared to toroidal cutters under similar conditions.

After the completion of the initial measurements, the 6 milling cutters subjected to analysis were kept in an ambient environment, characterized by relatively constant temperature and humidity fluctuations, without being involved in processing processes, manipulated, or subjected to technical interventions. As for the temperature ranges, they are between 10 °C and 22 °C without exposure to corrosion gases, with humidity varying between 35% and 45%. Also, no corrosion protection measures were applied during exposure. These cutters were left in a state of inactivity for 5 years, during which the ambient conditions varied naturally. Currently, the wear of the cutting part will be measured again, using the same measurement methods and conditions applied at the time of the initial assessment, in order to allow an objective and precise comparison of the evolution of the wear phenomenon.

The evolution of the condition of the tool cutting part used for machining at a 15° inclination angle is shown in Figure 10. Figure 10b shows the wear of the spherical cutter with a maximum length of 2.426 mm and a maximum width of 0.128 mm, with a wear area of 0.31419 mm^2. In Figure 10a, the wear of the toroidal cutter is shown as having a

maximum length of 3.660 mm and a maximum width of 0.234 mm, resulting in a wear area of 0.38008 mm^2.

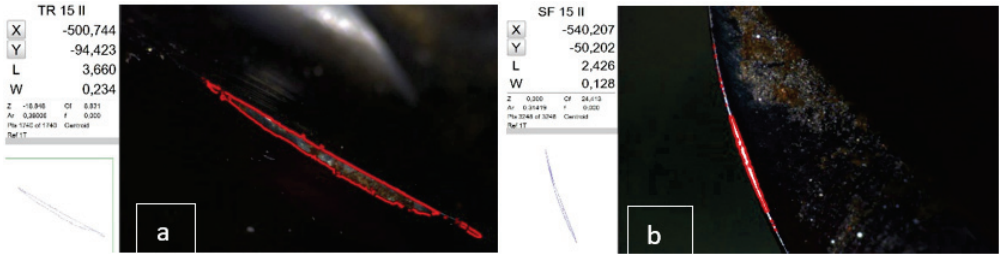


Figure 10. Evolution of wear of spherical and toroidal cutters used in machining with a 15° angle of inclination after five years. (**a**). Toroidal milling; (**b**). Spherical milling.

Changes in the wear of the cutting part of the tools used in machining processes at the 35° tilt angle are shown in detail in Figure 11. Figure 11b illustrates the wear of the spherical cutter, which has a maximum length of 4.252 mm and a maximum width of 0.149 mm, resulting in a wear area of 0.43704 mm^2. Similarly, Figure 11a details the wear of the toroidal cutter, which has a maximum length of 3.767 mm and a maximum width of 0.430 mm, with a wear area of 0.57925 mm^2.

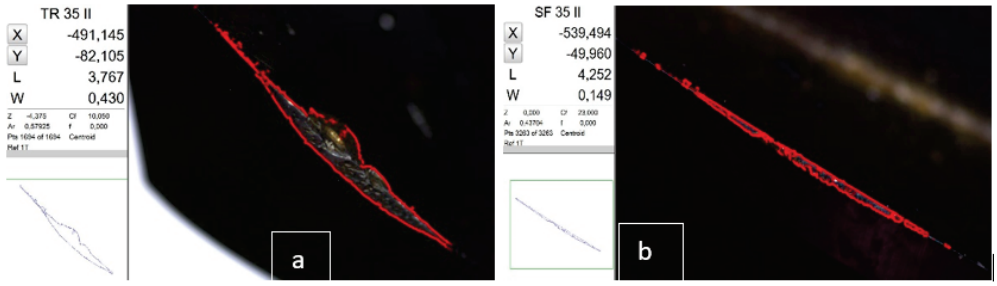


Figure 11. Wear Evolution of Spherical and Toroidal Milling Cutters Used in Machining with 35° Tilt Angle After Five Years. (**a**). Toroidal milling; (**b**). Spherical milling.

The wear transformations of the tool cutting part used in machining processes at the 55° tilt angle are shown in detail in Figure 12. In Figure 12b, the wear of the spherical cutter is illustrated, which records a maximum length of 4.252 mm and a maximum width of 0.149 mm, resulting in a wear area of 0.43704 mm^2. In the same figure, in Figure 12a, the wear of the toroidal cutter is highlighted, which has a maximum length of 3.767 mm and a maximum width of 0.430 mm, and the wear area is calculated at 0.57925 mm^2.

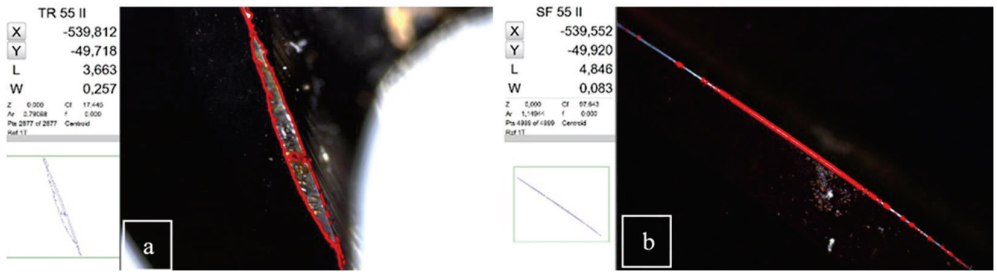


Figure 12. Wear Evolution of Spherical and Toroidal Milling Cutters Used in Machining with a 55° Angle of Inclination After Five Years. (**a**). Toroidal milling; (**b**). Spherical milling.

This data allows a detailed comparison of the changes suffered by the two types of cutters, highlighting values of initial wear and values of wear affected by corrosion.

Corrosion of tools stored for five years under ambient conditions (10–22 °C, 35–45% humidity) led to an increase in the area of worn surfaces, according to the measurements

made and presented in Table 3. This analysis examines the mechanisms of corrosion, the effects on worn surfaces, and the nature of the process (oxidation). In the absence of metallographic analysis, observations are based on macroscopic measurements, which can confirm the increase in the area of worn surfaces but do not provide information about microstructural or chemical changes.

Table 3. Comparison between the measured values of initial wear and tear after 5 years.

Type of Cutter	Tilt Angle	Initial Wear Area [mm^2]	Wear Area After 5 Years [mm^2]	Percentage of Wear Increase [%]
Toroidal milling 1	15°	0.27127	0.38006	40.1
Toroidal milling 2	35°	0.44564	0.57925	29.98
Toroidal milling 3	55°	0.48123	0.79088	64.34
Spherical milling 1	15°	0.27160	0.31419	15.68
Spherical milling 2	35°	0.35776	0.43704	22.16
Spherical milling 3	55°	1.02941	1.14944	11.66

The observed corrosion is mainly a chemical reaction, in which oxidation plays a central role. Oxidation involves the reaction of the tool material, cobalt metal carbides, with oxygen in the air, forming oxides (CoO). The humidity of 35–45% facilitates the formation of a thin layer of water, which acts as an electrolyte, accelerating the process.

Analysis of the data presented in Table 3 and the Graph in Figure 13 reveals a significant increase in worn surface due to corrosion for all six milling cutters subjected to the experiment. The results indicate a percentage change in surface wear, with a minimum increase of 11.66% and a maximum increase of 64.34%. These values highlight the notable impact of corrosion on the worn surfaces of cutting tools, highlighting the need to take this phenomenon into account when assessing tool performance and durability.

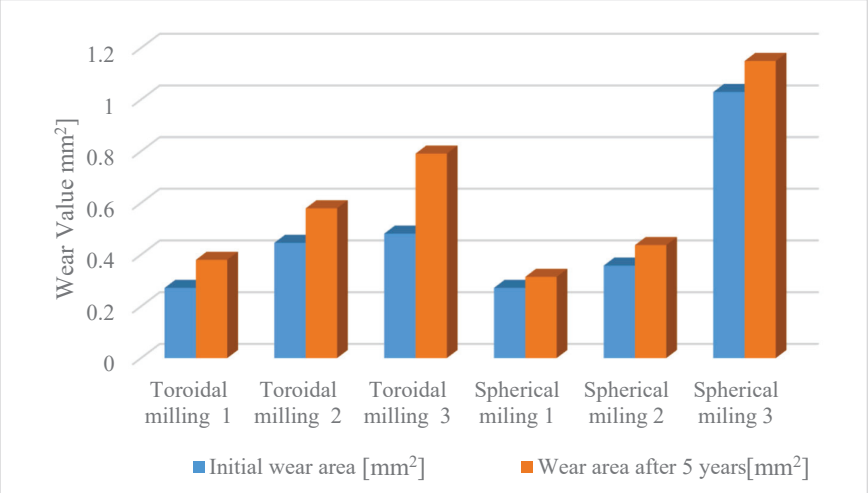


Figure 13. Graphical representation of measured values.

4. Conclusions

Evaluation and comparison of milling cutter wear

The main purpose of the study was to analyze and compare the degree of wear of toroidal milling cutters and ball end milling cutters in the context of processing five types of surfaces, with the tool axis inclined at three distinct angles (15°, 35°, and 55°). The research

was based on experimental results, focusing exclusively on comparing tool wear, without analyzing the specific stages of wear, and taking into account only the number of machined parts. Tool wear was quantitatively assessed by measurements made with the MM1-200 microscope, which provided accurate tool degradation data after machining 45 surfaces with each cutter.

The results obtained highlighted the following:

1. **Differences in the degree of wear**: Ball end cutters experienced a 38% higher degree of wear compared to toroidal cutters, indicating a superior strength of toroidal cutters under the tested conditions.
2. **Influence of tilt angle**: The highest wear for both types of cutters was observed at a tilt angle of 55°. At this angle, the wear difference between the ball end mill and the toroidal cutter was 113%, which underlines the significant impact of the angle on tool performance.
3. **Minimal wear**: The lowest wear was recorded in both types of cutters during machining at an angle of 15°, suggesting that the smaller angles reduce mechanical stresses on the tool.

Influence of corrosion on tool wear

A secondary objective of the study was to investigate the effects of corrosion on the wear of the milling cutters analyzed, especially under conditions of prolonged inactivity. Based on practical observations, tool wear has been found to include a preliminary stage of corrosive wear, which occurs before advanced mechanical wear, especially in the case of stored tools. Although mechanical wear remains the main factor in tool degradation, the effects of corrosion cannot be neglected, as they influence the geometric stability of the tool edge and, implicitly, its durability.

In the context of corrosion analysis, it was observed that tools used intensively and then stored for a long term (five years) in unfavorable environmental conditions have the following characteristics:

1. **Stagnation of wear**: Regardless of the initial degree of wear, after the period of inactivity, there has been no significant progress in mechanical wear, this being replaced by the effects of corrosion.
2. **Corrosion wear variation**: The increase in wear due to corrosion ranged from 11.66% to 64.34%, with an average of 30.64%. Notably, the milling cutter with the highest initial mechanical wear exhibited the least increase in corrosive wear, indicating a complex interaction between mechanical and corrosive wear.
3. **Impact of inactivity**: Prolonged inactivity has a significant impact on the condition of the tool edge, especially in the case of tools with special specifications, which are often stored for future use in complex machining.

Practical recommendations

Although new tools are protected by anti-corrosion coatings, the initial mechanical wear compromises these layers, exposing tool surfaces to corrosion. Therefore, it is recommended to use tools until the permissible wear limit is reached in order to minimize the effects of corrosion during storage and maximize their operational efficiency. This practice is particularly relevant for tools with common specifications, which are frequently used in production, but also for special tools, which can be subjected to long periods of inactivity.

Author Contributions: Conceptualization, A.O.; methodology, A.O.; software, A.O.; validation, M.B. and A.O.; formal analysis, A.O.; data curation, A.O.; writing—original draft preparation, A.O.; writing—review and editing, M.B.; visualization, M.B.; supervision, M.B. All authors have read and agreed to the published version of the manuscript.

Funding: This research received no external funding.

Institutional Review Board Statement: Not applicable.

Informed Consent Statement: Not applicable.

Data Availability Statement: All data supporting the findings of this study are included within the article.

Conflicts of Interest: The authors declare no conflict of interest.

References

1. Ben Said, M.; Saï, K.; Saï, W.B. An investigation of cutting forces in machining with worn ball-end mill. *J. Mater. Process. Technol.* **2009**, *209*, 3198–3217. [CrossRef]
2. Koshy, P.; Dewes, R.C.; Aspinwall, D.K. High speed end milling of hardened AISI D2 tool steel (58 HRC). *J. Mater. Process.* **2009**, *127*, 266–273. [CrossRef]
3. Sokovic, M.; Kopac, J.; Dobrzanski, L.A. Wear of PVD-coated solid carbide end mills in dry high-speed cutting. *J. Mater. Process. Technol.* **2004**, *157*, 422–426. [CrossRef]
4. Ko, T.J.; Kim, H.S.; Lee, S.S. Selection of the machining inclination angle in high-speed ball end milling. *Int. J. Adv. Manuf. Technol.* **2001**, *17*, 163–170. [CrossRef]
5. Krolczyk, G.M.; Nieslony, P.; Legutko, S. Determination of tool life and research wear during duplex stainless steel turning. *Arch. Civ. Mech. Eng.* **2015**, *15*, 347–354. [CrossRef]
6. Krolczyk, G.; Legutko, S.; Nieslony, P. Study of the surface integrity microhardness of austenitic stainless steel after turning. *Teh. Vjesn.* **2014**, *21*, 1307–1311.
7. Osan, A.; Banica, M.; Nasui, V. The influence of inclination of the axis of the toroidal on a flat surface roughness. In Proceedings of the 23nd edition of Innovative Manufacturing Engineering&Energy International Conference—ImanE&E 2019, Pitești, Romania, 22–24 May 2019.
8. Oşan, A.; Bănică, M.; Năsui, V.; Slătineanu, L.; Merticaru, V.; Mihalache, A.; Dodun, O.; Ripanu, M.; Nagit, G.; Coteata, M.; et al. Processing of Convex Complex Surfaces with Toroidal Milling Versus Ball Nose End Mill. *MATEC Web Conf.* **2018**, *178*, 01003. [CrossRef]
9. Przestacki, D.; Jankowiak, M. Surface roughness analysis after laser assisted machining of hard to cut materials. *J. Phys. Conf. Ser.* **2014**, *483*, 012019. [CrossRef]
10. García-Hernández, C.; Valdivia-Sánchez, J.-J.; Ubieto-Artur, P.; García-Arbués, M.; Tzotzis, A.; Garde-Barace, J.-J.; Valdivia-Calvo, F.; Huertas-Talón, J.-L. Improved Use of the Full Length of Milling-Tool Flutes in Processes of Air-Contour Milling. *J. Manuf. Mater. Process.* **2025**, *9*, 150. [CrossRef]
11. Zhang, X.; Li, Z.; Zhang, B.; Wang, J.; Elmi, S.A.; Bai, Z. Optimization and Finite Element Simulation of Wear Prediction Model for Hot Rolling Rolls. *Metals* **2025**, *15*, 456. [CrossRef]
12. Hioki, D.; Diniz, A.E.; Sinatora, A. Influence of HSM cutting parameters on the surface integrity characteristics of hardened AISI H13 steel. *J. Braz. Soc. Mech. Sci. Eng.* **2013**, *35*, 537–553. [CrossRef]
13. Magri, M.L.; Diniz, A.E.; Button, S.T. Influence of surface topography on the wear of hot forging dies. *Int. J. Adv. Manuf. Technol.* **2012**, *65*, 459–471. [CrossRef]
14. Sadilek, M.; Kratochvi, J.; Petru, J. Cutting tool wear monitoring with the use of impedance layers. *Teh. Vjesn.* **2014**, *21*, 639–644.
15. He, Z.; Shi, T.; Chen, X. An Innovative Study for Tool Wear Prediction Based on Stacked Sparse Autoencoder and Ensemble Learning Strategy. *Sensors* **2025**, *25*, 2391. [CrossRef]
16. Castañeda-Quilcaro, F.D.; Cordova-Yavar, C.L.; Vidal Endara, R.F. Product Design to Improve the Measurement and Projection of Mill Liner Wear. *Eng. Proc.* **2025**, *83*, 4.
17. de Lacalle, L.N.L.; Lamikiz, A.; Muñoa, J.; Salgado, M.A.; Sanchez, J.A. Improving the high-speed finishing of forming tools for advanced high-strength steels (AHSS). *Int. J. Adv. Manuf. Technol.* **2006**, *29*, 49–63. [CrossRef]
18. Urbikain, G.; López de Lacalle, L.N. Modelling of surface roughness in inclined milling operations with circle-segment end mills. *Simul. Model. Pract. Theory* **2018**, *84*, 161–176. [CrossRef]
19. Silva, F.J.G.; Martinho, R.P.; Magalhães, L.L.; Fernandes, F.; Sales-Contini, R.C.M.; Durão, L.M.; Casais, R.C.B.; Sousa, V.F.C. A Comparative Study of Different Milling Strategies on Productivity, Tool Wear, Surface Roughness, and Vibration. *J. Manuf. Mater. Process.* **2024**, *8*, 115. [CrossRef]
20. Wojciechowski, S. Machined surface roughness including cutter displacements in milling of hardened steel. *Metrol. Meas. Syst.* **2011**, *18*, 429–440. [CrossRef]
21. Toh, C.K. A study of the effects of cutter path strategies and orientations in milling. *J. Mater. Process. Technol.* **2004**, *152*, 346–356. [CrossRef]

22. Tonshoff, H.K.; Arendt, C.; Ben Amor, R. Cutting of hardened steel. *Cirp Ann.* **2000**, *49*, 547–566. [CrossRef]
23. Schulz, H.; Hock, S. High-speed milling of die and moulds—Cutting conditions and technology. *Ann. CIRP* **1995**, *44*, 35–38. [CrossRef]
24. Knápek, T.; Dvořáčková, Š.; Váňa, M. The Effect of Clearance Angle on Tool Life, Cutting Forces, Surface Roughness, and Delamination during Carbon-Fiber-Reinforced Plastic Milling. *Materials* **2023**, *16*, 5002. [CrossRef] [PubMed]
25. Zwierzycki, W.; Stachowiak, A.; Górny, K. Material selection for knife to cutting bell pepper. *Tribocorrosion Res. Tribol.* **2013**, *5*, 139–148.
26. Beer-Lech, K.; Surowska, B. Research on resistance to corrosive wear of dental CoCrMo alloy containing post- production strap. *Eksploat. I Niezawodn. Maintenace Reliab.* **2015**, *17*, 90–94. [CrossRef]
27. Gauvent, M.; Rocca, E.; Meausoone, P.J.; Brenot, P. Corrosion of Materials Used as Cutting Tools of Wood. *Wear* **2006**, *261*, 1051–1055. [CrossRef]
28. Zhang, Y.; Fu, Y.; Li, Q.; Zhang, K.; Liu, K. Study on the Cutting Performance and Remaining Life Prediction of Micro-Texture Ball End Milling Cutters for Titanium Alloys. *Coatings* **2024**, *14*, 814. [CrossRef]
29. *ISO 8688*; Tool Life Testing Milling. International Organization for Standardization: Geneva, Switzerland, 1989.

Disclaimer/Publisher's Note: The statements, opinions and data contained in all publications are solely those of the individual author(s) and contributor(s) and not of MDPI and/or the editor(s). MDPI and/or the editor(s) disclaim responsibility for any injury to people or property resulting from any ideas, methods, instructions or products referred to in the content.

applied sciences

MDPI

Article

Performance Investigation of Coated Carbide Tools in Milling Procedures

Paschalis Charalampous [1,2]

[1] Centre for Research and Technology Hellas—Information Technologies Institute (CERTH/ITI), 57001 Thessaloniki, Greece; pcharalampous@iti.gr
[2] Laboratory for Machine Tools and Manufacturing Engineering, Mechanical Engineering Department, Aristotle University of Thessaloniki, 54124 Thessaloniki, Greece

Abstract: The optimization of the manufacturing conditions in milling processes composes a crucial task for enhancing machining efficiency and extending the tool's lifespan. This study presents an investigation of the cutting tool's performance under varying machining parameters via the generation of an experimental dataset that was obtained through laboratory-controlled milling operations. Based on this dataset, artificial intelligence (AI) models, including artificial neural network (ANN), k-nearest neighbors (KNN), and support vector regression (SVR), were developed in order to predict the tool's life as a function of the milling conditions. Additionally, finite element method (FEM) simulations were conducted to estimate tool wear and analyze the manufacturing process at a numerical level. In particular, FE models were utilized to compute the milling forces and the corresponding developed stress fields, as well as to assess the cutting tool's performance based on certain machining variables. Furthermore, a comparative analysis between AI-driven forecasts and FEM simulations was performed to evaluate their effectiveness and reliability. The findings provide insights into the advantages and limitations of both methodologies, guiding the optimization of coated carbide tool performance. The outcomes of this study contribute to the advancement of predictive modeling in machining processes, offering a data-driven approach for improved tool wear assessment.

Keywords: manufacturing technologies; simulation; machine learning; optimization; machining; finite element analysis

1. Introduction

Milling is one of the most widely applied machining processes in manufacturing, playing a pivotal role in shaping, finishing, and fabricating components across industries such as aerospace, automotive, furniture, and medical devices [1]. Moreover, machining composes a cornerstone of modern manufacturing, enabling the production of high-precision components with complex geometries [2]. As manufacturing technologies advance, milling continues to evolve with innovations like CNC machining, high-speed milling, and additive-subtractive hybrid processes, driving greater efficiency and capabilities. This subtractive manufacturing procedure involves the removal of material using rotating cutting tools to produce components with high accuracy and surface quality. It should be noted that the efficiency of the cutting tools in milling operations is among the most critical factors influencing the manufacturing performance, product quality, and operational costs [3]. In recent years, advancements in manufacturing technologies, coating materials, and computer-aided manufacturing (CAM) systems have expanded the capabilities of milling procedures via the development of high-performance cutting tools, which

have enabled the machining of difficult-to-cut materials like titanium alloys, composites, and hardened steels [4]. Among the available tool materials, coated carbide tools have gained significant attention due to their superior hardness, wear resistance, and ability to withstand high temperatures [5]. These coatings are typically composed of materials such as titanium nitride (TiN), titanium aluminum nitride (TiAlN), aluminum chromium nitride (AlCrN), or chromium nitride (CrN) that provide additional protection against abrasive wear, adhesion, and thermal degradation [6].

Despite these advantages, the progressive wear of coated carbide tools remains a critical issue, affecting machining precision, surface finish, and the overall manufacturing costs [7]. In addition, the performance of coated carbide tools is influenced by a complex interplay of factors, including the cutting parameters, coating materials, and workpiece properties. Hereupon, a deep comprehension of the wear mechanisms of coated carbide tools is essential for improving machining efficiency, maximizing tool life, and reducing downtime due to frequent tool replacements [8]. In general, tool wear is related to several factors, including cutting speed, feed rate, depth of cut, workpiece material, tool material, coating, and cutting fluid, among others [7,8]. The interplay between these parameters determines the extent of wear mechanisms such as abrasion, adhesion, and diffusion, which directly impact tool life and machining performance [9]. To study these effects, experimental approaches have been commonly used, where milling tests are conducted under different conditions to evaluate tool wear behavior. However, experimental investigations alone can be time-consuming and expensive, necessitating the development of predictive models to estimate tool life based on machining conditions [10]. Therefore, in the past decades, numerical approaches have developed in order to inspect the machining procedure and assess the performance of the applied milling operation [11].

Traditionally, the finite element method (FEM) has been employed to simulate machining processes and predict tool wear through numerical modeling. Finite element analysis (FEA) is a powerful numerical simulation technique widely utilized in machining research to investigate the performance and wear behavior of carbide tools in milling processes [12]. Specifically, FEA enables the detailed study of stress distribution and thermal effects, as well as the tool-workpiece interactions under different machining conditions, providing critical insights into wear mechanisms such as abrasion, adhesion, and diffusion. By discretizing the tool and workpiece into smaller finite elements, the method allows researchers to simulate complex physical phenomena, including chip formation, heat generation, and material deformation [13]. Moreover, advanced material models and boundary conditions could also be incorporated in order to enhance the accuracy of simulations, allowing for realistic predictions of tool wear progression over time. Additionally, FEA facilitates the analysis of cutting forces, temperature gradients, and residual stresses, which are essential factors in determining tool longevity and machining efficiency. It is worth mentioning that even FEA is computationally intensive and requires precise material property data; it remains a valuable tool for optimizing milling operations, as it enables the prediction of tool performance under various machining conditions without the need for extensive experimental testing [14]. However, FEM simulations require extensive computational resources, precise material characterization, and accurate boundary conditions to achieve reliable predictions. As an alternative methodology, artificial intelligence (AI)-based approaches have emerged in the past years as effective tools for predictive analysis in machining operations.

In particular, AI algorithms have become increasingly valuable in manufacturing research, particularly in predicting the performance and wear behavior in machining procedures [15]. AI techniques, such as artificial neural network (ANN), deep learning (DL), k-nearest neighbors (KNN), and support vector regression (SVR), could utilize exper-

imental datasets in order to develop predictive models capable of estimating tool life, wear rate, and manufacturing efficiency based on key process parameters. These algorithms analyze vast amounts of data, identifying complex relationships between input parameters and tool wear that may not be easily captured by traditional empirical models [16]. Unlike FEA, which requires extensive material characterization and computational resources, AI models can rapidly process new data and adapt to different milling conditions with minimal computational cost. These models offer fast and accurate predictions with significantly lower processing effort compared to FEM simulations. Furthermore, machine learning (ML)-based approaches could enable real-time monitoring and optimization of machining processes, allowing manufacturers to implement data-driven decision-making for improving tool longevity and efficiency [17]. On the other hand, AI models require a large amount of data in order to identify patterns and correlations between input features, where the quality, quantity, and relevance of the data directly impact the model's performance.

The objective of the present research work is to investigate the performance of coated carbide tools in milling operations by combining experimental, numerical, and AI-based methodologies. An experimental dataset was created in a controlled laboratory environment to examine the effects of varying machining conditions on tool wear. Additionally, AI models were developed to predict tool life based on this dataset, while FEM simulations were utilized to estimate the tool wear through numerical analysis of the milling process, as well as to simulate the perpendicular impact test on the examined coated tools. Finally, a comparative evaluation of AI-driven predictions and FEM simulations was conducted to assess the advantages and limitations of the employed methodologies. The findings of this study could contribute to the optimization of milling procedures by providing a data-driven approach towards the enchantment of tool performance, the reduction of wear, and the improvement of the overall manufacturing efficiency. The rest of the present research paper is organized as follows: Firstly, Section 2 outlines the investigated coated cutting tool and the workpiece properties. Moreover, the experimental setup of the impact test and the milling operations are displayed within the chapter. Next, Section 3 presents the developed ML and FE models coupled with their outcomes. This is followed by an algorithm considering the optimization of the manufacturing parameters. Finally, Section 4 discusses the obtained results, as well as some prospects for future research.

2. Materials and Methods

2.1. Coated Cutting Tools and Workpiece

The machining investigations of the present study were conducted via a tool holder of 63 mm external diameter and cemented carbide inserts of HW-K05/K20 ISO specifications using the DIJET cutting insert WDMW080520ZTR, as displayed in Figure 1a. The geometrical characteristics of the tool holder and the cemented carbide inserts are illustrated in Figure 1b. The chamfer length on the inserts' rake face measures approximately 280 μm, while the cutting-edge radius is 20 μm. Generally, chamfering on a carbide insert composes a critical design feature that enhances tool performance, durability, and machining quality in milling procedures [18]. In particular, chamfer geometries reinforce the cutting edge, making it less prone to chipping or breaking, especially during interrupted cuts or when machining hard materials. Furthermore, by strengthening the edge, the chamfer reduces wear and extends the lifespan of the insert, aiding in maintaining consistent performance over time, even under high-stress conditions. The flank wear VB was measured via an optical microscope, and typical results are exhibited in Figure 1c at various stages of the tool wear evolution.

Regarding the mechanical properties of the coating and substrate, these were evaluated using an FEM-based analysis of the nanoindentation experimental process. The

employed nanoindentation device was the Fischerscope H100 using a Vickers diamond pyramid. In order to minimize the impact of surface roughness on the indentation depth, 30 experiments per material investigation were conducted for stabilizing the moving average of the maximum indentation depth, as exhibited in Figure 2a. The estimation of the stress-strain curves of the investigated coating and its substrate was based on the 'SSCUBONI' (Stress–Strain CUrves Based on NanoIndentation) algorithm [19]. Particularly, the algorithm continuously simulates indenter penetration into the coating material and calculates the corresponding reaction force up to a maximum load of 15 mN as a function of penetration depth. Hereupon, the elastic modulus and stress-strain behavior of the material were determined by comparing the simulated force-depth relationship with the experimentally obtained indentation load-depth data. In addition, it should be noted that the plastic deformation of the coating was approximated using stepwise linear intervals in the stress-strain curve. The calculated stress-strain curves provided key material properties, including the elastic modulus (E), equivalent yield stress (S_Y), and rupture stress (S_M), as documented in Figure 2b. These properties were subsequently incorporated into the FEM simulations presented in Section 3.2.

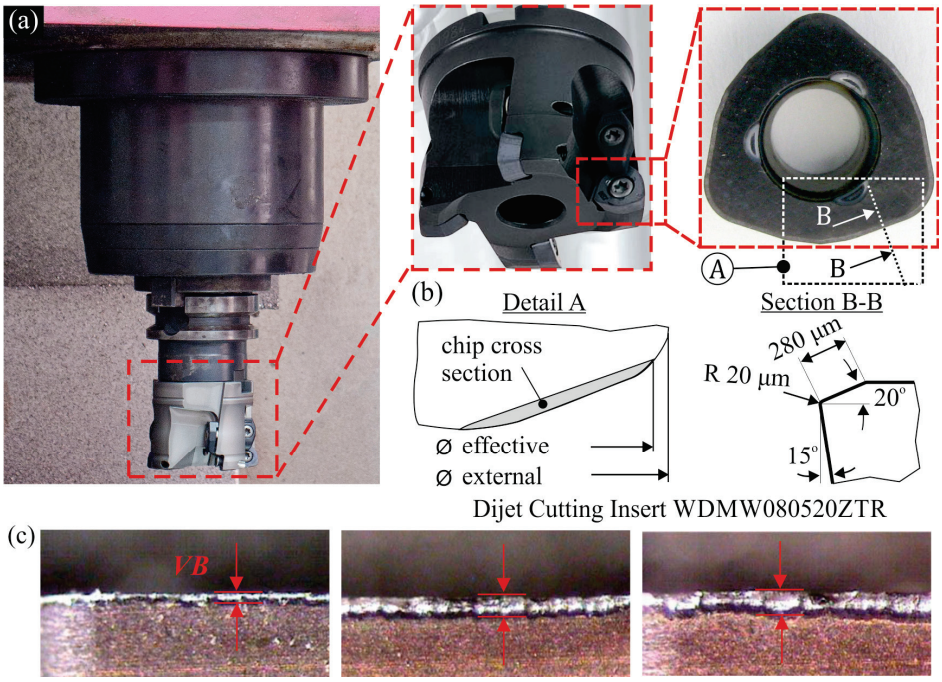


Figure 1. (**a**) Experimental setup; (**b**) Geometrical characteristics of the investigated milling cutter; (**c**) Characteristic tool wear evolution on the flank surface.

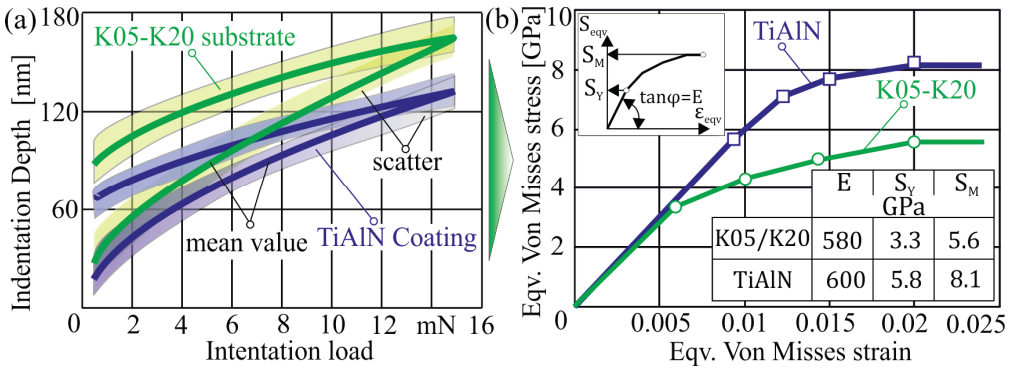


Figure 2. (**a**) Nanoindentation analysis; (**b**) The corresponding material constitutive stress-strain laws of the examined coated insert and its substrate.

In the present work, a modified AISI P20 steel that is equivalent to DIN 1.2311 steel was employed as the workpiece material, which is a pre-hardened mold steel with very good polishing and texturing properties that is widely used in applications that require high toughness, good polishability, and wear resistance [20]. Its balanced mechanical properties make it a popular choice for mold-making and tooling applications [21]. Specifically, AISI P20 is commonly utilized for plastic injection mold bases, cavities, and cores due to its good machinability, fatigue strength, high hardness, and reliability. It is also suited for producing automotive parts, consumer goods, and general constructional parts. Moreover, it is exploited in low-pressure die casting for non-ferrous metals such as aluminum, zinc, and magnesium, where moderate wear resistance is required. Finally, AISI P20 can be used for tooling applications that require toughness and moderate wear resistance, including jigs, fixtures, and precision die holders. Table 1 documents the chemical composition and the strength properties of the employed workpiece material as provided by the supplier [20].

Table 1. Mechanical properties and chemical composition of the AISI P20 Steel [20].

AISI P20 Steel					
Composition In weight %	C	Si	Cr	Mn	Ni
	0.37	0.3	2.0	1.4	2.0
Mechanical Properties	Tensile Strength (MPa)	Yield Strength (MPa)	Hardness (HRB)	Elastic Modulus (GPa)	Fracture Elongation A [%]
	900	1020	310	205	20

2.2. Perpendicular Impact Test

In general, perpendicular impact experiments on coated tools are conducted to evaluate their mechanical durability, adhesion strength, and resistance to dynamic loads, which are critical for manufacturing applications [22]. It is worth mentioning that in milling procedures, cutting tools experience intermittent cutting forces due to the cyclic engagement and disengagement with the workpiece. These impact forces can lead to micro-chipping, coating delamination, and premature tool failure. In particular, milling involves repeated mechanical shocks as the tool enters and exits the workpiece. Hence, perpendicular impact tests could replicate these conditions in a controlled environment to analyze how coatings withstand cyclic loading [23]. Moreover, the repeated impacts help assess the fatigue resistance of both the coating and substrate, so a material that could withstand multiple impact cycles without significant degradation is more suitable for milling applications. Therefore, by performing perpendicular impact tests, manufacturers can optimize coating selection, improve milling tool longevity, and enhance machining efficiency, ultimately leading to cost savings and better surface quality in industrial milling operations. Taking into account the above-mentioned, an impact tester was exploited in order to identify the maximum impact force that the investigated coated cutting insert can endure without failing [23]. As presented in Figure 3, the ceramic ball is repeatedly driven into the examined coating under an adjustable maximum force. Using a PID controller, the output voltage of a variable transformer is regulated via a DC motor in order to maintain consistent impact force peaks throughout the entire experiment, enabling that way the characterization of the coating's fatigue endurance stress.

In order to quantify the fatigue endurance stress of the investigated coated carbide inserts, the imprint depths during the impact test were recorded across various load conditions. Specifically, the fatigue fracture behavior of the coating was examined after 10^6 impact cycles at different impact force amplitudes, as exhibited in Figure 4a. To determine the portion of the remaining imprint depth associated with plastic deformation

in the substrate, impact tests were initially conducted for 10^4 cycles, a level at which no coating failure is expected [19]. The difference in imprint depths between 10^6 and 10^4 cycles represents the coating failure depth (CFD), a critical indicator of coating degradation, which was determined to be approximately 0.5 μm [19]. The bottom part of Figure 4b presents characteristic results regarding imprint depths at different impact cycles, while the upper part displays a typical 3D imprint derived from the perpendicular impact test. The imprint depth measurements were carried out via the μsurf confocal microscope of NanoFocus AG. It is evident from Figure 4a that at an impact load amplitude of 800 N, the imprint depths after 10^4 and 10^6 cycles are nearly identical, indicating that there is no significant coating damage due to the low CFD value. However, at a higher impact load of 950 N, the remaining imprint depth after 10^6 cycles exceeded that of 10^4 cycles, achieving a CFD equal to the criterion, suggesting the onset of micro-fatigue mechanisms that could lead to coating fracture and removal. Furthermore, it must be noted that as the impact force increased, coating wear accelerated, resulting in higher CFD values and more pronounced fatigue-induced failure.

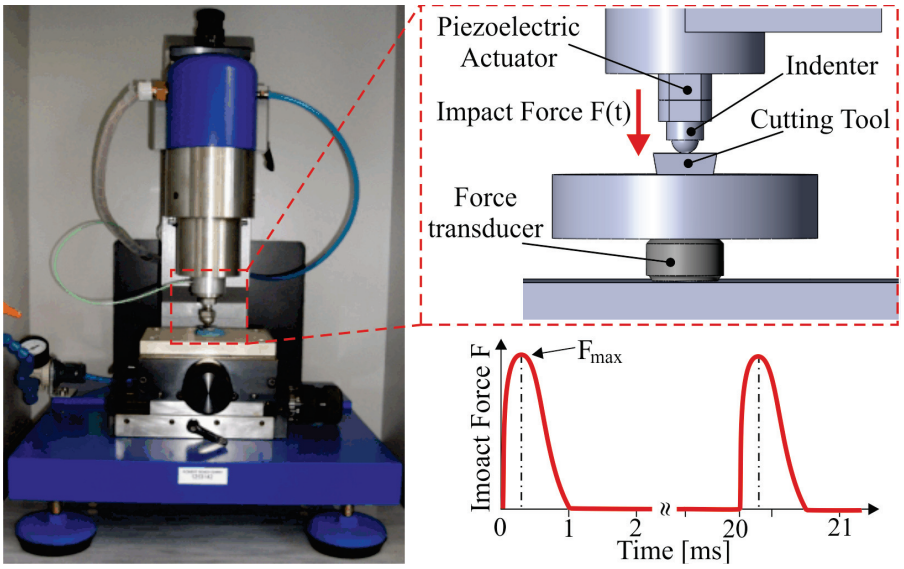


Figure 3. The employed impact tester arrangement for the fatigue endurance investigation.

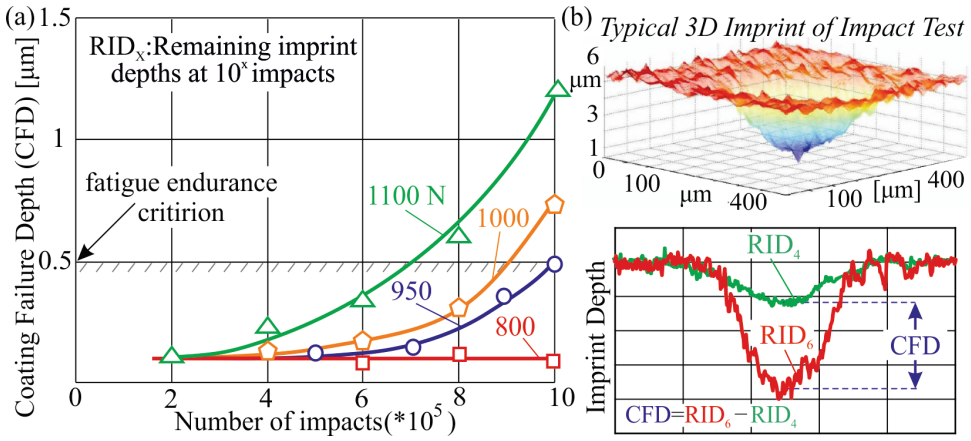


Figure 4. (**a**) Fatigue endurance determination based on coating failure depth; (**b**) a typical 3D imprint of the impact test and characteristic remaining imprint depths.

2.3. Milling Investigations

The milling process is a highly dynamic process characterized by intermittent cutting forces, cyclic thermal loads, and high mechanical stresses, leading to various wear

mechanisms on coated carbide tools [6–8]. In particular, abrasive wear takes place in situations where hard particles from the workpiece material rub against the tool surface, causing gradual material removal that induces flank wear and an increase in cutting forces, eventually degrading tool performance. At lower cutting speeds, material adhesion occurs due to interaction between the tool coating and the workpiece that leads to localized coating detachment, exposing the carbide substrate to further wear. On the contrary, high cutting speeds instigate extreme temperatures, prompting chemical interactions between the coating and oxygen (oxidation) or between the coating and workpiece material (diffusion). Finally, mechanical overstressing and surpassing the fatigue strength primarily cause micro-chipping of the coating, particularly in the transitional cutting-edge region between the flank and the tool's rake. Therefore, in the present study, several experiments were conducted with various values on critical machining conditions, such as feed rate, velocity, and radial depth, in order to capture various wear phenomena on the examined coated tools. Explicitly, four levels were considered for the feed rate and the radial depth of cut and three levels for the cutting speed, generating 48 combinations of the investigated parameters. The values for the feed rate were 0.1, 0.2, 0.3, and 0.4 (mm/rev); for the cutting speed, 100, 200, and 300 (m/min); and for the radial depth of cut, 1, 3, 13, and 20 (mm). The milling experiments were performed utilizing a three-axis numerically controlled milling center, and Table 2 exhibits all of the 48 cutting condition combinations along with the achieved tool's life in each set. A flank wear width criterion equal to 0.15 mm was considered in the tests, resulting in an accumulative tool life $T_{0.15}$, which was calculated with the aid of the following equation:

$$T_{0.15} = NC_{0.15} \times \frac{l_{cu}}{V} \quad (1)$$

where V is the applied cutting speed, l_{cu} composes the undeformed chip length, and $NC_{0.15}$ corresponds to the number of cuts (NC) leading to a flank wear width equal to 0.15 mm.

Table 2. The obtained experimental dataset for the coated tools' life.

f_z = 0.1 [mm/rev]		f_z = 0.3	f_z = 0.5	f_z = 1
a_e [mm]	V = 100 [m/min]			
a_e = 1	31.08 [min]	32.25	28.88	25.72
a_e = 3	32.59	34.56	30.41	27.02
a_e = 13	38.71	40.88	36.37	31.64
a_e = 20	43.49	45.3	41.64	35.85
V = 200				
a_e = 1	11.44	12.56	10.18	9.22
a_e = 3	12.15	13.42	10.85	9.98
a_e = 13	17.32	18.78	15.51	13.92
a_e = 20	23.09	24.56	21.75	18.09
V = 300				
a_e = 1	2.72	3.01	2.35	2
a_e = 3	3.11	3.42	2.56	2.14
a_e = 13	4.34	4.88	3.32	2.91
a_e = 20	4.91	5.57	3.78	3.21

3. Results

3.1. Machine Learning Models

The integration of ML models in milling operations is revolutionizing the manufacturing industry, offering data-driven approaches to extend tool life, optimize performance,

and reduce operational costs. By leveraging historical and real-time data collected from milling operations, ML algorithms were trained to identify patterns and relationships between the input parameters and the tool's wear. ML techniques are particularly useful in creating regression models, which can predict the lifespan of the employed cutting insert as a continuous output, enabling manufacturers to optimize tool usage and reduce downtime. In particular, three learning-based models were developed within the present study that are capable of estimating the performance of the machining operation considering the values of crucial manufacturing parameters like feed rate (f_z), velocity (V_c), and radial depth (a_e). Taking into account the generated dataset presented in Table 2, various ML algorithms were employed to build regression models, namely SVR, KNN, and more advanced methods like ANN networks. These models are trained on the labeled dataset, where the target variable is the tool's life and the input features are the milling conditions.

3.1.1. Artificial Neural Network

A regression-based AI model was developed using an ANN with PyTorch v2.6, where the model was designed to take three input features, pass them through a hidden layer with 64 neurons, and output a single continuous value as illustrated in Figure 5. The dataset was preprocessed using StandardScaler, which standardized the input features to have zero mean and unit variance before feeding them into the network. The ANN architecture consisted of an input layer with three neurons (representing f_z, V_c, and a_e), a hidden layer with 64 neurons that applied the ReLU (rectified linear unit) activation function, and a final output layer with a single neuron to produce the regression prediction that corresponds to the accumulative tool life of $T_{0.15}$. The mean squared error loss (MSELoss) function was utilized to measure the difference between the predicted and actual values, ensuring the model minimized squared errors during training. The Adam optimizer was employed to update the model's weights efficiently, balancing learning speed and convergence stability. Training was performed over 500 epochs, where the model iteratively adjusted its parameters using backpropagation. During each epoch, the optimizer refined the network weights based on the computed loss, gradually improving the accuracy of predictions. The final trained model was capable of capturing complex relationships within data, making it well-suited for regression tasks, as revealed in the next paragraph.

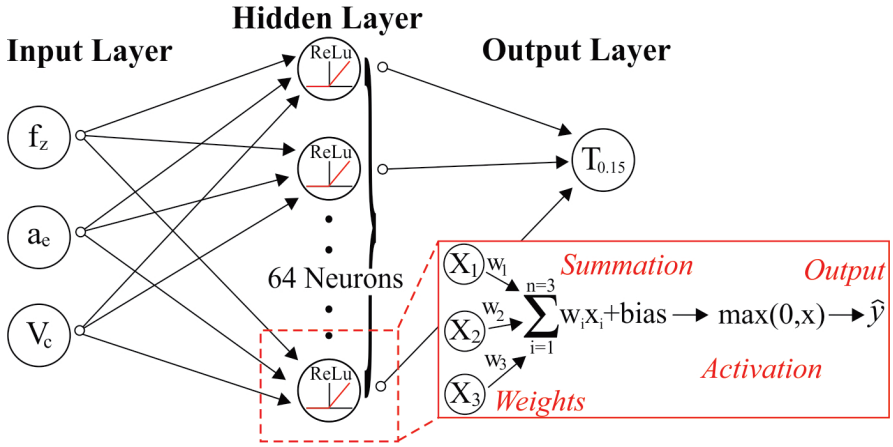


Figure 5. Architecture of the developed artificial neural network.

It must be noted that a test set was also considered in order to ensure that the developed AI models could perform efficiently not only on the data it was trained on but also on unseen conditions. Generally, the deployment of a test set in ML models composes a critical step in validating the robustness and generalization capability of the model, serving as a simulation of unseen data and providing an unbiased evaluation of the model's

performance. During the training phase, the model learns patterns and relationships from the training dataset, which consists of labeled examples. However, if the model is evaluated solely on this training data, there is a risk of overfitting, where the model memorizes the training data rather than learning to generalize from it. Overfitting leads to poor performance on new, unseen data, even if the model achieves high accuracy on the training set. Hereupon, a test set was also created that demonstrates the ability of the ML models to handle new inputs effectively. Regarding the efficiency of the ANN model, the left part of Figure 6 visually compares the actual target values with the model's predicted outputs on the test set. Theoretically, a perfect model would produce a 45-degree diagonal line, meaning all predictions exactly match the true values, whereas in the case of the developed ANN, only small deviations are observed. Finally, the right part of Figure 6 tracks how the loss function evolves during the training phase, such as the training loss, which displays how well the ANN model fits the training data, while the test loss, which reflects generalization to unseen data.

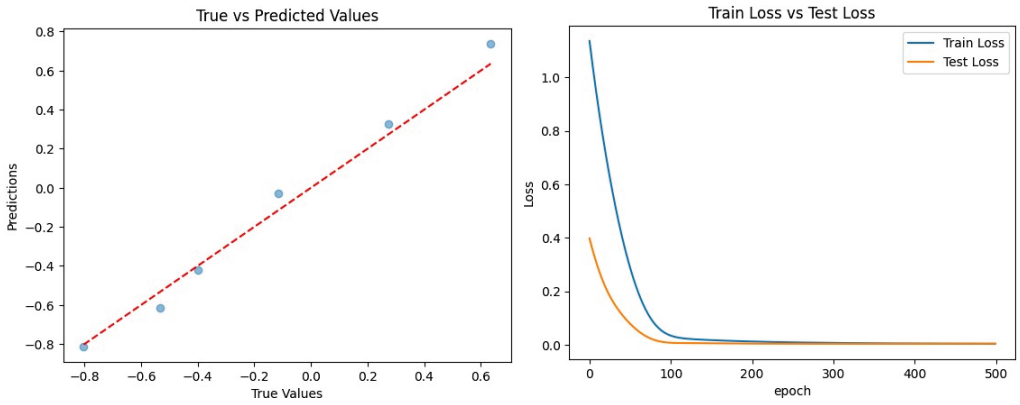


Figure 6. Evaluation of the ANN model predicting the lifespan of a tool based on milling conditions.

3.1.2. Regression with KNN and SVR

Another two regression-based ML models were developed applying the KNN and SVR algorithms, with three input features (f_z, V_c, a_e) and a single continuous output value ($T_{0.15}$), as in the case of the ANN. In particular, the KNN model operates by identifying the 'k' most similar data points (neighbors) in the training set and computing the output as a weighted or unweighted average of their values, allowing it to capture complex, non-linear relationships within the data. A small 'k' allowed the model to capture finer details but risked overfitting, whereas a larger 'k' smoothed predictions but could lead to underfitting. Unlike parametric models, KNN does not make explicit assumptions about the underlying data distribution but instead relies on distance metrics such as Euclidean distance to determine similarity between points, as displayed in Figure 7a. Considering the hyperparameters of the model: the number of neighbors was equal to fourteen, the algorithm used to compute the nearest neighbor was selected to be 'kd_tree', the employed weight function for the predictions was set to 'distance', the 'leaf size' passed to KDTree was equivalent to twenty, and the metric to use for distance computation was the 'minkowski'.

Regarding the SVR model, it extends the principles of support vector machines (SVM) to regression tasks, aiming to compute a function that best fits the data while maintaining a margin of tolerance around the true values. Unlike traditional regression models, SVR does not minimize the error directly but instead seeks to keep predictions within a specified threshold, known as the epsilon-insensitive tube, where deviations within epsilon are not penalized, as schematically illustrated in Figure 7b. Firstly, the input data were standardized to ensure proper distance measurements within the kernel function. During training, SVR identified a subset of the training samples, known as support vectors, which defined the

regression function and contributed to predictions. By leveraging these support vectors and the non-linear mapping provided by the kernel, the SVR model effectively captured intricate patterns in the data, making it highly suitable for non-linear regression tasks where the relationship between inputs and outputs is relatively complex, as in the tool's lifespan case. The main hyperparameters of the developed SVR model were the following: the kernel that was selected was 'poly', the degree of the polynomial kernel function was equivalent to three, the independent term in the kernel function 'coef0' = 1.68, and the 'epsilon' of the SVR model was equal to 0.1.

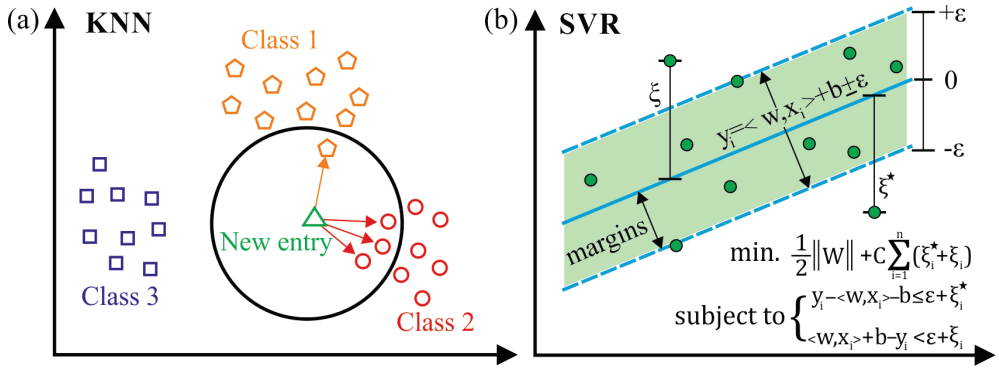


Figure 7. Schematic representation of the (**a**) KNN and (**b**) SVR machine learning algorithms.

Table 3 presents the test set of the ML algorithms, which are additional milling experiments that were excluded from the training phase and instead used for validating the developed ML models. The table also illustrates the models' performance in predicting the tool's lifespan based on the applied values at certain milling conditions. To assess forecasting accuracy, three performance metrics were employed: mean squared error (MSE), mean absolute error (MAE), and the discrepancies between predicted and actual experimental values. These metrics were calculated using the following equations:

$$MSE = \frac{1}{N}\sum_{k=1}^{N}(y_k - \hat{y_k})^2 \quad (2)$$

$$MAE = \frac{1}{N}\sum_{k=1}^{N}|y_k - \hat{y_k}| \quad (3)$$

$$Error = \frac{|y_k - \hat{y_k}|}{y_k} \quad (4)$$

where N represents the total number of data points, while y_k and $\hat{y}_k$ denote the actual and predicted values, respectively.

Finally, it is worth mentioning that ML models typically require large datasets to generalize well. Nevertheless, when the underlying relationships in the data are not very complex, simpler ML models like regression could be effective even with small datasets [24]. These models possess fewer parameters and are less prone to overfitting, making them suitable for cases where the data exhibit clear, straightforward patterns. In addition, in situations where the data are of high quality, containing minimal noise and outliers, small datasets can still be effective. So, high-quality data with clear, meaningful patterns can enable models to learn robust relationships without requiring large volumes of data. Furthermore, as in the present investigated case, problems that are well-constrained and the feature space is relatively small, ML models can perform well with relatively limited data [25].

Table 3. Outcomes and metrics of the developed ML models on the test set.

Algorithm	Exper. No.	V_c [m/min]	a_e [mm]	f_z [mm]	MSE/ MAE	Prediction	Measured	Error %
SVR	1	125	8	0.40	1.502/ 1.070	28.62	26.53	7.89
	2	150	5	0.25		22.67	21.58	5.07
	3	175	11	0.90		17.78	16.25	9.45
	4	225	2	0.15		9.92	10.54	5.92
	5	250	17	0.60		11.63	12.40	6.18
	6	275	15	0.80		6.56	6.87	4.49
KNN	1	125	8	0.40	2.499/ 1.371	28.02	26.53	5.62
	2	150	5	0.25		22.88	21.58	6.01
	3	175	11	0.90		19.18	16.25	18.01
	4	225	2	0.15		11.40	10.54	8.19
	5	250	17	0.60		12.03	12.40	2.98
	6	275	15	0.80		8.15	6.87	18.59
ANN	1	125	8	0.40	0.865/ 0.810	27.93	26.53	5.28
	2	150	5	0.25		22.30	21.58	3.35
	3	175	11	0.90		17.43	16.25	7.28
	4	225	2	0.15		9.44	10.54	10.36
	5	250	17	0.60		12.07	12.40	2.63
	6	275	15	0.80		6.72	6.87	2.06

3.2. Tool Performance Estimation Using FEA

FEM is a powerful computational tool that can simulate the physical behavior of materials and structures under various conditions, making it well-suited for analyzing the complex interactions between cutting tools and workpieces during milling operations. Firstly, a simulation of the perpendicular impact test was conducted in order to estimate the maximum developed stresses on the coated cutting tool, aiding that way in the creation of the coating's corresponding 'Woehler' diagram (also known as 'Stress-Number of cycles' diagram). Then, a FE model was employed to determine the cutting forces, predicting also the distribution of stresses on the cutting edge. Finally, the combination of the coating's fatigue behavior, using the S-N diagram, coupled with the numerically calculated stresses on the cutting insert, provided the necessary insights to assess the lifespan of the coated tool using FEA.

3.2.1. Fatigue Endurance Strength Determination

A 2D FE model was utilized using the ANSYS 2024 R2 software to analyze the coated surface response under quasi-static loads, which was based on [26]. The model, along with the boundary conditions and finite element discretization, is depicted in the left part of Figure 8a. To mesh the 2D geometry of the carbide ball, coating, and substrate, plane elements were selected, resulting in approximately 27,000 elements. In addition, contact elements were utilized to define the interface between the ball indenter and the coating, where the contact elements can be used in the simulation such that no penetration could take place between the indenter and the examined coating. Hence, the nodes on the contact surfaces will be prevented from unrealistic penetration into the volume of the target surface, as well as ensuring proper load transmission. In addition, the adhesion properties of the coating and substrate interface could also be simulated through the implementation of appropriate contact elements. However, it must be noted that in the case of the perpendicular impact test, the adhesion between the coating and its substrate does not affect its performance [26]. Moreover, a Y-axis constraint was imposed on the nodes at the bottom surface of the substrate. The deformation induced in the coating

and substrate by the slow penetration of the carbide ball into the film was evaluated at predefined indentation depths. Using this FE model, both maximum indentation depth and remaining imprint depth (RID) after coating relaxation were determined as functions of the reaction force amplitude, leading to an equivalent resulting pressure, which deforms the investigated coated tool, as presented in the middle part of Figure 8a.

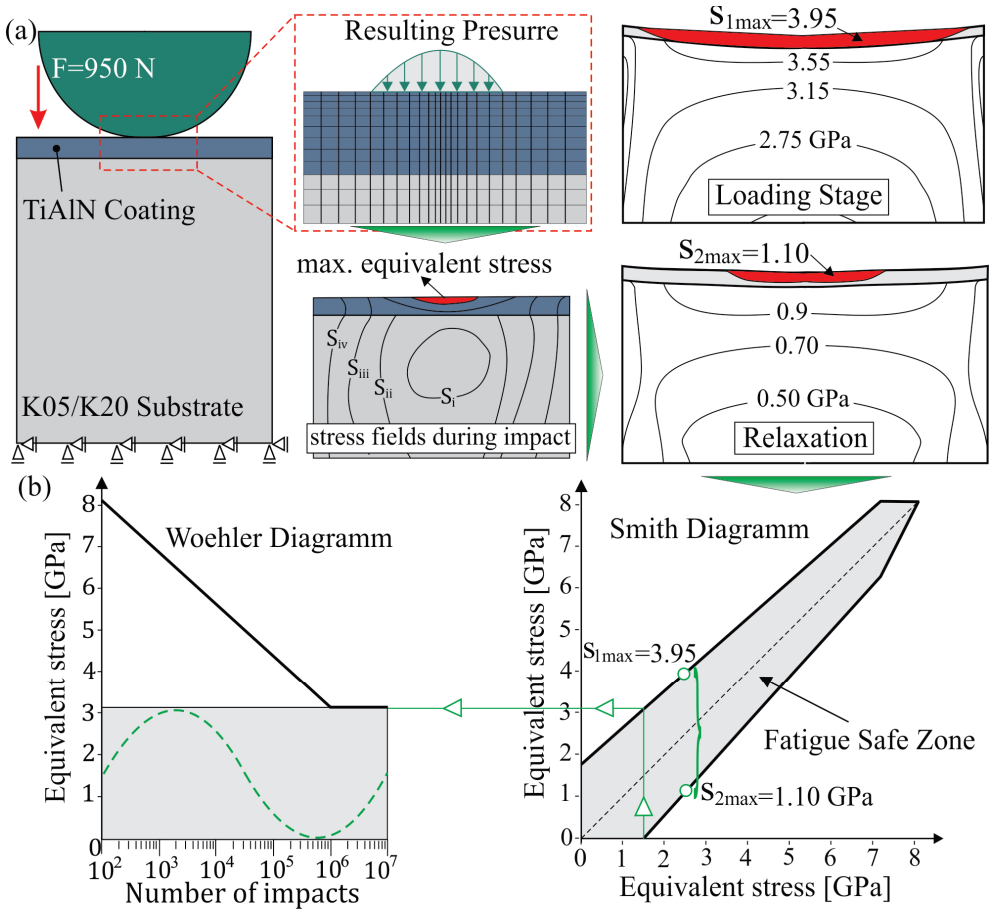


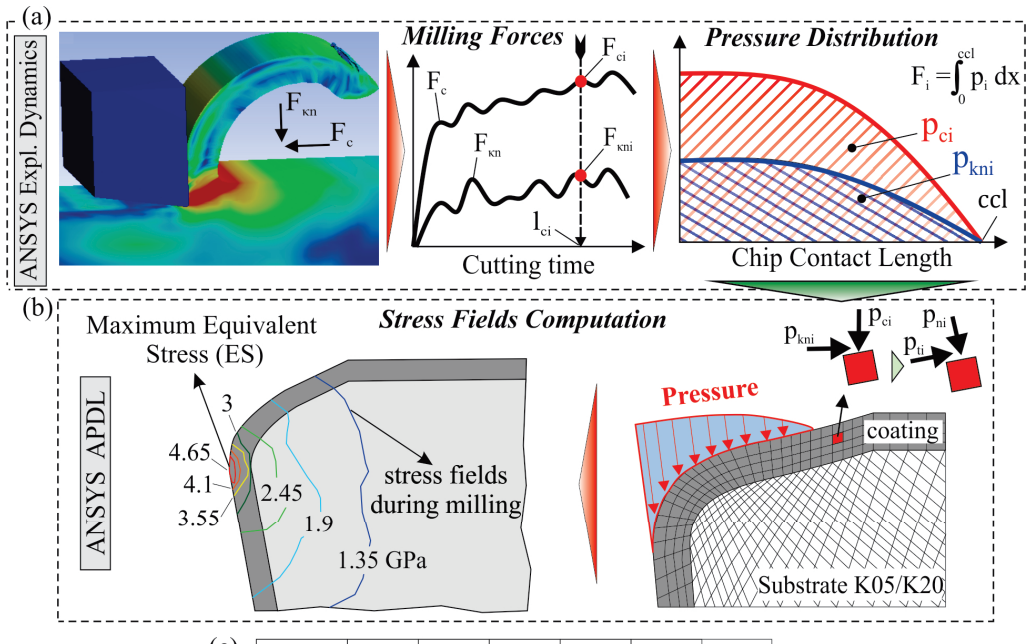
Figure 8. (**a**) Numerical simulation of the perpendicular impact test; (**b**) Generation of Smith-like and Woehler diagrams based on FEA results.

Taking into account that at the maximum impact force Fmax, which corresponds to the fatigue threshold force of 950 N (see Figure 4), the correlated maximum equivalent stress in the coating during its loading is equal to 3.95 GPa, and the remaining one due to the substrate plastic deformation is 1.10 GPa. Utilizing these data, the Smith-like diagram exhibited in the right part of Figure 8b was constructed [19]. This diagram enables the determination of the coating fatigue endurance stress under cyclic loading, where the load varies from zero to a specified maximum value. Based on the obtained values, the Woehler-like diagram was also created, as depicted in the left part of Figure 8b. This diagram is essential for understanding how materials respond to repeated loading and predicting their fatigue life. Finally, it is worth mentioning that the data used to generate these graphs are independent of the coating's adhesion, as the film experiences only vertical loading during the perpendicular impact test.

3.2.2. Stress Distribution During the Milling Process

Considering the computation of the developed forces during the machining process, a numerical model was used applying explicit dynamics analysis based on [11]. In the FE model, the workpiece was treated as a plastic material, while the tool was considered rigid.

The mechanical properties of the coated insert were modeled via a bilinear anisotropic approach to account for elastic–plastic deformations, based on Figure 2. To ensure an accurate FEA simulation of the milling procedure, a flow stress model was incorporated to represent the material's constitutive behavior under large deformations and high-speed cutting conditions. In particular, the Johnson–Cook constitutive model was utilized, which describes the flow stress of the workpiece material as a function of strain, strain rate, and temperature. Moreover, the FE model incorporates the kinematics of face milling and the applied cutting conditions, including cutting speed, radial depth of cut, and feed rate. This approach accurately represents the motion of the cutting insert, its engagement with the workpiece material, and their subsequent interactions. The definition of the interactions between the cutting tool and the workpiece material was modeled using a frictional contact formulation. The stress fields generated during the process were concentrated near the contact area between the workpiece and the coated cutting insert, as depicted in Figure 9a. It is worth mentioning that the cutting forces F_c and F_{kn} are the result of the integration of the developed stress fields over the elements that remain in contact with the cutting tool and are calculated by the software. Next, these force distributions were approximated using a second-degree polynomial curve, where the pressure distributions (p_{ci}, p_{kni}) along the chip contact length (ccl) are presented in the right section of Figure 9a. As a result, the associated superficial normal 'p_n' and tangential 'p_t' pressures were applied to the respective elements within the ccl, as illustrated in the right section of Figure 9b. Taking into account the calculated cutting forces as well as the chip contact lengths and by applying a FE simulation model of the material removal process based on [19], the developed stresses at the cutting edge were also determined, as illustrated in the left part of Figure 9b. Finally, results of the maximum equivalent stresses on the test set are documented in Figure 9c.

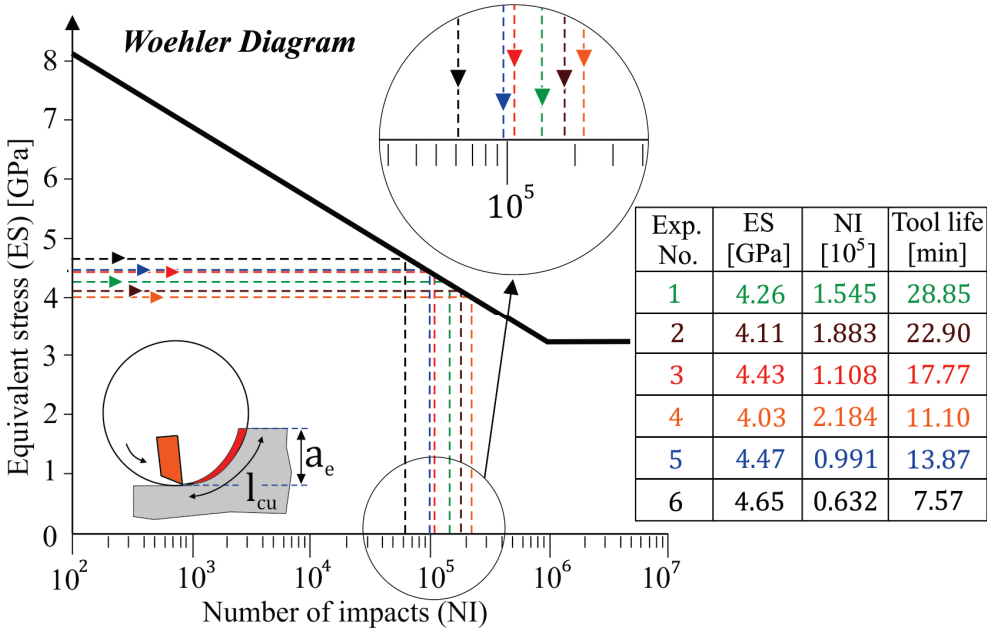


(c)

Exp. No.	1	2	3	4	5	6
ES [GPa]	4.26	4.11	4.43	4.03	4.47	4.65

Figure 9. (**a**) Computation of the milling forces and the corresponding pressure distribution; (**b**) Determination of the stress fields in the cutting edge; (**c**) Maximum equivalent stresses at the test set.

The outcomes of the milling FE simulation model coupled with the experimentally defined S-N diagram were considered in order to estimate the lifespan of the employed cutting tools on the test set. In particular, Figure 10 displays the forecasted number of cuts for each experiment of the test set, such as to achieve a flank wear equal to the predefined criterion. More specifically, the horizontal axis represents the number of cycles to failure (N) on a logarithmic scale, and the vertical axis shows the stress amplitude applied to the material during cyclic loading. Hence, the diagram indicates how many machining cycles the coated tool can endure before failure occurs. The main idea is that higher stress fields during the machining process (calculated via the FEM model in Figure 9c) would lead to a smaller number of cuts due to the determined Woehler diagram of Figure 8b [19].



Exp. No.	ES [GPa]	NI [10^5]	Tool life [min]
1	4.26	1.545	28.85
2	4.11	1.883	22.90
3	4.43	1.108	17.77
4	4.03	2.184	11.10
5	4.47	0.991	13.87
6	4.65	0.632	7.57

Figure 10. FEM-based calculation of the coated tool's lifespan based on the maximum stress of the cutting edge.

3.3. Comparison of Learning-Based Models and FEM-Supported Simulations

Figure 11 presents a comparison between the numerical predictions of the FE and the ML-based models on the test set. Three key conclusions can be drawn from the data shown in the figure. Firstly, the comparison indicates a strong agreement between the predicted and actual accumulated tool life across all the developed predictive models. In addition, ML models, particularly the ANN, demonstrated higher accuracy compared to the other approaches while also requiring significantly less computation time compared to the FE model. However, the FE simulation eliminates the need for time-consuming milling experiments, which are otherwise required to collect datasets for each specific workpiece material. Finally, despite the relatively small dataset, the AI-based forecasts exhibit a high level of convergence, further reinforcing their reliability.

3.4. Cutting Tool Performance Optimization

The developed ANN model was also utilized to calculate the optimal values of the milling parameters. Specifically, a routine is implemented to identify the machining conditions that maximize the lifespan of the coated inserts. Since a standard optimization routine might only identify local maxima of the objective function, a repetitive procedure was necessary to locate the global maximum. To address this, a loop with multiple starting points within the boundaries of the machining parameters was applied. This allowed the optimization algorithm to run repeatedly, computing various local maxima. During each

iteration, the calculated local maximum was compared to the global maximum, and if an improvement was found, the global maximum was updated. The pseudocode for this methodology is provided in Algorithm 1. As a result of this process, the values of the milling parameters yielding the longest lifespan for the cutting tool were determined.

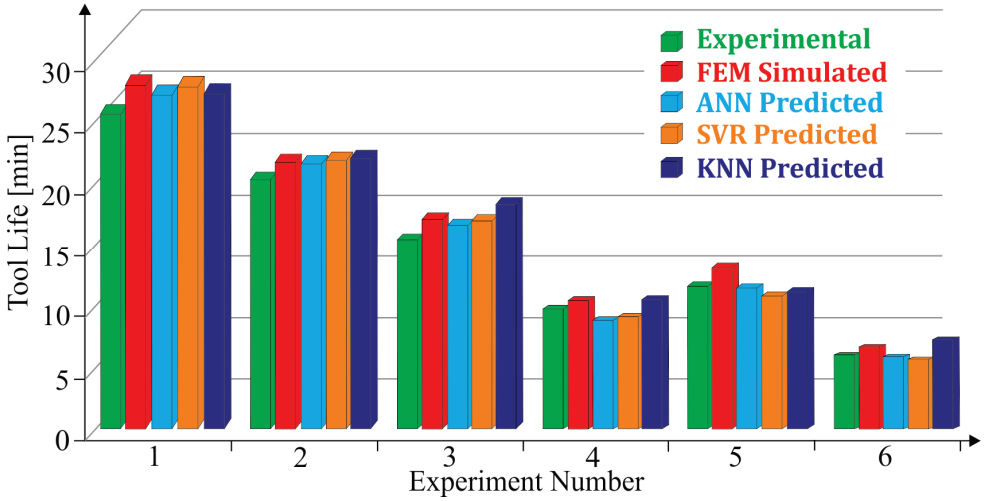


Figure 11. Comparison between the experimental results and the numerical and AI predictions on the cutting tool's performance.

Algorithm 1: Pseudocode for the parameter's optimization pipeline

Input:
V_{cmin}, V_{cmax}: min., max. Cutting speed
a_{emin}, a_{emax}: min., max. Radial depth
f_{zmin}, f_{zmax}: min., max. Feed rate
V_{step}, a_{step}, f_{step}: Step increments

initialize: $V_c = V_{cmin}$, $a_e = a_{emin}$, $f_z = f_{zmin}$
global_max = 0
for $V_c = V_{cmin}$ && $V_c \leq V_{cmax}$
  for $a_e = V_{cmin}$ && $a_e \leq a_{emax}$
    for $f_z = f_{zmin}$ && $f_z \leq f_{zmax}$
      tensor_data = X (V_c, a_e, f_z)
      Tool_Life_Prediction = Model(tensor_data)
      if Tool_Life_Prediction > global_max **then**
        $V_{copt} = V_c$, $a_{eopt} = a_e$, $f_{zopt} = f_z$
        global_ max = Tool_Life_Prediction
      end if
      $f_z = f_z + f_{step}$
    end for
    $a_e = a_e + a_{step}$
  end for
  $V_c = V_c + V_{step}$
end for
return global_ max, V_{copt}, a_{eopt}, f_{zopt}

Output:
Optimized Manufacturing Conditions ($V_c = 100$, $a_e = 20$, $f_z = 0.2$)

4. Conclusions

The optimization of coated carbide tools in milling procedures composes an essential task for improving machining efficiency, reducing costs, and extending tool life. The present work focused on investigating the wear behavior of coated tools under varying machining conditions, including feed rate, velocity, and radial depth, through an experimentally generated dataset. To enhance predictive capabilities, machine learning models such as artificial neural network, k-nearest neighbors, and support vector regression were developed to estimate tool life based on these machining parameters. In parallel, FEM simulations were also conducted to numerically model the wear mechanisms and analyze the milling process under different operating conditions. A comparative analysis of AI-based predictions and FEM simulations provided valuable insights into the strengths and limitations of both methodologies. In particular, AI techniques demonstrated the ability to deliver rapid, data-driven predictions with minimal computational cost, making them well-suited for real-time tool wear monitoring and manufacturing parameters optimization. On the other hand, FEM models provide a deeper physical understanding of the wear mechanisms at play, allowing for precise analysis of stress distribution, heat generation, and material deformation during milling procedures.

The findings of this study contribute to the ongoing advancements of predictive manufacturing and process optimization in machining operations. By leveraging AI-driven models for tool wear prediction and FEM simulations for in-depth wear analysis, manufacturers can make informed decisions to enhance tool life, reduce downtime, and improve overall productivity. Future research may further refine the developed models by integrating more experimental data for the training phase of the AI algorithms, as well as investigate additional parameters such as coating composition and tool geometry. Moreover, future work could study hybrid AI models that combine multiple learning techniques for improved accuracy. Furthermore, deep learning, reinforcement learning, and convolutional neural networks could also be explored to refine tool wear predictions. Ultimately, the combination of AI and FEM methodologies could offer a powerful framework for the intelligent optimization of coated tools in milling applications, paving the way for more efficient and cost-effective manufacturing processes. By exploring these future directions, the machining industry can further enhance the accuracy, reliability, and applicability of predictive models for tool wear estimation and process optimization, contributing to smarter and more efficient manufacturing systems.

Funding: This research received no external funding.

Institutional Review Board Statement: Not applicable.

Informed Consent Statement: Not applicable.

Data Availability Statement: The original contributions presented in this study are included in the article. Further inquiries can be directed to the corresponding author.

Conflicts of Interest: The author declares no conflicts of interest.

References

1. Li, W. Advanced Manufacturing and Precision Machining. *Appl. Sci.* **2024**, *14*, 11642. [CrossRef]
2. Silva, F.J.G.; Martinho, R.P.; Magalhães, L.L.; Fernandes, F.; Sales-Contini, R.C.M.; Durão, L.M.; Casais, R.C.B.; Sousa, V.F.C. A Comparative Study of Different Milling Strategies on Productivity, Tool Wear, Surface Roughness, and Vibration. *J. Manuf. Mater. Process.* **2024**, *8*, 115. [CrossRef]
3. Abellán-Nebot, J.V.; Vila Pastor, C.; Siller, H.R. A Review of the Factors Influencing Surface Roughness in Machining and Their Impact on Sustainability. *Sustainability* **2024**, *16*, 1917. [CrossRef]
4. Sambo, A.M.; Younas, M.; Njuguna, J. Insights into Machining Techniques for Additively Manufactured Ti6Al4V Alloy: A Comprehensive Review. *Appl. Sci.* **2024**, *14*, 10340. [CrossRef]

5. Sousa, V.F.C.; Castanheira, J.; Silva, F.J.G.; Fecheira, J.S.; Pinto, G.; Baptista, A. Wear Behavior of Uncoated and Coated Tools in Milling Operations of AMPCO (Cu-Be) Alloy. *Appl. Sci.* **2021**, *11*, 7762. [CrossRef]
6. Sousa, V.F.C.; Silva, F.J.G. Recent Advances on Coated Milling Tool Technology—A Comprehensive Review. *Coatings* **2020**, *10*, 235. [CrossRef]
7. Muhamad, S.S.; Ghani, J.A.; Che Haron, C.H.; Yazid, H. Wear Mechanism of Multilayer Coated Carbide Cutting Tool in the Milling Process of AISI 4340 under Cryogenic Environment. *Materials* **2022**, *15*, 524. [CrossRef]
8. Chowdhury, M.S.I.; Bose, B.; Rawal, S.; Fox-Rabinovich, G.S.; Veldhuis, S.C. Investigation of the Wear Behavior of PVD Coated Carbide Tools during Ti6Al4V Machining with Intensive Built Up Edge Formation. *Coatings* **2021**, *11*, 266. [CrossRef]
9. Bazaz, S.M.; Ratava, J.; Lohtander, M.; Varis, J. An Investigation of Factors Influencing Tool Life in the Metal Cutting Turning Process by Dimensional Analysis. *Machines* **2023**, *11*, 393. [CrossRef]
10. Paszkiewicz, A.; Piecuch, G.; Żabiński, T.; Bolanowski, M.; Salach, M.; Rączka, D. Estimation of Tool Life in the Milling Process—Testing Regression Models. *Sensors* **2023**, *23*, 9346. [CrossRef]
11. Charalampous, P. Prediction of cutting forces in milling using machine learning algorithms and finite element analysis. *J. Mater. Eng. Perform.* **2021**, *30*, 2002–2013. [CrossRef]
12. Reeber, T.; Wolf, J.; Möhring, H.-C. A Data-Driven Approach for Cutting Force Prediction in FEM Machining Simulations Using Gradient Boosted Machines. *J. Manuf. Mater. Process.* **2024**, *8*, 107. [CrossRef]
13. Rodríguez, J.M.; Carbonell, J.M.; Jonsén, P. Numerical Methods for the Modelling of Chip Formation. *Arch. Comput. Methods Eng.* **2020**, *27*, 387–412. [CrossRef]
14. Vishwakarma, P.; Sharma, A. 3D Finite Element Analysis of milling process for non-ferrous metal using deform-3D. *Mater. Today Proc.* **2020**, *26*, 525–528. [CrossRef]
15. Munaro, R.; Attanasio, A.; Del Prete, A. Tool Wear Monitoring with Artificial Intelligence Methods: A Review. *J. Manuf. Mater. Process.* **2023**, *7*, 129. [CrossRef]
16. Val, S.; Lambán, M.P.; Lucia, J.; Royo, J. Analysis and Prediction of Wear in Interchangeable Milling Insert Tools Using Artificial Intelligence Techniques. *Appl. Sci.* **2024**, *14*, 11840. [CrossRef]
17. Kaliyannan, D.; Thangamuthu, M.; Pradeep, P.; Gnansekaran, S.; Rakkiyannan, J.; Pramanik, A. Tool Condition Monitoring in the Milling Process Using Deep Learning and Reinforcement Learning. *J. Sens. Actuator Netw.* **2024**, *13*, 42. [CrossRef]
18. Gao, P.; Liang, Z.; Wang, X.; Li, S.; Zhou, T. Effects of different chamfered cutting edges of micro end mill on cutting performance. *Int. J. Adv. Manuf. Technol.* **2018**, *96*, 1215–1224. [CrossRef]
19. Skordaris, G.; Bouzakis, K.-D.; Charalampous, P.; Kotsanis, T.; Bouzakis, E.; Bejjani, R. Bias Voltage Effect on the Mechanical Properties, Adhesion and Milling Performance of PVD Films on Cemented Carbide Inserts. *Wear* **2018**, *404–405*, 50–61. [CrossRef]
20. Uddeholm. Available online: http://www.uddeholm.gr/Storage/Media/Shared/SteelBrochures/Impax%20Supreme/PB_impax_supreme_english.pdf (accessed on 1 March 2025).
21. Abbas, A.T.; Abdelnasser, E.; Naeim, N.; Alqosaibi, K.F.; Al-Bahkali, E.A.; Elkaseer, A. Effect of Milling Strategy on the Surface Quality of AISI P20 Mold Steel. *Metals* **2024**, *14*, 48. [CrossRef]
22. Wang, T.; Zha, X.; Chen, F.; Wang, J.; Lin, L.; Xie, H.; Lin, F.; Jiang, F. Research on cutting performance of coated cutting tools by a new impact test method considering contact stress condition caused by segmented chips. *J. Manuf. Process.* **2021**, *68*, 1569–1584. [CrossRef]
23. Bouzakis, E.; Bouzakis, K.-D.; Skordaris, G.; Charalampous, P.; Kombogiannis, S.; Lemmer, O. Fatigue strength of diamond coating-substrate interface assessed by inclined impact tests at ambient and elevated temperatures. *Diam. Relat. Mater.* **2014**, *50*, 77–85. [CrossRef]
24. Sevgin, F. Machine Learning-Based Temperature Forecasting for Sustainable Climate Change Adaptation and Mitigation. *Sustainability* **2025**, *17*, 1812. [CrossRef]
25. Shobayo, O.; Adeyemi-Longe, S.; Popoola, O.; Okoyeigbo, O. A Comparative Analysis of Machine Learning and Deep Learning Techniques for Accurate Market Price Forecasting. *Analytics* **2025**, *4*, 5. [CrossRef]
26. Bouzakis, K.-D.; Asimakopoulos, A.; Michailidis, N.; Kompogiannis, S.; Maliaris, G.; Giannopoulos, G.; Pavlidou, E.; Erkens, G. The inclined impact test, an efficient method to characterize coatings' cohesion and adhesion properties. *Thin Solid Film.* **2004**, *469–470*, 254–262. [CrossRef]

Disclaimer/Publisher's Note: The statements, opinions and data contained in all publications are solely those of the individual author(s) and contributor(s) and not of MDPI and/or the editor(s). MDPI and/or the editor(s) disclaim responsibility for any injury to people or property resulting from any ideas, methods, instructions or products referred to in the content.

applied sciences

MDPI

Article

Construction of a Cutting-Tool Wear Prediction Model through Ensemble Learning

Shen-Yung Lin * and Chia-Jen Hsieh

Department of Mechanical and Computer-Aided Engineering, National Formosa University, Yunlin 63201, Taiwan; 11020130@gm.nfu.edu.tw
* Correspondence: sylin@nfu.edu.tw; Tel.: +886-919-051127

Abstract: This study begins by conducting side milling experiments on SKD11 using tungsten carbide TiAlN-coated end mills to compare the surface roughness performance between two combinations of milling process parameters (feed rate and radial depth of cut), along with three ultrasonic-assisted methods (rotary, dual-axis, and rotary combined with dual-axis). The results suggest that the rotary (*z*-axis oscillation) ultrasonic-assisted method may provide better performance. Subsequently, this superior ultrasonic-assisted method was applied both with and without laser locally preheating assistance, respectively. Using a Taguchi orthogonal array, milling process parameters (spindle speed, feed rate, and radial depth of cut) were planned for experiments with the same cutting tool and the workpiece just mentioned above. The surface roughness serves as the objective function while being constrained by cutting-tool life. The characteristics of the smaller-the-better in the Taguchi method were applied to determine the optimal combination of process parameters. Based on the optimal milling process parameters obtained and the superior hybrid-assisted method adopted, milling experiments were repeatedly performed to collect the data on cutting force and cutting-tool wear. Feature engineering was performed on the cutting force signals, and different domain characteristics from both the time and frequency domains were extracted. Hereafter, feature selection by random forest and data standardization were further applied to feature extractions, and the data processing was thus completed. For the processed data, a cutting-tool wear prediction model was constructed by ensemble learning. This method leverages various machine learning regression models, including decision tree, random forest, extremely randomized tree, light gradient boosting machine, extreme gradient boosting, AdaBoost, stochastic gradient descent, support vector regression, linear support vector regression, and multilayer perceptron. After hyper-parameter tuning, the ensemble voting regression prediction was performed based on these ten mentioned models. The experimental results demonstrate that the ensemble voting regression model surpasses the performance of each individual machine learning regression model. In addition, this regression model achieves a coefficient of determination (R^2) of 0.94576, a root mean square error (RMSE) of 0.24348, a mean squared error (MSE) of 0.05928, and a mean absolute error (MAE) of 0.18182. Therefore, the ensemble learning approach has been proven to be a feasible and effective method for monitoring cutting-tool wear.

Keywords: SKD11; rotary ultrasonic; laser preheating; machine learning; ensemble learning

1. Introduction

When the demand for new products rapidly emerges, bringing with it new mold requirements, manufacturers must efficiently design and produce molds while maintaining precision. Among the various mold requirements, SKD11 alloy tool steel is a widely used material for mold manufacturing. SKD11 finds extensive applications in the automotive, household appliance, and electronics manufacturing industries. It is a high-carbon and high-chromium alloy steel that exhibits exceptionally high hardness and toughness. This steel also incorporates elements such as molybdenum (Mo) and vanadium (V), giving

it wear resistance, low deformation, high fatigue strength, and impact resistance characteristics. These qualities make it one of the preferred materials for various applications, including stamping dies and plastic molds. Heat-treated SKD11 alloy tool steel can achieve a hardness of HRC 58-62. However, these excellent properties of SKD11 make it a difficult-to-cut material. Difficult-to-cut materials have poor machinability, high-cutting-power requirements, and tend to generate a significant amount of cutting heat, resulting in elevated cutting temperatures, reduced tool life, and decreased production efficiency.

As cutting-tool wear increases, the magnitude and fluctuation pattern of cutting forces also undergo variations. Cutting-tool wear can lead to irregular fluctuations in cutting forces, causing vibrations during the cutting processes. By analyzing the characteristics of cutting force fluctuations, the degree of the cutting-tool wear can be inferred, allowing for the prediction of remaining cutting-tool life. Therefore, in the process of establishing a cutting-tool wear prediction model, precise monitoring and analysis of cutting force fluctuations contribute to achieving real-time awareness of the cutting-tool condition, enhancing the stability and efficiency of the manufacturing processes.

The necessity of establishing a cutting-tool wear prediction model lies in enhancing the efficiency, quality, and safety of the manufacturing processes. By predicting cutting-tool wear, the production line can promptly initiate cutting-tool replacement, thereby reducing downtime and production costs. Furthermore, the cutting-tool wear prediction model can be employed to optimize cutting parameters, improving machining efficiency. This helps prevent excessive wear or premature cutting-tool replacement, thus saving costs and extending cutting-tool life.

With the advancement of the times and the rapid development of technology, product iteration speeds have increased. At the same time, there is a need to deal with higher manufacturing complexity and shorter production cycles, which, undoubtedly, raise research and development costs, as well as production pressures in the industry. Finding more efficient and cost-effective ways to shorten production cycles is a challenge for the manufacturing sector [1,2].

The high strength, hardness, and toughness of SKD11 result in poor machinability. To meet the precision, stability, and shorter production cycles required for molds, there are numerous factors to consider during the machining process. These factors include, but are not limited to, machining parameters, machining assistance, and the impact of tool wear. Firstly, machining parameters such as cutting speed and feed rate play a crucial role. Cutting speed directly affects the machining time and tool wear rate, while the feed rate impacts material removal rates and surface roughness. Secondly, machining assistance significantly influence the machining process. Effective machining assistance can extend tool life and enhance product quality. Lastly, tool wear directly affects machining efficiency and workpiece quality. As tool wear increases, it results in reduced accuracy and increased surface roughness. Excessive tool wear can also lead to increased cutting forces, accelerating further tool wear and reducing production efficiency. Therefore, to improve the machinability of SKD11, enhance machining efficiency, and reduce production costs, it is essential to identify optimal process parameters and cutting assistance that can help minimize costs and improve machining efficiency [3].

A literature review on ultrasonic-assisted milling examines the influence of ultrasonic assistance on cutting performance. Kadhim Mejbel et al. [4] proposed axial ultrasonic vibration on the rotating mill to conduct experiments on hardened AISI H11 tool steel, using a carbide flat end mill. The experiments involved slot milling under wet cutting conditions with variations in cutting speed, feed rate, and milling depth in both conventional milling and ultrasonic vibration-assisted milling. The study aimed to investigate the effect of ultrasonic-assisted machining on surface roughness, surface topography, and subsurface microhardness. The results indicated that the surface produced by axial ultrasonic-assisted milling was uniform, and the peak-to-peak value remained consistent, thereby enhancing surface finish. Additionally, the study verified the importance of axial ultrasonic vibration on rotary tooling for improving machining surface quality, as this vibration imparts a

hammering action on the cutting-tool tip, making the cutting marks left by the teeth flat. Compared to conventional milling, ultrasonic-assisted milling resulted in a significant reduction of surface roughness, Ra, with up to 89.7% improvement. Tsai et al. [5] utilized cemented carbide flat end mills to conduct the ultrasonic-assisted end milling of AISI420 mold steel by varying the ultrasonic vibration frequencies and amplitudes, the rake angles and helix angles of the cutting-tool. The study aimed to improve machined surface roughness and cutting-tool wear via the assisted system. In addition, the effects of the input voltage, cutter stretch length, and holding force on the amplitude of the ultrasonic vibration system were also investigated. The results showed that the ultrasonic amplitude increased with increasing stretch length and input voltage. In addition, a proper holding force and an optimum amplitude, which are related to the best surface finish, were ascertained. The machined surfaces with ultrasonic-assisted milling exhibited better uniformity and smoothness as compared to those machined under the same conditions without assistance. In addition, the cutting-tool wear was slower during ultrasonic-assisted milling, which leads to an extension of tool life. Cutter geometry, such as positive rake angle with a larger helix angle of 45°, and vibration parameters, such as a frequency of 50 kHz and an amplitude of 2.2 μm, provided better surface smoothness and smaller cutting-tool wear during ultrasonic-assisted milling. Ding et al. [6] investigated cutting machinability improvement in two-dimensional ultrasonic-assisted micro-end-milling on hardened tool steel. By varying the vibration parameters, such as amplitude and the frequency of ultrasonic assistance, experiments were conducted for both conventional and ultrasonic-assisted milling to examine their effects on surface roughness and cutting-tool wear under process parameter conditions. The results showed that cutting-tool wear in ultrasonic-assisted milling was reduced by approximately 5 to 20%. As the amplitude and frequency of the ultrasonic-assisted system increased, both cutting-tool wear and surface roughness decreased. Compared to conventional milling, this two-dimensional ultrasonic assistance effectively enhanced the overall machining performance. Gao et al. [7] performed the dry milling of Ti-6Al-4V with the assistance of longitudinal ultrasonic vibration to enhance machinability and surface quality. By varying the ultrasonic amplitude, an investigation was made with respect to cutting forces, cutting temperature, surface topography, and 3D surface roughness. The results showed that the average cutting forces along the feed and longitudinal direction, the maximum and average cutting temperature and the mean values of 3D surface roughness, Sa and Sq, all exhibited reductions from a specific percentage to a larger extent, respectively, as the ultrasonic amplitude increased from 0 to 6 μm. These are attributed to the increased amplitude, which increased the separation distance between the cutting-tool and the workpiece, with friction constraint and contact time between them being thus reduced.

A literature review on laser-assisted milling examines the effect of thermal preheating on cutting performance. Kumar and Melkote [8] compared the advantages of laser-assisted micro milling on process responses, such as material removal rates, cutting-tool wear, cutting force, and surface finish. They utilized TiAlN-coated tungsten carbide end mills to perform micro slot milling experiments on A2 tool steel (62 HRC), with and without laser assistance, under a proper micro milling condition. The results showed an average reduction in cutting force of up to 69% with laser assistance. They also indicated that cutting-tool wear is significantly less with laser assistance, even when the material removal rates are increased by six times higher than the cutting conditions recommended by the tool manufacturer. Through the proper selection of cutting-tool diameter relative to laser spot size to handle the proper laser thermal preheating, better surface roughness and reduced cutting-tool wear can be obtained due to reduced burr height formation. Brecher et al. [9] studied the impact of laser-assisted milling on advanced materials' cutting forces and tool flank wear without cooling lubricants. They proposed an innovative laser-assisted equipment that guides the laser beam through an HSK tool interface, directing irradiation onto the cutting surface of the workpiece in the machining area. The milling experiments were conducted on Inconel 718, using cemented carbide end mills with TiAlN coatings on

a 5-axis machining center. The results showed that the cutting forces along F_x, F_y, and F_z directions were reduced by 40%, 60%, and 60%, respectively, for the local plastification of workpiece material in laser assistance. Laser assistance may effectively reduce the cutting forces and flank wear with optimized laser parameters. Woo and Lee [10] studied the machining characteristics of laser-assisted milling on cylindrical shape workpieces, focusing on AISI 1045 and Inconel 718. They proposed a method for three-dimensional laser-assisted milling suitable for cylindrical workpieces and investigated its effects on surface roughness and cutting forces. Firstly, finite element analysis was conducted for both materials to determine the proper preheating temperature and effective cutting depth. Subsequently, milling experiments were performed, comparing them with conventional milling to observe variations in surface roughness and cutting forces. The results showed that finite element analysis for thermal analysis was effective in similar machining processes. Compared to conventional methods, laser-assisted milling significantly reduced cutting forces and surface roughness by some specific extent for AISI 1045 and Inconel 718. Additionally, as the milling position angle increased, both cutting forces and surface roughness increased. It was suggested to rotate the workpiece clockwise to decrease the angle or utilize tool edge machining to improve surface roughness and tool life. For AISI 1045, cutting forces decreased and surface roughness improved with three-dimensional laser assistance, while for Inconel 718, down milling demonstrated better results.

In their related literature review on high-speed milling, Wang et al. [11] utilized the split Hopkinson pressure bar technique to obtain stress-strain curves under high temperature and high strain-rate conditions. They also considered the negative strain rate and temperature effects of the material to modify the traditional empirical Johnson–Cook constitutive equation for SKD11 hardened steel. Based on the modified Johnson–Cook constitutive equation, they proposed a two-dimensional plane-strain finite-element model, coupled with thermal and mechanical loads for high-speed milling of SKD11. The FE model aims to simulate the geometric characteristics of chip formations during the high-speed milling processes and conduct the stress-and-strain quantitative analyses in the shear band. The cutting forces, cutting temperatures, and cutting performance of coated tools are also analyzed in the model. The results indicated that a critical value of cutting speed exists within a specific range. At this speed, stress and strain values increase, causing changes in stress and strain distributions in the shear band. This leads to the formation of a sawtooth chip. As the cutting speed continued to increase, the stress, strain, and temperature values in the shear band also increased, while the distribution in chip region remained unchanged, resulting in a more pronounced sawtooth chip pattern. The cutting forces decreased as the cutting speed increased, with temperature exerting a significant influence on cutting forces. The greater the temperature difference, the faster the decrease in cutting forces. Wang et al. [12] used TiAlN- and TiSiN-coated carbide tools for the high-speed milling of hardened steel to determine the wear and breakage mechanisms of the cutting-tool. The effects of the tool angle, diameter, extended length, cutting forces, and cutting-induced vibrations on tool conditions were also investigated. The results showed that the primary patterns of tool wear observed included flank wear, rake face wear, breakage, and micro-chipping. The breakage modes were coating peeling, chipping, and tip breakage. Increasing the tool extended length led to increased cutting forces and tool wear, thereby decreasing surface quality. The abnormal states that occurred after tool wear could be detected through the signals of cutting forces and cutting-induced vibrations. The TiSiN-coated tools had a significantly longer tool life compared to the TiAlN-coated tools. Furthermore, experiments revealed that using cutting tools with a smaller rake angle, a smaller right clearance angle, and a large helix angle effectively reduced cutting forces, extended tool life, and facilitated smoother cutting processes. Gong et al. [13] conducted milling experiments on H13 steel and SKD11 hardened steel by using coated carbide tools to investigate the tool wear and breakage mechanisms. The results indicated that the hardness of the workpiece had a dominant effect on tool failure patterns. In milling H13 steel, the tool failure pattern is flank wear, while in milling SKD11 hardened steel, tools

were prone to breakage of the rake face due to the initiation and propagation of cracks. Furthermore, the geometry model of tool wear and breakage was established to explore the variations in cutting-tool angles resulting from the tool's wear or breakage mechanisms. Flank wear in H13 reduced the working clearance angle, while the breakage of the rake face in SKD11 reduced the working rake angle. Additionally, the effects of tool wear and breakage on cutting forces and chip formation were analyzed. In milling H13 steel, flank wear increased the friction coefficient between the tool and the workpiece, leading to increased cutting forces and the formation of wave-shaped chips. In contrast, in milling SKD11 hardened steel, the breakage of the rake face increases chip deformation and reduces the sharpness of the cutting edge, resulting in the curling and separation of sawtooth chips. Pu and Singh [14] conducted high-speed ball nose end milling experiments on AISI A2 tool steel using PCBN and coated tungsten carbide tools on a 5-axis machining center, with variations in milling length and cutting speed to assess changes in the tool wear mechanism and surface roughness. The results revealed that coated carbide tools performed poorly within the high-speed machining range, while high-CBN-content PCBN tools are relatively suitable for this hardened steel. Under normal cutting speeds, the surface roughness of coated carbide tools was twice that of the PCBN tools. In addition, it led to work hardening on the workpiece, increased hardness, material drag, surface cracks, and microstructural changes. The failure mode of PCBN tools is flaking and edge chipping due to the fact that toughness is insufficient for application when the cutting edge is worn out. Moreover, low-CBN-content PCBN tools lack of the required toughness and abrasion resistance for the application. Gong et al. [15] conducted high-speed face milling of the hardened steel SKD11 to investigate the failure patterns and failure mechanism of a double-layer-coated cemented carbide tool. Additionally, the effects of cutting-tool damage on cutting forces, surface roughness, and tool failure surface morphology were also studied. The results showed that the dominating failure pattern of the coated tool in this study was fatigue fracture, accompanied by chipping. At low cutting speeds, many fatigue cracks were observed on the rake face, while fatigue striations and river patterns were observed at the fatigue crack propagation zone with the increase in cutting speed. In addition, fatigue steps and secondary cracks were found on the fatigue propagation area under higher cutting speeds. The main fracture modes were intergranular and transgranular fractures at lower and higher cutting speeds, respectively. The cutting force had a large influence on tool life in the initial tool wear stage. However, when the tool breakage and coating peeling occurred, the cutting temperature was the dominating factor for tool life. With increased flank wear and cutting forces, the values of machined surface roughness constantly increased.

With regard to the literature review on machine learning, Twardowski et al. [16] applied two different forms of machine learning classification trees to conduct a study, utilizing vibration acceleration measurements as the physical parameters, to predict the possibility of tool wear during the milling process of EN-GJL-250 cast iron. The experiments were carried out using a four-edge cemented-carbide end mill cutter, with vibration acceleration serving as the input data for the models to forecast tool wear. The study obtained the vibration acceleration results during the experiments and utilized machine learning techniques, particularly decision trees, to classify tool wear conditions. The experimental results showed that, compared to regression models, machine learning methods exhibited significantly smaller errors in predicting tool wear than those reached by the regression model. Niu et al. [17] used different machine tools conducting two milling-tool life tests to collect cutting performance data, such as cutting force, vibration, and cutting sound to construct a tool-wear monitoring model of titanium alloy milling. In the experiments, the above-mentioned raw signals were captured by multiple sensors and features were extracted on time, frequency, and time-frequency domains. Then, feature dimensionality reduction was achieved using an information measurement-based feature selection method, introducing symmetrical uncertainty to select relevant features. Finally, a multiclass support vector machine model was developed to identify the wear stages of the tool. The results demonstrated that the classifier using multiple sensors achieved an overall identifi-

cation accuracy of 96.7%, while the classifiers based on single-force sensors and vibration sensors exhibited performances of 96.7% and 92.5%, respectively. Mahmood et al. [18] conducted a study on the prediction of tool wear in various machining processes using machine learning. They performed different machining experiments such as milling, drilling, and turning for IN718 material, and each machining process employed six tools in different states of wear. Initially, experimental data on cutting force from three machining processes were utilized to extract 15 features. Subsequently, singular spectrum analysis and principal component analysis were employed for feature selection and dimensionality reduction, respectively. The severity of tool wear was categorized into five levels, and a prediction was performed using LightGBM and an ensemble model combining six algorithms: LR, RF, CART, NB, SVM, and KNN. The results demonstrated the outstanding performance of the LightGBM model in terms of speed and efficiency, effectively handling huge datasets. Additionally, the model overcame some of the deficiencies present in previous tool wear models, such as high dimensionality and overfitting. This improvement is attributed to the application of dropout and early stopping techniques. Zhou et al. [19] proposed a milling tool wear prediction method for multi-condition classification and rapid selection of prediction models based on linear discriminant analysis (LDA) and the ensemble method. First, the whole wear process of the cutting tool is divided into five stages. Next, the time domain, frequency domain, and wavelet packet of the raw data are extracted, and the RF and XGBoost algorithms are used for multi-algorithm feature screening. The LDA algorithm is used to fuse and downscale the screened features, which are then combined with the K-means clustering algorithm to group similar working conditions. The samples are expanded and balanced using the SMOTE algorithm. Then, separate regression and classification prediction models are created for each group of working conditions. These models are integrated with an algorithm to determine the optimal prediction model for each group of working conditions. Compared with the traditional transfer learning algorithms, the proposed method allows for the rapid selection of a prediction model, which is achieved by dividing new conditions into groups with reduced dimensionality. The test results demonstrate the method's effectiveness in addressing the challenges of selecting prediction models and reducing the number of model transfers. Kilundu et al. [20] explored the use of data mining techniques for monitoring the tool condition in metal cutting. The study focused on the analysis of vibration signals, particularly employing the pseudo-local singular spectrum analysis (SSA) method. The methodology includes the integration of SSA and band-pass filtering to process vibration signals, aiming to eliminate irrelevant noise components. A major advantage of this approach is its ability to extract relevant information from high-frequency vibration components. Additionally, the study explores the use of the SSA method to define features that are highly sensitive to tool wear, enabling the monitoring of tool condition. The results demonstrate that this method exhibits a high recognition rate in identifying tool wear conditions. However, its recognition rate is lower for dysfunctions in the cutting process, such as chip jamming and unproductive passes. This highlights the potential application of data mining techniques in tool condition monitoring. Huang et al. [21] proposed an indirect tool-wear measurement method based on multi-information fusion by hybrid machine-learning techniques, to increase the utilization efficiency of multi-sensor signals and improve the measurement accuracy of tool wear. Triaxial cutting forces and vibration signals are collected and then preprocessed by wavelet packet denoising. The time, frequency, and time-frequency domain features are extracted to reduce information redundancy, and the kernel principal component analysis is applied to fuse the most sensitive characteristics. A fusion model combining least squares support vector regression and particle swarm optimization algorithms is established to learn the dependency relationship between the fused features and tool flank wear. They conducted milling experiments under multiple working conditions to validate the effectiveness of the proposed method. The experimental results show that the overall performance of the proposed method is superior to that of other comparison methods.

Cutting forces play a crucial role in the machining process, providing vital information about the cutting tool's condition, being widely applied in various aspects of manufacturing. Firstly, by monitoring the changes in cutting force, effective cutting-tool wear monitoring can be achieved. As the cutting tool wears down, the magnitude and trends in the cutting force undergo fluctuations, and feature extraction of the cutting force can be used for analyzing the cutting tool's condition. Secondly, vibration analysis of cutting forces can be utilized to assess the stability of a machine tool, thereby detecting the presence of vibrations or resonances. Additionally, abnormal variations in cutting forces may indicate collisions between the tool and the workpiece or fixture, facilitating collision detection to ensure production stability and prevent damage. Cutting force data can also be employed for optimizing cutting parameters by establishing cutting force models to enhance processing efficiency and quality.

Machine learning and ensemble learning techniques have demonstrated excellent performance in constructing cutting-tool wear prediction models. Machine learning can automatically learn and extract complex features, enhancing the model's generalization capability. Ensemble learning, combining predictions from multiple models, effectively overcomes the limitations of individual models, thereby improving the overall predictive performance. Through these technologies, it can more accurately predict the trends in cutting-tool wear variations, achieving precise control over the cutting processes. Cutting force is a complex nonlinear function influenced by various factors, such as material properties, cutting-tool geometry, and cutting conditions. Utilizing cutting force as input parameters for prediction models comprehensively reflects the characteristics and variations of the cutting processes. By establishing cutting-tool wear models, the production line can promptly initiate cutting-tool replacement, thereby reducing downtime and production costs.

This study aims to identify the better assisted milling technology and optimal process parameter combinations for SKD11 hardened steel to enhance cutting performance and machining quality. Based on these foundations, a cutting-tool wear prediction model through machine learning is further developed to improve the production efficiency and cost reductions. The model can predict cutting-tool wear in real-time, reducing the replacement times of premature tool disposal, enhancing the rate of high-quality products, minimizing the degradation of cutting quality due to excessive tool wear, and further enabling intelligent automatic cutting-tool changing. The goal is to achieve automated and intelligent manufacturing that maintains both product quality and high efficiency in the production of hardened steels.

2. Theoretical Foundation

2.1. Cutting-Tool Wear

The cutting-tool wear processes may be divided into three stages: (1) initial wear; the cutting edge is relatively rough in this stage, and the contact area among the cutting tool, workpiece, and chips is small. The cutting forces are concentrated at the cutting edge, leading to a relatively rapid cutting-tool wear in this stage. (2) Normal wear; after the initial wear occurred in the first stage, the cutting edge gradually becomes smoother, and the contact area among the cutting tool, workpiece, and chips increases. As a result, cutting forces are not concentrated at the cutting edge, leading to a slower wear rate. The cutting tool enters a phase of normal wear during this stage. (3) Severe wear; when wear progresses to a certain extent, the machined surface becomes rough, and the friction between the cutting edge and the workpiece increases. The rise in cutting forces and temperatures leads to an accelerated wear rate. At this point, the cutting edge loses its ability to remove the workpiece material effectively. The relationship between cutting-tool wear and machining time for these three stages is depicted in Figure 1.

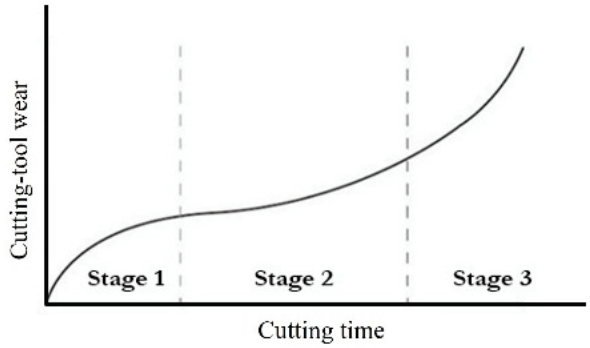


Figure 1. Cutting-tool wear processes.

2.2. Machine Learning

Machine learning is a critical branch of artificial intelligence that has seen extensive application in recent years, including our daily lives. In recent times, machine learning has also gained considerable attention and application in the industrial sector. According to retrospective studies [22], it can be used for equipment anomaly detection, equipment monitoring, early prevention of equipment failures, reducing downtime, lowering maintenance costs, and improving production efficiency, all of which hold significant importance. The core objective of machine learning is to address complex problems, build models capable of learning from large volumes of data, and discover patterns within the data. It can be broadly categorized into four main types: (1) supervised learning; supervised learning primarily involves training models using labeled training data. The model learns the underlying relationship between inputs and outputs, enabling it to predict the desired output from input data. (2) Unsupervised learning; in contrast to supervised learning, unsupervised learning does not require labeled training data. It classifies and clusters data based on relationships or similarities among data points. (3) Reinforcement learning; reinforcement learning allows models to learn through interaction with their environment. Models adjust their behavior based on rewards or penalties received for their actions. This type of learning is suitable for scenarios where models need to learn through trial and error, closely resembling human learning. (4) Semi-supervised learning; semi-supervised learning is a combination of supervised and unsupervised learning. It involves training on both labeled and unlabeled data to improve prediction accuracy.

Different machine learning methods have their strengths, weaknesses, and suitable application scenarios. The choice of which method to use should be based on the task objectives and context assessment.

2.3. Ensemble Learning

In the application of machine learning, the ideal scenario involves training a single model that learns the patterns or underlying rules within the provided data and makes accurate predictions for the task at hand. However, in reality, this is often not the case. The complexity of data, imbalanced data distributions, and the presence of significant noise, among other factors, make it challenging for a single model to achieve ideal predictive outcomes. As per the research presented by Sarker [23], these challenges can limit the performance of a single model.

Ensemble learning is a machine learning strategy that combines predictions from multiple machine learning models to improve overall predictive accuracy. According to a review study [24], ensemble learning can enhance generalization capability by training multiple models and combining their predictions. It has found wide application across various domains. The following are some common ensemble methods, including bagging, boosting, stacking, and voting. (1) Bagging is based on random sampling from the raw data to create multiple different training datasets. Several models are then trained on these datasets, and the predictions from each model are averaged or voted on to enhance model performance. Random sampling is achieved through the bootstrap method, where

subsets are randomly selected, with replacement, from the raw data. For classification problems, the final output is determined by voting according to the predictions of each model. For regression tasks, the final output is the average of the predictions from the models. (2) Boosting is an iterative ensemble learning method. It relies on adjusting sample weights and iteratively optimizing the model. Each round of learning depends on the previous round's results. Errors in predictions are given higher weights to improve performance in the subsequent round. Each model learns from and corrects errors in the previous model, resulting in improved predictive accuracy. (3) Stacking aims to combine the strengths of multiple base models. This approach first trains multiple different base models, and the final output is derived from a meta-learner that is trained on the predictions of the base models and their correspondence with the true values. This method leverages the power of multiple models to enhance overall predictive accuracy. (4) Voting combines predictions from multiple models. For classification tasks, each model makes predictions, and the final output is determined by majority voting. In regression problems, the final prediction is the average of the base models' predictions. Voting can be effective when the base models have different strengths and weaknesses, allowing them to complement each other.

Ensemble learning is widely applied and studied in the field of machine learning. It leverages the combination of different machine learning models to enhance predictive capabilities and achieve more accurate results.

3. Approach Methods and Procedures

The side milling experiments of SKD11 alloy tool steel conducted in this study may be divided into two phases. The 1st phase tries to explore a better ultrasonic-assisted method for further application in the 2nd phase. Locally, laser preheating assistance is additionally incorporated with better ultrasonic-assistance to constitute hybrid-assisted milling, in which process parameter combinations are planned based on Taguchi orthogonal arrays. In addition, the optimal process parameter can be determined by the Taguchi method. This study aims to investigate and analyze the influence of milling process parameters and different assisted machining methods on surface roughness, surface morphology, and cutting tool wear. Finally, experiments were repeatedly conducted by using the optimal cutting parameter combination and a hybrid-assisted system to collect the data of cutting force and cutting-tool wear. Based on these data, a cutting-tool wear prediction model is constructed through the ensemble learning method. The entire procedure executed in this study is illustrated in Figure 2.

3.1. Milling Experimental Setup

This study aims to explore various assistance methods and process parameters for SKD11 milling. The investigation is divided into two phases. In the first phase of the milling experiment, the focus is on the analysis of cutting performance with no assistance, rotary ultrasonic assistance, dual-axis ultrasonic assistance, and a combination of rotary and dual-axis ultrasonic assistance (triple-axis ultrasonic). In the second phase, based on the results of the first phase analysis, a better assistance method is selected for the second phase of the milling experiment. The milling parameters are planned by using an L9 orthogonal array. During the experiment processes, observations and measurements are made for surface roughness, cutting forces, surface morphology, and cutting-tool wear. A series of result analyses and discussions are conducted.

The first phase of the experiment aims to explore the effects of different ultrasonic-assisted methods, namely rotary, dual-axis, and triple-axis, on milling performance. In this phase, two sets of process parameters are planned, as shown in Table 1. These two sets of process parameters, with or without assisted methods, respectively, are all conducted in the experiment, and a total of 8 experiments are executed in this phase. Two factors with individually extreme levels were designated in this phase.

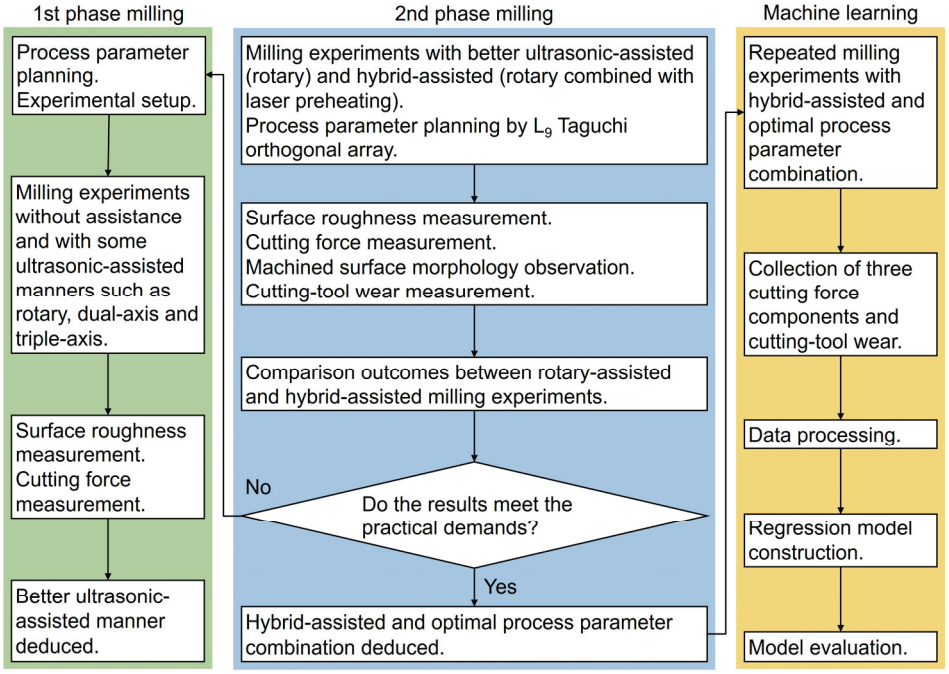


Figure 2. Entire list of procedures executed in this study.

Table 1. Process parameter planning for milling experiment of SKD11 in 1st phase.

Set	Spindle Speed, n (rpm)	Radial Depth of Cut, a_e (mm)	Feed Rate, F (mm/min)	Axial Depth of Cut, a_p (mm)
1	8000	0.1	1000	10
2	8000	0.3	1500	10

The superior ultrasonic-assisted method obtained from the first phase is adopted in the second phase both in conjunction with and without locally laser preheating assistance, respectively. The process parameter planning for the milling experiment of SKD11 is shown in Table 2. Three factors were considered, and each factor had three levels in the 2nd phase. The Taguchi orthogonal array was applied to design milling process parameter combinations, resulting in a total of 18 experiments, as shown in Table 3. Surface roughness and cutting-tool life serve as the objective function and constraint, respectively, and the optimal combination of process parameters was thus determined by the characteristics of smaller-the-better in the Taguchi method. Based on the optimal milling process parameters obtained and the superior hybrid-assisted method adopted, milling experiments were repeatedly performed to collect the data on cutting force and cutting-tool wear.

Table 2. Process parameter planning for milling experiment of SKD11 in the 2nd phase.

Milling Cutter Diameter, d (mm)	Φ6
Axial depth of cut, a_p (mm)	10
Spindle speed, n (rpm)	8000, 9000, 10,000
Radial depth of cut, a_e (mm)	0.1, 0.3, 0.5
Feed rate F, (mm/min)	1000, 1500, 2000

Based on the results from the second phase of the milling experiments, the optimal process parameters were determined to be a spindle speed of 10,000 rpm, a feed rate of 1000 mm/min, and a radial depth-of-cut of 0.1 mm, along with a hybrid-assisted method of rotary ultrasonic combined with local laser preheating. The experiments for data collection were conducted with these process parameters and assisted configurations.

Figures 3 and 4 show the milling experimental setup and a photo depicting equipment configurations. In this setup, rotary ultrasonic-assisted milling is controlled by adjusting the voltage levels through an ultrasonic driver, and the ultrasonic cutting-tool holder is driven by a non-contact power transmitter. The resonant effect was used to achieve the z-axis reciprocal oscillations at a high-frequency of 20 to 40 kHz. Laser assistance involves localized preheating of the workpiece surface by a laser spot through a laser tube. Data collection was performed using a dynamometer to capture cutting force signals along the x, y, and z directions. Through a charge amplifier, the cutting force signals were amplified and converted into voltage signals. Signal acquisition cards were used to capture the three cutting force components during machining processes at a sampling rate of 50 kHz, as shown in Figure 5a. Each data set of the cutting force signal consists of three portions for each force component during milling processes, i.e., before engagement, engagement, and after engagement. After each machining operation was completed, the cutting tool was photographed using a tool microscope, and its flank wear was observed and measured, as shown in Figure 5b. A total of 90 sets of cutting force signals and cutting-tool wear were collected for use in building subsequent regression models.

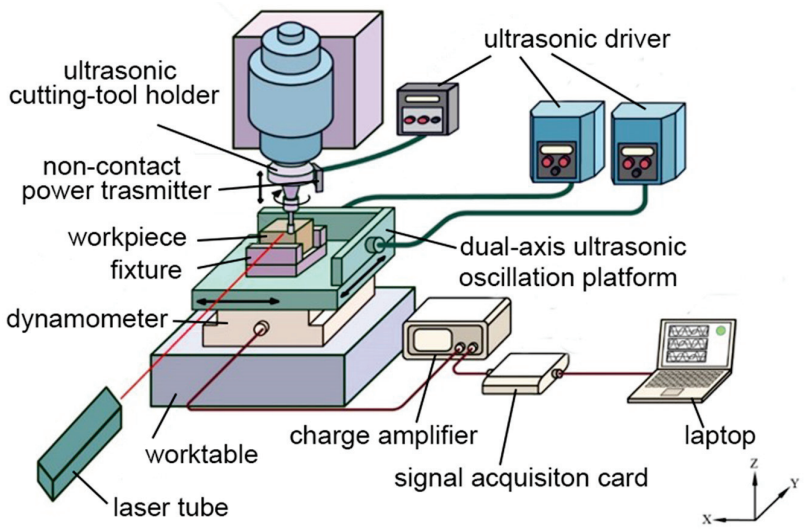


Figure 3. Milling experimental setup.

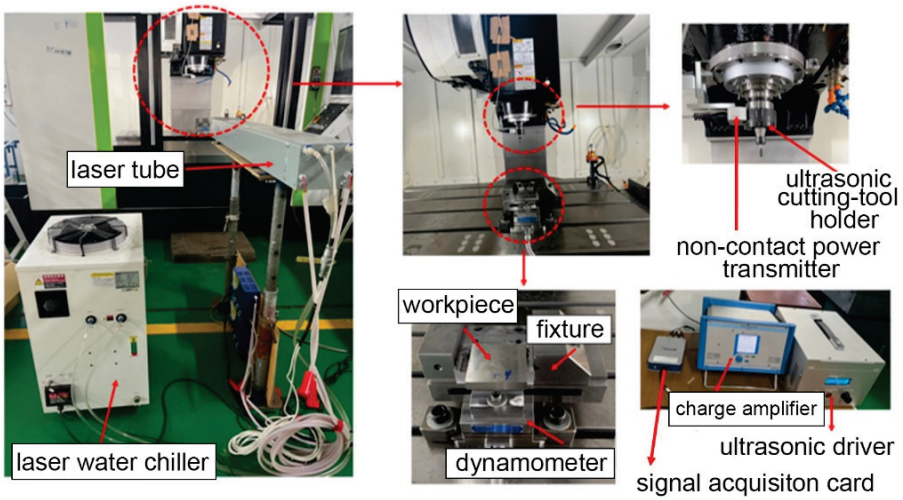
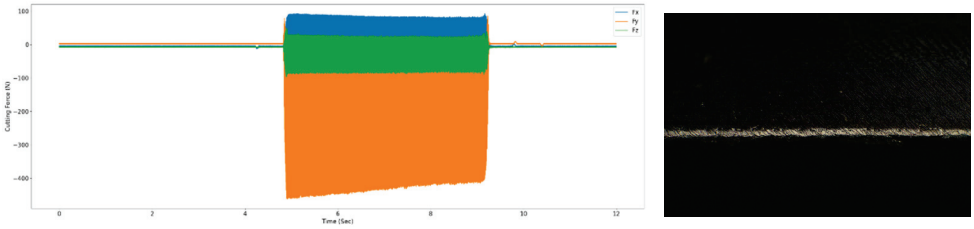


Figure 4. Photograph for experimental equipment configurations.



(**a**) (**b**)

Figure 5. Three cutting force components and cutting-tool wear. (**a**) Three cutting force component signals. (**b**) Cutting-tool wear.

Table 3. Process parameter combinations by L9 orthogonal array in the 2nd phase.

Sets \ Process Parameter	Spindle Speed Level	Radial Depth of Cut Level	Feed Rate Level
1	1	1	1
2	1	2	2
3	1	3	3
4	2	1	2
5	2	2	3
6	2	3	1
7	3	1	3
8	3	2	1
9	3	3	2

3.2. Machine Learning Architecture

This study, based on predicting cutting-tool wear using a better assisted milling method and milling process parameter combinations, consists of the following processes. First, the data collected in the milling experiments in Section 3.1 undergo data processing, including data cleaning, feature extraction, data splitting, data standardization, and feature selection. The purpose of these procedures is to prepare the proper data for constructing a variety of machine learning models. Second, the dataset is randomly split into an 80% training set and a 20% test set. Various machine learning models are constructed using the training set, with hyperparameter optimization and model evaluation conducted through grid search and cross-validation to optimize the basic models. Finally, an ensemble regression model is constructed, and it is evaluated using the test set data. The framework is illustrated in Figure 6.

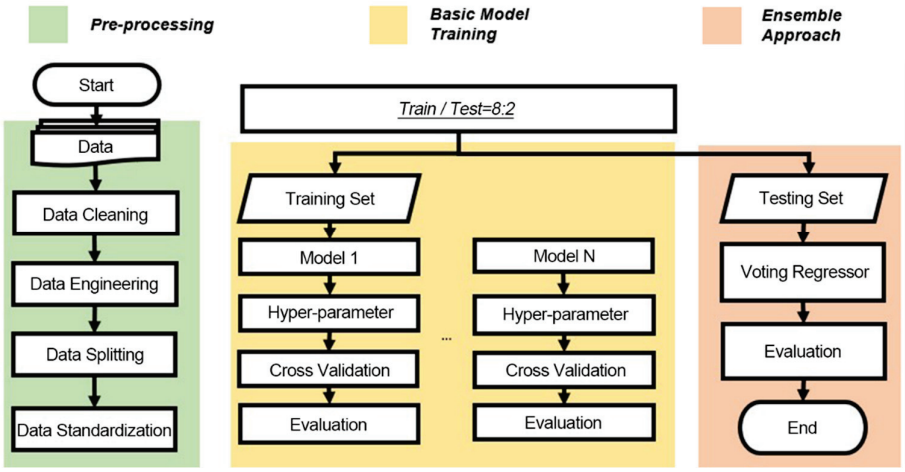


Figure 6. An architecture for machine learning processes.

3.3. Data Processing

In the experiments, x, y, and z-axis cutting force signals were sampled, as shown in Figure 7. The raw cutting force signals include three portions, i.e., before cutting-tool engagement, the milling process, and after cutting-tool engagement. The signals before and after the cutting-tool engagement portions, highlighted by the red dashed boxes, are removed, while only the stable cutting force signals during the milling process, as indicated by the green dashed box, are reserved for use.

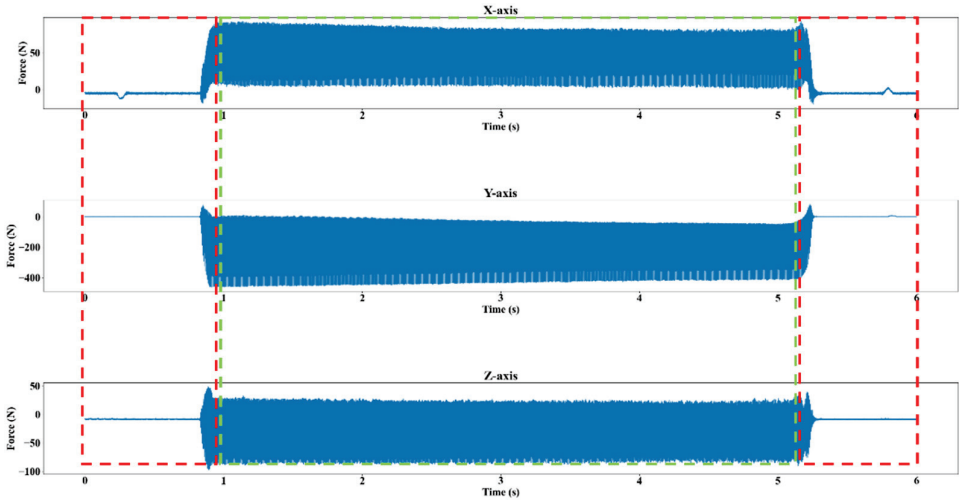


Figure 7. Three cutting force component signals sampled from experiments.

In a study investigating the relationship between cutting forces and cutting-tool wear [25], it was found that by performing a Fourier transform on the cutting force signals, changes in the amplitudes of rotational speed frequency, tooth passing frequency, and their harmonics were observed due to cutting-tool wear. Following this research, this study applied a Fourier transform to the cleaned cutting force signals to analyze them in the frequency domain, as shown in Figure 8. From the graph, it can be observed that the dominant frequencies are low-frequency signals, with a frequency of 166 Hz, associated with a spindle speed of 10,000 rpm and a frequency of 664 Hz, associated with the 4-flute end mill. The other frequencies are harmonics of spindle speed or tooth passing frequencies. Since the cutting force signals are predominantly low-frequency signals, a low-pass filter was applied to complete the data cleaning process.

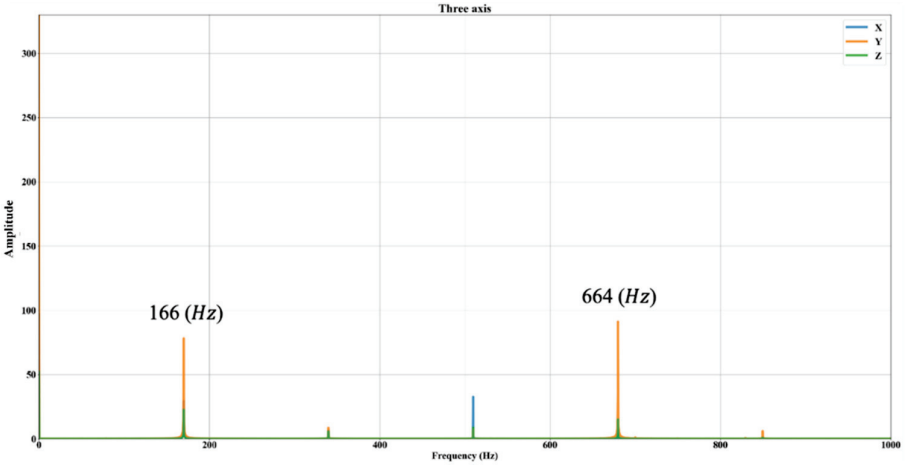


Figure 8. Three cutting force components exhibited in frequency domain.

The cutting force signals contain various environmental noises and, therefore, it is essential to extract significant features that reflect cutting-tool wear during the cutting

processes. As cutting-tool wear progresses, it affects the geometrical shape of the cutting edges of the end mill, which, in turn, impacts the contact area between the cutting-tool and the workpiece, resulting in increased cutting forces. Therefore, analyzing variations in cutting forces in the time domain can provide valuable insights into cutting-tool wear [26]. Moreover, variations in cutting forces also lead to variations in the frequency domain. Extracting features on frequency domain can also be used to assess the cutting-tool wear conditions [27]. Therefore, extracting features from different domains in the raw signals can effectively increase the relevance to cutting-tool wear [28,29]. In this study, feature extraction was performed on the cleaned cutting force signals, with their expressions, as indicated in Table 4. The sampling frequency for the cutting forces in this study was set at 50 kHz. Thus, each cleaned cutting force signal for one component contains approximately 200,000 data points. The relevant details are stated as follows:

1. For the x, y, and z axes, 9 features in the time domain and 4 features in the frequency domain were extracted from the cutting force signals.
2. For the x, y, and z axes, the cutting force signals were divided into 10 windows, with each window containing around 20,000 data points, as shown in Figure 9. Nine features in the time domain were then extracted for each window.
3. For the x, y, and z axes, the cutting force signals were transformed into the frequency domain using a Fourier transform. The frequencies of spindle speed at 10,000 rpm and 4-flute tooth passing in the experiments were approximately 166 Hz and 644 Hz, respectively. Therefore, these frequencies within ± 5 Hz were extracted, and their amplitudes were used as features.

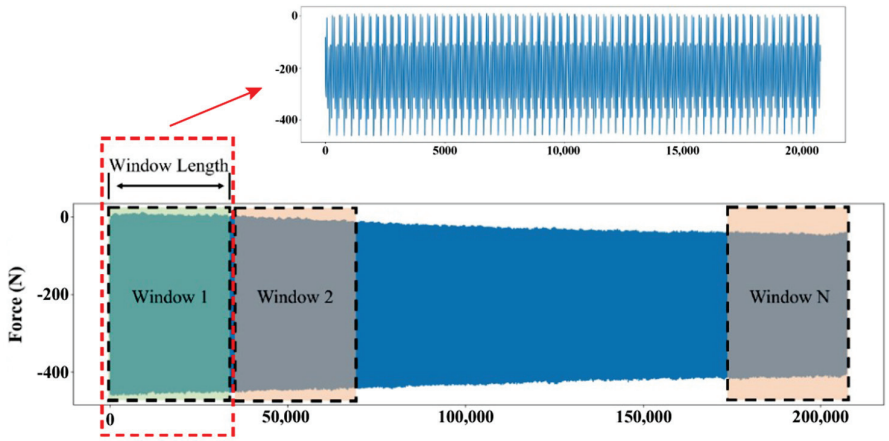


Figure 9. Segmentation on y-component cutting force signal.

After completing the data feature extraction, the dataset is randomly split into a training set and a test set, with an 80% and 20% ratio, respectively. Subsequently, data standardization is performed. Features from different domains may have varying scales or range differences. Standardizing the data ensures that all feature magnitudes are within the same range, facilitating better model training and evaluation. This reduces biases and errors introduced by differences in feature magnitudes, allowing the model to learn more about trends between numerical values.

In this study, Z-score normalization is utilized for data standardization. The Z-score is calculated using the formula shown in Equation (1), where the variables are defined as follows: z represents the standardized value, x denotes the raw data points after feature extractions, μ corresponds to the mean of the dataset, and σ is the standard deviation of the dataset. After this processing, the mean of the standardized dataset is 0, and the standard deviation is 1.

$$z = \frac{x - \mu}{\sigma} \tag{1}$$

After standardizing the training and test data, feature selection is subsequently performed. Feature extraction is based on the three cutting force component signals after data cleaning, and it involves three main aspects:

1. For the cleaned cutting force signals, 9 time-domain features and 4 frequency-domain features were extracted.
2. Each cutting force component signal is segmented into 10 windows, and 9 time-domain features are extracted in each window.
3. The cleaned cutting force signals are transformed into frequency-domain, and the amplitudes correspond to spindle speed and tooth passing frequencies, and their harmonics are extracted.

After feature engineering, the extraction of features related to cutting-tool wear results in a relatively large number of features. Therefore, feature selection is conducted in order to find an optimal subset of features. Feature selection is a crucial step in machine learning, as an excessive number of features can lead to overfitting, causing a decline in prediction model performance. Through feature selection, irrelevant or redundant features can be eliminated, and those that contribute to predicting the target variable are retained. Reducing the number of features can also lower the computational cost of model training and prediction. In this study, the method employed for feature selection is based on the feature importance in random forests.

Table 4. Expressions for extracted features.

Domain	Feature	Expression
Time domain	Absolute maximum value	$x_{max} = MAX\|x_i\|$
	Mean	$\overline{x} = \frac{1}{N}\sum_{i=1}^{N} x_i$
	Variance	$x_{\text{var}} = \frac{1}{N}\sum_{i=1}^{N} (x_i - \overline{x})^2$
	Skewness	$x_{skew} = \frac{1}{N-1}\frac{\sum_{i=1}^{N} (x_i - \overline{x})^3}{x_{std}^3}$
	Kurtosis	$x_{kurt} = \frac{1}{N-1}\frac{\sum_{i=1}^{N} (x_i - \overline{x})^4}{x_{std}^4}$
	Peak-to-peak	$x_{p-p1} = x_{max} - x_{\min}$
	Peak factor	$C = \frac{x_{p-p1}}{x_{rms}}$
	Pulse factor	$S_m = \frac{x_{p-p1}}{\frac{1}{N}\sum_{i=1}^{N} \|x_i\|}$
	Waveform factor	$S_b = \frac{x_{rms}}{\frac{1}{N}\sum_{i=1}^{N} \|x_i\|}$
Frequency domain	Average amplitude value	$S_1 = \frac{1}{N}\sum_{i=1}^{N} p_i$
	Center of gravity frequency	$f_c = \frac{\sum_{i=1}^{N} f_i p_i}{\sum_{i=1}^{N} p_i}$
	Mean square frequency	$ms_f = \frac{\sum_{i=1}^{N} f_i^2 p_i}{\sum_{i=1}^{N} p_i}$
	Frequency variance	$v_f = \frac{\sum_{i=1}^{N} (f_i - f_c)^2 p_i}{\sum_{i=1}^{N} p_i}$

4. Results and Discussion

The side milling experiments on SKD11 were conducted in two phases to determine a better assisted method and optimal process parameters. In the first phase, eight experiments were carried out under two sets of process parameters both without assistance and with several ultrasonic-assisted methods, such as rotary, dual-axis, and triple-axis. This was undertaken to explore and identify the most effective assisted system. In the second phase, a superior ultrasonic-assisted method was further combined with or without assistance from local laser preheating to conduct L9 orthogonal array milling experiments, totaling

18 experiments. Thus, the effects of spindle speed, feed rate, and radial depth of cut, along with hybrid-assisted and rotary-assisted methods on surface roughness, cutting force, and machined surface morphology of SKD11 were investigated.

4.1. Surface Roughness

Due to the high hardness and toughness of the SKD11 tool steel, various issues may arise during the machining process. Different assisted methods and machining parameters are crucial factors affecting machining performance. Table 1 shows the planning of process parameters in the first phase of the experiment, while Figure 10 shows the relationship between surface roughness and process parameter combination in this phase without assistance and with different ultrasonic-assisted methods. Here, the surface roughness parameter measured is Ra, and its measurement device is a contact-type surface roughness-measuring instrument (Mitutoyo SJ-410). The experimental results indicate that a small depth of cut and a slow feed rate result in better surface roughness than a large depth of cut and a fast feed rate, both without assistance and with different ultrasonic-assisted methods. Among them, the rotary ultrasonic-assisted method proves superior to both the absence of assistance and the other ultrasonic-assisted methods. However, the absence of assistance yields better performance than both dual-axis and triple-axis ultrasonic assistance. It is speculated that dual-axis and triple-axis ultrasonic assistance, which involve radial vibration, are less effective in removing material due to the high toughness property of the workpiece material. This deduction suggests poorer performance. Compared to no assistance, rotary ultrasonic assistance can reduce surface roughness by approximately 5%. Therefore, the effects of both no assistance and different ultrasonic-assisted methods on the surface roughness of SKD11 milling are investigated, and the best assisted method is ascertained. This superior ultrasonic-assisted method, rotary, will be applied in the second phase milling experiments.

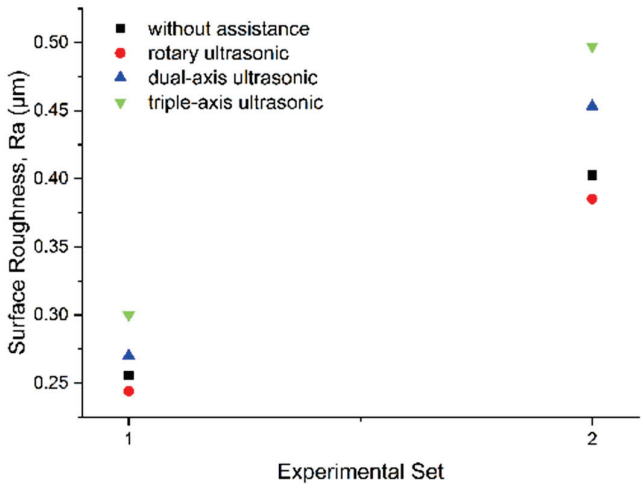


Figure 10. The relationship between surface roughness and process parameter combinations in the 1st phase experiment without assistance and with different ultrasonic-assisted methods.

The superior ultrasonic-assisted method obtained from the first phase is adopted in the second phase in conjunction with and without laser locally preheating assistance, hybrid-assisted, and rotary ultrasonic-assisted, respectively, in which the process parameter planning for the milling experiment on SKD11 is shown in Table 2. An ANOVA (analysis of variance) is performed on the sampling data to examine the influence and contribution of various factors to surface roughness. The contribution rates are shown in Tables 5 and 6, and the corresponding factor responses are illustrated in Figure 11a,b, respectively. It can be observed that under both of these assisted methods, the most significant factor affecting the surface roughness of SKD11 milling is the feed rate, followed by radial depth of cut, and lastly spindle speed. The experimental process parameter design for milling experiments

through L9 orthogonal arrays is presented in Table 2, and the corresponding experimental sets are shown in Table 3. Comparing surface roughness between hybrid-assisted and rotary ultrasonic-assisted methods for process parameter combinations in the L9 orthogonal array, as shown in Figure 12, it is evident that the hybrid-assisted method can reduce surface roughness by up to 30%, compared to rotary ultrasonic-assisted alone. Among them, lower feed rates result in better surface roughness. Higher feed rates may accelerate the cutting progression but may cause vibrations between the cutting edge and the workpiece surface, leading to deteriorated surface roughness. Meanwhile, a slower feed rate allows for an increase in laser preheating time during the cutting processes, effectively achieving a sufficient preheating phenomenon, and thereby enhancing the surface roughness of the machined surface.

Table 5. Variance analysis of surface roughness for rotary ultrasonic-assisted milling.

Factor	Factor Level (S/N)			Sum of Squares (SS)	Contribution Rate (ρ%)
	1	2	3		
n (A)	9.08	9.42	9.71	0.6	0.72
a_e (B)	11.33	10.2	6.69	35.2	42.65
F (C)	11.73	10.2	6.32	46.5	56.36
Error				0.22	0.27
Total				82.47	100.00

Table 6. Variance analysis of surface roughness for hybrid-assisted milling.

Factor	Factor Level (S/N)			Sum of Squares (SS)	Contribution Rate (ρ%)
	1	2	3		
n (A)	7.74	10.1	10.8	15.1	17.65
a_e (B)	11.1	9.76	7.76	16.6	19.45
F (C)	12.1	10.2	6.32	51.6	60.34
Error				2.19	2.56
Total				82.49	100.00

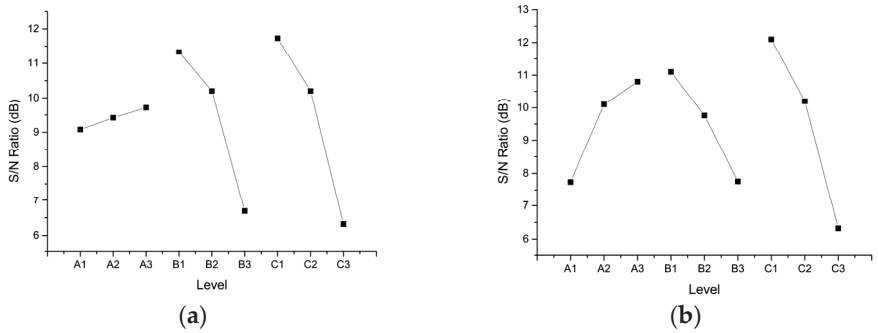


Figure 11. Factor response plot of surface roughness for rotary ultrasonic-assisted and hybrid-assisted milling. (**a**) Rotary ultrasonic-assisted. (**b**) Hybrid-assisted.

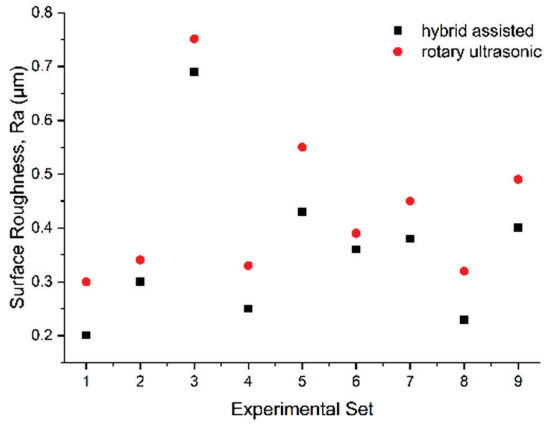


Figure 12. Surface roughness comparison between hybrid-assisted and rotary-assisted methods for process parameter combinations in L9 orthogonal array.

4.2. Cutting Force

Figure 13 shows the cutting force comparison both among different ultrasonic-assisted methods and without assistance for two sets of process parameters planned for the first phase of the experiment. It can be observed that in the first phase of the milling experiment, the cutting force with triple-axis ultrasonic assistance is the highest, while the cutting force with rotary ultrasonic assistance is significantly lower than with the other assistances. The cutting force without assistance is lower than that with dual-axis and triple-axis ultrasonic assistances. Therefore, in this phase, it is evident that rotary ultrasonic assistance can effectively reduce cutting forces. It is speculated that since dual-axis and triple-axis ultrasonic assistance methods include radial vibration, the material's high hardness and toughness prevent effective disruption of the material structure, leading to less effective material removal. Additionally, it increases the contact area and cutting load. In the case of triple-axis ultrasonic assistance, the radial vibration, unable to disrupt the workpiece material structure effectively, is combined with *z*-axis oscillation, increasing the contact area and cutting load compared to dual-axis ultrasonic assistance, resulting in an increase in cutting forces. On the other hand, rotary ultrasonic oscillation is along the *z*-axis, and its high-frequency oscillation can reduce the contact area in the cutting area. Simultaneously, it creates a vacuum region between the cutting tool and the workpiece material, facilitating air to enter the cutting area. This contributes to chip evacuation, reduced cutting forces, and lower cutting temperatures. Therefore, cutting forces with rotary ultrasonic assistance are the lowest among all the assistance methods. Compared to no assistance, rotary ultrasonic assistance can reduce cutting forces by approximately 16%.

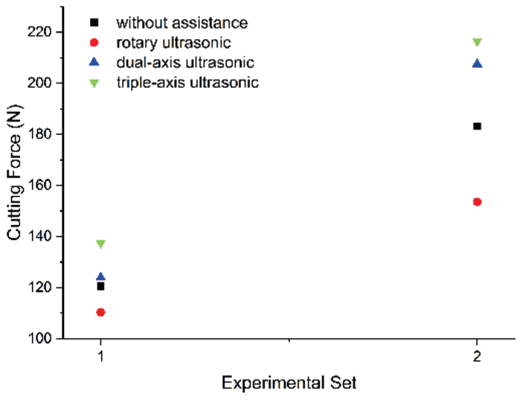


Figure 13. Cutting force comparison among both different ultrasonic-assisted methods and without assistance for two sets of process parameters planned in the 1st phase of the experiment.

In this section, the laser locally preheating temperature is approximately 620 °C, which elevates the localized temperature of SKD11 to achieve material softening, resulting in mechanical properties that are distinct from those at room temperature, consequently reducing cutting forces. As shown in Figure 14, with the assistance of laser preheating, the hybrid assistance of laser, combined with rotary ultrasonic assistance, exhibits lower overall cutting forces compared to rotary ultrasonic assistance alone. In comparison to rotary ultrasonic assistance, the hybrid assistance of laser, combined with rotary ultrasonic assistance, can reduce cutting forces by up to 16%. Specifically, hybrid assistance demonstrates lower cutting forces at a spindle speed of 10,000 rpm, a radial depth of cut of 0.1 mm, and a feed rate of 1000 mm/min. Under fixed feed-rate conditions, cutting forces increase with the radial depth of cut. The trend of decreasing cutting forces is less apparent at a feed rate of 2000 mm/min, suggesting that an excessively rapid cutting feed rate may result in inadequate laser preheating due to the fixed laser irradiation point on the front edge of the cutting-tool and its movement with the worktable, causing insufficient preheating time and a less-noticeable reduction in cutting forces. Under fixed radial depth of cut conditions, cutting forces increase with the feed rate. It is inferred that a deeper radial depth of cut may lead to insufficient effective preheating depth by the laser, and the feed rate also affects the laser preheating temperature, resulting in inadequate preheating effects and, therefore, ineffective reduction in cutting forces.

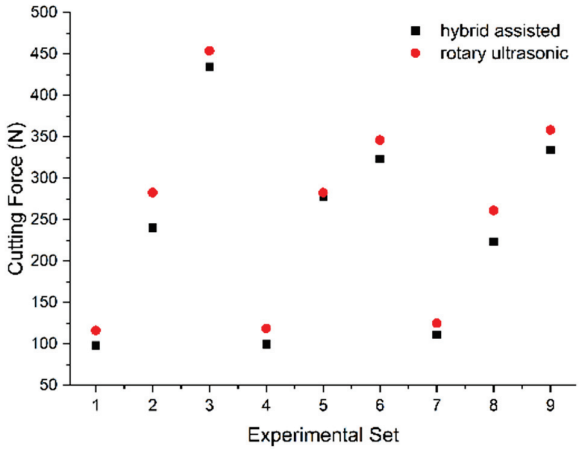


Figure 14. Cutting force comparison between hybrid assistance and rotary assistance for process parameter combinations in an L9 orthogonal array.

4.3. Machined Surface Morphology

After completing the milling experiments, the test samples were adequately cleaned and placed on a tool microscope with a 20× objective lens to observe the upper edge of the machined surface morphology. This section focuses on comparing the surface morphology under different process parameters along with rotary ultrasonic-assisted and hybrid-assisted methods in the second-phase of the experiment. Figure 15 shows the machined surface morphology comparisons for some specific combinations of process parameters and assisted milling methods. It can be observed that the machined surface morphology of the hybrid-assisted method performs better than the rotary ultrasonic-assisted method alone under the same process parameters. The rotary ultrasonic assistance method can reduce the contact area in the cutting zone and create a vacuum region between the cutting tool and the workpiece material, aiding chip evacuation and reducing cutting forces and temperature. This is beneficial because the high hardness and strength of SKD11 may lead to surface edge fracture or damage, especially at high feed rates. It can be observed that under high feed rates and large radial depths of cut, defects in the surface morphology are more pronounced. Under the same cutting process parameters, hybrid-assisted milling has a better surface morphology. This assistance combines the advantages of rotary ultrasonic assistance with the local softening of SKD11 by the laser

spot, providing better machinability. The maximum locally measured laser preheating temperature in this experiment is approximately 620 °C. According to reference [30], maintaining surface temperatures between 600 °C and 750 °C on SKD11 workpieces results in better machinability. Therefore, compared to rotary ultrasonic assistance alone, it can reduce the occurrence of surface edge defects. At a feed rate of 2000 mm/min, the surface edge of rotary ultrasonic assistance shows significant fracture and damage. In addition, with an increase in radial depth of cut, the defects in the surface morphology become more pronounced. At a feed rate of 1500 mm/min, a similar trend is observed. When the feed rate is reduced to 1000 mm/min, defects in the surface morphology become more apparent, with an increase in radial depth of cut. However, compared to feed rates of 2000 mm/min and 1500 mm/min, the defects are significantly reduced, and the integrity of the surface morphology is better. Increasing the feed rate leads to an increase in the number of cutting-tool edges engagement in the workpiece material per minute, enhancing cutting forces accordingly. Excessive cutting forces may cause vibration, resulting in more severe defects in the surface morphology. From Figure 15, it is evident that hybrid-assisted milling provides significantly better surface morphology integrity than rotary ultrasonic assistance alone. Although high feed rates and deeper radial depths of cut may affect the laser irradiation preheating time and preheating depth on SKD11, the hybrid assistance method achieves localized preheating and softening, resulting in a more complete surface morphology as compared to rotary ultrasonic assistance.

4.4. Cutting-Tool Wear

After completing the milling experiments, the cutting tools were removed from the spindle system and cleaned, and they were placed on a tool microscope with a 10× objective lens to observe cutting-tool flank wear. The photographs of cutting-tool flank wear shown in Figure 16 for each experiment are all captured at the end of milling state, i.e., 70 mm milling distance. The comparison involved 18 milling cutters used in the Taguchi experiments, with two assisted methods. Different factors affecting cutting-tool wear were also investigated. From Figure 16, it can be observed that under rotary ultrasonic assistance, cutting-tool wear is more severe, with instances of broken and chipped cutting-tool edges. As the feed rate and depth of cut increase, rotary ultrasonic assistance shows larger areas of wear and breakage, following a similar trend to machined surface edge. At a feed rate of 2000 mm/min, the cutting tools under rotary ultrasonic assistance exhibit clear fracture and damage, and with an increase in radial depth of cut, the width of cutting-tool wear also significantly increases. At the radial depths of cut of 0.3 mm and 0.5 mm, severe fracture and chipping occur. At a radial depth of cut of 0.1 mm, the wear width and cutting-tool edge damage are reduced. At a feed rate of 1500 mm/min, an increase in radial depth of cut leads to a corresponding increase in cutting-tool wear width. However, as compared to a feed rate of 2000 mm/min, cutting-tool edge chipping and fracture are significantly reduced. At a feed rate of 1000 mm/min, the improvement in wear width and cutting-tool edge defects is most apparent. Under the same process parameters, hybrid-assisted milling shows a significant reduction in cutting-tool wear width and edge fracture. This is attributed to the localized preheating on SKD11 by laser assistance, providing better machinability. Additionally, the rotary ultrasonic oscillation factor shortens the contact time between the cutting-tool edge and the workpiece, reducing the load on the cutting-tool edge and effectively ejecting chips, reducing the occurrence of cutting-tool edge fracture and significantly extending cutting-tool life. However, at a feed rate of 2000 mm/min and radial depths of cut of 0.3 mm and 0.5 mm, there are still instances of cutting-tool edge fracture. In situations with deeper radial depths of cut and faster feed rates, preheating locally with laser has a shorter preheating time on the machined surface. Despite the local softening of the material, the preheating time and depth are insufficient, and the material's high hardness, combined with the dynamic load, cutting-tool debris, and material chip effects, result in faster cutting-tool wear during machining.

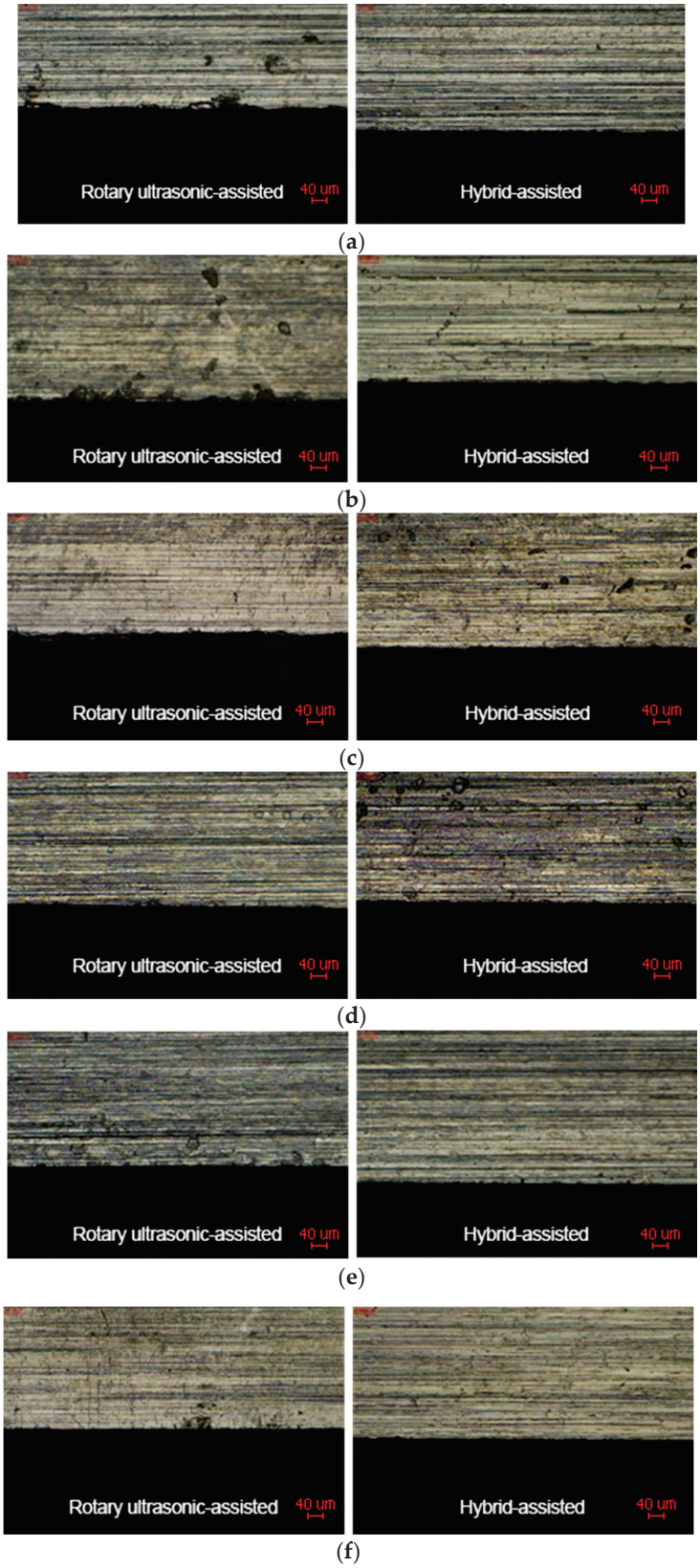


Figure 15. Machined surface morphology comparisons for some specific combinations of process parameter and assisted-milling methods: (**a**) n = 8000, a_e = 0.5 mm, F = 2000 mm/min; (**b**) n = 10,000, a_e = 0.5 mm, F = 1500 mm/min; (**c**) n = 9000, a_e = 0.3 mm, F = 2000 mm/min; (**d**) n = 10,000, a_e = 0.3 mm, F = 1000 mm/min; (**e**) n = 9000, a_e = 0.1 mm, F = 1500 mm/min; (**f**) n = 8000, a_e = 0.1 mm, F = 1000 mm/min.

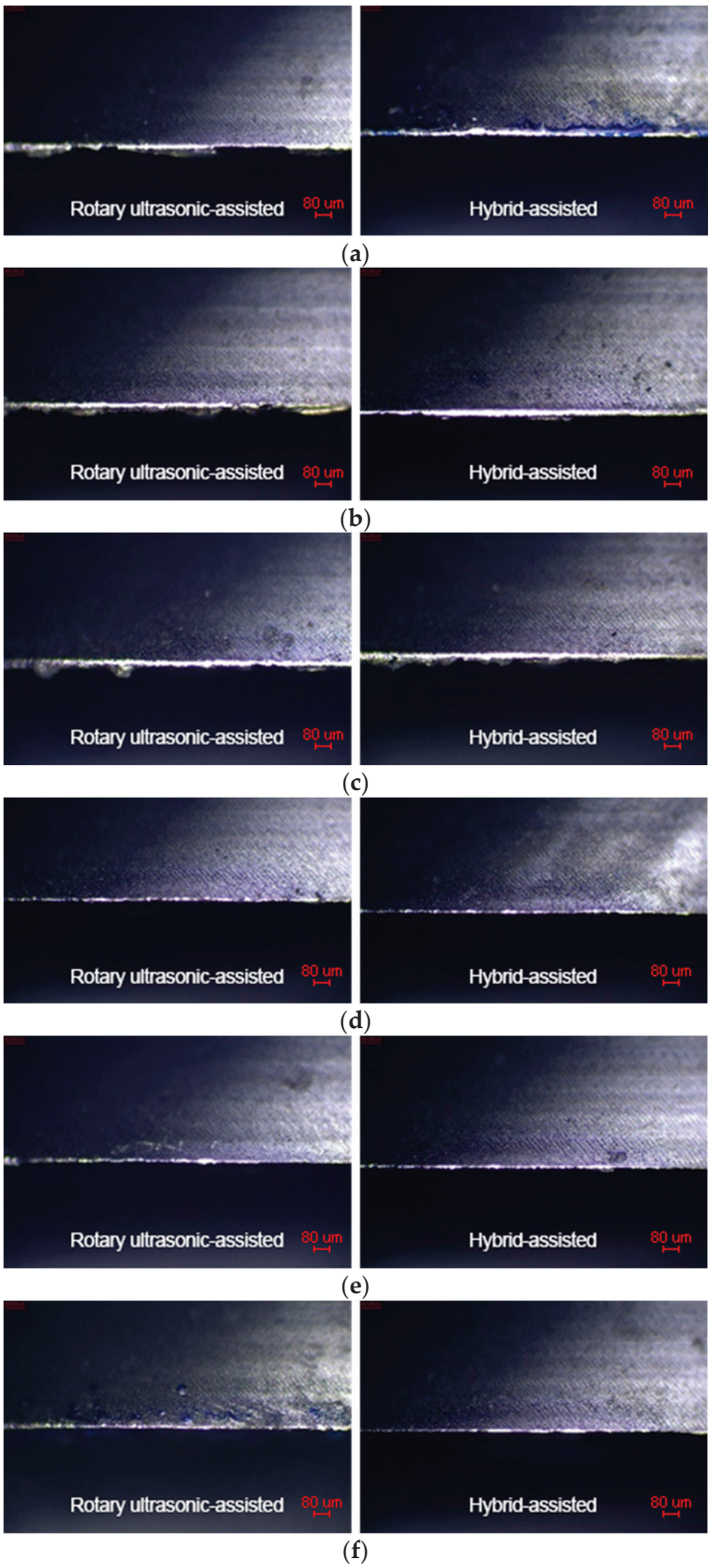


Figure 16. Cutting-tool wear comparisons for some specific combinations of process parameters and assisted milling methods: (**a**) n = 8000, a_e = 0.5 mm, F = 2000 mm/min; (**b**) n = 10,000, a_e = 0.5 mm, F = 1500 mm/min; (**c**) n = 9000, a_e = 0.5 mm, F = 1000 mm/min; (**d**) n = 10,000, a_e = 0.1 mm, F = 2000 mm/min; (**e**) n = 9000, a_e = 0.1 mm, F = 1500 mm/min; (**f**) n = 8000, a_e = 0.1 mm, F = 1000 mm/min.

4.5. Machine Learning

The model training process involves hyperparameter tuning using the training dataset and evaluating the model through 5-fold cross-validation. The hyperparameter combination that performs the best is selected as the model's parameter configuration. Finally, the optimized base regression models, including decision tree (DT), random forest (RF), extra trees, XGBoost (XGB), LightGBM (LGBM), AdaBoost, stochastic gradient descent (SGD), support vector regressor (SVR), least squares support vector regressor (LSVR), and multi-layer perceptron (MLP), comprising ten models, are used to construct a voting regression model for predicting the test set. The predictive performance of different machine learning models is compared to assess whether there are differences in predictive performance between ensemble learning and individual machine learning models. The evaluation metrics used in this experiment include the coefficient of determination (R^2), the root mean squared error (RMSE), the mean squared error (MSE), and the mean absolute error (MAE) to assess the model's performance.

The coefficient of determination (R-squared, R^2) ranges between 0 and 1, with a value closer to 1 indicating that the model can fully explain all variations, while a value closer to 0 suggests that the model cannot explain any variations. A higher R^2 implies a better predictive performance of the model. The relevant formula is given by Equation (2), where N represents the sample size, y_i represents the actual values, $\hat{y}_i$ represents the predicted values, and $\overline{y}$ denotes the mean of the actual values.

$$R^2 = 1 - \frac{\frac{1}{N}\sum_{i=1}^{N}(y_i - \hat{y}_i)^2}{\frac{1}{N}\sum_{i=1}^{N}(y_i - \overline{y})^2} \tag{2}$$

The mean squared error (MSE) is the average of the squared differences between actual values and predicted values. A smaller MSE indicates a better predictive performance of the model. The relevant formula is given by Equation (3), where N represents the sample size, y_i represents the actual values, and $\hat{y}_i$ represents the predicted values.

$$\text{MSE} = \frac{1}{N}\sum_{i=1}^{N}(y_i - \hat{y}_i)^2 \tag{3}$$

The root mean square error (RMSE) is a commonly used evaluation metric in regression tasks. It is the square root of the average of the squared differences between actual values and predicted values. A smaller RMSE indicates a better predictive performance of the model. The relevant formula is given by Equation (4), where N represents the sample size, y_i represents the actual values, and $\hat{y}_i$ represents the predicted values.

$$\text{RMSE} = \sqrt{\frac{1}{N}\sum_{i=1}^{N}(y_i - \hat{y}_i)^2} \tag{4}$$

The mean absolute error (MAE) is a commonly used evaluation metric in regression tasks. It is the average of the absolute differences between actual values and predicted values. A smaller MAE indicates a better predictive performance of the model. The relevant formula is given by Equation (5), where N represents the sample size, y_i represents the actual values, and $\hat{y}_i$ represents the predicted values.

$$\text{MAE} = \frac{1}{N}\sum_{i=1}^{N}|y_i - \hat{y}_i| \tag{5}$$

4.5.1. Machine Learning Results

In this section, machine learning metric scores are based on the results from the test dataset. Each model has different metric scores, as shown in Table 7 and Figure 17. The

decision tree (DT) model performs the worst among all models, with an R^2 of 0.69132, RMSE of 0.58086, MSE of 0.3374, and MAE of 0.4311. This is speculated to be because the model is too simple to capture the complex relationships in the data. The extra trees model performs the best on all metrics, with an R^2 of 0.91737, RMSE of 0.30053, MSE of 0.09032, and MAE of 0.21134. This is likely due to the introduction of more randomness and the fact that the model's generalization capability could be enhanced. Different models exhibit different performances, indicating that various machine learning models have distinct performance advantages. This can also be observed in Figure 18, which shows scatter plots for each regression model. It is evident that extra trees, AdaBoost, RF, and XGB have better predictive results, while DT and SVR perform poorly, with higher errors compared to other models. The figure also illustrates that each model has a different trend in predicting results.

Table 7. Performance comparisons among different machine learning models.

Models \ Indicators	R^2	RMSE	MSE	MAE
DT	0.69132	0.58086	0.3374	0.43112
RF	0.90902	0.31534	0.09944	0.22303
Extra Trees	0.91737	0.30053	0.09032	0.21134
XGB	0.90144	0.32822	0.10773	0.22051
LGBM	0.78587	0.48379	0.23405	0.32589
AdaBoost	0.91051	0.31276	0.09782	0.23232
SGD	0.85313	0.40066	0.16053	0.2977
SVR	0.70355	0.56924	0.32403	0.36844
LSVR	0.81672	0.44758	0.20033	0.27107
MLP	0.88668	0.35195	0.12387	0.28653

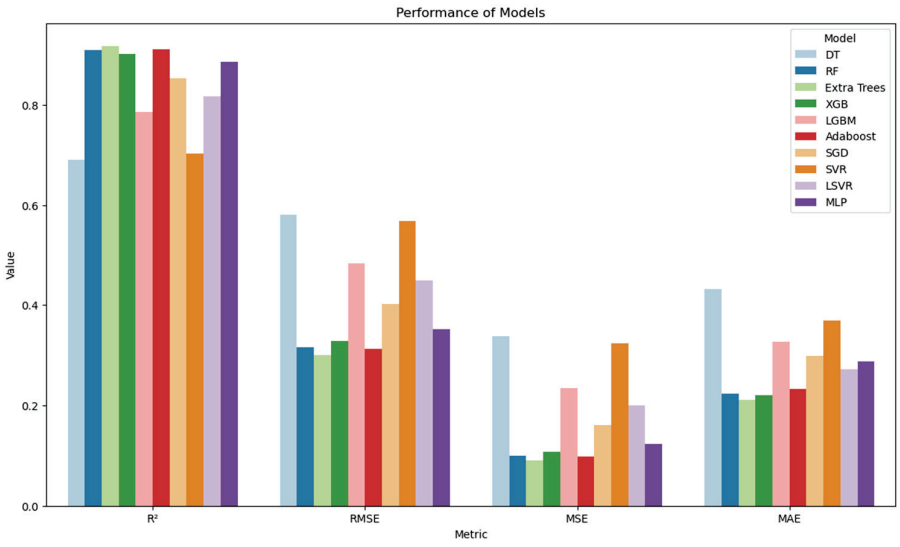


Figure 17. Performance comparisons among different machine learning models.

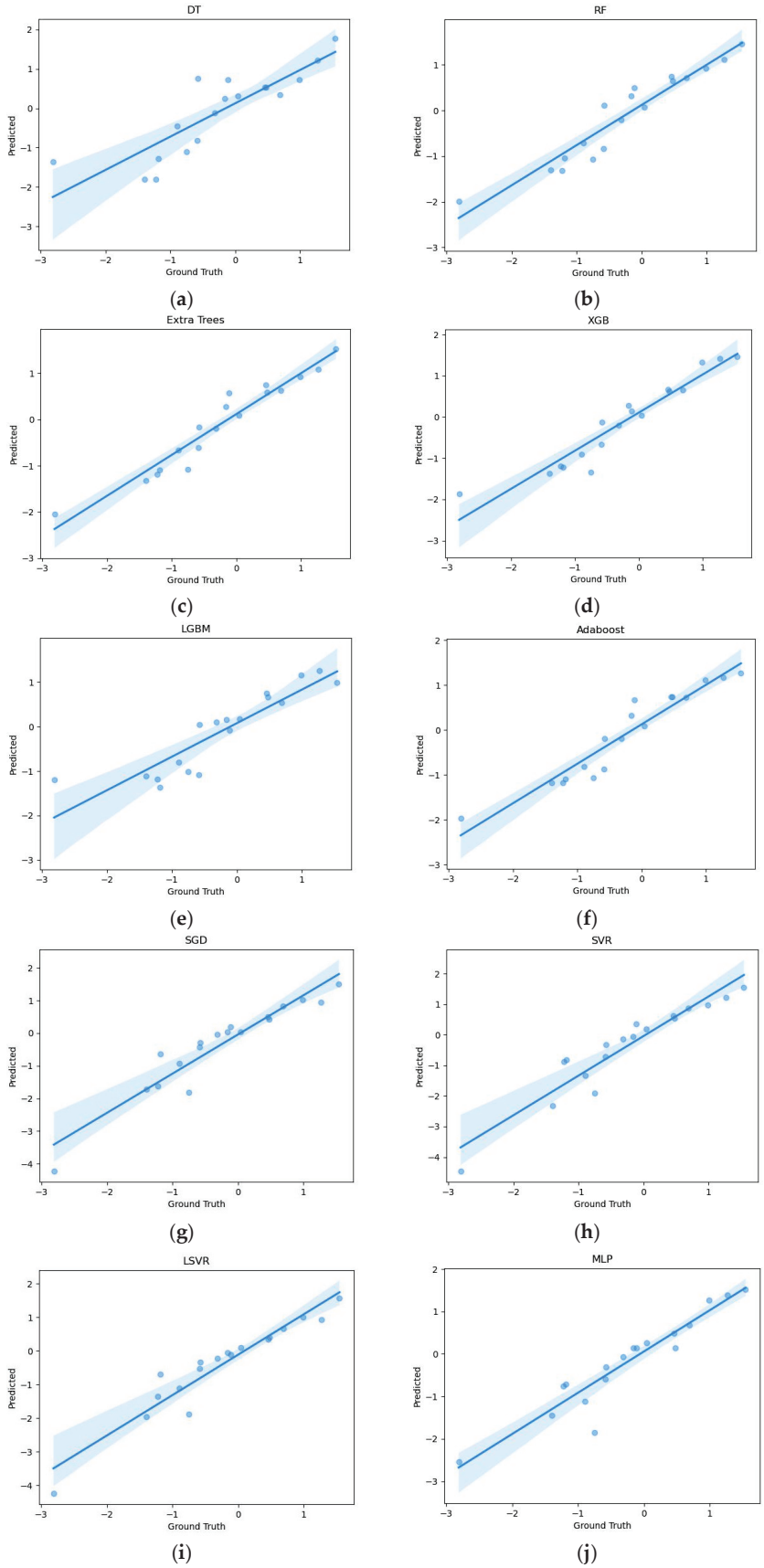


Figure 18. Scatter plots showing the relationship between predicted values and ground truth across different machine learning models: (**a**) DT, (**b**) RF, (**c**) extra trees, (**d**) XGB, (**e**) LGBM, (**f**) AdaBoost, (**g**) SGD, (**h**) SVR, (**i**) LSVR, (**j**) MLP.

4.5.2. Machine Learning and Ensemble Learning Results

Similarly, the machine learning metric scores are based on the results from the test dataset in this section. The ensemble voting regression model, composed of the basic regression models, including DT, RF, extra trees, XGB, LGBM, AdaBoost, SGD, SVR, LSVR, and MLP, is constructed to predict the test dataset. It is compared with the best-performing model in all metrics from the machine learning models in Section 4.5.1, which is the extra trees model. As shown in Figure 19 and Table 8, the performance of the voting regression model surpasses that of the extra trees model. The extra trees model is the best-performing model among the ten basic regression models, indicating that the voting regressor outperforms other machine learning models. The metric scores for this model are an R^2 of 0.94576, RMSE of 0.24348, MSE of 0.05928, and MAE of 0.18182. The residual plots in Figure 20 demonstrate that different models have distinct interpretations and levels of significance for the data. By combining multiple models, a better prediction of data characteristics can be achieved. Using multiple models allows for balance, even if one model's predictive performance is poor; the results from the other models can help compensate, providing a more stable prediction. As shown in Figure 21, the residual values of the voting regression model are closer to the central 0 line on the horizontal axis compared to other models, indicating a more centered distribution.

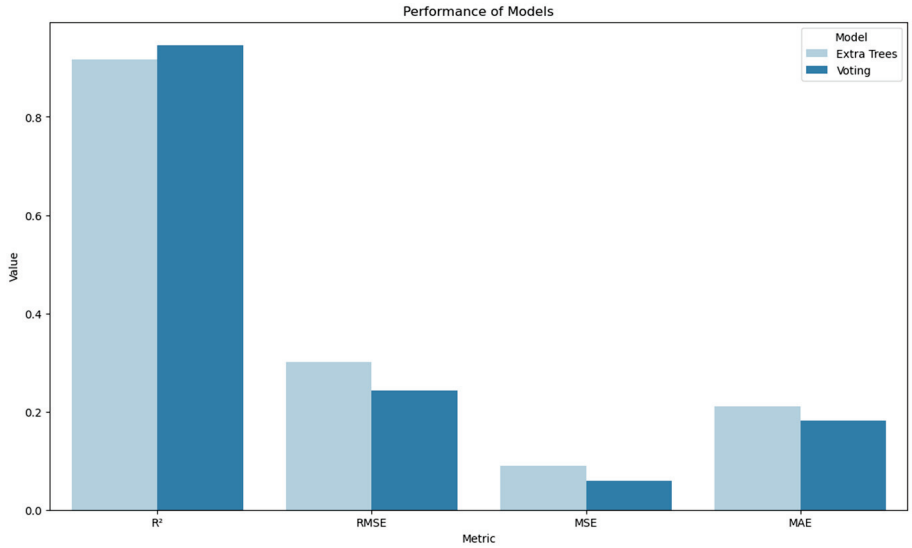


Figure 19. Performance comparisons between extra trees machine learning and ensemble learning models.

Table 8. Performance comparisons between extra trees machine learning and ensemble learning models.

Models \ Support	R^2	RMSE	MSE	MAE
Extra Trees	0.91737	0.30053	0.09032	0.21134
Voting	0.94576	0.24348	0.05928	0.18182

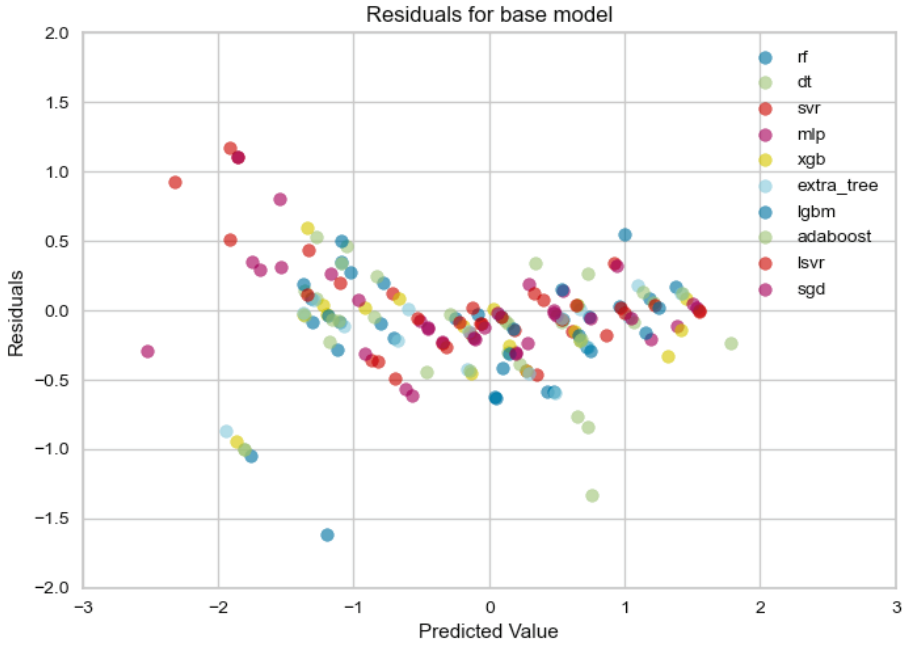


Figure 20. Relationship between residuals and predicted values for various machine learning models.

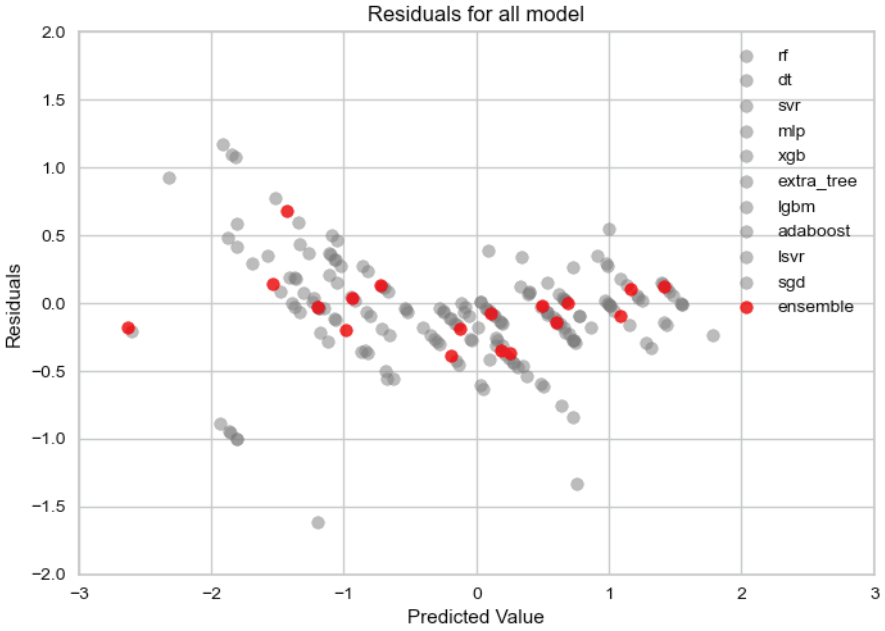


Figure 21. Relationship between residuals and predicted value for various machine learning models and ensemble learning model.

5. Conclusions

This study conducted side-milling experiments on SKD11 in two phases. The first phase aimed to explore the effects of different ultrasonic-assisted methods, including rotary, dual-axis and triple-axis, on milling performance. The better ultrasonic-assisted method obtained from the first phase was then adopted in the second phase both in conjunction with and without assistance from locally preheating with a laser, in which the Taguchi orthogonal array was applied for milling process parameter planning. The surface roughness and cutting-tool life served as the objective function and constraint, respectively, and the optimal combination of process parameters was thus determined by the characteristics of the smaller-the-better in the Taguchi method. Based on the optimal milling process parameters obtained and the superior hybrid-assisted method adopted, milling experiments

were repeatedly performed to collect the data of cutting force and cutting-tool wear. An ensemble learning method was applied to construct a cutting-tool wear prediction model after the data underwent the processes of cleaning, feature extraction, data standardization, and feature selection. From the above analyses, the following conclusions can thus be drawn:

1. As various ultrasonic-assisted methods compared with no assisted milling in the first phase experiments, it was found that ultrasonic-assisted machining could improve machining quality, reduce cutting force, and enhance surface roughness. Among them, rotary ultrasonic-assisted showed the best cutting performance.
2. As compared to the method without assisted milling, the rotary-assisted ultrasonic method could reduce surface roughness by approximately 5% and cutting force by 16%. When compared to rotary ultrasonic assistance, hybrid-assisted milling could reduce surface roughness by 30% and cutting force by 16%.
3. Among the multiple machine learning models in this study, extra trees exhibited the best performance, with an R^2 of 0.91737, RMSE of 0.30053, MSE of 0.09032, and MAE of 0.21134.
4. The ensemble voting regression model for cutting-tool wear prediction on the test dataset, can achieve an R^2 of 0.94576, RMSE of 0.24348, MSE of 0.05928, and MAE of 0.18182.
5. As compared to all the individual regression models in this study, the ensemble voting regression model exhibited the best generalization capabilities. This method can integrate the complementary predictive capabilities among different individual models and its generalization capabilities can be enhanced by combining the strengths of the multiple models. Therefore, ensemble machine learning is a feasible and effective method for monitoring cutting-tool wear.

Author Contributions: Conceptualization, supervision, writing, S.-Y.L.; methodology, analysis, C.-J.H. All authors have read and agreed to the published version of the manuscript.

Funding: This research received no external funding.

Institutional Review Board Statement: Ethical review and approval were waived for this study since it did not involve research with living organisms.

Informed Consent Statement: Not applicable.

Data Availability Statement: Correspondence and requests for materials should be addressed to Shen-Yung Lin. The data are not publicly available due to patent in review.

Acknowledgments: The authors acknowledge the National Formosa University for their support in this research.

Conflicts of Interest: The authors declare no conflicts of interest.

References

1. Abellan-Nebot, J.V.; Subirón, F.R. A review of machining monitoring systems based on artificial intelligence process models. *Int. J. Adv. Manuf. Technol.* **2010**, *47*, 237–257. [CrossRef]
2. Liang, S.Y.; Hecker, R.L.; Landers, R.G. Machining process monitoring and control: The state-of-the-art. *J. Manuf. Sci. Eng.* **2004**, *126*, 297–310. [CrossRef]
3. Anderson, M.; Patwa, R.; Shin, Y.C. Laser-assisted machining of Inconel 718 with an economic analysis. *Int. J. Mach. Tools Manuf.* **2006**, *46*, 1879–1891. [CrossRef]
4. Mejbel, M.K.; Khalaf, M.M.; Kwad, A.M. Improving the machined surface of AISI H11 tool steel in milling process. *J. Mech. Eng. Res. Dev.* **2021**, *44*, 58–68.
5. Tsai, M.Y.; Chang, C.T.; Ho, J.K. The machining of hard mold steel by ultrasonic assisted end milling. *Appl. Sci.* **2016**, *6*, 373. [CrossRef]
6. Ding, H.; Ibrahim, R.; Cheng, K.; Chen, S.-J. Experimental study on machinability improvement of hardened tool steel using two dimensional vibration-assisted micro-end-milling. *Int. J. Mach. Tools Manuf.* **2010**, *50*, 1115–1118. [CrossRef]
7. Gao, H.; Ma, B.; Zhu, Y.; Yang, H. Enhancement of machinability and surface quality of Ti-6Al-4V by longitudinal ultrasonic vibration-assisted milling under dry conditions. *Measurement* **2022**, *187*, 110324. [CrossRef]

8. Kumar, M.; Melkote, S.N. Process capability study of laser assisted micro milling of a hard-to-machine material. *J. Manuf. Process.* **2012**, *14*, 41–51. [CrossRef]
9. Brecher, C.; Emonts, M.; Rosen, C.-J.; Hermani, J.-P. Laser-assisted milling of advanced materials. *Phys. Procedia* **2011**, *12*, 599–606. [CrossRef]
10. Woo, W.-S.; Lee, C.-M. A study of the machining characteristics of AISI 1045 steel and Inconel 718 with a cylindrical shape in laser-assisted milling. *Appl. Therm. Eng.* **2015**, *91*, 33–42. [CrossRef]
11. Wang, C.; Ding, F.; Tang, D.; Zheng, L.; Li, S.; Xie, Y. Modeling and simulation of the high-speed milling of hardened steel SKD11 (62 HRC) based on SHPB technology. *Int. J. Mach. Tools Manuf.* **2016**, *108*, 13–26. [CrossRef]
12. Wang, C.Y.; Xie, Y.X.; Qin, Z.; Lin, H.S.; Yuan, Y.H.; Wang, Q.M. Wear and breakage of TiAlN-and TiSiN-coated carbide tools during high-speed milling of hardened steel. *Wear* **2015**, *336–337*, 29–42. [CrossRef]
13. Gong, F.; Zhao, J.; Ni, X.; Liu, C.; Sun, J.; Zhang, Q. Wear and breakage of coated carbide tool in milling of H13 steel and SKD11 hardened steel. *SN Appl. Sci.* **2019**, *1*, 1111. [CrossRef]
14. Pu, Z.; Singh, A. High speed ball nose end milling of hardened AISI A2 tool steel with PCBN and coated carbide tools. *J. Manuf. Process.* **2013**, *15*, 467–473. [CrossRef]
15. Gong, F.; Zhao, J.; Jiang, Y.; Tao, H.; Li, Z.; Zang, J. Fatigue failure of coated carbide tool and its influence on cutting performance in face milling SKD11 hardened steel. *Int. J. Refract. Met. Hard Mater.* **2017**, *64*, 27–34. [CrossRef]
16. Twardowski, P.; Czyżycki, J.; Felusiak-Czyryca, A.; Tabaszewski, M.; Wiciak-Pikuła, M. Monitoring and forecasting of tool wear based on measurements of vibration accelerations during cast iron milling. *J. Manuf. Process.* **2023**, *95*, 342–350. [CrossRef]
17. Niu, B.; Sun, J.; Yang, B. Multisensory based tool wear monitoring for practical applications in milling of titanium alloy. *Mater. Today Proc.* **2020**, *22*, 1209–1217. [CrossRef]
18. Mahmood, J.; Mustafa, G.-E.; Ali, M. Accurate estimation of tool wear levels during milling, drilling and turning operations by designing novel hyperparameter tuned models based on LightGBM and stacking. *Measurement* **2022**, *190*, 110722. [CrossRef]
19. Zhou, H.; Gao, S.; Xie, Y.; Zhang, C.; Liu, J. Multi-condition wear prediction and assessment of milling cutters based on linear discriminant analysis and ensemble methods. *Measurement* **2023**, *216*, 112900. [CrossRef]
20. Kilundu, B.; Dehombreux, P.; Chiementin, X. Tool wear monitoring by machine learning techniques and singular spectrum analysis. *Mech. Syst. Signal Process.* **2011**, *25*, 400–415. [CrossRef]
21. Huang, Z.; Shao, J.; Guo, W.; Li, W.; Zhu, J.; Fang, D. Hybrid machine learning-enabled multi-information fusion for indirect measurement of tool flank wear in milling. *Measurement* **2023**, *206*, 112255. [CrossRef]
22. Çınar, Z.M.; Nuhu, A.A.; Zeeshan, Q.; Korhan, O.; Asmael, M.; Safaei, B. Machine learning in predictive maintenance towards sustainable smart manufacturing in industry 4.0. *Sustainability* **2020**, *12*, 8211. [CrossRef]
23. Sarker, I.H. Machine learning: Algorithms, real-world applications and research directions. *SN Comput. Sci.* **2021**, *2*, 160. [CrossRef] [PubMed]
24. Sagi, O.; Rokach, L. Ensemble learning: A survey. *Wiley Interdiscip. Rev. Data Min. Knowl. Discov.* **2018**, *8*, e1249. [CrossRef]
25. Elbestawi, M.; Papazafiriou, T.; Du, R. In-process monitoring of tool wear in milling using cutting force signature. *Int. J. Mach. Tools Manuf.* **1991**, *31*, 55–73. [CrossRef]
26. Kuljanic, E.; Sortino, M. TWEM, a method based on cutting forces—Monitoring tool wear in face milling. *Int. J. Mach. Tools Manuf.* **2005**, *45*, 29–34. [CrossRef]
27. Gierlak, P.; Burghardt, A.; Szybicki, D.; Szuster, M.; Muszyńska, M. On-line manipulator tool condition monitoring based on vibration analysis. *Mech. Syst. Signal Process.* **2017**, *89*, 14–26. [CrossRef]
28. Qin, Y.; Liu, X.; Yue, C.; Zhao, M.; Wei, X.; Wang, L. Tool wear identification and prediction method based on stack sparse self-coding network. *J. Manuf. Syst.* **2023**, *68*, 72–84. [CrossRef]
29. Mao, X.; Zhang, F.; Wang, G.; Chu, Y.; Yuan, K. Semi-random subspace with Bi-GRU: Fusing statistical and deep representation features for bearing fault diagnosis. *Measurement* **2021**, *173*, 108603. [CrossRef]
30. Xavierarockiaraj, S.; Kuppan, P. Investigation of cutting forces, surface roughness and tool wear during Laser assisted machining of SKD11Tool steel. *Procedia Eng.* **2014**, *97*, 1657–1666. [CrossRef]

Disclaimer/Publisher's Note: The statements, opinions and data contained in all publications are solely those of the individual author(s) and contributor(s) and not of MDPI and/or the editor(s). MDPI and/or the editor(s) disclaim responsibility for any injury to people or property resulting from any ideas, methods, instructions or products referred to in the content.

applied sciences

MDPI

Article

Additive Manufacturing of Ceramic Reference Spheres by Stereolithography (SLA)

Víctor Meana [1], Pablo Zapico [1], Eduardo Cuesta [1,*], Sara Giganto [2], Lorenzo Meana [1] and Susana Martínez-Pellitero [2]

[1] Department of Construction and Manufacturing Engineering, University of Oviedo, Campus of Gijon, 33203 Gijon, Spain; meanavictor@uniovi.es (V.M.); zapicopablo@uniovi.es (P.Z.); lorenzomeanaperez@gmail.com (L.M.)
[2] Area of Manufacturing Engineering, University of Leon—Universidad de León, Campus of Vegazana, 24071 Leon, Spain; sgigf@unileon.es (S.G.); susana.martinez@unileon.es (S.M.-P.)
* Correspondence: ecuesta@uniovi.es

Abstract: Additive Manufacturing (AM) is advancing technologically towards the production of components for high-demand mechanical applications with stringent dimensional accuracy, leveraging metallic and ceramic raw materials. The AM process for ceramic components, known as Ultraviolet Laser Stereolithography (SLA), enables the fabrication of unique parts or small batches without substantial investments in molds and dies, and avoids the problems associated with traditional manufacturing, which involves multiple stages and final machining for precision. This study addresses the need to produce reference elements or targets for metrological applications, including verification, adjustment, or calibration of 3D scanners and mid- to high-range optical sensors. Precision spheres are a primary geometry in this context due to their straightforward mathematical definition, facilitating rapid and accurate error detection in equipment. Our objective is to exploit this novel SLA process along with the advantageous optical properties of technical ceramics (such as being white, matte, lightweight, and corrosion-resistant) to materialize these reference objects. Specifically, this work involves the fabrication of alumina hemispheres using SLA. The manufacturing process incorporates four design variables (wall thickness, support shape, fill type, and orientation) and one manufacturing variable (the arrangement of spheres on the printing tray). To evaluate the impact of the design variables, dimensional and geometric parameters (GD&T), including diameters, form errors, and their distribution on the surface of the sphere, have been characterized. These measurements are conducted with high accuracy using a Coordinate Measuring Machine (CMM). The study also examines the influence of these variables in the dimensional and geometric accuracy of the spheres. Correlations between various parameters were identified, specifically highlighting critical factors affecting process precision, such as the position of the piece on the print tray and the wall thickness value. The smallest diameter errors were recorded at the outermost positions of the tray (rear and front), while the smallest shape errors were found at the central position, in both cases with errors in the range of tens of micrometers. In any case, the smallest deformations were observed with the highest wall thickness (2 mm).

Keywords: additive manufacturing; stereolithography; ceramics; alumina; reference spheres

1. Introduction

The benefits of additive manufacturing (AM) compared to traditional manufacturing methods are widely acknowledged for its capacity to produce parts from various materials, intricate shapes, with great speed, enough precision, cost-effectiveness, and eliminating the need for fixtures and jigs [1–3]. These advantages are particularly significant when considering ceramic components, where their properties such as high melting temperatures, low ductility, and susceptibility to thermal shock, make conventional forming methods

expensive and difficult, often resulting in faulty parts, with defects and surface microcracks. But these issues, that have persisted for years in conventional methods, continue nowadays in additively manufactured ceramic parts due to the lack of on-site inspection and systematic procedures throughout the design, processing, and post-processing stages.

Among the various AM technologies for advanced ceramics, those based on photopolymerization stand out for producing parts with superior mechanical properties, high precision, and excellent surface finish [4]. Within this category, Vat Photopolymerization by Ultraviolet Laser for Ceramics technique (VPP-UVL/C according to ISO/ASTM 52900 [5]), commonly known as stereolithography (SLA), has shown promising results, particularly with materials like alumina, zirconia, and hydroxyapatite [6].

The SLA process for ceramics involves four critical stages in two phases: printing (production phase), cleaning, debinding, and sintering (post-processing phase). The raw material consists of a paste containing a suspension of ceramic particles in a photosensitive resin, along with diluents and binders. In the initial printing stage, a green (oversized) part is fabricated via photopolymerization, layer by layer, facilitated by ultraviolet light acting upon the photosensitive resins [7]. The paste is evenly distributed onto the printing bed using a blade that adjusts the layer height during each pass. Throughout this phase, layer displacements may occur, and microbubbles can form due to air entrapment during paste application [8]. The strategic use of supports is crucial to prevent structural failure resulting from the forces exerted during the process, which could lead to deformation, breakage of thin sections, or detachment of the part from the bed [9]. The stresses induced are contingent upon the rheological properties of the paste and the velocity and thickness of the layers, all relative to a given blade geometry.

The cleaning stage is critical, as the printed parts do not have sufficient consistency and are susceptible to breakage when the surrounding paste is removed. This involves removing all the ceramic paste that has not been photopolymerized and that not only surrounds the piece but is also stored in the hollows and interstices of the piece's geometry.

In the debinding stage, which constitutes the second phase, the removal of the organics of the photopolymerized resin is achieved through high temperature-time cycles. This process involves a combination of polymer evaporation, oxidation-induced decomposition, and thermal degradation. It stands as the most crucial stage, as any cracks or deformations occurring during debinding due to a significant reduction in the volume and, therefore, cannot be rectified in subsequent sintering phases. Initially, the evaporation of diluents creates an open porosity, facilitating the diffusion and subsequent evaporation of polymeric components undergoing pyrolysis. At the end of this stage, parts exhibit significant porosity, reaching up to 40%, resulting in a low mechanical strength of the parts [10].

In the fourth stage, known as sintering, the ceramic component devoid of resins undergoes exposure to high temperatures. During this phase, the porous structure is densified, fostering a robust bond among the ceramic particles. This densification invariably leads to volumetric contraction, ultimately resulting in the part attaining its intended design dimensions. Sintering conducted in ambient air typically yields material densities ranging from 95% to 99% of the theoretical maximum; however, sintering under vacuum or pressure conditions further reduces porosity levels. Studies have demonstrated that ceramic density and bending strength exhibit enhancement with increasing sintering temperature [11,12].

Alumina is a very versatile ceramic material, and its properties make it especially suitable for applications where temperature or biocompatibility are critical factors [13]. Due to its high hardness and stability, it serves as an abrasive, as a protective oxide on metal surfaces, as a refractory for furnaces and as a high-quality electrical insulator due to its high electrical resistance over a wide temperature range. Due to its excellent biocompatibility, it is used in biomedical applications. The white color, the dimensional stability with temperature, and the lightness of alumina has also aroused interest in the field of optical measuring equipment calibration [14], where reduction of weight for large-range master gauges and calibration devices makes the use of lightweight ceramics even more interesting [15].

Indeed, it is common to find research studies examining the metrological behaviors of ceramic reference elements, such as those made from alumina [16–18]. However, ceramic artifacts produced by conventional methods are solid and therefore heavy. Additionally, precision ceramic spheres typically have excellent dimensional qualities and surface finishes. They often use G5, G10 grades [19], which require very low roughness (Ra < 0.02 μm), resulting in shiny finishes that are unsuitable for use with many optical sensors (e.g., laser 3D scanners) [20]. To address this issue, it is beneficial to fabricate lightweight reference elements with high thermal stability and a matte finish that make them suitable for 3D scanners used in optical metrology and reverse engineering. The additive manufacturing processes for alumina spheres are promising candidates for producing these elements. This technique enables the creation of hollow, matte white spheres with relatively large diameters (up to 50 mm or more), reducing their weight and thus minimizing their impact on the deformation of the supporting structures, which is particularly advantageous for the calibration of medium- and high-range scanners.

However, there is a lack of research focused on this field using alumina parts fabricated through additive manufacturing processes involving ultraviolet laser photopolymerization. The chosen design for manufacturing the artifacts is based on a canonical sphere geometry, widely used as a reference element for equipment calibration. It is noteworthy that spheres represent a geometry that is straightforwardly definable in measurement software and ensures traceability of comparisons between measurements obtained by contact from a coordinate measuring machine (CMM).

In this work, artifacts based on hemispheres are designed and manufactured using four design variables (wall thickness, support shape, fill type, and orientation) and one manufacturing variable (arrangement of spheres on the printing tray) in order to analyze the influence of each on the achieved dimensional and geometric quality. For this purpose, diameters, shape errors, and the distribution of these errors on the surface of the spheres will be considered.

The following sections describe the equipment used for both the fabrication and measurement of the artifacts, the research methodology, the experimentation conducted, the results obtained, and the conclusions reached. Specifically, Section 2 is dedicated to presenting the equipment used and the methodology followed, from the initial step of proposing different designs to the final phase of analysis, including the fabrication of the parts and contact measurement using high-precision equipment. Section 3 details the experimentation, providing comprehensive information on the part designs, the parameters of the manufacturing stages, and the measurement processes. Section 4 presents the results of the geometric and dimensional parameter measurements. Finally, Section 5 enumerates the research conclusions based on the data analysis from the previous section.

2. Materials and Methodology

The work conducted in this experiment was carried out in four phases: design, manufacturing, measurement, and analysis. This sequence of operations is illustrated in Figure 1 and described in the following sections.

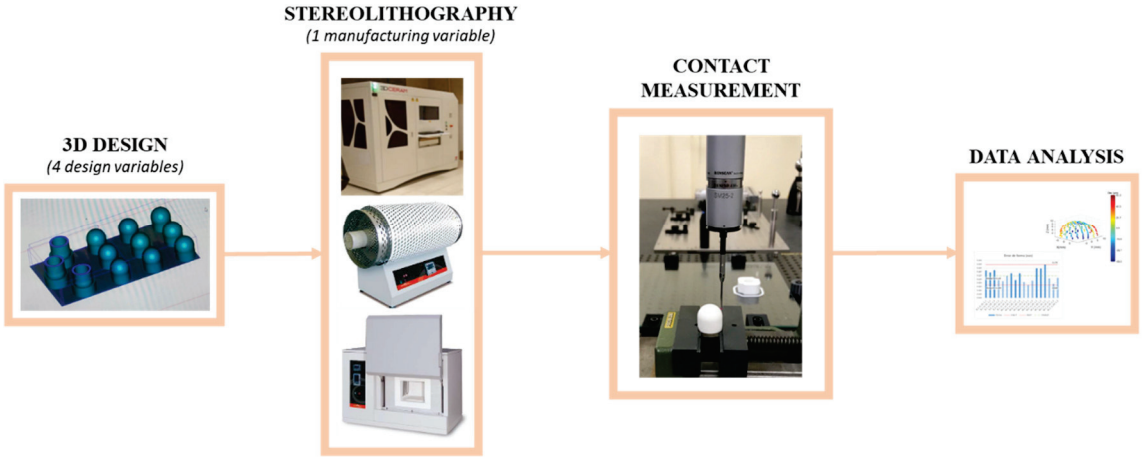


Figure 1. Methodology used for the experimentation.

2.1. Test Spheres Design

To achieve the objective of fabricating reference elements for 3D optical scanners, it is necessary to have some type of support that can be attached (usually by gluing) to the bottom of the spheres for securing them. Additionally, it is essential that the spheres have a well-defined diameter. Therefore, the solution involves manufacturing "extended hemispheres", producing these elements from the pole to a "safety zone" below the equator, or vice versa (depending on the additive process strategy). Thus, starting from the CAD model of this extended hemisphere, different geometries of the master pattern have been designed, considering the manufacturer's recommendations, as well as the limitations of the additive manufacturing process (SLA), mainly in the stages following printing (post-processing of the green part). According to the manufacturer's recommendations, the maximum wall thicknesses should not exceed 5 mm, since deformations and cracks could appear during the removal of organics in the debinding stage. For this reason, and due to the search for lightweight structures that can be deployed as high and mid-range calibration and qualification standards, two wall thicknesses were used in the designed artifacts. As mentioned, the design of manufacturing' supports are a crucial part of the design process, to avoid layer displacements during printing [21]. Different types of "set-up printing configurations" were considered. Figure 2 shows a 3D design of the layout of the test spheres on the printing tray. The colors represent different configurations of manufactured spheres which will be explained below (Section 3).

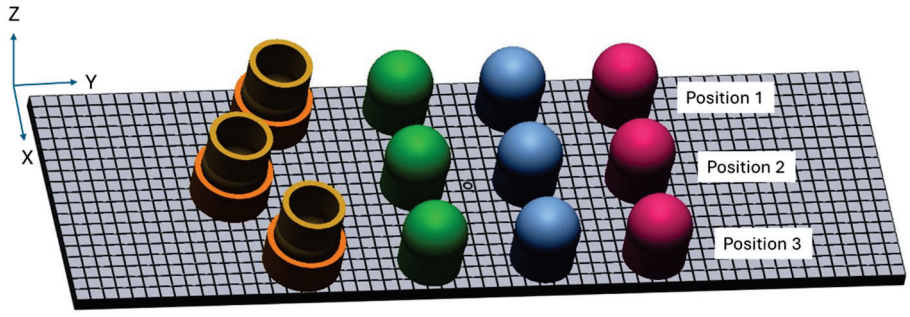


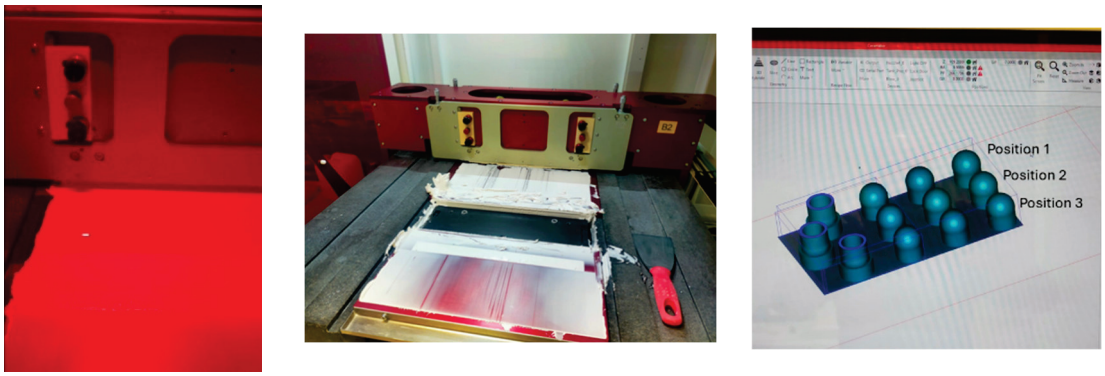
Figure 2. Layout of the CAD artifacts.

2.2. Additive Manufacturing by SLA

Once the different options to be evaluated were designed, the pieces were fabricated using stereolithography (SLA). As previously mentioned, this process involves several stages: printing, debinding, and sintering. There is also an intermediate cleaning process between the first and second stages. This cleaning is performed using a specific solution,

3DMIX Ceraclean (3DCeram, Bonnac-la-Côte, France), supplied by the manufacturer. The complete stereolithography system consists of the additive printer, a debinding furnace, and a sintering furnace.

The C900 Flex printer (3DCeram, Bonnac-la-Côte, France), Figure 3, has open parameters and is ideal for printing functional parts or small series, enabling the fabrication of ceramic parts by stereolithography with a maximum volume of 300 × 300 × 100 mm, a layer thickness of 50 µm, and a laser wavelength of 355 nm. The Ceradel PTF 16/130/610 (3DCeram, Bonnac-la-Côte, France) debinding furnace can reach a maximum temperature of 1300 °C. The tube has a diameter of 130 mm, and the heated length is 500 mm. It features a manual adjustment for airflow and nitrogen to meet the heating requirements of the pieces. The sintering furnace is the HTL 20/17 (Thermoconcept, Bremen, Germany), with internal dimensions of 200 × 250 × 200 mm and a power of 8 kW, capable of reaching a maximum temperature of 1750 °C.



(**a**) (**b**) (**c**)

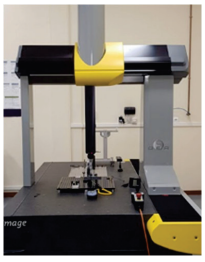
Figure 3. AM printer: (**a**) during the printing and light-curing process. (**b**) Printing tray after removal of the parts. (**c**) Spheres' layout on the AM machine display.

2.3. Measurement

The next step involved measuring the pieces using the Coordinate Measuring Machine (CMM), model DEA Global Image (Hexagon, Stockholm, Sweden). The machine was equipped with a PH10MQ indexing head (Renishaw, Gloucestershire, UK) and the probe used in this work was the SP25M (Renishaw, Gloucestershire, UK) with a tip of 40 mm long ceramic stylus with a Ø4 mm ruby sphere end. The accuracy of this CMM is given by the manufacturer according to ISO 10360-2 [22], Table 1.

Table 1. Coordinate Measuring Machine features.

Model	DEA Global Image 091508
Measurement field	900 × 1500 × 800 mm
Maximum permissible error	2.2 + 0.003 L µm (L in mm)
Maximum radial error	2.2 µm (in repeatability)
Maximum accuracy work Temp	20 ± 2 °C
Software	PC-DMIS, v2018 R2



The inspection software controlling the machine is PC-DMIS 2018 R2. This equipment was used to carry out the measurements, providing reference values for the diameters and form errors of the spheres. To obtain these values, 100 contact points were recorded on each sphere, adhering to the criteria defined in ISO 10360-5 [23].

2.4. Analysis

Finally, the data obtained from the measurements conducted with the Coordinate Measuring Machine were analyzed. From this information, the diameter values and form errors were determined, which allowed for assessing the dimensional and geometric quality levels of the different spheres. Given the amount of data collected and the complexity of the variables involved, various scripts were developed using the Matlab programming platform to aid in data analysis and facilitate comparisons. A coding system was implemented to easily identify the structural characteristics of the manufactured models. The different graphical representations developed enabled the identification of correlations between variables from both dimensional and geometric analysis perspectives.

3. Experimentation

To carry out the experiment, a total of 24 pieces were manufactured (Table 2) in two different series, with 12 units in each. All the artifacts are spherical caps with a nominal diameter of 20 mm, each featuring different support geometries. These designs were intended to allow the artifacts to be placed on interchangeable supports for use as reference elements or targets in metrological applications.

Table 2. Artifacts manufactured according to the design variables.

		Artifacts Ø 20 mm			
		WT [1] = 1 mm		WT [1] = 2 mm	
		Mushroom [3]	Bullet [3]	Mushroom [3]	Bullet [3]
UP [2]	Reticular filling (L)	-	-	3	-
	With inner support (F)	3	3	3	3
	Without inner support (E)	3	-	3	-
DOWN [2]	Without inner support (E)	-	-	3	-

[1] Wall Thickness; [2] Artifact orientation; [3] External geometry.

To enrich the study and enable an analysis of the influence of the manufacturing process, four design variables were considered:

- Vertical orientation (VO), which can be either Up (U) if the sphere has the pole up or Down (D) if the pole is down.
- Interior structure (IS), with three options: without internal support (E), with internal support (F), and with a lattice-type infill (L), see Figure 4. In the case of the solid support without contact, the gap part/support was 0.3 mm.
- External geometry of the artifact (EG), with two basic shapes considered: mushroom (M) and bullet (B). See Figure 5.
- Wall thickness (WT), either 1 or 2 mm.



Without support (E)—1 mm wall thickness | With solid inner support (F)—1 mm wall thickness | With solid inner support (F)—2 mm wall thickness | With reticular filling (L)—2 mm wall thickness

Figure 4. Different types of filling.



(**a**) (**b**)

Figure 5. Different types of shape. (**a**) Bullet type with inner support. (**b**) Mushroom type with inner support.

There was one manufacturing variable:

– Position on the printing tray, rear (1), center (2), and front (3) (see Figures 2 and 3c).

Furthermore, thinking about the subsequent placement of the artifacts in another base device, the hemispheres were designed with two different shapes: Bullet type (B) (Figure 5a) and Mushroom type (M) (Figure 5b).

However, during the printing process of the first series, three units were discarded from the metrological analysis due to visible defects in the "green" state, the state before debinding (mushroom-type pieces without internal support, down position, and 2 mm wall thickness) (Figure 6a). Additionally, another three pieces (mushroom-type with lattice internal structure and 2 mm wall thickness) were discarded because they showed shape deviations greater than 0.3 mm after undergoing the complete process. These deformations were caused by the stresses produced by the lattice structure during the sintering phase (Figure 6b). Therefore, the subsequent metrological analysis considered only the remaining 18 artifacts.



(**a**) (**b**)

Figure 6. (**a**) Mushroom-type artifacts, down orientation, E support and WT = 2 mm. (**b**) Mushroom-type artifact, Up orientation, L support and WT = 2 mm.

As previously mentioned, the printing process was carried out using Vat Photopolymerization by Ultraviolet Laser for Ceramics (VPP-UVL/C) in two series, each lasting approximately 18 h, using 3DMIX ALUMINA AL-F02 alumina paste supplied by the printer's provider (3DCeram, Bonnac-la-Côte, France). This phase of the additive manufacturing process is the most sensitive regarding the potential to damage the pieces during handling, as the pieces do not yet have their final mechanical properties. In fact, once the print bed is removed from the printer, the pieces are not in sight (Figure 7a) as they are covered by the uncured ceramic paste, making their handling even more difficult. Cleaning to remove all traces of ceramic paste is meticulously carried out under an extraction hood (Figure 7b) to prevent the operator from inhaling gases emitted by the cleaning solution recommended by the manufacturer. This phase took 8 h, performed by a technician with specific training.



(**a**) (**b**)

Figure 7. (**a**) Printing tray with parts filled with ceramic paste. (**b**) Cleaning of parts under the extraction hood.

The next phase in the artifact production process was debinding. This is a key step in the manufacturing process that consists of removing organics to leave only the ceramic matrix. The ceramic paste has a high binder content (40–60%) that must be eliminated by burning at high temperatures. During this stage, the resins are removed through a combination of evaporation of low molecular weight polymers, oxidative decomposition, and thermal degradation. The organic matrix burns off at temperatures up to 550 °C. In the initial phase, the diluent evaporates. As it does so, it creates open porosity within the green piece. This facilitates the diffusion and evaporation of the polymeric components that are subsequently pyrolyzed [24]. Table 3 shows the stages of the debinding process. Up to 800 °C it takes place with a constant nitrogen flow of 0.5 L/min. When 800 °C is reached, the progressive change from nitrogen to air is made. From 800 °C to the end of the process, it is carried out with a constant air flow of 0.5 L/min.

Table 3. Thermal stages in the debinding process.

	Environment	Temperature (°C)	Ramp (°C/min)	Stage (min)
1	N_2	20–240	0.2	1100
2		240	-	20
3		240–460	0.1	2200
4		460	-	20
5		460–800	0.3	1133
6	$N_2 \rightarrow$ Air	800	-	120
7	Air	800–1050	1	250
8		1050	-	5
9		1050–20	−2	515

In total, almost 4 days were required to complete this stage of the process, during which the thermal treatment was conducted in a nitrogen environment to achieve a smoother surface and higher density of the final pieces. Additionally, nitrogen was used to prevent porosity formation, thereby ensuring the quality and durability of the pieces. Figure 8 shows the debinding process with a time–temperature graph according to the parameters provided by the supplier of the raw material. This graph illustrates the different thermal stages, including the final heating to a maximum temperature of 1050 °C and subsequent cooling in an air environment.

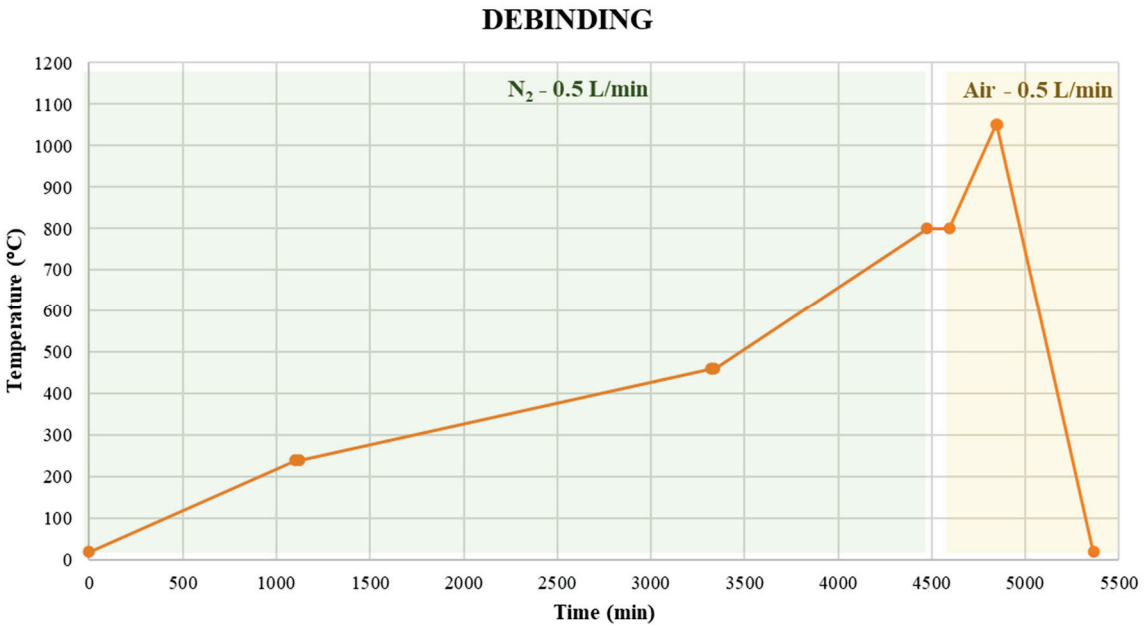
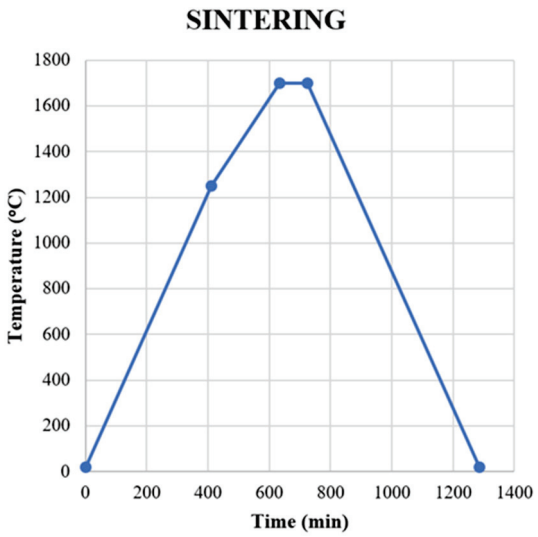


Figure 8. Thermal evolution in the debinding process.

Finally, the pieces underwent a new thermal treatment (air environment), this time for sintering. The goal of this stage was to achieve a dense and robust structure by eliminating porosities and providing the pieces with the necessary strength so that handling would not alter the designed dimensions and geometries. This research does not aim to achieve specific mechanical properties (strength, hardness, etc.), as previously mentioned. Instead, the intention is to utilize the material's thermal stability and the lightweight design enabled by additive manufacturing to create metrological reference elements. According to the manufacturer's specifications, this process involves reaching a maximum temperature of 1700 °C and lasts approximately 22 h, including both heating and cooling stages. Figure 9 shows the data and corresponding graph for the sintering process.



	Temperature (°C)	Ramp (°C/min)	Stage (min)
1	20–1250	3	410
2	1250–1700	2	225
3	1700	-	90
4	1700–20	−3	560

Figure 9. Sintering stage configuration and time vs. temperature diagram.

4. Results and Discussion

For the 18 spheres that were measured and analyzed, a nomenclature (Figure 10) was necessary to identify them according to their shape (B—bullet, M—mushroom), infill (ultimately only two types: F—with internal support, E—without internal support), orientation

(U—pole up, D—pole down), diameter in mm (20), wall thickness WT in mm (1, 2), and position on the tray (1, 2, 3).

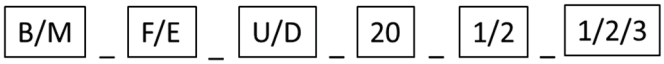


Figure 10. Artifact nomenclature.

Additionally, to validate the process and conduct a metrological analysis that allowed for the evaluation of the influence of the proposed design variables, two parameters were evaluated: one dimensional (the diameter) and one geometric (the form error).

The results for the diameter values (Table 4) of the different spheres measured by contact with the CMM ranged from 20.033 mm, measured on the sphere M_E_U_20_2_1 (artifact with mushroom geometry, without internal support, oriented upwards, Ø20 mm, 2 mm wall thickness, in position 1 on the tray), to 19.916 mm, obtained on the sphere B_F_U_20_1_2 (artifact with bullet geometry, with internal support, oriented upwards, Ø20 mm, 1 mm wall thickness, in position 2 on the tray). Thus, the diameter range was 117 µm, with the average diameter of all spheres being only 9 µm below the nominal value (Figure 11).

Table 4. Diameters of the ceramic spheres manufactured by SLA.

Tray Location	Artifact Code (Bullet Shape, with Inner Support, Pole Upwards)	Diameter (mm)	Artifact Code (Mushroom Shape, without Inner Support, Pole Upwards)	Diameter (mm)	Artifact Code (Mushroom Shape, with Inner Support, Pole Upwards)	Diameter (mm)
Rear	B_F_U_20_1_1	20.018	M_E_U_20_1_1	20.059	M_F_U_20_1_1	20.029
Centre	B_F_U_20_1_2	19.903	M_E_U_20_1_2	19.980	M_F_U_20_1_2	19.917
Front	B_F_U_20_1_3	19.986	M_E_U_20_1_3	19.992	M_F_U_20_1_3	19.989
Rear	B_F_U_20_2_1	20.034	M_E_U_20_2_1	20.044	M_F_U_20_2_1	20.045
Centre	B_F_U_20_2_2	19.959	M_E_U_20_2_2	19.984	M_F_U_20_2_2	19.992
Front	B_F_U_20_2_3	20.010	M_E_U_20_2_3	20.033	M_F_U_20_2_3	20.048

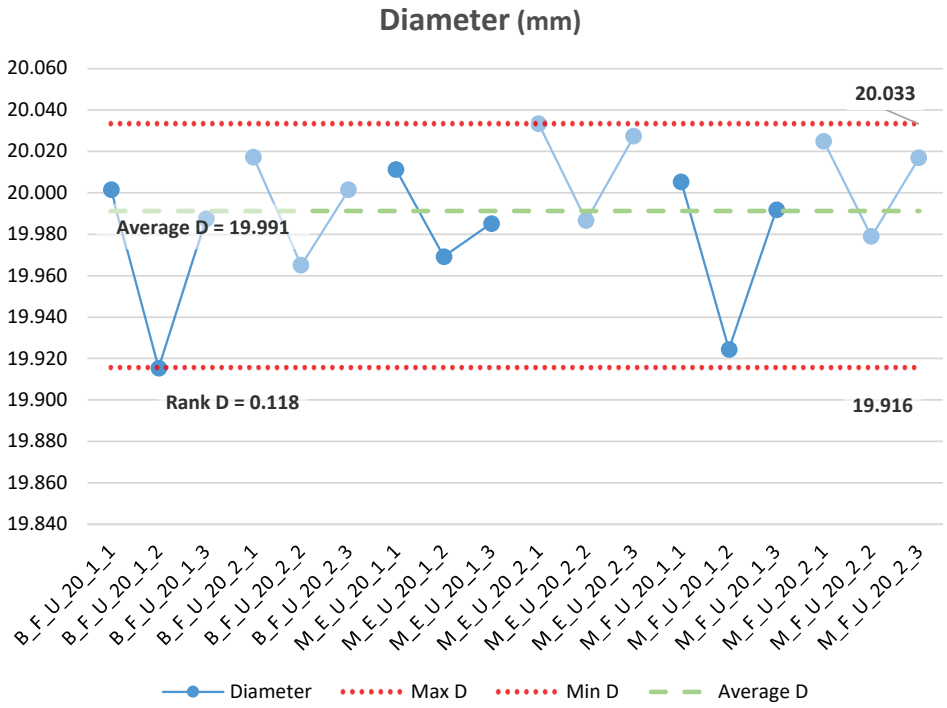


Figure 11. Dimensional quality chart of the different spheres.

Considering the arrangement of the different artifacts on the print tray, it can be observed that among the three possible positions, the intermediate position (position 2) always registers the smallest diameter values. It should also be noted that the values farthest from the nominal diameter, indicating the greatest contraction, correspond to the artifacts with the thinnest walls (1 mm) and internal support (B_F_U_20_1_2 and M_F_U_20_1_2). On the other hand, the average diameter of the spheres in position 3 deviates only 2 μm from the nominal diameter, with the values being closest to the nominal. Additionally, when examining the values corresponding to position 1, it is noted that in all cases, the values are always above the average diameter of all spheres (19.991 μm) and even above the nominal value. Regardless of the design variables and considering only the position on the print tray, it is significant to see the V-shaped distribution of all artifacts, which indicates the influence of the artifact's position.

Regarding geometric quality, the data obtained for the form error (Table 5) shows a behavior similar to that of the diameter. The intermediate position (position 2) records, for all artifacts, the smallest value among the three measured for each type of artifact (the same V-shaped distribution). In this case, the smallest value, 69 μm, was obtained for the artifact M_E_U_20_2_2 (artifact with mushroom geometry, without internal support, oriented upwards, Ø20 mm, 2 mm wall thickness, and in position 2 on the tray), while the largest form error, 178 μm, was recorded for the artifact M_F_U_20_1_3 (artifact with mushroom geometry, with internal support, oriented upwards, Ø20 mm, 2 mm wall thickness, and in position 1 on the tray). In this case, the range of form error measurements is 109 μm, while the average value of all form errors measured by contact is also slightly above one-tenth of a millimeter, 118 μm (Figure 12).

Table 5. Form errors of the spheres.

Tray Location	Artifact Code (Bullet Shape, with Inner Support, Pole Upwards)	Form Error (mm)	Artifact Code (Mushroom Shape, without Inner Support, Pole Upwards)	Form Error (mm)	Artifact Code (Mushroom Shape, with Inner Support, Pole Upwards)	Form Error (mm)
Rear	B_F_U_20_1_1	0.125	M_E_U_20_1_1	0.123	M_F_U_20_1_1	0.132
Center	B_F_U_20_1_2	0.096	M_E_U_20_1_2	0.075	M_F_U_20_1_2	0.112
Front	B_F_U_20_1_3	0.125	M_E_U_20_1_3	0.094	M_F_U_20_1_3	0.142
Rear	B_F_U_20_2_1	0.085	M_E_U_20_2_1	0.089	M_F_U_20_2_1	0.096
Center	B_F_U_20_2_2	0.077	M_E_U_20_2_2	0.075	M_F_U_20_2_2	0.071
Front	B_F_U_20_2_3	0.083	M_E_U_20_2_3	0.088	M_F_U_20_2_3	0.086

It is also observed that the highest geometric quality, with the smallest form errors, is recorded when the artifact walls are 2 mm thick, in both bullet (B) and mushroom (M) configurations. This clear dependency on wall thickness is even more pronounced when the artifact is manufactured without internal support, such that the model M_E_U_20_2_2 exhibits the smallest form error, as previously mentioned.

Additionally, analyzing the residuals obtained from the point clouds captured by contact with the SP25M (Renishaw, Gloucestershire, UK) on the 18 available spheres, it can be noted that all of them exhibit some ovalization error in the horizontal plane (OXY) and some flattening in the vertical direction (Z) across all possible combinations of design variables and positions. As an example, Figure 13 shows the magnified residuals of three evaluated artifacts.

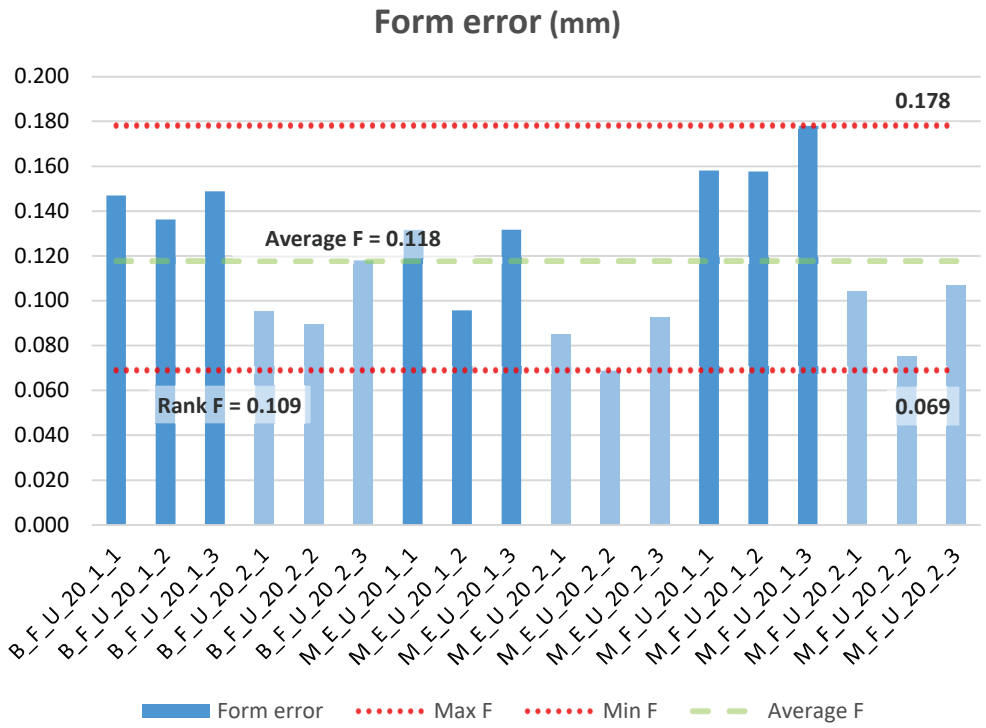
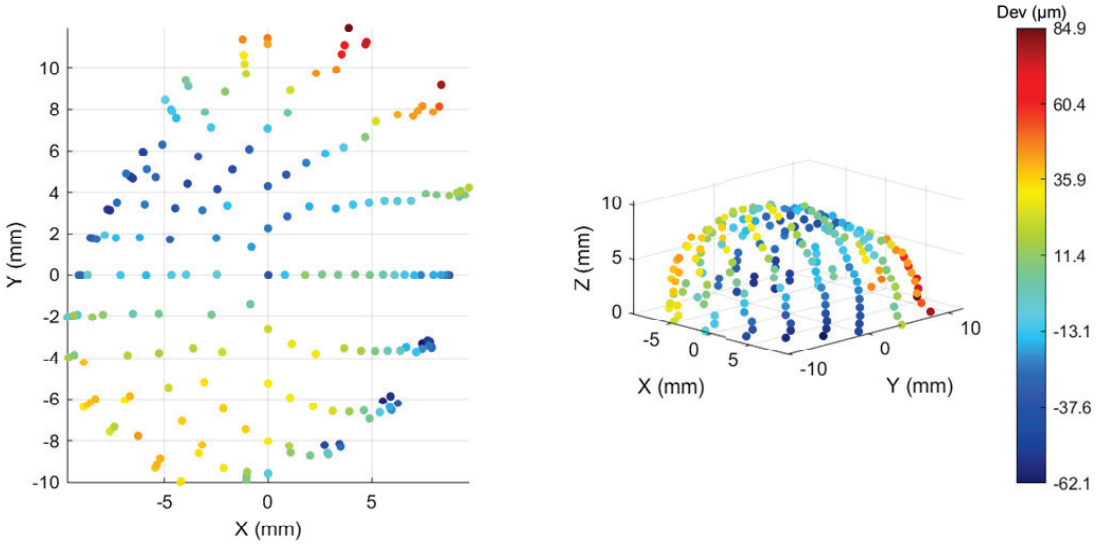
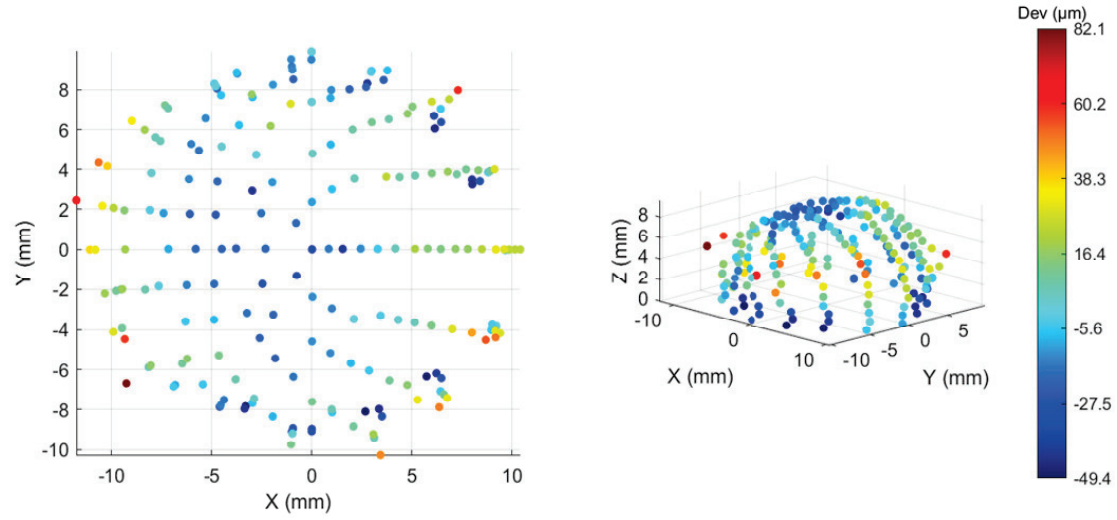


Figure 12. Geometrical quality chart of the different spheres.

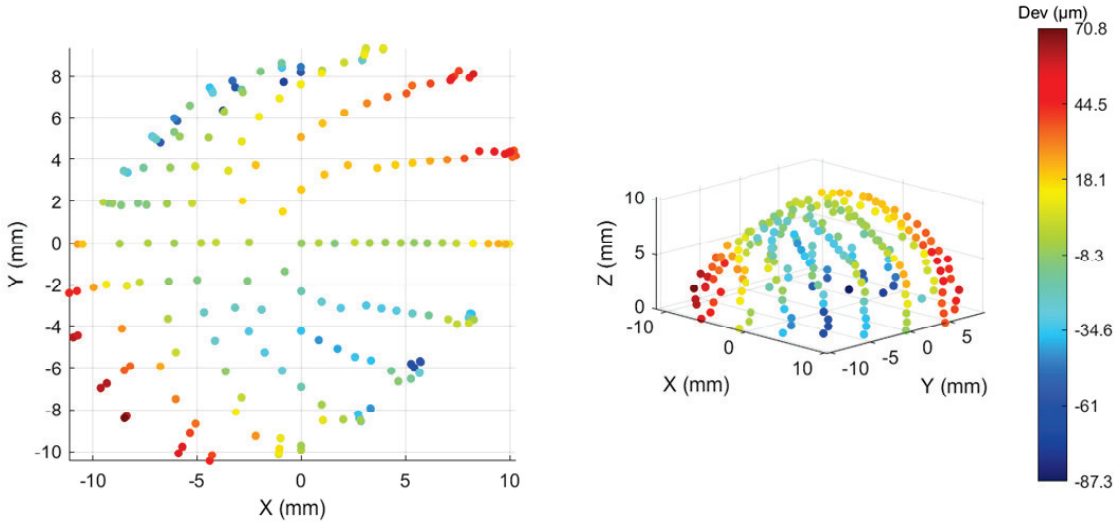


(**a**)

Figure 13. *Cont.*



(**b**)



(**c**)

Figure 13. Examples of residuals with graphical magnification of deviations for different artifacts: (**a**) Bullet & Filled & Upwards B_F_U_20_1_1, (**b**) Mushroom & Empty & Upwards M_E_U_20_1_1 y (**c**) Mushroom & Filled & Upwards M_F_U_20_1_1.

Based on the above observations, it was decided to analyze the influence of process parameters on the quality indicators of the spheres, i.e., to determine whether using a sphere with different shape, infill, thickness, orientation, or position on the printing tray could yield a geometry closer to the nominal (with less diameter deviation and/or less form error). Ultimately, this analysis aimed to identify if a specific combination of design parameters could achieve a sphere with less deformation. The following correlations between design parameters and deviations (DesvD or DesvF) are highlighted from this analysis:

DesvD (Diameter Deviation): There is a correlation between the position in which the spheres are manufactured and the diameter deviation they exhibit. Spheres manufactured in positions 1 or 3 are better, followed by those made in position 2, which in all cases resulted in a smaller average size (Figure 14a).

DesvF (Form Error): (1) There is a correlation between wall thickness and observed form error, being smaller in spheres with a 2 mm thickness than in those with 1 mm (Figure 14b). (2) There is a correlation between infill and form error, with empty spheres (E) performing slightly better than filled ones (F) (Figure 14c). (3) There is some correlation,

though inconclusive, between position and form error, with the best spheres being those in position 2, followed by positions 1 and 3 (Figure 14d).

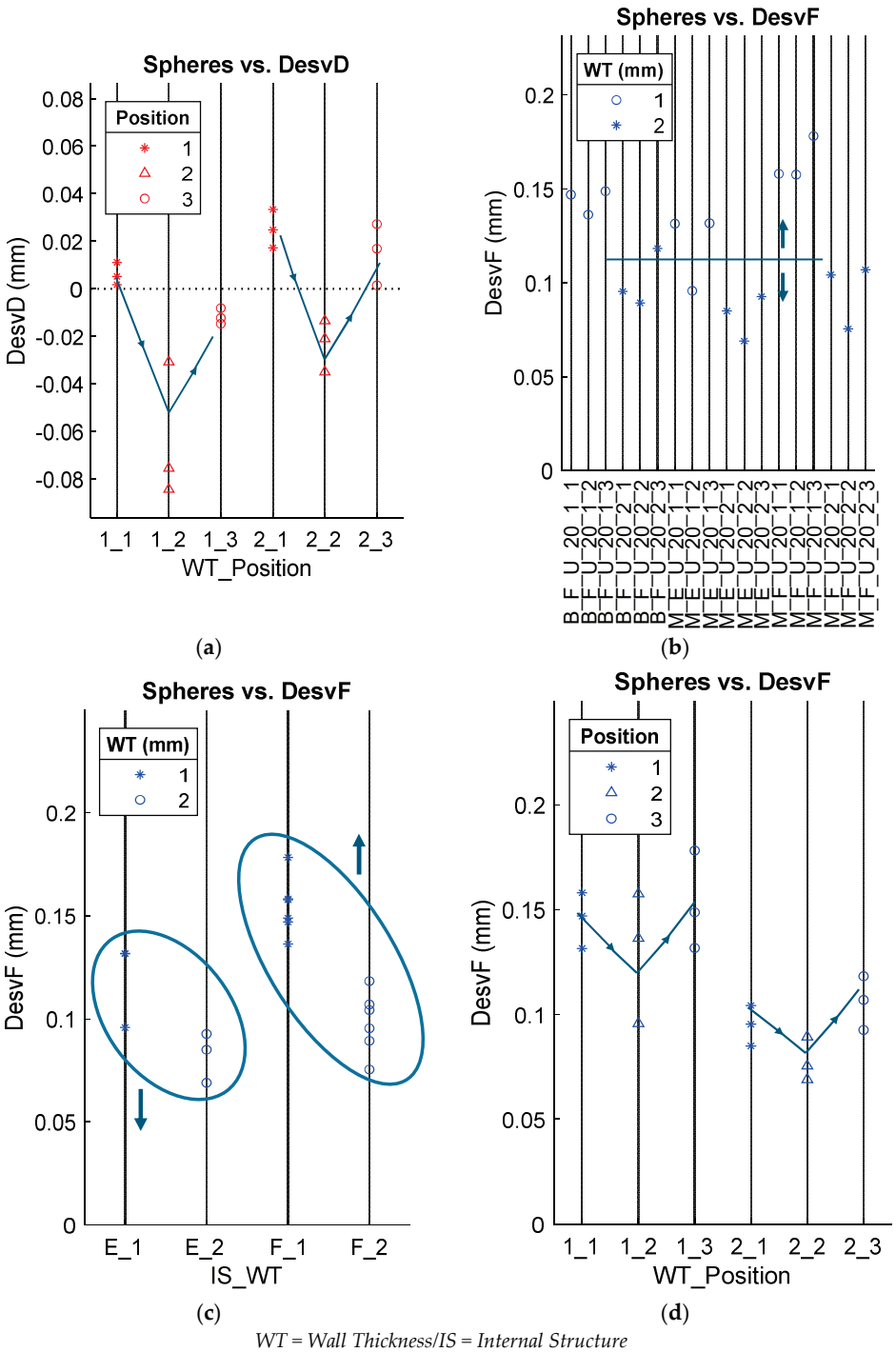


Figure 14. Different correlations between design variables and deviations of diameter and form error. (**a**) Correlation between the position and diameter deviations, (**b**) Correlation between wall thick-ness and form error deviations, (**c**) Correlation between infill and form error deviations, (**d**) Correlation between position and form error deviations.

5. Summary and Conclusions

This work analyses the influence of different design parameters on alumina parts obtained through additive manufacturing. The technology used was stereolithography (SLA) with an ultraviolet laser, and the fabricated parts were spheres with different supports and structures. These fabricated and analyzed artifacts could be used as reference elements or targets in metrological applications. The analysis also considered the position of the parts on the print tray. The influence of parameters (wall thickness, shape, infill, and orientation) was determined for the dimensional analysis of the spheres through the diameter and for the geometric analysis through the form error. The values of both characteristics were obtained by contact measurement of the spheres using a high-precision coordinate measuring machine (CMM). The entire manufacturing process (printing, cleaning, debinding, and sintering) was carried out according to the parameters specified by 3D Ceram, the supplier of the printing machine, the raw material, and the cleaning material.

The maximum deviations found in the diameter range between +33 μm and −84 μm, while the form error deviations range from 69 μm to 178 μm. Although the precision obtained in the diameter is on the order of hundredths and below two-tenths for the form error, these values are considered, a priori, too high for the spheres to be considered as reference elements in low-range metrology. It should be noted that the qualification/calibration spheres used in this range typically have much lower form errors, even submicrometric.

While all parts exhibit slight ovalization in the horizontal plane (OXY) and some flattening along the vertical axis (Z), with errors in the range of tens of micrometers, those positioned in positions 1 and 3 of the print tray (outer positions) show better results concerning the dimension (diameter). These parts not only exhibit less deviation from the nominal value but also show less dispersion in the values of the different spheres. Among these spheres, those fabricated with a 2 mm wall are the best quantitatively. On the other hand, the results indicate that the highest geometric quality of the spheres is achieved in those fabricated with a 2 mm wall, with an empty interior (no internal support) and, again, in position 2 of the print tray. It is clear that a thin wall (1 mm) is not sufficient to prevent deformation during the manufacturing process of alumina spheres via ultraviolet light stereolithography.

In any case, these observed deformations in the spheres could originate from two sources: machine errors and/or process errors. Probably, the deformations result from a combination of both, as the ovalization in the horizontal plane seems to be due to a squaring error of the X and Y axes, while the flattening in the vertical direction appears to be a linear error of the machine's Z axis, or a deformation caused in the material during the sintering process (flattening due to its own weight).

One of the most evident disadvantages observed during the experimentation is the high failure rate in manufacturing (25%) as well as the overall time required for production with this technology. However, these drawbacks are inherent to the process given the current state of development of this technology (ceramic parts manufactured via SLA).

As a summary, and based on the dimensional and geometric error results, it can be concluded that, as of now, the SLA process is not suitable for calibration artifacts in low-range and/or high-precision sensors. However, for medium- and long-range sensors and in the verification of master parts, this technology is viable, as deviations of less than 84 μm in diameter and 178 μm in form errors have been observed.

Future Works

Future studies could focus on validating the process for manufacturing alumina reference spheres which, when placed on supports made of lightweight and thermally stable materials, could be used to qualify medium- and high-range distance meters. There is a clear need to manufacture spheres of suitable sizes for various optical metrology equipment (3D scanners using photogrammetry, structured light, and/or laser profilometers), both portable (handheld models or integrated with AACMMs) and fixed (integrated with CMMs or robotic systems).

The technical feasibility of using ceramic materials as reference elements should be explored, considering their favorable properties such as being relatively lightweight, thermally stable, corrosion-resistant, and optically friendly (non-specular surfaces).

Nevertheless, the need to manufacture spheres of a size appropriate to their measurement field for various optical metrology equipment, both portable and fixed is evident.

In fact, as future work, the production of these elements in larger diameters, up to 50 mm (the limit of the available printing machine's capacity), is planned. This new range of diameters will be particularly important for the verification of medium- and high-range sensors.

Additionally, there is an intention to compare the manufacturing of these ceramic reference elements with other additive manufacturing technologies different from the SLA used in this research, such as Direct Light Processing (DLP) technology.

Author Contributions: Conceptualization, V.M. and P.Z.; methodology, V.M. and E.C.; validation, P.Z., S.G. and L.M.; writing—original draft preparation, V.M.; writing—review and editing, E.C., P.Z., S.G. and L.M.; visualization, S.G. and L.M.; supervision, E.C., P.Z. and S.M.-P.; project administration, V.M. and S.M.-P. All authors have read and agreed to the published version of the manuscript.

Funding: This research was funded by University Institute of Industrial Technology of Asturias (IUTA), grant number SV-23-GIJON-1-01 and also by MICIU/AEI/10.13039/501100011033 and, as appropriate, by "ERDF A way of making Europe", by "ERDF/EU", by the European Union; grant number PID2021–125992OB-I00.

Institutional Review Board Statement: Not applicable.

Informed Consent Statement: Not applicable.

Data Availability Statement: The raw data supporting the conclusions of this article will be made available by the authors on request.

Conflicts of Interest: The authors declare that they have no known competing financial interests or personal relationships that could have appeared to influence the work reported in this paper.

References

1. Chadha, U.; Abrol, A.; Vora, N.P.; Tiwari, A.; Shanker, S.K.; Selvaraj, S.K. Performance evaluation of 3D printing technologies: A review, recent advances, current challenges, and future directions. *Prog. Addit. Manuf.* **2022**, *7*, 853–886. [CrossRef]
2. Dilberoglu, U.M.; Gharehpapagh, B.; Yaman, U.; Dolen, M. The Role of Additive Manufacturing in the Era of Industry 4.0. *Procedia Manuf.* **2017**, *11*, 545–554. [CrossRef]
3. Shahrubudin, N.; Lee, T.C.; Ramlan, R.J.P.M. An overview on 3D printing technology: Technological, materials, and applications. *Procedia Manuf.* **2019**, *35*, 1286–1296. [CrossRef]
4. Bove, A.; Calignano, F.; Galati, M.; Iuliano, L. Photopolymerization of Ceramic Resins by Stereolithography Process: A Review. *Appl. Sci.* **2022**, *12*, 3591. [CrossRef]
5. *ISO/ASTM 52900:2021*; Additive Manufacturing—General Principles—Fundamentals and Vocabulary. International Organization for Standardization (ISO): Geneva, Switzerland, 2021.
6. Kushwaha, A.K.; Rahman, M.H.; Hart, D.; Hughes, B.; Saldana, D.A.; Zollars, C.; Rajak, D.K.; Menezes, P.L. *3*-Fundamentals of stereolithography: Techniques, properties, and applications. *Tribol. Addit. Manuf. Mater.* **2022**, 87–106.
7. Riccio, C.; Civera, M.; Grimaldo Ruiz, O.; Pedullà, P.; Rodriguez Reinoso, M.; Tommasi, G.; Vollaro, M.; Surace, C. Effects of Curing on Photosensitive Resins in SLA Additive Manufacturing. *Appl. Mech.* **2021**, *2*, 942–955. [CrossRef]
8. Zhang, G.; Zou, B.; Wang, X.; Yu, Y.; Chen, Q. Design, manufacturing and properties of controllable porosity of ceramic filters based on SLA-3D printing technology. *Ceram. Int.* **2023**, *49*, 1009–1019. [CrossRef]
9. Pateloup, V.; Michaud, P.; Chartier, T. Optimization of part orientation and adapted supports for manufacturing of ceramic parts by stereolithography using finite element simulations. *Open Ceram.* **2021**, *6*, 100132. [CrossRef]
10. Li, H.; Liu, Y.; Liu, Y.; Hu, K.; Lu, Z.; Liang, J. Investigating the relation between debinding atmosphere and mechanical properties of stereolithography-based three-dimensional printed Al_2O_3 ceramic. *Proc. Inst. Mech. Eng. B J. Eng. Manuf.* **2020**, *234*, 1686–1694. [CrossRef]
11. Li, H.; Liu, Y.; Colombo, P.; Li, W.; Liu, Y.; Hu, K.; Lu, Z. The influence of sintering procedure and porosity on the properties of 3D printed alumina ceramic cores. *Ceram. Int.* **2021**, *47*, 27668–27676. [CrossRef]
12. Li, H.; Liu, Y.; Li, W.; Liu, Y.; Zeng, Q. The effect of sintering on the properties of calcium oxide promoted alumina-based ceramic cores via 3D printing. *Mater. Chem. Phys.* **2021**, *263*, 124443. [CrossRef]

13. Melchels, F.P.; Feijen, J.; Grijpma, D.W. A review on stereolithography and its applications in biomedical engineering. *Biomaterials* **2010**, *31*, 6121–6130. [CrossRef] [PubMed]
14. Cuesta, E.; Alvarez, B.J.; Martinez-Pellitero, S.; Barreiro, J.; Patiño, H. Metrological evaluation of laser scanner integrated with measuring arm using optical feature-based gauge. *Opt. Lasers Eng.* **2019**, *121*, 120–132. [CrossRef]
15. Carmignato, S.; De Chiffre, L.; Bosse, H.; Leach, R.K.; Balsamo, A.; Estler, W.T. Dimensional artefacts to achieve metrological traceability in advanced manufacturing. *CIRP Ann. Manuf. Technol.* **2020**, *69*, 693–716. [CrossRef]
16. Zapico, P.; Meana, V.; Cuesta, E.; Mateos, S. Optical Characterization of Materials for Precision Reference Spheres for Use with Structured Light Sensors. *Materials* **2023**, *16*, 5443. [CrossRef] [PubMed]
17. Harmatys, W.; Gąska, P.; Gąska, A.; Gruza, M.; Jedynak, M.; Kobiela, K.; Marxer, M. Applicability Assessment of Different Materials for Standards Ensuring Comparability of Optical and Tactile Coordinate Measurements. *Materials* **2022**, *15*, 4128. [CrossRef] [PubMed]
18. Cai, Y.; Xie, B.; Ling, S.; Fan, K.C. On-Line Measurement Method for Diameter and Roundness Error of Balls. *Nanomanuf. Metrol.* **2020**, *3*, 218–227. [CrossRef]
19. *DIN 5401: 2002-08*; Rolling Bearings—Balls for Rolling Bearings and General Industrial Use. DIN: Berlin, Germany, 2002.
20. Meana, V.; Cuesta, E.; Álvarez, B.J. Testing the Sandblasting Process in the Manufacturing of Reference Spheres for Non-Contact Metrology Applications. *Materials* **2021**, *14*, 5187. [CrossRef] [PubMed]
21. Martínez-Pellitero, S.; Souto, A.M.; Peláez Peláez, S.; Barreiro García, J.; Castro Sastre, M.Á. Design of supports to avoid deformations in the process of alumina printing by stereolithography. *Key Eng. Mat.* **2023**, *958*, 67–75. [CrossRef]
22. *ISO 10360-2:2009*; Geometrical Product Specifications (GPS)—Acceptance and Reverification Tests for Coordinate Measuring Machines (CMM): Part 2: CMMs Used for Measuring Linear dimensions. International Organization for Standardization (ISO): Geneva, Switzerland, 2009.
23. *ISO 10360-5:2010*; Geometrical Product Specifications (GPS)—Acceptance and Reverification Tests for Coordinate Measuring Systems (CMS)—Part 5: Coordinate Measuring Machines (CMMs) Using Single and Multiple Stylus Contacting Probing Systems Using Discrete Point and/or Scanning Measuring Mode. International Organization for Standardization (ISO): Geneva, Switzerland, 2010.
24. Pfaffinger, M.; Mitteramskogler, G.; Gmeiner, R.; Stampfl, J. Thermal Debinding of Ceramic-Filled Photopolymers. *Mater. Sci. Forum* **2015**, *825*, 75–81. [CrossRef]

Disclaimer/Publisher's Note: The statements, opinions and data contained in all publications are solely those of the individual author(s) and contributor(s) and not of MDPI and/or the editor(s). MDPI and/or the editor(s) disclaim responsibility for any injury to people or property resulting from any ideas, methods, instructions or products referred to in the content.

applied sciences

MDPI

Article

Three-Dimensional Printed Attachments: Analysis of Reproduction Accuracy Compared to Traditional Attachments

Angela Mirea Bellocchio, Elia Ciancio, Ludovica Ciraolo, Serena Barbera and Riccardo Nucera *

Department of Biomedical and Dental Sciences and Morpho-Functional Imaging, Section of Orthodontics, School of Dentistry, University of Messina, 98125 Messina, Italy; angelamirea@live.it (A.M.B.); ciancioelia.97@hotmail.it (E.C.); ludovicaciraolo@gmail.com (L.C.); serena.barbera93@gmail.com (S.B.)
* Correspondence: riccardo.nucera@unime.it; Tel.: +39-3286976304

Abstract: Background: The aim of this study was to propose a new 3D printing method for attachment production and compare the reproduction accuracy of traditional attachments with the proposed 3D-printed attachments. Methods: A standardized 3D model attachment was created with the dimensions of 3, 2, and 2 mm for the apico-coronal, mesio-distal, and vestibulo-lingual dimensions, respectively. A 3D ideal model of the maxillary arch was used to apply four standardized attachments on the vestibular surface of selected teeth. The obtained model with placed attachments was used to reproduce composite attachments via the conventional method. A transfer template was used to bond with the flow composite resin 3D-printed attachment on a new arch model without attachments. The models with traditional attachments and 3D-printed attachments were scanned and overlapped with the original CAD model with attachments. To assess the attachment precision, vertical and horizontal cutting planes were used on the overlapped models. The outcome selection focused on puff analysis (excess composite material evaluation) and shape analysis (attachment accuracy evaluation). Results: The results indicated that the 3D-printed attachments showed significant differences ($p < 0.05$) compared to the traditional attachments. The descriptive statistics showed the higher discrepancies compared to the CAD model of the traditionally created attachments in the shape (0.85 mm) and puff dimension (1.02 mm). Conclusion: Custom 3D-printed attachment production is an effective method for achieving greater attachment precision.

Keywords: aligners; attachments; digital dentistry; 3D-printed attachments; reproduction accuracy; attachment manufacture

1. Introduction

In recent years, there has been an increase in patients needing aesthetic orthodontic treatment such as clear aligner therapy. The influence of traditional orthodontic appliances, such as brackets, on patients' aesthetic perceptions and quality of life has been widely studied. For example, Barrera-Chaparro and colleagues examined the orthodontic treatment need, types of brackets, and oral health-related quality of life, highlighting the importance of considering these factors in treatment planning [1].

In addition to the aesthetic impact of orthodontic appliances, patients increasingly seek optimal aesthetic results by focusing on, for example, the incisor position and arch symmetry; therefore, the current orthodontic research focuses on improving the performance of clear aligners during orthodontic treatment, which is also associated with the use of mini-screws to address complex treatments in order to combine the aesthetic need during treatment and the need for an optimal aesthetic result [2,3].

In addition to the cosmetic aspect, the literature has also focused on the effects of aligner treatment on tooth structures by comparing it to conventional treatment with special attention paid to root resorption; some studies have shown minimal or insignificant differences in root resorption between the two treatment groups, while others have suggested

that patients treated with clear aligners may have slightly lower levels of root resorption than those treated with fixed brackets [4–7].

The literature has also addressed the advantages of aligner removability. In fact, although the ability to remove the aligner is an advantage because it makes it less invasive for patients by allowing better oral hygiene than traditional fixed braces [8], it can also be a disadvantage because it requires patient cooperation [9].

The performance of aligner therapy is related to aligner and attachment characteristics [10].

To improve the performance of aligners in managing tooth movement, the use of attachments was introduced [11].

Attachments are composite buttons that are transferred to the tooth surface using an adhesive technique through a template. They serve as a force transfer device from the aligner to the tooth, enhance retention, and improve specific tooth movements [11,12].

Attachments can have different designs, with various shapes and sizes, chosen according to the planned tooth movement. These supports are virtually placed and subsequently bonded on the tooth surfaces using specific placement templates [13–15].

The clinical reproduction of the attachment shape is influenced by various clinical variables, such as the transfer template material [10,16], the attachment construction material [17], and the type of polymerization [18].

This study's aim is to propose a new technique for attachment reproduction. It involves the creation of attachments with 3D printing technology and the subsequent bonding of pre-made attachments with assisted clear templates. Moreover, this study aims to compare traditional attachment fabrication and the originally proposed technique in terms of the reproduction accuracy.

2. Materials and Methods

The research protocol was reviewed and approved by the Ethics Committee of the University of Messina (Prot.33-20 obtained on 4 March 2020). The following experimental study was conducted according to the guidelines of the Declaration of Helsinki.

The sample for this experimental study included an STL file of the dental cast records of 30 subjects (mean age 30.9 $\pm$ 7.0 y.o.), including 15 males (mean age 31.2 $\pm$ 7.7 y.o.) and 15 females (mean age 30.7 $\pm$ 5.2 y.o.) selected from the digital archive of the Orthodontic Clinic of the University Polyclinic of Messina.

The selection criteria for the included patients were as follows:

- Permanent dentition.
- Patients with Class I malocclusion.

The exclusion criteria were as follows:

- Patients with dental caries.
- Gingival recessions.
- Crown or periodontal abnormalities.
- Presence of dental crowding.

For each selected patient, the upper model was imported into the Meshmixer software (Autodesk Inc., San Francisco, CA, USA). A geometric tridimensional object with a parallelepiped shape was imported into the software interface and used as the attachment for the aligner therapy. The parallelepiped presented the following dimensions: 3, 2, and 2 mm for the apico-coronal, mesio-distal and vestibulo-lingual dimensions, respectively. This attachment was duplicated three times in order to obtain four identical attachments.

The parallelepiped attachments created were then placed on the vestibular faces of 1.1, 2.1, 1.6 and 2.6 and consequently overlapped, moving the attachment 0.3 mm in the direction of the vestibular surface.

The attachments were merged along with the upper model to constitute a single STL file (stereolithographic file format), named Model Master (MM) (Figure 1).

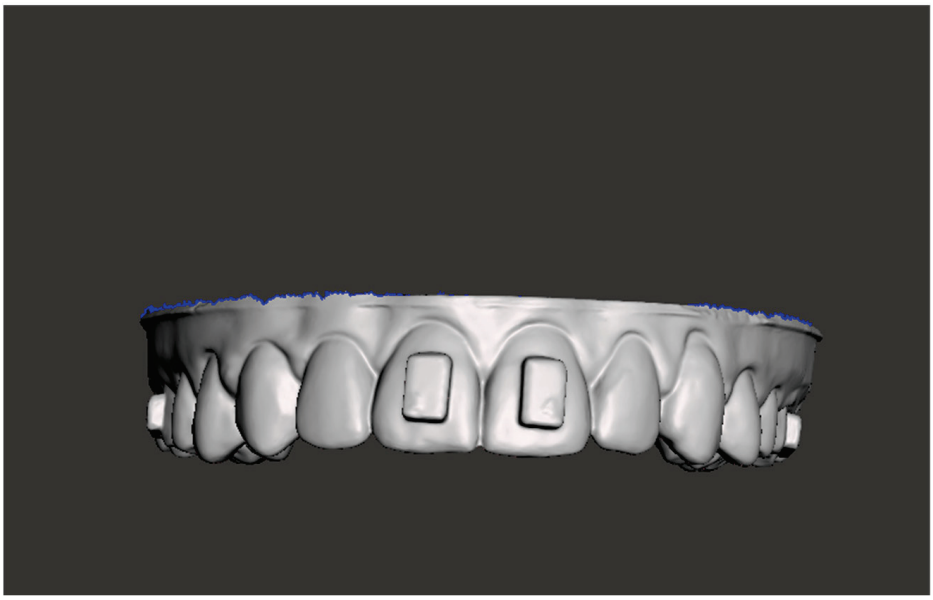


Figure 1. Model Master (MM).

The Boolean operation was performed by subtracting the model from the attachment shape, thus obtaining attachments with a customized base plate according to the dental anatomy.

Subsequently, the created custom attachments (CA), the MM model, and two models without attachments (M1, M2) were produced by a 3D printing process using a Liquid Crystal Precision 1.5 3D printer (Photocentric Inc., Avondale, AZ, USA) with Daylight Precision Dental Model White Resin (Photocentric Inc., Avondale, AZ, USA) (Figure 2).

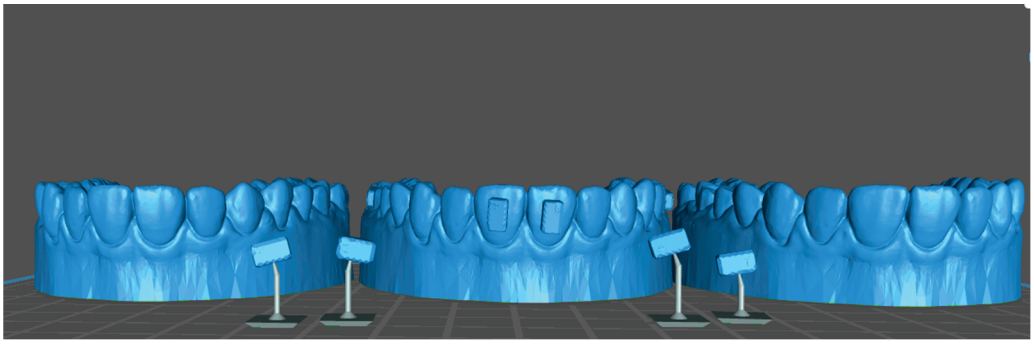


Figure 2. Printing plate on the CHITUBOX program: 2 models without attachment, 1 with attachment (MM), and custom 4 attachments.

The MM model was used to fabricate, via the thermoforming process (Erkoform 3D Motion, Erkodent Erich Kopp GmbH, Pfalzgrafenweiler, Germany), the 0.8 mm glycol-modified polyethylene terephthalate transfer template (Pet-G-Erkodur, Erkodent Erich Kopp GmbH, Pfalzgrafenweiler, Germany) used to support the clinician in the attachment-bonding process.

This template will be used for both the clinical formation of the traditional attachments (TA) and the transfer of the 3D-printed attachments (CA) (Figure 3).



Figure 3. Thermoformed transfer templates were used for the two bonding protocols.

2.1. Attachment Transfer: Operating Procedure

After obtaining the MM model, two transfer templates were created using two sheets of 0.8 mm PET-G to facilitate the two bonding procedures:

- Bonding of 3D-printed attachments (CA)
- Bonding of traditional attachment (TA)

The bonding procedure for the 3D-printed attachments was carried out by dividing the transfer template into three pieces. The custom 3D-printed attachment was inserted into the transfer template and a standardized (a drop of flow composite that covered about 50% of the attachment surface) amount of flow composite (Enaflow-Micerium Spa, Avegno, Genoa, Italy) was applied for bonding. Adhesive was then applied into the model, and each part of the template was inserted into the model and cured with a UV Grand Valo lamp (Ultradent, 505 West Ultradent Drive South Jordan, UT 84095, USA) (Figure 4).



Figure 4. Three-dimensional printed bonding attachment protocol: Placement of the attachment in the template and positioning of the flow composite.

The traditional transfer procedure involved the creation of a direct-flow attachment (Enaflow-Micerium Spa, Avegno, Genoa, Italy). Inside the special slot created in the transfer template, the flow composite was inserted, then the adhesive was applied in the model, and finally, through the transfer template inserted in the model the attachments were

transferred and cured. The attachments were created with flow composite according to the previously standardized procedure.

The models with the conventional attachments and the model with the bonded 3D-printed attachment were both scanned with the Maestro 3D MDS500 Desktop Scanner (AGE Solutions S.r.l., Pisa, Italy; www.maestro3d.com).

Each model with attachments (CA and TA) was digitally superimposed into the Master model (MM) using exocad 2.2 Valletta (DentalCAD; exocad GmbH, Darmstadt, Germany) software to assess the precision of the attachment fabrication through the two distinct procedures.

The discrepancies between the overlapping models were evaluated using the following two cutting planes:

- Vertical (following the long axis of the tooth).
- Horizontal (perpendicular to the long axis of the tooth) (Figure 5).

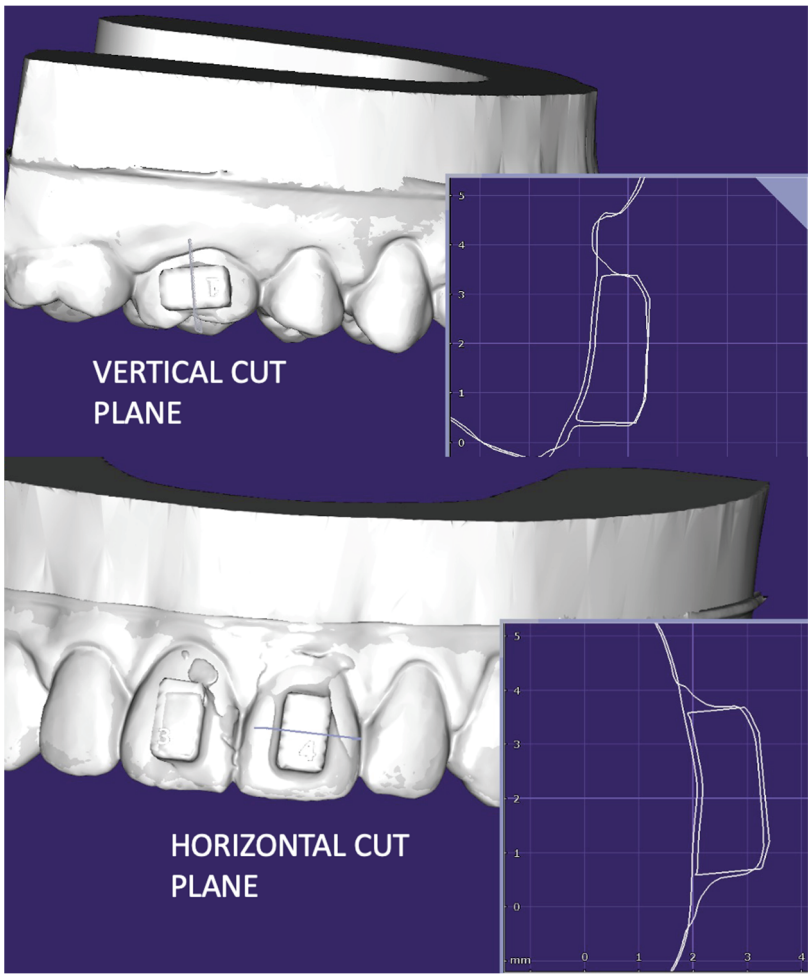


Figure 5. Reference planes used to assess discrepancies: The vertical cutting plane (Ver) and the horizontal cutting plane (Hor).

Measurements were performed between the two attachment profiles.

In the vertical cutting plane, the comparison of the superimposed models involved the assessment of two key outcomes:

- Puff analysis

The amount of excess composite material at the level of the attachment–model interface was measured. The excess composite was measured in the most gingival portion

(GverpuffPoint) and the occlusal portion (OverpuffPoint), and the greatest model profile discrepancy was estimated (Figure 6).

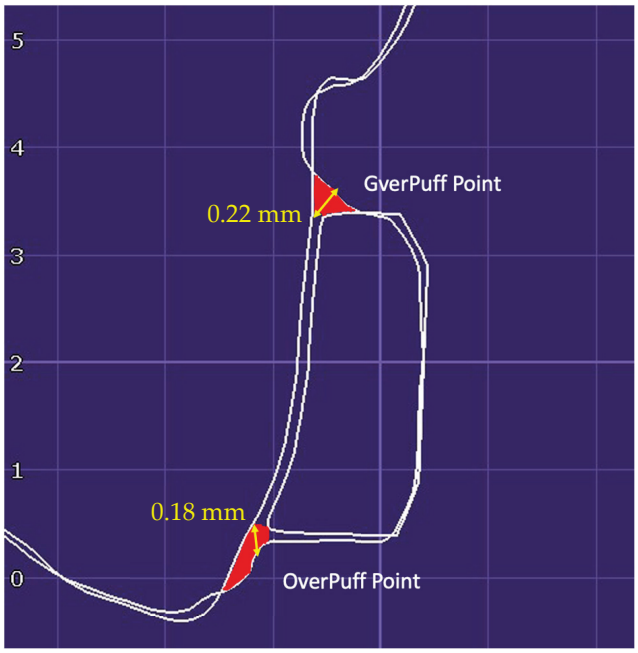


Figure 6. Measuring points used for the puff analysis in the vertical cutting plane.

- Shape analysis

The analysis focused on the accuracy of the shape of the attachment. The shape analysis evaluated the average discrepancy of the two considered attachment profiles at three different levels: the gingival level (GvershapePoint), central level (CvershapePoint), and occlusal level of the attachment (OvershapePoint) (Figure 7).

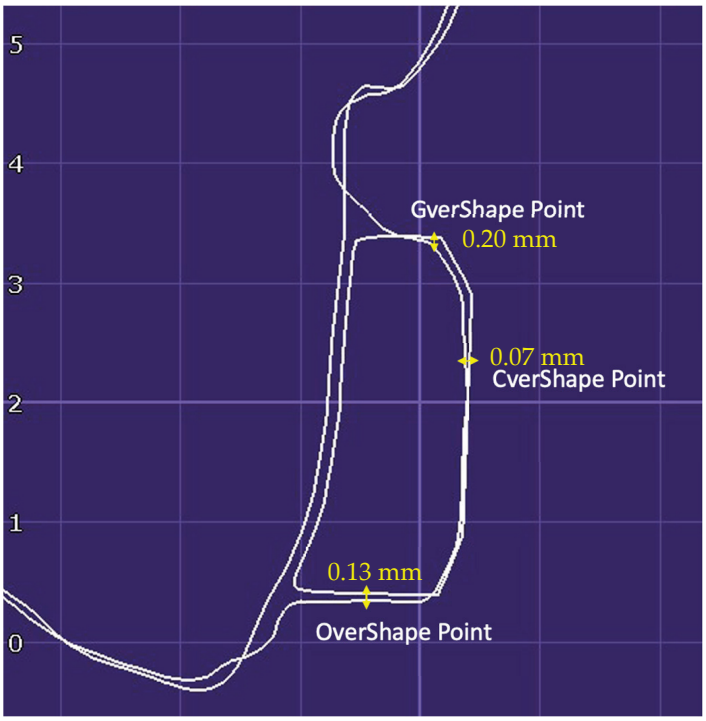


Figure 7. Measuring points used for the shape analysis in the vertical cutting plane.

On the horizontal shear plane, the same assessment was performed:

Puff Analysis

The assessment was carried out at the points of maximum mesial (MhorpuffPoint) and distal discrepancies along the attachment–model interface (DhorpuffPoint) (Figure 8).

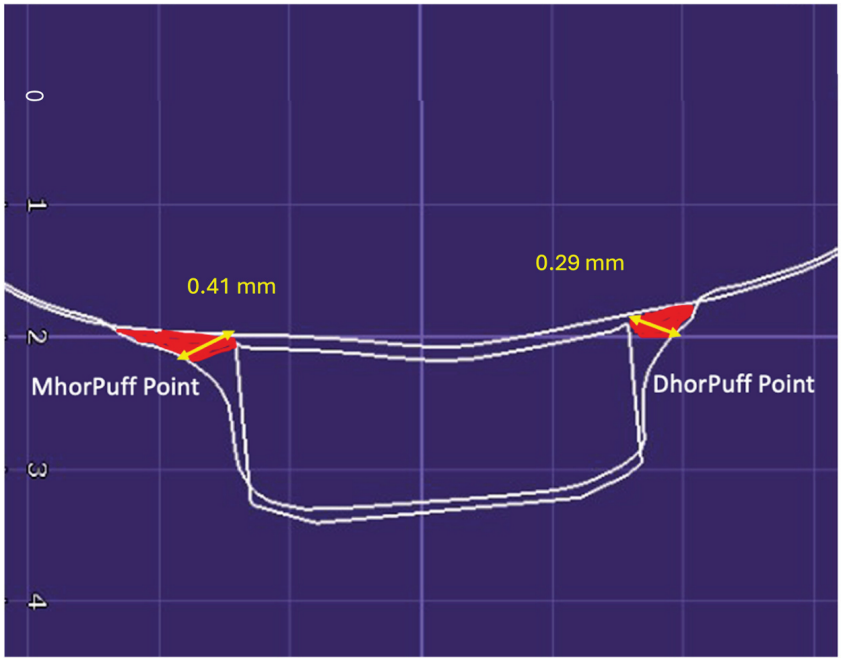


Figure 8. Measuring points used for the puff analysis in the horizontal cutting plane.

Shape Analysis

The accuracy of the shape of the attachment at the midpoint of the discrepancy was assessed at the mesial (MhorshapePoint), central (ChorshapePoint), and distal profiles of the attachment (DhorshapePoint) (Figure 9).

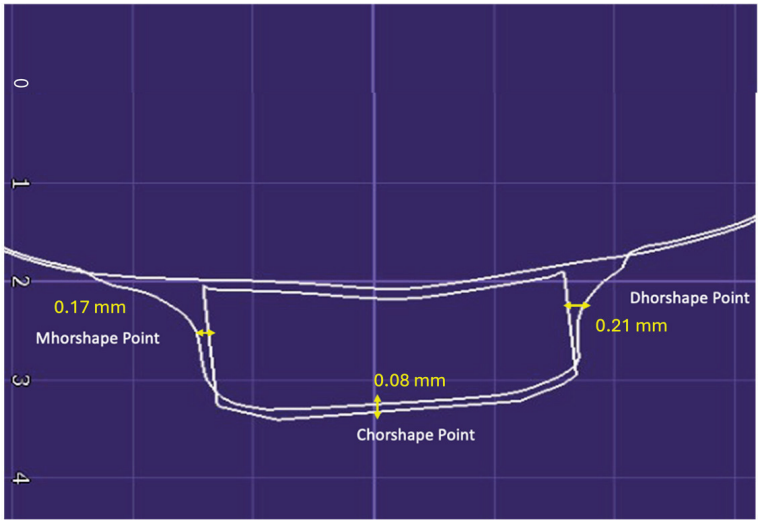


Figure 9. Measuring points used for the shape analysis in the horizontal cutting plane.

For each attachment, 16 cutting sections were evaluated and 40 measurements were performed.

2.2. Statistical Analysis

The statistical analyses were carried out using SPSS statistical software, version 25.0 (IBM Corporation, Armonk, NY, USA). The significance levels were set at $p < 0.05$. The normality of the data distribution was evaluated using the Shapiro–Wilk test, and Levene's test was applied to assess the homogeneity of the variance. Parametric ANOVA multiple comparison tests were utilized for the inferential statistics.

Methodological Error Assessment:

To evaluate the methodological error associated with the scanning and model overlapping procedures, a comparison was performed between the outcomes of the MA-CA and MA-TA models. The intra-operator reliability was assessed using paired T-tests and the intraclass correlation coefficient (ICC). The magnitude of the random error was determined using Dahlberg's formula. No statistically significant differences ($p < 0.05$) were observed between the two assessments, indicating high reliability. A preliminary power analysis was performed on the first five patients enrolled according to the methodology described above.

The analysis was conducted by considering the preliminary mean difference values between the results evaluating the relative linear discrepancy GvershapePoint MM vs. GvershapePoint CA and GvershapePoint MM vs. GvershapePoint TA. The value obtained between the averages was 0.51 mm and the standard deviation (SD) was 0.38 mm. These values were used as the results to perform the power analysis calculation.

The analysis was performed with a power of 80% and the significance level was set at 0.05.

The analysis showed a sample size of 27 cases. Enrollment was set at 30 patients to minimize the risk of false negatives.

3. Results

The findings of this study indicate that the discrepancies in the attachment shape between the planned design and the actual attachment were more pronounced for the traditionally created attachments compared to those produced through 3D printing. Specifically, descriptive statistics revealed larger disparities in shape (0.85 mm) (Table 1) and puff (Table 2) (1.02 mm) for the traditionally created attachments, particularly at the gingival level.

Table 1. Vertical and horizontal outcomes considered in the shape analysis.

	Materials	**Tooth**	**GverShapePoint**			**CverShapePoint**			**OverShapePoint**		
			Mean ± SD (mm)	Min (mm)	Max (mm)	Mean ± SD (mm)	Min (mm)	Max (mm)	Mean ± SD (mm)	Min (mm)	Max (mm)
Vertical Cutting Plane	MM-TA	2.6	0.53 ± 0.24	0.15	0.85	0.19 ± 0.1	0.09	0.35	0.19 ± 0.03	0.15	0.22
	MM-TA	2.1	0.44 ± 0.23	0.07	0.65	0.22 ± 0.17	0.04	0.51	0.14 ± 0.15	0.04	0.39
	MM-TA	1.1	0.71 ± 0.04	0.68	0.78	0.15 ± 0.06	0.04	0.2	0.09 ± 0.08	0.04	0.24
	MM-TA	1.6	0.36 ± 0.16	0.16	0.57	0.26 ± 0.15	0.13	0.44	0.15 ± 0.05	0.08	0.19
	MM-CA	2.6	0.13 ± 0.06	0.06	0.22	0.05 ± 0.03	0.02	0.1	0.14 ± 0.07	0.06	0.21
	MM-CA	2.1	0.13 ± 0.04	0.07	0.17	0.06 ± 0.04	0.01	0.13	0.23 ± 0.05	0.17	0.3
	MM-CA	1.1	0.09 ± 0.07	0.02	0.2	0.08 ± 0.05	0.02	0.13	0.20 ± 0.1	0.05	0.3
	MM-CA	1.6	0.19 ± 0.11	0.09	0.32	0.23 ± 0.21	0.04	0.5	0.20 ± 0.13	0.05	0.4
	Materials	**Tooth**	**MhorShapePoint**			**ChorShapePoint**			**DhorShapePoint**		
			Mean ± SD (mm)	Min (mm)	Max (mm)	Mean ± SD (mm)	Min (mm)	Max (mm)	Mean ± SD (mm)	Min (mm)	Max (mm)
Horizontal Cutting Plane	MM-TA	2.6	0.25 ± 0.12	0.12	0.43	0.17 ± 0.09	0.07	0.29	0.22 ± 0.1	0.11	0.35
	MM-TA	2.1	0.08 ± 0.05	0.03	0.14	0.15 ± 0.05	0.1	0.22	0.14 ± 0.05	0.09	0.22
	MM-TA	1.1	0.15 ± 0.06	0.11	0.24	0.15 ± 0.06	0.05	0.2	0.08 ± 0.03	0.06	0.14
	MM-TA	1.6	0.38 ± 0.32	0.1	0.9	0.28 ± 0.15	0.1	0.47	0.31 ± 0.11	0.16	0.46
	MM-CA	2.6	0.16 ± 0.07	0.06	0.23	0.05 ± 0.03	0.01	0.07	0.08 ± 0.04	0.03	0.14
	MM-CA	2.1	0.08 ± 0.03	0.05	0.12	0.05 ± 0.04	0.02	0.11	0.13 ± 0.08	0.04	0.23
	MM-CA	1.1	0.21 ± 0.17	0.07	0.43	0.07 ± 0.03	0.03	0.09	0.17 ± 0.11	0.01	0.29
	MM-CA	1.6	0.19 ± 0.08	0.11	0.32	0.22 ± 0.2	0.04	0.45	0.12 ± 0.11	0.02	0.5

MM, TA, and CA indicate Model Master, traditional attachment, and customized attachment.

Table 2. Vertical and horizontal outcomes considered in the puff analysis.

	Materials	**Tooth**	**OverPuffPoint**			**GverPuffPoint**		
			Mean ± SD (mm)	Min (mm)	Max (mm)	Mean ± SD (mm)	Min (mm)	Max (mm)
Vertical Cutting Plane	MM-TA	2.6	0.39 ± 0.34	0.1	0.87	0.65 ± 0.42	0.05	1.02
	MM-TA	2.1	0.29 ± 0.01	0.28	0.3	0.32 ± 0.08	0.21	0.42
	MM-TA	1.1	0.34 ± 0.08	0.28	0.47	0.42 ± 0.22	0.27	0.8
	MM-TA	1.6	0.27 ± 0.14	0.08	0.4	0.31 ± 0.14	0.2	0.55
	MM-CA	2.6	0.28 ± 0.24	0.1	0.68	0.48 ± 0.35	0.08	0.92
	MM-CA	2.1	0.34 ± 0.19	0.18	0.66	0.16 ± 0.1	0.09	0.32
	MM-CA	1.1	0.28 ± 0.12	0.17	0.43	0.20 ± 0.07	0.11	0.29
	MM-CA	1.6	0.26 ± 0.19	0.01	0.5	0.43 ± 0.27	0.15	0.74
			DhorPufPoint			**MhorPuffPoint**		
Horizontal Cutting Plane			Mean ± SD (mm)	Min (mm)	Max (mm)	Mean ± SD (mm)	Min (mm)	Max (mm)
	MM-TA	2.6	0.28 ± 0.13	0.09	0.44	0.35 ± 0.09	0.24	0.45
	MM-TA	2.1	0.41 ± 0.05	0.34	0.47	0.26 ± 0.06	0.17	0.31
	MM-TA	1.1	0.20 ± 0.06	0.15	0.3	0.43 ± 0.07	0.33	0.5
	MM-TA	1.6	0.30 ± 0.17	0.14	0.5	0.24 ± 0.05	0.17	0.31
	MM-CA	2.6	0.18 ± 0.07	0.1	0.29	0.21 ± 0.07	0.09	0.27
	MM-CA	2.1	0.3 ± 0.06	0.24	0.38	0.24 ± 0.1	0.1	0.38
	MM-CA	1.1	0.25 ± 0.19	0.09	0.58	0.34 ± 0.19	0.13	0.62
	MM-CA	1.6	0.24 ± 0.2	0.02	0.5	0.29 ± 0.15	0.08	0.46

MM, TA, and CA indicate Model Master, traditional attachment, and customized attachment.

Furthermore, inferential statistics were employed to assess which type of attachment, traditional or 3D-printed, demonstrated fewer deviations from the planned design. The results revealed that the 3D-printed attachments exhibited greater accuracy in terms of the shape reproduction and displayed less puff at the attachment–model interface compared to traditionally created attachments (Table 3).

Table 3. Inferential statistics and multiple comparisons (univariate ANOVA). [a] means significant differences with $p < 0.05$ were detected; [b] means no significant differences were detected.

	MM-TA vs. MM-CA				
	GverShape Point	CverShape Point	OverShape Point	OverPuff Point	GverPuff Point
VERTICAL CUTTING PLANE	0.01 [a]	0.02 [a]	0.032 [a]	0.47 [b]	0.05 [a]
	Mhorshape Point	Chorshape Point	Dhorshape Point	Mhorshape Point	Dhorpuff Point
HORIZONTAL CUTTING PLANE	0.432 [b]	0.01 [a]	0.07 [a]	0.22 [a]	0.083 [b]

	MM-TA vs. MM-CA	
	Vertical	**Horizontal**
Analysis of the Shape	0.01 [a]	0.01 [a]
Analysis of the Puff	0.031 [a]	0.048 [a]

MM, TA, and CA indicate Model Master, traditional attachment, and customized attachment.

These findings suggest that utilizing 3D printing technology for attachment creation may lead to improved accuracy and reduced discrepancies between the planned and actual attachment shapes, particularly when compared to traditional attachment fabrication methods.

4. Discussion

The attachments used in clear aligner therapy are intended to enhance the clinical performance of orthodontic treatment. The inadequate design or placement of these attachments could hinder their ability to exert the necessary force to achieve the desired dental

positioning [11]. Another factor influencing the effectiveness of clear aligner treatment and its clinical results is the accuracy of replicating the shape of the attachments [17,19].

Many studies have assessed the effects of various forms of attachments on dental movement [13,18,20,21].

However, only a limited number of studies have evaluated the accuracy of reproducing the programmed shape required for the desired tooth displacement [17,19].

To the best of our knowledge, this is the first study in the literature that proposes 3D-printed custom attachments and evaluates their reproduction accuracy of the planned shape and the presence of blowouts after bonding compared with traditional attachments created from composite flow.

The accuracy of attachment replication can be affected by various factors, including the material of the transfer template, the material composition of the attachment, and the intraoperative skill of the operator.

A recent study [19] assessed the accuracy and reproducibility of the attachment shape by comparing the attachment transfer with two different types of templates: Pet-G (glycol-modified polyethylene terephthalate template) and PE (polyethylene template); the study concluded that Pet-G allows more accurate reproduction of the attachment shape than PE. In addition, these authors also evaluated the influence of composite resin materials with different viscosities in reproducing the shape of the attachments, revealing that the accuracy of high-viscosity and low-viscosity composites is equivalent.

Other authors carried out a comparative analysis of flowable and packable composite materials [22], concluding that flowable composite materials necessitated less time for preparation and showing no statistically significant differences in terms of damage when compared to packable composites at the one-year evaluation. More authors have shown that 3D-printed materials offer good accuracy and reproducibility of details, including composite attachments; however, they may show lower strength than traditional materials, especially in terms of the resistance to forces applied during orthodontic treatment [23]. Based on data from the previous literature [19,22], a PET-G template was used in the present study to transfer both the traditional and 3D-printed attachments; in addition, the use of a flow composite was chosen to create the traditional attachments.

The results of this study show statistically significant differences ($p < 0.05$) in the accuracy between the 3D-printed custom attachments and the traditional flow-made attachments.

On average, the 3D-printed custom attachments exhibited over 50% higher accuracy, with the most significant discrepancies observed on the gingival side. The greater inaccuracy in transferring the attachments at the gingival level (0.78 mm) can be due to the "tenting effect" that occurs during the thermoforming process. The tenting effect is when the thermoformed material tends to pull upward along the gingival as it cools [24].

This phenomenon can lead to challenges in achieving the optimal adherence of the thermoformed tray to the teeth, especially in the gingival area, resulting in a greater inaccuracy in the shape reproduced in the template and, consequently, in the final attachment shape. These results are consistent with the study conducted by Park SY and colleagues, in which the median gap of thermoformed transparent aligners was evaluated using micro CT and a spectrophotometer, showing that the median gap at the gingival level consistently exceeded that at the occlusal surface [25].

Another factor contributing to the greater inaccuracy of traditional bindings made from flow composite is the difficulty of standardizing the amount of composite material used during the creation of the binding, which can lead to an inconsistency between the programmed shape and the actual shape. On the contrary, the use of custom 3D-printed attachments allows for better standardization of the composite amount flow during the bonding procedure by using a standardized amount of composite.

The findings of this research indicate the potential benefits of customized 3D-printed attachments in the clear aligner therapy. However, additional investigations are necessary to assess the clinical impact of different amounts of attachment accuracy reproduction on

the efficacy of clear aligners when it comes to achieving different types of dental movement. The limitation of this study is that the reliability of the reproducibility of the attack in relation to the different possible forms is not evaluated. In the future, well-designed clinical studies with a control group will be able to better evaluate these aspects of clear aligner therapy.

5. Conclusions

The presence of puffs in 3D-printed custom attachments is significantly reduced compared to the puffs present at the attachment–model interface of traditional attachments.

In the future, custom attachments made by 3D printing could be a valid alternative to traditional attachments made to improve attachment reproduction.

Author Contributions: Conceptualization, A.M.B., E.C., L.C., S.B., R.N., A.M.B., E.C., L.C. and S.B.; methodology, A.M.B., E.C., L.C., S.B. and R.N.; software, A.M.B., E.C. and L.C.; validation, A.M.B., E.C. and L.C.; formal analysis, A.M.B. and E.C.; investigation, A.M.B., E.C., L.C. and S.B. resources, A.M.B., E.C., L.C. and S.B.; data curation, A.M.B., E.C., L.C. and S.B.; writing—original draft preparation, A.M.B. and R.N.; writing—review and editing, A.M.B. and R.N.; visualization, A.M.B. and R.N.; supervision, A.M.B. and R.N.; project administration, A.M.B. and R.N.; funding acquisition, A.M.B., E.C., L.C., S.B. and R.N. All authors have read and agreed to the published version of the manuscript.

Funding: This research received no external funding.

Institutional Review Board Statement: This study was conducted in accordance with the Declaration of Helsinki and approved by the Institutional Review Board (or Ethics Committee) of the University of Messina (protocol code 33-2020, 04/03/2020).

Informed Consent Statement: Informed consent was obtained from all the subjects involved in the study.

Data Availability Statement: The data presented in this study are available on request from the corresponding author.

Conflicts of Interest: The authors declare no conflicts of interest.

References

1. Barrera-Chaparro, J.P.; Plaza-Ruíz, S.P.; Parra, K.L.; Quintero, M.; Velasco, M.D.P.; Molinares, M.C.; Álvarez, C. Orthodontic treatment need, the types of brackets and the oral health-related quality of life. *Dent. Med. Probl.* **2023**, *60*, 287–294. [CrossRef] [PubMed]
2. Putrino, A.; Barbato, E.; Galluccio, G. Clear Aligners: Between Evolution and Efficiency—A Scoping Review. *Int. J. Environ. Res. Public Health* **2021**, *18*, 2870. [CrossRef] [PubMed]
3. Muro, M.P.; Caracciolo, A.C.A.; Patel, M.P.; Feres, M.F.N.; Roscoe, M.G. Effectiveness and predictability of treatment with clear orthodontic aligners: A scoping review. *Int. Orthod.* **2023**, *21*, 100755. [CrossRef] [PubMed]
4. Fang, X.; Qi, R.; Liu, C. Root resorption in orthodontic treatment with clear aligners: A systematic review and meta-analysis. *Orthod. Craniofacial Res.* **2019**, *22*, 259–269. [CrossRef] [PubMed]
5. Li, Y.; Deng, S.; Mei, L.; Li, Z.; Zhang, X.; Yang, C.; Li, Y. Prevalence and severity of apical root resorption during orthodontic treatment with clear aligners and fixed appliances: A cone beam computed tomography study. *Prog. Orthod.* **2020**, *21*, 1. [CrossRef] [PubMed]
6. Nucera, R.; Giudice, A.L.; Matarese, G.; Artemisia, A.; Bramanti, E.; Crupi, P.; Cordasco, G. Analysis of the characteristics of slot design affecting resistance to sliding during active archwire configurations. *Prog. Orthod.* **2013**, *14*, 35. [CrossRef]
7. Cordasco, G.; Farronato, G.; Festa, F.; Nucera, R.; Parazzoli, E.; Grossi, G.B. In vitro evaluation of the frictional forces between brackets and archwire with three passive self-ligating brackets. *Eur. J. Orthod.* **2009**, *31*, 643–646. [CrossRef]
8. Rouzi, M.; Zhang, X.; Jiang, Q.; Long, H.; Lai, W.; Li, X. Impact of Clear Aligners on Oral Health and Oral Microbiome during Orthodontic Treatment. *Int. Dent. J.* **2023**, *73*, 603–611. [CrossRef]
9. Kravitz, N.D.; Kusnoto, B.; BeGole, E.; Obrez, A.; Agran, B. How well does Invisalign work? A prospective clinical study evaluating the efficacy of tooth movement with Invisalign. *Am. J. Orthod. Dentofac. Orthop.* **2009**, *135*, 27–35. [CrossRef]
10. Paradowska-Stolarz, A.; Wezgowiec, J.; Malysa, A.; Wieckiewicz, M. Effects of Polishing and Artificial Aging on Mechanical Properties of Dental LT Clear® Resin. *J. Funct. Biomater.* **2023**, *14*, 295. [CrossRef]
11. Barreda, G.J.; Dzierewianko, E.A.; Muñoz, K.A.; Piccoli, G.I. Surface wear of resin composites used for Invisalign® attachments. *Acta Odontol. Latinoam.* **2017**, *30*, 90–95. [PubMed]

12. Jedliński, M.; Mazur, M.; Greco, M.; Belfus, J.; Grocholewicz, K.; Janiszewska-Olszowska, J. Attachments for the Orthodontic Aligner Treatment—State of the Art—A Comprehensive Systematic Review. *Int. J. Environ. Res. Public Health* **2023**, *20*, 4481. [CrossRef] [PubMed]
13. Gomez, J.P.; Peña, F.M.; Martínez, V.; Giraldo, D.C.; Cardona, C.I. Initial force systems during bodily tooth movement with plastic aligners and composite attachments: A three-dimensional finite element analysis. *Angle Orthod.* **2015**, *85*, 454–460. [CrossRef] [PubMed]
14. Nucera, R.; Dolci, C.; Bellocchio, A.M.; Costa, S.; Barbera, S.; Rustico, L.; Farronato, M.; Militi, A.; Portelli, M. Effects of Composite Attachments on Orthodontic Clear Aligners Therapy: A Systematic Review. *Materials* **2022**, *15*, 533. [CrossRef] [PubMed]
15. Weckmann, J.; Scharf, S.; Graf, I.; Schwarze, J.; Keilig, L.; Bourauel, C.; Braumann, B. Influence of attachment bonding protocol on precision of the attachment in aligner treatments. *J. Orofac. Orthop.* **2020**, *81*, 30–40. [CrossRef] [PubMed]
16. Valeri, C.; Aloisio, A.; Mummolo, S.; Quinzi, V. Performance of Rigid and Soft Transfer Templates Using Viscous and Fluid Resin-Based Composites in the Attachment Bonding Process of Clear Aligners. *Int. J. Dent.* **2022**, *2022*, 1637594. [CrossRef] [PubMed]
17. D'antò, V.; Muraglie, S.; Castellano, B.; Candida, E.; Sfondrini, M.F.; Scribante, A.; Grippaudo, C. Influence of Dental Composite Viscosity in Attachment Reproduction: An Experimental in Vitro Study. *Materials* **2019**, *12*, 4001. [CrossRef] [PubMed]
18. Gazzani, F.; Bellisario, D.; Quadrini, F.; Danesi, C.; Alberti, A.; Cozza, P.; Pavoni, C. Light-curing process for clear aligners' attachment reproduction: Comparison between two nanocomposites cured by the auxiliary of a new tool. *BMC Oral Health* **2022**, *22*, 376. [CrossRef] [PubMed]
19. Bellocchio, A.M.; Portelli, M.; Ciraolo, L.; Ciancio, E.; Militi, A.; Peditto, M.; Barbera, S.; Nucera, R. Evaluation of the Clinical Variables Affecting Attachment Reproduction Accuracy during Clear Aligner Therapy. *Materials* **2023**, *16*, 6811. [CrossRef] [PubMed]
20. Ferlias, N.; Dalstra, M.; Cornelis, M.A.; Cattaneo, P.M. In Vitro Comparison of Different Invisalign® and 3Shape® Attachment Shapes to Control Premolar Rotation. *Front. Bioeng. Biotechnol.* **2022**, *10*, 840622. [CrossRef]
21. Laohachaiaroon, P.; Samruajbenjakun, B.; Chaichanasiri, E. Initial Displacement and Stress Distribution of Upper Central Incisor Extrusion with Clear Aligners and Various Shapes of Composite Attachments Using the Finite Element Method. *Dent. J.* **2022**, *10*, 114. [CrossRef] [PubMed]
22. Lin, S.; Huang, L.; Li, J.; Wen, J.; Mei, L.; Xu, H.; Zhang, L.; Li, H. Assessment of preparation time and 1-year Invisalign aligner attachment survival using flowable and packable composites. *Angle Orthod.* **2021**, *91*, 583–589. [CrossRef] [PubMed]
23. Cole, D.; Bencharit, S.; Carrico, C.K.; Arias, A.; Tüfekçi, E. Evaluation of fit for 3D-printed retainers compared with thermoform retainers. *Am. J. Orthod. Dentofac. Orthop.* **2019**, *155*, 592–599. [CrossRef] [PubMed]
24. Takahashi, M.; Satoh, Y.; Iwasaki, S. Effect of thermal shrinkage during thermoforming on the thickness of fabricated mouthguards: Part 2 pressure formation. *Dent. Traumatol.* **2017**, *33*, 106–109. [CrossRef]
25. Park, S.Y.; Choi, S.-H.; Yu, H.-S.; Kim, S.-J.; Kim, H.; Kim, K.B.; Cha, J.-Y. Comparison of translucency, thickness, and gap width of thermoformed and 3D-printed clear aligners using micro-CT and spectrophotometer. *Sci. Rep.* **2023**, *13*, 10921. [CrossRef]

Disclaimer/Publisher's Note: The statements, opinions and data contained in all publications are solely those of the individual author(s) and contributor(s) and not of MDPI and/or the editor(s). MDPI and/or the editor(s) disclaim responsibility for any injury to people or property resulting from any ideas, methods, instructions or products referred to in the content.

applied sciences

MDPI

Article

Neuro-Fuzzy Model Evaluation for Enhanced Prediction of Mechanical Properties in AM Specimens

Emmanouil-Marinos Mantalas [1], Vasileios D. Sagias [1], Paraskevi Zacharia [2,*] and Constantinos I. Stergiou [1]

[1] Department of Mechanical Engineering, University of West Attica, Egaleo, 12241 Athens, Greece; mech19392205@uniwa.gr (E.-M.M.); sagias@uniwa.gr (V.D.S.); stergiou@uniwa.gr (C.I.S.)
[2] Department of Industrial Design and Production Engineering, University of West Attica, Egaleo, 12241 Athens, Greece
* Correspondence: p.zacharia@uniwa.gr

Abstract: This paper explores the integration of adaptive neuro-fuzzy inference systems (ANFIS) with additive manufacturing (AM) to enhance the prediction of mechanical properties in 3D-printed components. Despite AM's versatility in producing complex geometries, achieving consistent mechanical performance remains challenging due to various process parameters and the anisotropic behavior of printed parts. The proposed approach combines the learning capabilities of neural networks with the decision-making strengths of fuzzy logic, enabling the ANFIS to refine printing parameters to improve part quality. Experimental data collected from AM processes are used to train the ANFIS model, allowing it to predict outputs such as stress, strain, and Young's modulus under various printing parameters values. The predictive performance of the model was assessed with the root mean square error (RMSE) and coefficient of determination (R^2) as evaluation metrics. The study initially examined the impact of key parameters on model performance and subsequently compared two fuzzy partitioning techniques—grid partitioning and subtractive clustering—to identify the most effective configuration. The experimental results and analysis demonstrated that ANFIS could dynamically adjust key printing parameters, leading to significant improvements in the prediction accuracy of stress, strain, and Young's modulus, showcasing its potential to address the inherent complexities of additive manufacturing processes.

Keywords: additive manufacturing; adaptive neuro-fuzzy inference system (ANFIS); 3D printing; mechanical properties prediction; intelligent manufacturing systems

1. Introduction

The continuous advancement of modern industry has generated a significant demand for high-performance constructions and materials with pre-designed mechanical properties. Modern industry, and thus, industry 4.0, embraces concepts such as additive manufacturing (AM) [1] and artificial intelligence (AI), among others [2]. The mechanical properties of AM parts gather great research interest [3–7], as the traditional approaches cannot be applied to additive-manufactured parts for predicting mechanical properties and experimentation can be time- and cost-consuming.

The integration of AM and AI is of interest to the research community for mechanical properties prediction [8–14], allowing researchers to extract meaningful patterns from large datasets to accelerate material design and improve overall performance. By employing machine learning algorithms, valuable insights into material behavior can be obtained,

leading to faster design iterations and enhancing material properties without extensive empirical testing.

Among innovative fabrication methods, additive manufacturing (AM), or 3D printing, has emerged as a highly flexible technique. By building structures layer by layer, AM enables the production of complex geometries that are challenging to achieve with traditional manufacturing processes. This capability has broadened AM's applications across industries, allowing for the rapid prototyping and production of parts with intricate designs and customizable features.

Despite its versatility, AM faces several limitations in ensuring consistent mechanical performance across manufactured parts. The mechanical properties of AM-fabricated components are influenced by various manufacturing parameters, such as layer thickness, build orientation, temperature, material selection, and more, leading to challenges in predicting the behavior of these parts.

To address these challenges, artificial intelligence (AI) methodologies, particularly, adaptive neuro-fuzzy inference systems (ANFIS), offer promising solutions [8,9,15]. ANFIS combines the adaptability of neural networks with the interpretability of fuzzy logic, making it well-suited for modeling the nonlinear relationships in complex systems like AM. As a convergence of neural networks and fuzzy modeling, ANFIS can capture intricate input–output relationships based on experimental data and "if–then" rules, thereby establishing accurate predictive models for mechanical properties. This hybrid approach has already shown potential in other AI applications [16–20], such as automated control and decision-making systems, and it can now be applied in AM to enhance the precision and efficiency of part production.

ANFIS has been effectively applied to model the relationships between inputs and outputs, combining neural network and fuzzy logic principles. It has demonstrated reliable predictive accuracy in various additive manufacturing (AM) contexts. The key advantages of this method include the following:

- Rapid learning capability, even with limited or unevenly distributed data across the process window.
- Robust modeling performance, especially effective in handling noisy data within nonlinear systems.
- Ease of adaptation and application of neural network principles to specific problem domains.
- Efficient processing, providing time-effective performance for complex tasks.

Nawafleh and AL-Oqla [21] developed a sophisticated ANFIS to predict the mechanical behavior of 3D-printed thermoset carbon fiber composites. By leveraging the neuro-fuzzy inference model, the research addresses challenges in the experimental evaluation of complex composite structures with variable fiber fractions, especially given issues like fiber aggregation and nozzle blockage at higher load levels. The model effectively predicts critical mechanical properties such as flexural stress, modulus, and elongation at break, based on real experimental data. Notably, the ANFIS model achieves high prediction accuracy by integrating artificial neural networks with fuzzy inference systems, demonstrating reliability across different fiber compositions. This approach offers significant advancements in technical evaluation, supporting broader applications of carbon fiber composites in industries where high predictability and mechanical resilience are essential.

Wei et al. [22] developed a Takagi–Sugeno (T–S) fuzzy neural network to predict and optimize the tensile strength of polylactic acid (PLA) components fabricated using fused deposition modeling (FDM) 3D printing. This model incorporated four critical printing parameters—layer thickness, printing speed, temperature, and fill density—to enhance tensile performance. Experimental validation demonstrated the T–S model's accuracy, with

relative errors between the predicted and actual tensile strengths ranging from 5% to 10%. The results highlighted the model's capacity to capture the nonlinear relationships within AM processes, providing an efficient method for optimizing tensile strength.

Sagias et al. [15] developed an ANFIS model aimed at predicting the mechanical properties—specifically, maximum stress, strain, and Young's modulus—of PLA specimens produced through fused filament fabrication (FFF). The study utilized experimental data from three-point bending tests, incorporating various manufacturing parameters such as infill pattern, layer thickness, and extrusion temperature to train the model. This approach enabled accurate mapping between inputs and output mechanical properties, validating the model's effectiveness in predicting material behavior in additive manufacturing (AM) contexts.

Analytical models, such as those based on the foundational work of [23], provide a theoretical framework that is invaluable for guiding initial design decisions. However, analytical and numerical methods can face limitations when addressing the complex, nonlinear interactions inherent in AM processes [24]. Such limitations arise due to the anisotropic properties of printed parts and the multitude of interdependent variables, including layer thickness, infill density, material composition, and printing parameters. Prada-Parra et al. [24] also highlighted that while analytical methods are computationally efficient, they may not fully account for real-world deviations in AM components. Their study demonstrated that nonlinear machine learning models, despite requiring higher computational resources, performed better in predicting mechanical properties.

ANFIS presents an innovative and practical solution for addressing the complexities of additive manufacturing (AM). By combining the adaptive learning capabilities of neural networks with the interpretability of fuzzy logic, ANFIS effectively models the nonlinear relationships between AM parameters and mechanical properties. This study builds on this foundation by expanding the application of ANFIS to a broader range of AM technologies and materials, enhancing its predictive scope and adaptability. The primary aim is to integrate ANFIS with AM processes to develop a robust model capable of predicting critical mechanical properties—such as stress, strain, and Young's modulus—of 3D-printed components.

The research advances existing methodologies by addressing the complex, nonlinear interactions inherent in AM processes. The key contributions of this work include the following:

- Integration of ANFIS with AM Processes: The study applies ANFIS to predict critical mechanical properties—such as stress, strain, and Young's modulus—by dynamically adapting to diverse AM configurations and material properties.
- Comparison of Fuzzy Partitioning Techniques: The research evaluates grid partitioning and subtractive clustering to identify the most effective technique for capturing input–output relationships, with subtractive clustering demonstrating superior performance.
- Focus on Data-Driven Refinement: The model uses experimental data to fine-tune parameters, improving prediction accuracy and addressing the limitations of traditional trial-and-error methods.
- Efficiency and Practicality: The study emphasizes computational efficiency while maintaining high prediction reliability, offering a scalable tool for industrial applications in AM.

By incorporating multiple AM configurations, the model demonstrates a strong ability to capture complex relationships, enabling more accurate and reliable predictions. This novel approach not only bridges the gap between theoretical predictions and experimental outcomes but also provides a systematic framework for refining manufacturing parameters. Ultimately, this work broadens the potential applications of AM, offering a data-driven

solution for improving the mechanical integrity and performance of 3D-printed parts across various industries.

The structure of the paper is organized as follows. Section 2 provides a concise overview of the ANFIS architecture used for the prediction of mechanical properties. Section 3 describes the evaluation metrics used to assess model performance. Section 4 outlines the experimental framework, including dataset preparation, parameter investigation, and the results of the comparative analysis of grid partitioning and subtractive clustering techniques. Lastly, Section 5 presents the conclusions and suggests potential directions for future research.

2. The ANFIS Architecture for Mechanical Properties Prediction

The adaptive neuro-fuzzy inference System (ANFIS) [25] is a hybrid model that combines the learning abilities of artificial neural networks (ANN) with the interpretability of fuzzy logic to predict complex, nonlinear relationships between input and output parameters. ANFIS operates through an architecture consisting of five layers that sequentially process inputs and apply fuzzy inference to produce accurate, adaptable predictions. This model has demonstrated particular effectiveness in applications where traditional models may encounter difficulties with inconsistent or noisy data, a common characteristic of AM processes.

ANFIS is structured into five key layers (Figure 1), each responsible for a specific aspect of processing:

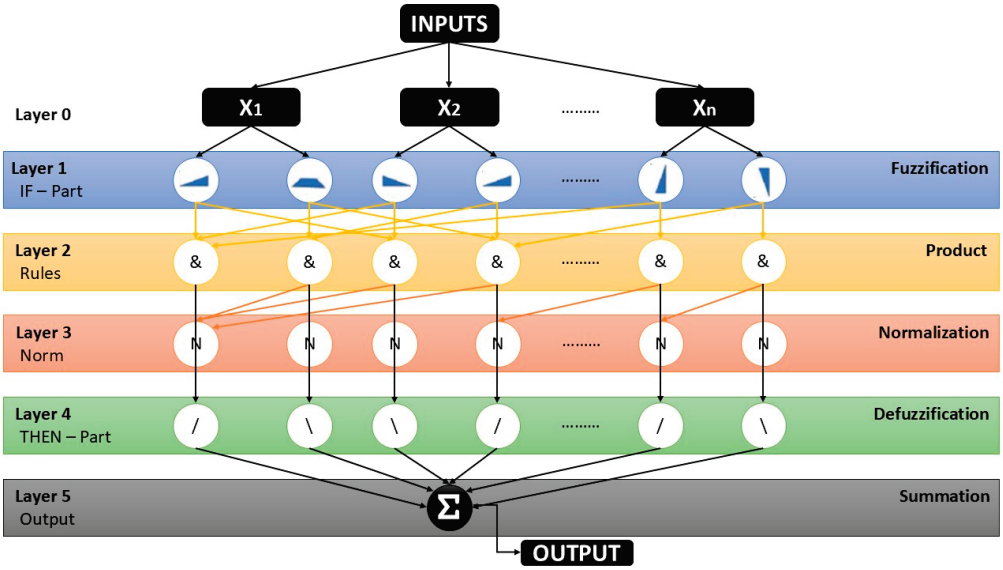


Figure 1. ANFIS architecture with n inputs and 1 output.

Fuzzification Layer (Layer 1): In this initial layer, input variables are converted into fuzzy sets by applying membership functions. Each node in this layer corresponds to a linguistic term (e.g., "low", "medium", "high") of the input parameters, with membership values indicating the degree to which an input belongs to each fuzzy set. For this study, factors such as infill density, layer thickness, and temperature are fuzzified.

Rule Layer (Layer 2): Layer 2 processes the output from Layer 1 by forming combinations of fuzzy rules. Using the Sugeno fuzzy inference model, each rule represents a specific relationship between input variables, defined by "if–then" statements. Each node calculates the strength (firing strength) of the rule by taking the product of the incoming membership values.

Normalization Layer (Layer 3): This layer normalizes the firing strengths of each rule by calculating the ratio of a specific rule's firing strength to the sum of all rule strengths. This normalization process enables ANFIS to handle varying input ranges and maintain a stable output range, ensuring that each rule contributes proportionately to the final output.

Defuzzification Layer (Layer 4): In this layer, the normalized firing strength from Layer 3 is multiplied by a rule-specific linear function. These linear functions represent the consequent part of the Sugeno fuzzy rules and are typically of the form $f_i = p_i x + q_i y + r_i$, where p_i, q_i, and r_i are consequent parameters. This layer's output reflects the weighted effect of each rule on the final prediction.

Output Layer (Layer 5): The final layer aggregates the outputs from Layer 4, producing the ANFIS model's output by summing all incoming signals. This aggregated output represents the predicted mechanical property, such as maximum stress, strain, or Young's modulus, based on the input conditions and the rules in place.

Figure 1 illustrates the ANFIS architecture with n inputs and a single output. The system utilizes a hybrid learning approach, combining gradient descent and least-squares estimation, to adjust membership function parameters in Layers 1 and 4. This dual mechanism enhances the model's predictive accuracy by iteratively learning from experimental data, making ANFIS a valuable tool for AM applications where varying process parameters and material types demand a flexible and robust predictive model.

To implement the fuzzy inference process effectively, ANFIS requires the partitioning of the input space into multiple subspaces, each modeled with a consistent set of fuzzy rules. This partitioning can be accomplished using two primary methods: grid partitioning (GP) and subtractive clustering (SC). These approaches facilitate the systematic generation of fuzzy rules by either dividing the input space into evenly spaced intervals (GP) or identifying potential cluster centers based on data density (SC). The following subsections provide a detailed explanation of both methods and their application in this study.

2.1. Grid Partitioning

Grid partitioning is a technique used in ANFIS to define fuzzy rules by dividing the input space into a structured grid based on the range of input variables. In this approach, each input variable is divided into several intervals, and a membership function is assigned to each interval, representing different linguistic terms (e.g., "low", "medium", "high"). The combination of these intervals across all input variables forms a grid that represents all possible rules for the fuzzy inference system. Each grid cell corresponds to a unique fuzzy rule that links a specific input variable to an output value. While grid partitioning provides a straightforward way to generate fuzzy rules, it can lead to a rapid increase in the number of rules, especially as the number of input variables grows, creating a "curse of dimensionality". Nevertheless, in applications with a manageable number of inputs, grid partitioning enables ANFIS to systematically cover the input space, allowing for the precise rule-based modeling of complex, nonlinear systems. This makes it particularly useful in scenarios where distinct input–output relationships must be captured accurately, such as in predicting mechanical properties in additive manufacturing processes.

2.2. Subtractive Clustering

Subtractive clustering [26] is a data clustering technique commonly used in ANFIS to generate an optimal number of fuzzy rules by identifying potential cluster centers within the input–output data. This method is particularly advantageous for ANFIS as it automates the selection of cluster centers, which serve as the basis for creating fuzzy rules, without requiring a predetermined number of clusters. Subtractive clustering calculates the density of each data point in a multidimensional space by measuring its distance to all other points.

Points with higher density values are considered potential cluster centers, as they are surrounded by more data points. Once a cluster center is established, the algorithm reduces the density of nearby points, preventing the formation of closely spaced clusters. This process continues iteratively until all relevant clusters are identified, yielding an efficient structure for the fuzzy inference system. In ANFIS, subtractive clustering enables the model to efficiently capture nonlinear relationships in complex datasets, making it highly suitable for applications in predictive modeling, such as in additive manufacturing contexts where various parameters impact mechanical properties.

3. Performance Evaluation Metrics

To assess the effectiveness of the developed models, two key evaluation metrics are utilized: root mean square error (RMSE) and the coefficient of determination (R^2). These metrics provide a comprehensive measure of the model's predictive accuracy and its ability to explain the variability in the observed data.

Root mean square error (RMSE). The RMSE is a common way to measure the accuracy of a predictive model by calculating the difference between predicted and observed values. It provides an estimate of the average discrepancy between the predicted values and the actual observed data points. Lower RMSE values indicate better model performance. The formula for RMSE is

$$\sqrt{\frac{1}{n}\sum_{i=1}^{n}(y_i - \hat{y}_i)^2} \tag{1}$$

where n is the number of data points, y_i is the actual value of the ith data point, and $\hat{y}_i$ is the predicted value of the ith data point.

Coefficient of determination (R^2). The R^2 measures the degree to which a model's predictions align with the actual data. It indicates the proportion of variance in the dependent variable that can be explained by the independent variables. An R^2 of 1 indicates a perfect fit, while an R^2 of 0 indicates that the model fails to explain any of the variance in the target variable. The formula for R^2 is

$$R^2 = 1 - \frac{\sum_{i=1}^{n}(y_i - \hat{y}_i)^2}{\sum_{i=1}^{n}(y_i - \overline{y})^2} \tag{2}$$

where n is the number of data points, y_i is the actual value of the ith data point, $\hat{y}_i$ is the predicted value of the ith data point, and $\overline{y}$ is the mean value of all data points.

4. Methodological Framework for Enhancing ANFIS Model

The ANFIS model utilized in this study employs a five-layer architecture that combines neural network and fuzzy logic principles (Figure 2). The structure includes an input layer where membership functions calculate the degree of membership for each input variable, a rule layer that applies fuzzy rules, a normalization layer to standardize firing strengths, a defuzzification layer that computes weighted outputs, and an output layer that aggregates these results into a final prediction. This architecture enables ANFIS to effectively capture complex nonlinear relationships in the data while adaptively tuning fuzzy rules and membership functions during training.

The methodology for developing and improving the ANFIS model includes several structures, designed to ensure the model's accuracy and effectiveness in predicting the mechanical properties of additive manufacturing (AM) parts.

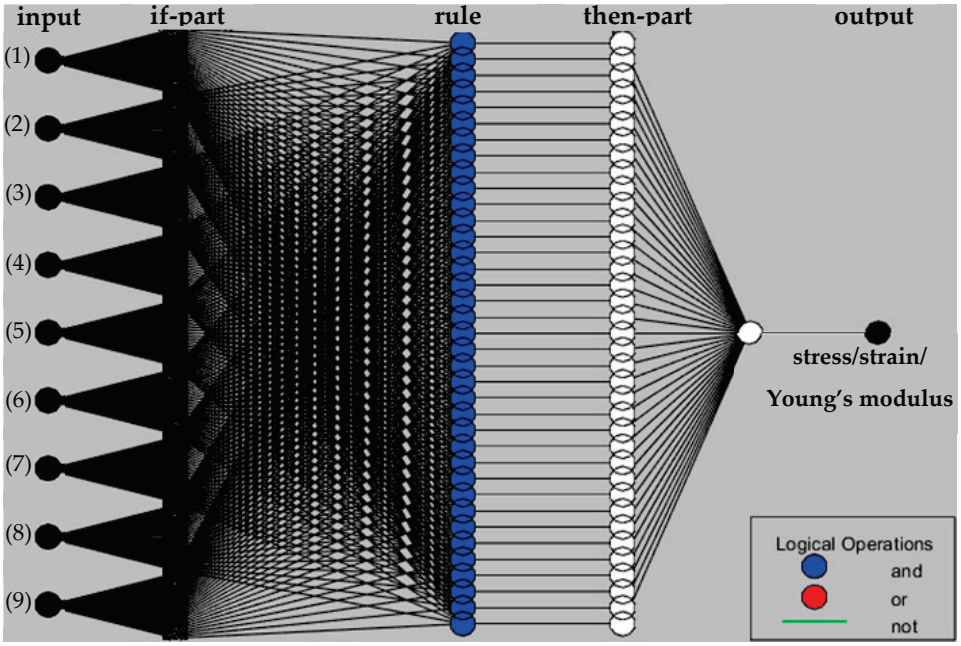


Figure 2. The proposed ANFIS model with 9 inputs and 1 output.

The initial phase of this research comprised an extensive literature review, focusing on two key areas: AM and neural-fuzzy systems, specifically, ANFIS. The research on AM is focused on the factors that influence the mechanical properties of printed parts, such as the printing parameters, material, and AM technology. Concurrently, the exploration of neural networks and fuzzy systems aimed at understanding predictive modeling techniques and how fuzzy model structures can enhance prediction accuracy and reliability.

4.1. Experimental AM Data

Based on previous work [3,15] and literature review [4–7], the printing parameters that influence the mechanical properties of the AM specimens were defined. By selecting these factors, tension, bending and torsion tests were conducted by using multiple AM technologies (FFF, SLA, SLS, DED, and PBF) and various materials (ABS, PLA, PA12, etc.) (Figure 3). All data were gathered and analyzed to obtain the stress, strain and Young's modulus of every specimen/experiment.

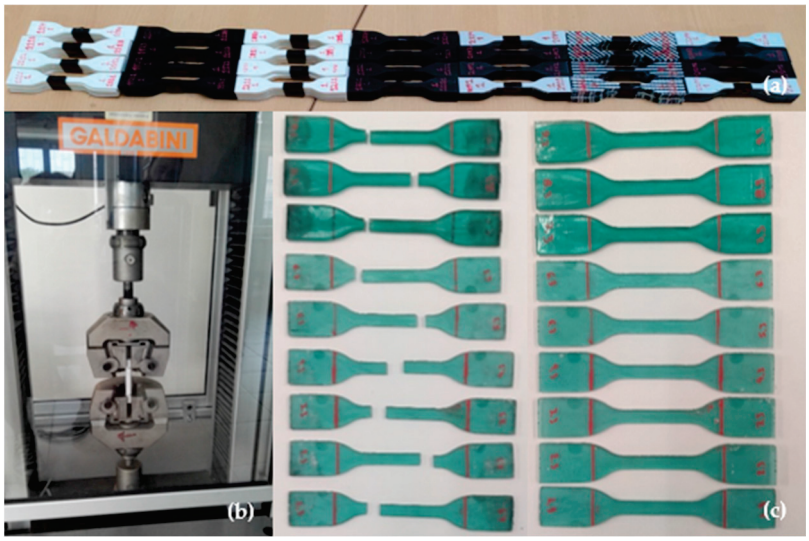


Figure 3. Specimens, according to ASTM D638, for different materials (ABS and PLA (**a**)) and AM methods (FFF (**a**) and SLA (**c**)) and sample tension test (**b**).

All AM processes and materials used for this study were manufactured in the AM Laboratory and all mechanical tests were conducted at the Strength of Materials Laboratory, Mechanical Engineering Department, University of West Attica. All experiments were designed and conducted according to ASTM standards such as ASTM D638 [27], D695 [28], D7791 [29], D790 [30], and D5279 [31].

Experiments were conducted, as shown in Figures 3 and 4, using various AM processes, including FFF, SLS, SLA, and DED. The experiments involved multiple materials, testing methods, and a range of values for selected manufacturing parameters. A generalized model for handling all 21 AM parameters as input, was created based on previous work [15]. The parameters comprised (1) AM technology, (2) testing method, (3) material, (4) infill pattern, (5) infill percentage, (6) layer thickness, (7) wall thickness, (8) speed, (9) extruder temperature, (10) laser power ratio, (11) bed temperature, (12) position on printer bed, (13) incline against printer bed, (14) twist around axis of center of gravity, (15) raster angle, (16) layers for alternating raster angle, (17) percentage of first material, (18) curing time, (19) curing power, (20) layer composition, and (21) cross-section.

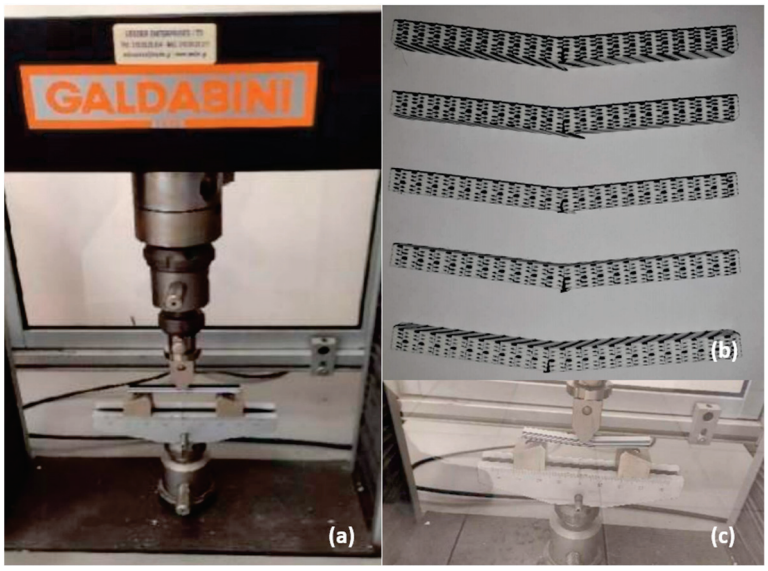


Figure 4. Sample bending test (**a**,**c**) and specimens (**b**), according to ASTM D790, for ABS and PLA material and FFF AM method.

The purpose of creating a generalized model is to be able to handle any AM technology, among FFF, SLS, SLA, or DED, and its selected manufacturing parameters applicable each time, as input and output stress, strain, or Young Modulus. According to the AM technology the applicable parameters were used each time.

For the three-point bending tests, presented in Figure 5, square section specimens were used (8 × 8 mm). The tests were conducted according to ASTM D790. Stress–strain curves were produced by importing the applied load and deflection, from the tests, to stress σ (Equation (3)) and strain ε (Equation (4)) equations.

$$\sigma = \frac{3PL}{2bd^2} \tag{3}$$

where σ is the stress (N/mm^2), P is the applied load (N), L is the stressed length (mm), b is the width of the specimen (mm), and d is the height of the specimen (mm).

$$\varepsilon = \frac{6Dd}{L^2} \tag{4}$$

where ε is the strain (%), D is the deflection (mm), L is the stressed length (mm), and d is the height of the specimen (mm).

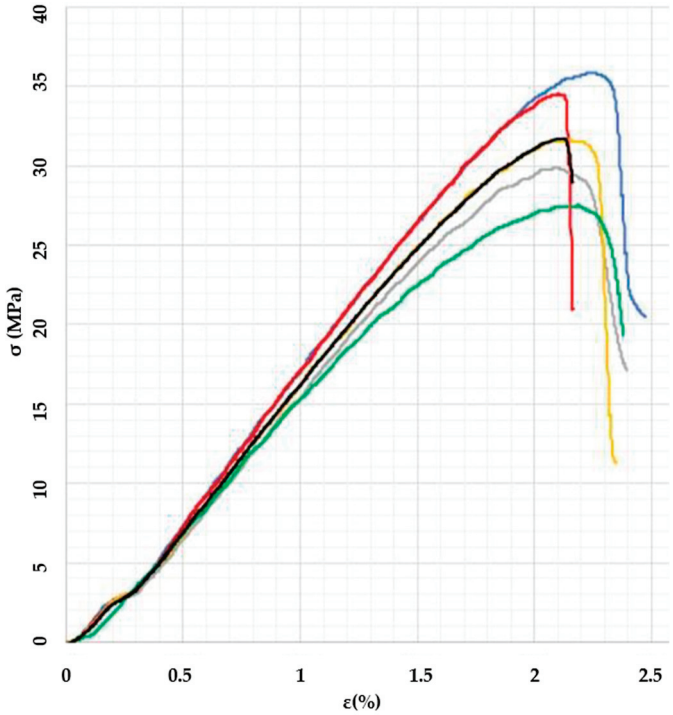


Figure 5. Stress–strain curve of bending test (indicative). Colored lines represent the five iterations of the test and the black the average.

4.2. The Initial Model

For the initial model creation, nine inputs were selected based on the FFF AM process, PLA material, and bending test: (1) infill pattern, (2) infill percentage, (3) layer thickness, (4) speed, (5) extruder temperature, (6) bed temperature, (7) position on printer bed, (8) incline against printer bed, and (9) raster angle.

For a fair comparison between the initial and the proposed model, the same experimental data were used as in previous work [15], as presented in Table 1.

Table 1. Datasheet of the ANFIS bending model.

Infill Pattern	Infill (%)	Layer Thickness (mm)	Speed (mm/s)	Temperature (°C)	Bed Temperature (°C)	Position on Bed	Twist Angle (°)	Inclination (°)
2	50	0.1	50	200	60	1	1	5
2	75	0.1	50	200	60	3	1	5
3	100	0.1	50	200	60	5	1	7
2	75	0.2	50	200	60	5	1	5
2	100	0.2	50	200	60	1	1	5
3	50	0.2	50	200	60	3	1	7
2	100	0.3	50	200	60	3	1	5
2	50	0.3	50	200	60	5	1	5
3	75	0.3	50	200	60	1	1	7

Based on the collected data, an initial ANFIS model is created that is then parameterized to predict three outputs: stress, strain, and Young's modulus. The model is then trained using a subset of the data.

In the context of AM, ANFIS's architecture is well-suited to predict mechanical properties affected by multiple, interdependent process parameters. Specifically, experimental data from AM processes, such as temperature, infill percentage, and layer thickness, were used to train the ANFIS model, enabling it to generalize across a range of AM configurations. Similarly, in this study, the ANFIS model is employed to predict the mechanical properties of AM-fabricated parts, focusing on refining the layer thickness, printing speed, and material characteristics to achieve accurate output predictions.

Input data is manually divided into training and checking subsets, using a predefined data percentage of 80% for training and 20% for checking. The initial model configuration includes using a subtractive clustering algorithm with the following parameters: range of influence (ROI), 0.5; squash factor (SQ), 1; accept ratio, 0.5; and reject ratio, 0.15.

We implemented subtractive clustering to partition the input space and derive fuzzy rules for the ANFIS model. This approach calculates the potential of data points based on their proximity to others and iteratively selects cluster centers in regions of high density. Following the method outlined in [26], cluster centers were refined to minimize overlap and ensure precise rule generation. This technique was selected for its computational efficiency and ability to model nonlinear relationships effectively, as demonstrated in previous works, such as in [32].

4.3. The Proposed Model

The proposed model retains the main functionalities of the initial ANFIS model while incorporating enhanced automation features. Users input only the experimental data relevant to the study, which are then processed through an automated sorting procedure. Throughout the execution, the algorithm provides the extraction of necessary diagrams for analysis before proceeding to subsequent tasks. This iterative approach ensures comprehensive evaluation at each stage, ultimately resulting in the development of the final refined model.

During preprocessing, the standard deviation of the output is calculated to identify high- and low-value ranges within the dataset, which are then used for further analysis.

Once the data preparation is complete, the next step involves generating random values for the training dataset and creating a corresponding checking dataset for validation purposes. A crucial step in this process is verifying that all values are included at least once in both the training and checking datasets. This ensures that all possible combinations of the data are represented. If this condition is met, the process proceeds using a dataset that yields the minimum RMSE and the highest R^2. Otherwise, an ANFIS model using subtractive clustering is constructed and subsequently assessed for its performance.

If the initial model configuration is chosen based on RMSE or R^2, the next step involves determining whether to adjust the membership functions used in the fuzzy inference system. If adjustments to the membership functions are necessary, a new ANFIS model employing grid partitioning is constructed and then evaluated for its performance. After several iterations with different membership functions, the system checks if all membership functions are applied at least once. If all membership functions have been applied, the process then explores further adjustments to specific parameters, such as the ROI or SQ. Depending on these adjustments, another variant of the ANFIS model with subtractive clustering is created and reevaluated.

If the adjustments do not lead to satisfactory performance, the procedure leads to an error state, indicating that the model's configuration may need a fundamental review. This

systematic approach ensures a thorough exploration of different model configurations to enhance the performance of the ANFIS system, balancing modifications in membership functions and parameter settings to improve prediction accuracy. The overall methodology is concisely summarized in the flowchart diagram presented in Figure 6.

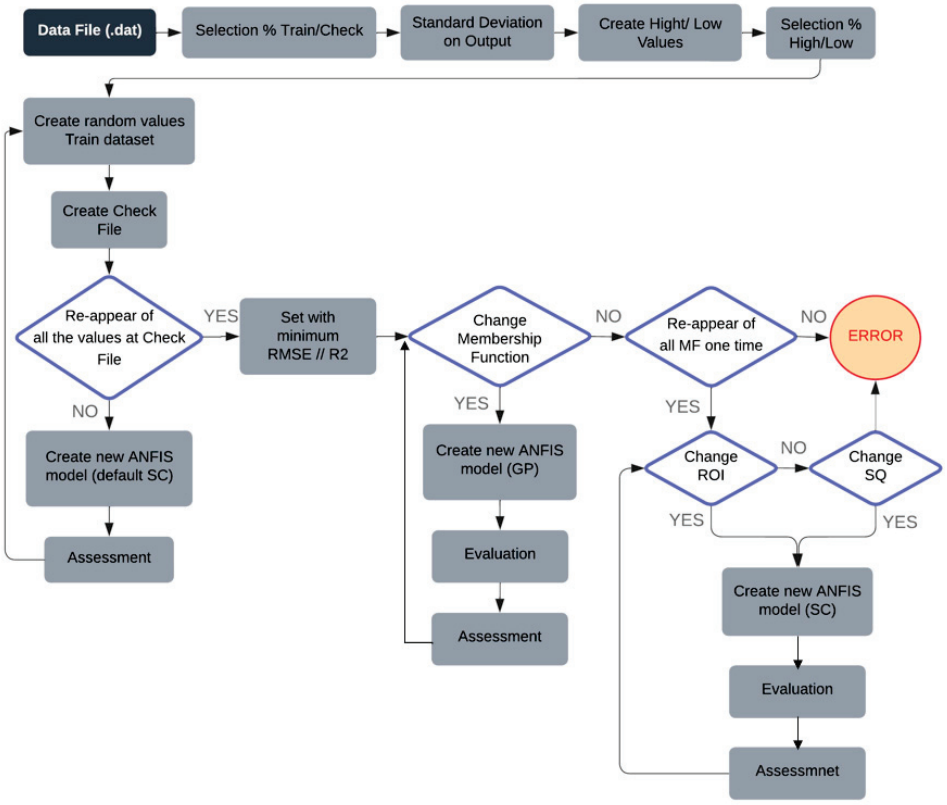


Figure 6. Flowchart diagram of the proposed model.

As described, all individual operations have been enhanced with a focus on automation and improving the accuracy and quality of the output results.

5. Model Implementation and Performance Analysis

All model implementations and simulations were conducted using MATLAB R2024a.

5.1. Dataset Preparation and Partitioning

In this study, the dataset is divided into two subsets: one for training and one for checking. Based on standard practices in the literature, an 80%/20% split is chosen for training and checking, respectively. The primary objective of this approach is to mimic the randomness of human selection, ensuring that both subsets represent the full range of the dataset's variability.

To achieve representative sampling across the full dataset range, a statistical normal distribution was applied to the output data. The mean (μ) and standard deviation (σ) of the data were calculated, and a confidence interval was established using the empirical rule, defined as $\mu \pm 1\sigma$ [33], as depicted in Figure 7. This method resulted in the formation of two distinct groups: one comprising data points within the confidence interval (high values) and the other containing data points outside this interval (low values).

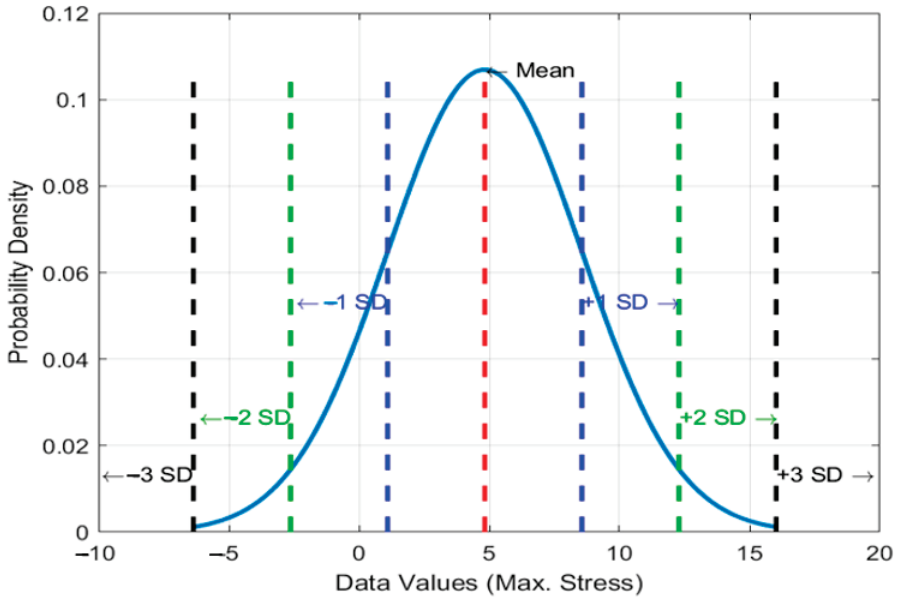


Figure 7. Normal distribution for maximum stress.

These two groups are then divided to enhance the randomness of the subset data. This division is done in such a way that both the training and checking subsets included a mix of data points from within the $\mu \pm 1\sigma$ range and from the broader range extending beyond $\mu \pm 3\sigma$ in a percentage of 70/30, respectively. This approach guarantees that each subset captures data representing the entire spectrum of values. The process begins with forming the training subset, followed by creating the checking subset from the remaining data. This procedure is repeated iteratively, ensuring that the initial data appear at least once in the checking subset, thus achieving a more balanced and representative sampling.

To select the most appropriate set of values from the iterative process that preceded it, a comparison method was used. More specifically, a subtractive clustering model using ANFIS was chosen, and each set was evaluated for its performance. In this way, the evaluation is objective, as the same algorithm is used for each set of values, ensuring that effective value placement is used for training and checking data.

Figure 8 presents scatter plots that illustrate the relationship between RMSE and R^2 across multiple iterations of the ANFIS model for three mechanical properties: maximum stress, maximum strain, and Young's modulus. The plots reveal an inverse relationship, where lower RMSE values are associated with higher R^2 values, indicating improved model performance. In these diagrams, the y-axis displays the evaluation metrics (RMSE and R^2), while the x-axis represents the iterations generated from the iterative process.

As the model is refined through iterations, the scatter plots show data points converging toward regions where R^2 is high and RMSE is low. This indicates that successive iterations are achieving both greater predictive accuracy (higher R^2) and lower prediction error (lower RMSE). This trend suggests that the iterative refinement process is effectively adjusting the model's parameters, enhancing its reliability (consistently accurate across different datasets) and precision (with smaller deviations between predicted and actual values). Consequently, the model improves its ability to predict the mechanical properties of 3D-printed parts as the iterations progress.

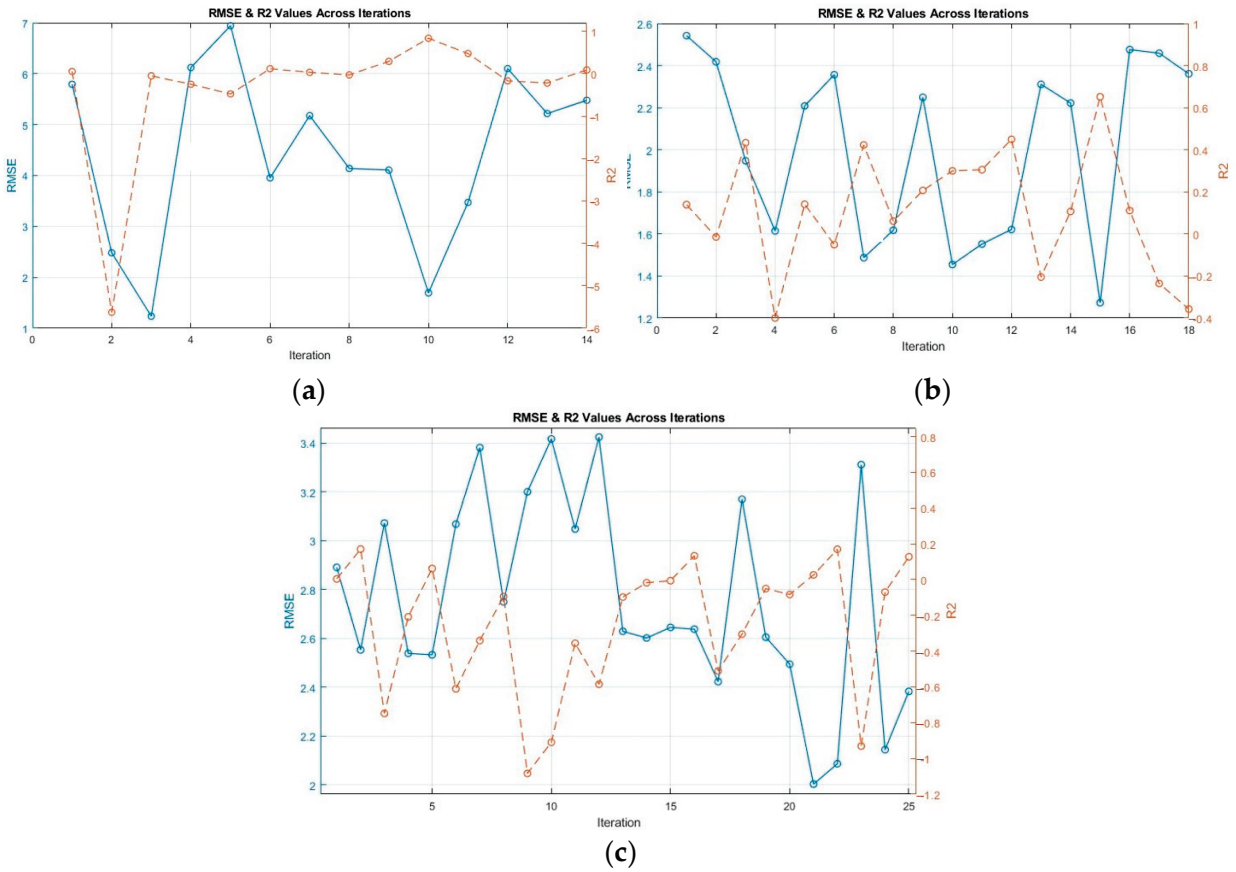


Figure 8. Scatter plots RMSE and R^2 across different iterations of train/check dataset between (**a**) maximum stress, (**b**) maximum strain, and (**c**) Young's modulus.

5.2. ANFIS Parameter Tuning and Performance Evaluation

For the effective implementation of an ANFIS model, it is crucial to carefully define the structural approach and key parameters beyond merely identifying the input and output data. This requires selecting and configuring specific techniques that enhance the model's performance. The two primary techniques available for this purpose are grid partitioning and subtractive clustering. In this phase of model development, both techniques were applied, and their performances were systematically compared to identify the most suitable approach for the given dataset through the assessment metrics.

A crucial component of ANFIS is the membership functions, which determine the degree of membership for each input variable. These functions, such as Gaussian or triangular membership functions, play a critical role in fuzzifying inputs and influencing the model's predictive performance.

In grid partitioning, the key parameters influencing the model's performance include the type and number of membership functions. To simplify the analysis, the number of membership functions was fixed at two, allowing a focus on evaluating different types of functions. The membership functions assessed in this study were triangular (trimf), trapezoidal (trapmf), bell (gbellmf), gaussian (gaussmf, gauss2mf), pi (pimf), and sigmoidal (dsigmf and psigmf. Each type of membership function was tested, and its performance was evaluated based on prediction accuracy using the metrics RMSE and R^2.

Initially, experiments were performed using the above-mentioned types of membership functions to evaluate their impact on the performance of the ANFIS model. Figures 9 and 10 present the comparative performance of these membership functions based on RMSE and R^2, respectively, including radar plots that depict the RMSE and R^2 across various membership functions. The radar plots provide a qualitative assessment of

how each membership function type influences the prediction accuracy for key mechanical properties such as maximum stress, maximum strain, and Young's modulus. The results indicate that the Gaussian membership function consistently yields lower RMSE and higher R^2 values, highlighting its superior performance in modeling the complex relationships in the dataset. This superior performance can be linked to its ability to represent smooth transitions between fuzzy sets, enabling more accurate predictions of mechanical properties.

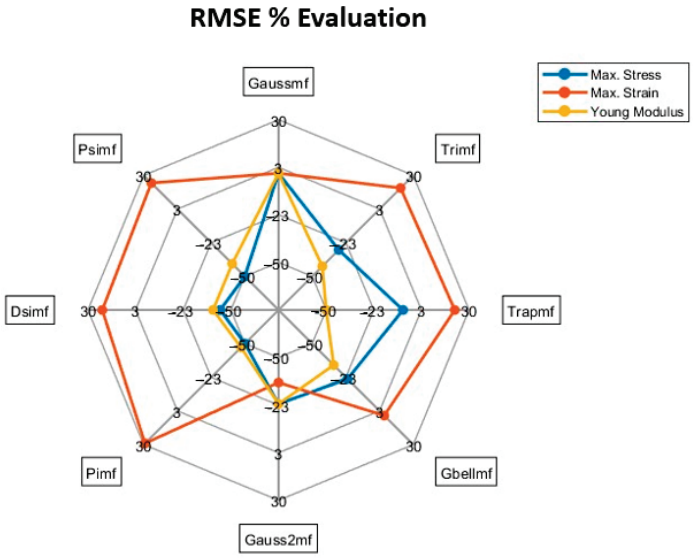


Figure 9. Radar plots comparing maximum stress, maximum strain, and Young's modulus across different membership functions, showing RMSE.

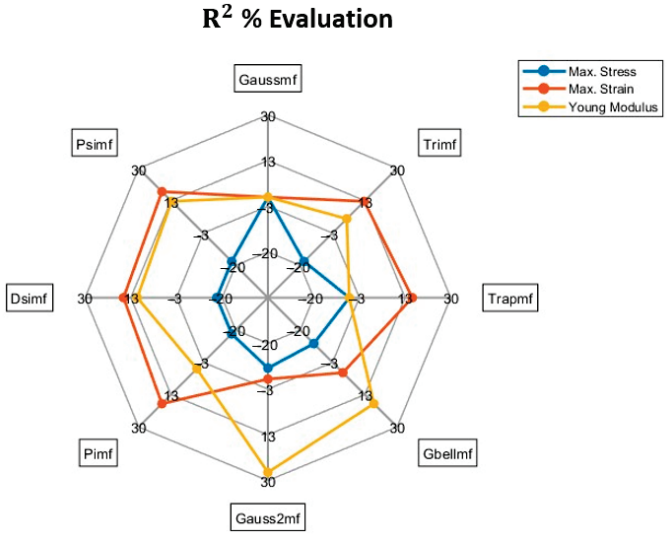


Figure 10. Radar plots comparing maximum stress, maximum strain, and Young's modulus across different membership functions, showing R^2.

The Gaussian membership function exhibited superior performance compared to other types in most cases tested. Specifically, as shown in Figures 9 and 10, applying the Gaussian membership function led to an average reduction in the mean algorithm error (RMSE) of up to 29% and an average improvement in the prediction accuracy (R^2) by as much as 27% relative to the initial model.

For subtractive clustering, the key parameters influencing model performance include the ROI, SQ, accept ratio, and reject ratio. This study focused on examining the effects of varying the ROI and SQ parameters, with ROI values tested within a range from 0 to 1 and SQ values between 0.7 and 5. The accept ratio and reject ratio were held constant at 0.5 and

0.15, respectively. The process involves systematically adjusting the ROI in increments of 0.1 and the SQ in increments of 0.2. All possible combinations of these parameter values were then evaluated using the RMSE and R^2 to identify the parameter settings that yielded the best model performance.

Figure 11 depicts surface plots that illustrate the impact of two key parameters, ROI SQ, on the RMSE for predicting three mechanical properties: maximum stress, maximum strain, and Young's modulus. The surface plots provide a visual representation of how changes in ROI and SQ influence the model's prediction error. Lower RMSE values, indicated by the darker regions on the plots, suggest improved model performance.

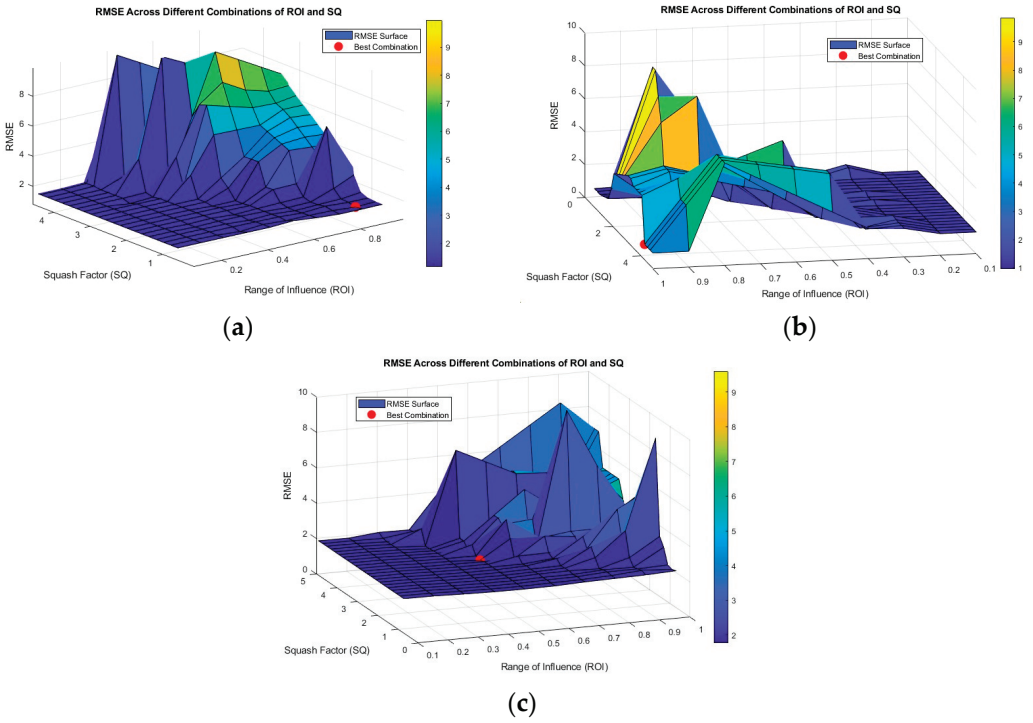


Figure 11. Surface plots RMSE across different combinations of ROI and SQ between (**a**) maximum stress dataset, (**b**) maximum strain dataset and (**c**) Young's modulus dataset.

Adjusting the ROI in subtractive clustering led to significant changes in the prediction accuracy, revealing the model's sensitivity to parameter tuning. Similarly, variations in SQ showed a notable impact on the RMSE, with optimal SQ values helping to maintain a balance between capturing details and avoiding overfitting. The plots reveal specific ranges for ROI and SQ where the RMSE is minimized, highlighting the importance of carefully fine-tuning these parameters to enhance the predictive accuracy of the ANFIS model.

After examining the impact of the parameters, experiments were performed to compare grid partitioning and subtractive clustering. The initial ANFIS model exhibited an average value error of ± 1.35 MPa and an accuracy of 0.77. After applying the subtractive clustering technique, the model improved to an average error value error of ± 1.15 MPa and an accuracy of 0.83. Subtractive clustering demonstrated superior adaptability in capturing nonlinear relationships, particularly in cases with noisy data, compared to grid partitioning, which exhibited limitations in processing high-dimensional input data efficiently.

As shown, the Gaussian membership function proved to be the most effective for both techniques, grid partition and subtractive clustering. The grid partition algorithm resulted in an average error of ± 2.24 MPa and an accuracy of 0.37, while subtractive clustering achieved significantly better results, with a 49% lower error and 55% higher accuracy. These findings highlight the importance of selecting both the appropriate membership function and an effective model configuration to accurately capture the inherent correlations

within the data. The final refinement phase involved a detailed analysis of the subtractive clustering parameters.

The diagrams in Figures 12–14 present the predicted values of the three models (initial, SC, and GP models) compared to the actual values, for the checking dataset for maximum stress (Figure 12), maximum strain (Figure 13) and Young's modulus (Figure 14). In all bar plots, the horizontal axis denotes the dataset index, corresponding to the row of input data from which the value was derived.

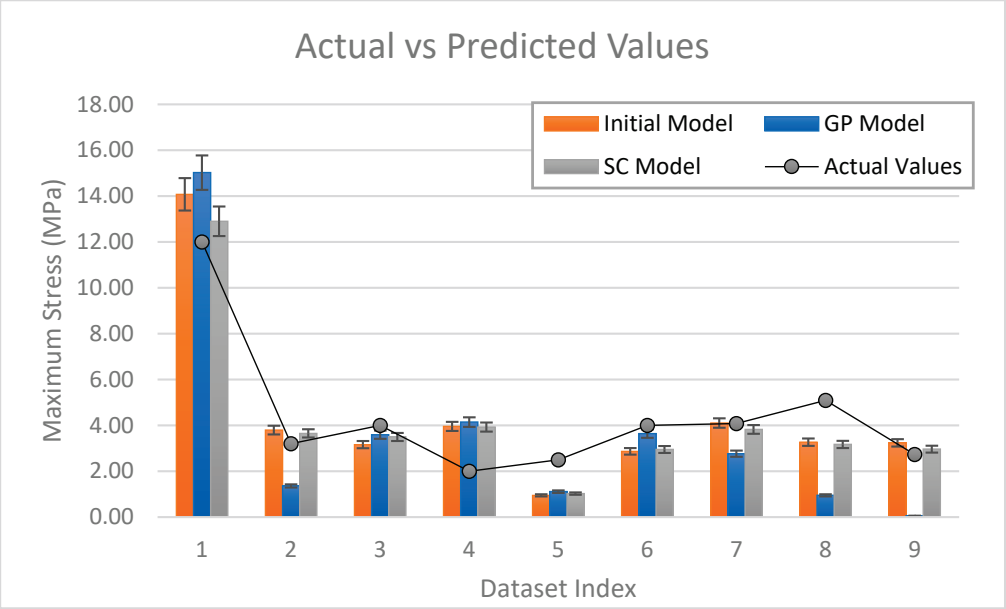


Figure 12. Bar plot of predicted values compared to actual values for 9 checking datasets (maximum stress).

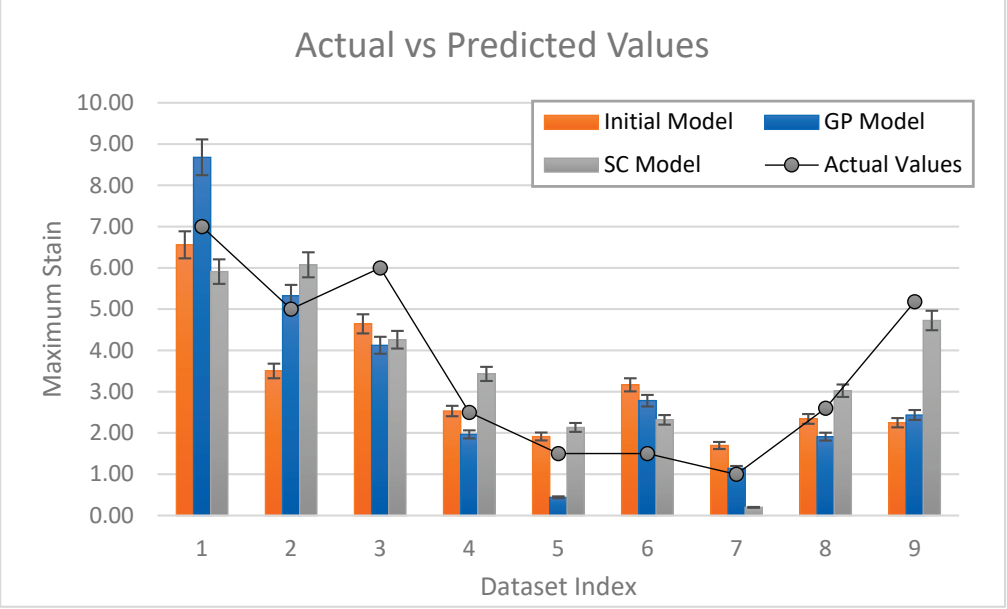


Figure 13. Bar plot of predicted values compared to actual values for 9 checking datasets (maximum strain).

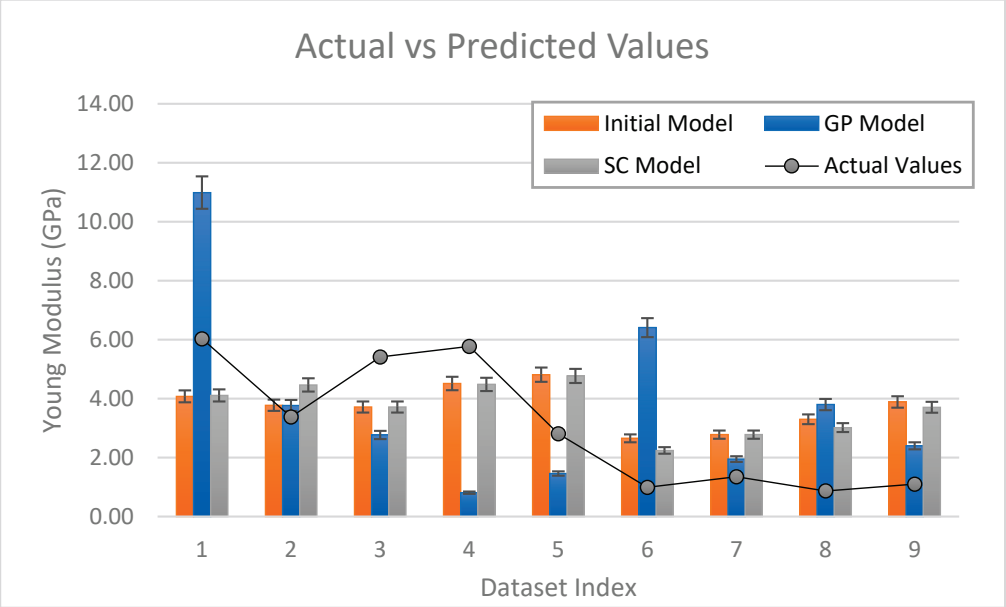


Figure 14. Bar plot of predicted values compared to actual values for 9 checking datasets (Young's modulus).

Figure 12 illustrates the predicted versus actual stress values for nine datasets, revealing key trends in the performance of the three models: initial, subtractive clustering (SC), and grid partitioning (GP). The stress value is slightly overestimated, with the GP model providing the closest prediction to the actual value. At data point 2, a significant overestimation is observed, particularly by the SC model, as the actual stress value is substantially lower. For data points 3 to 9, the predictions closely align with the actual values, especially for smaller stress magnitudes, with the GP model consistently demonstrating a reliable performance across the dataset. Overall, the models exhibit higher accuracy for moderate stress values, while larger deviations are evident in extreme cases, such as at data point 2.

The initial ANFIS model for maximum strain exhibited an average error of ± 1.34 with an accuracy of 0.58, which improved to an average error of ± 0.96 and an accuracy of 0.78. This improvement reflects a 28% reduction in error and a 25% increase in accuracy as depicted in Figure 13. In this case, the best membership function was the pi-shaped function for the gird partition algorithm, while for subtractive clustering, it remained Gaussian. The two techniques employ distinct methods for handling data subsets and different categorization, so they use different membership functions as the mathematical approach of the model itself changes.

Figure 13 illustrates the predicted versus actual strain values for nine data points. At data point 1, all models overestimate the strain, with the GP model providing the closest prediction to the actual value. At data point 2, significant overestimation is observed, particularly by the initial and SC models, as the actual strain value is considerably lower. For data points 3 to 9, the models generally produce predictions closer to the actual strain values, with the GP model demonstrating the most consistent performance. In contrast, the initial and SC models exhibit larger deviations, particularly in cases of extreme strain values, such as at data point 1.

The initial model for predicting the Young's modulus showed an average error of ± 1.85 GPa and an accuracy of 0.17. After applying the subtractive clustering algorithm, the model improved to an average value error of ± 1.77 GPa and an accuracy of 0.25. This improvement corresponds to a 5% reduction in error and a 32% increase in accuracy, as depicted in Figure 14. At data point 1, the GP model significantly overestimates the value, whereas the initial and SC models provide predictions closer to the actual value. For

data points 2 to 5, all models perform reasonably well, though the GP model exhibits slight overestimation. At data points 6 to 9, where the actual values approach zero, the initial and SC models deliver more accurate predictions, while the GP model continues to overestimate. Overall, the initial and SC models demonstrate superior performance for lower values, while the GP model shows larger deviations.

As demonstrated in this study, applying a common ANFIS model configuration to all three output cases would be unsuitable. The initial value selection and iterative process diagrams clearly show that each prediction model exhibited distinct characteristics, driven by significantly different initial data. The analysis underscores the importance of adapting the ANFIS configuration to each specific output, as a single model cannot adequately capture the unique relationships inherent in varying mechanical properties.

The analysis demonstrated that the ANFIS model effectively adjusted printing parameters based on the experimental AM data, resulting in significant improvements in stress, strain, and Young's modulus. The evaluation metrics confirmed the model's reliability in predicting the behavior of printed parts under diverse data. Although the limited sample size posed certain constraints, the results highlight the model's potential for further refinement through larger datasets and more comprehensive testing. Moreover, the experimental data and the obtained results confirm the effectiveness of ANFIS in enhancing the accuracy and efficiency of the printing process, reinforcing its applicability in data-driven manufacturing.

6. Conclusions

This study aims to evaluate different configurations of an ANFIS model to enhance the prediction of the mechanical properties of AM specimens by refining key model parameters. By integrating the adaptive learning capabilities of neural networks with the interpretability of fuzzy logic, this research addresses critical challenges associated with modeling the complex relationships inherent in additive manufacturing (AM) processes. These challenges include variations in layer thickness, infill pattern, printing speed, and material characteristics. The developed ANFIS model provides a robust and adaptive framework for predicting and enhancing the mechanical performance of AM-produced parts, as the prediction of mechanical properties of AM parts is a complex multifactorial problem.

The research highlights several key innovations. First, the implementation of ANFIS enables the adaptive refinement of printing parameters based on experimental data, significantly enhancing the accuracy of predictions for critical mechanical properties such as stress, strain, and Young's modulus. This capability not only enhances the quality and consistency of printed parts but also reduces the need for extensive physical testing and iterative prototyping, saving both time and resources. Furthermore, the study investigates two fuzzy partitioning techniques—grid partitioning and subtractive clustering—demonstrating the flexibility of ANFIS in capturing complex input–output relationships. Grid partitioning provided a structured framework for rule generation, while subtractive clustering significantly improved efficiency by identifying effective rule sets, even when handling noisy data.

Across all three cases examined, subtractive clustering demonstrated high effectiveness, achieving an improved predictive accuracy for mechanical properties such as stress, strain, and Young's modulus. For stress, the SC model produced accurate predictions that closely aligned with actual values, particularly for moderate stress levels, while minimizing deviations observed in extreme cases. In the case of strain predictions, the SC model consistently delivered estimates closer to the actual strain values, reducing the larger deviations observed in other configurations. Similarly, for Young's modulus, the SC model

provided the most accurate results, especially at lower values and near-zero actual values, outperforming other configurations that exhibited a tendency to overestimate.

Despite the computational challenges posed by the high dimensionality of input data in grid partitioning, the study successfully addressed these limitations by configuring the model to use two membership functions of the same type for each input. This adjustment ensured efficient processing without compromising accuracy, even in the absence of advanced computational resources. Overall, the final and the most suitable model has a mean obtained estimation error of 14.13%. These findings underscore the potential of ANFIS as a powerful, adaptive tool for additive manufacturing, capable of dynamically adjusting key parameters and efficiently handling complex data relationships. By leveraging subtractive clustering and dynamic parameter refinement, this study presents a scalable, data-driven framework that enhances the mechanical reliability of 3D-printed components, offering significant value across diverse manufacturing environments.

Future research could be focused on expanding the dataset with more diverse materials and advanced AM technologies to enhance the model's predictive accuracy and applicability. Incorporating real-time sensor data during the printing process could enable the development of a closed-loop feedback system, where the ANFIS model could dynamically adjust parameters to correct deviations and improve print quality on-the-fly. Additionally, future work may involve expanding the application of ANFIS and related machine learning technologies in AM by integrating real-time data and developing more sophisticated predictive models. A promising direction would be the development of autonomous manufacturing systems, enabling AM machines to adapt dynamically to new materials and geometries without the need for human intervention.

Author Contributions: Conceptualization, V.D.S. and P.Z.; methodology, V.D.S. and P.Z.; validation, E.-M.M., V.D.S. and P.Z.; formal analysis, E.-M.M., P.Z. and V.D.S.; investigation, E.-M.M., V.D.S. and P.Z.; resources, P.Z., V.D.S. and E.-M.M.; data curation, E.-M.M., V.D.S. and P.Z.; writing—original draft preparation, E.-M.M., P.Z. and V.D.S.; writing—review and editing, P.Z., V.D.S., E.-M.M. and C.I.S.; visualization, E.-M.M.; supervision, C.I.S. All authors have read and agreed to the published version of the manuscript.

Funding: This research received no external funding.

Data Availability Statement: The original contributions presented in this study are included in the article. Further inquiries can be directed to the corresponding author.

Conflicts of Interest: The authors declare no conflicts of interest.

References

1. Dubey, G.; Gupta, R.K.; Kumar, S.; Kumar, M. Study of industry 4.0 pillars and their uses in increasing productivity and reducing logistics defects. *Mater. Today Proc.* **2022**, *63*, 85–91. [CrossRef]
2. Soori, M.; Arezoo, B.; Dastres, R. Virtual manufacturing in Industry 4.0: A review. *Data Sci. Manag.* **2024**, *7*, 47–63. [CrossRef]
3. Sagias, V.D.; Giannakopoulos, K.; Stergiou, C. Mechanical properties of 3D printed polymer specimens. *Procedia Struct. Integr.* **2018**, *10*, 85–90. [CrossRef]
4. Amza, C.G.; Zapciu, A.; Constantin, G.; Baciu, F.; Vasile, M.I. Enhancing Mechanical Properties of Polymer 3D Printed Parts. *Polymers* **2021**, *12*, 562. [CrossRef]
5. Sedlak, J.; Joska, Z.; Jansky, J.; Zouhar, J.; Kolomy, S.; Slany, M.; Svasta, A.; Jirousek, J. Analysis of the Mechanical Properties of 3D-Printed Plastic Samples Subjected to Selected Degradation Effects. *Materials* **2023**, *16*, 3268. [CrossRef]
6. Tănase, M.; Portoacă, A.I.; Diniță, A.; Brănoiu, G.; Zamfir, F.; Sirbu, E.E.; Călin, C. Optimizing Mechanical Properties of Recycled 3D-Printed PLA Parts for Sustainable Packaging Solutions Using Experimental Analysis and Machine Learning. *Polymers* **2024**, *16*, 3268. [CrossRef]
7. Sadaghian, H.; Dadmand, B.; Pourbaba, M.; Jabbari, S.; Yeon, J.H. The Effect of Size on the Mechanical Properties of 3D-Printed Polymers. *Sustainability* **2024**, *16*, 356. [CrossRef]

8. Akbari, P.; Zamani, M.; Mostafaei, A. Machine learning prediction of mechanical properties in metal additive manufacturing. *Addit. Manuf.* **2024**, *91*, 104320. [CrossRef]
9. Yüksel, N.; Eren, O.; Börklü, R.; Sezer, H.K. Mechanical properties of additively manufactured lattice structures designed by deep learning. *Thin-Walled Struct.* **2024**, *196*, 111475. [CrossRef]
10. Yu, Q.; Zhang, M.; Mujumdar, A.S.; Li, J. AI-based additive manufacturing for future food: Potential applications, challenges and possible solutions. *Innov. Food Sci. Emerg. Technol.* **2024**, *92*, 103599. [CrossRef]
11. Ded, B.J.; Chowdhury, S.; Ali, N.M. An investigation of the ensemble machine learning techniques for predicting mechanical properties of printed parts in additive manufacturing. *Decis. Anal. J.* **2024**, *12*, 100492.
12. Rooney, K.; Dong, Y.; Basak, A.K.; Pramanik, A. Prediction of Mechanical Properties of 3D Printed Particle-Reinforced Resin Composites. *J. Compos. Sci.* **2024**, *8*, 416. [CrossRef]
13. Ali, A.; Riaz, R.D.; Malik, U.J.; Abbas, S.B.; Usman, M.; Shah, M.U.; Kim, I.; Hanif, A.; Faizan, M. Machine Learning-Based Predictive Model for Tensile and Flexural Strength of 3D-Printed Concrete. *Materials* **2023**, *16*, 4149. [CrossRef]
14. Moayyedian, M.; Qazani, M.R.C.; Cvorovic, V.; Asi, F.; Mussin, A.; Hedayati-Dezfooli, M.; Dinc, A. Tensile Test Optimization Using the Design of Experiment and Soft Computing. *Processes* **2023**, *11*, 3106. [CrossRef]
15. Sagias, V.D.; Zacharia, P.; Tempeloudis, A.; Stergiou, C. Adaptive Neuro-Fuzzy Inference System-Based Predictive Modeling of Mechanical Properties in Additive Manufacturing. *Machines* **2024**, *12*, 523. [CrossRef]
16. Zacharia, P.T. An Adaptive Neuro-fuzzy Inference System for Robot Handling Fabrics with Curved Edges towards Sewing. *J. Intell. Robot. Syst.* **2010**, *58*, 193–209. [CrossRef]
17. Panoiu, M.; Panoiu, C.; Mezinescu, S. Modelling and Prediction of Reactive Power at Railway Stations Using Adaptive Neuro Fuzzy Inference Systems. *Appl. Sci.* **2023**, *13*, 212. [CrossRef]
18. Kabengele, K.T.; Olayode, I.O.; Tartibu, L.K. Analysis of the Performance of a Hybrid Thermal Power Plant Using Adaptive Neuro-Fuzzy Inference System (ANFIS)-Based Approaches. *Appl. Sci.* **2023**, *13*, 11874. [CrossRef]
19. Jia, H.; Lu, X.; Cai, D.; Xiang, Y.; Chen, J.; Bao, C. Predictive Modeling and Analysis of Material Removal Characteristics for Robotic Belt Grinding of Complex Blade. *Appl. Sci.* **2023**, *13*, 4248. [CrossRef]
20. Stavrinidis, S.; Zacharia, P. An ANFIS-Based Strategy for Autonomous Robot Collision-Free Navigation in Dynamic Environments. *Robotics* **2024**, *13*, 124. [CrossRef]
21. Nawafleh, N.; AL-Oqla, F.M. An innovative fuzzy-inference system for predicting the mechanical behavior of 3D printing thermoset carbon fiber composite materials. *Int. J. Adv. Manuf. Technol.* **2022**, *121*, 7273–7286. [CrossRef]
22. Wei, H.; Tang, L.; Qin, H.; Wang, H.; Chen, C.; Li, Y.; Wang, C. Optimizing FDM 3D printing parameters for improved tensile strength using the Takagi–Sugeno fuzzy neural network. *Mater. Today Commun.* **2024**, *38*, 108268. [CrossRef]
23. Gibson, L.; Ashby, M. *Cellular Solids*; Cambridge University Press: Cambridge, UK, 2014.
24. Prada Parra, D.; Ferreira, G.R.B.; Díaz, J.G.; Gheorghe de Castro Ribeiro, M.; Braga, A.M.B. Supervised Machine Learning Models for Mechanical Properties Prediction in Additively Manufactured Composites. *Appl. Sci.* **2024**, *14*, 7009. [CrossRef]
25. Jang, J.-S. ANFIS: Adaptive-network-based fuzzy inference system. *IEEE Trans. Syst. Man Cybern.* **1993**, *23*, 665–685. [CrossRef]
26. Chiu, S. Method and software for extracting fuzzy classification rules by subtractive clustering. In Proceedings of the North American Fuzzy Information Processing, Berkeley, CA, USA, 19–22 June 1996; pp. 461–465.
27. *ASTM D638-14*; Standard Test Method for Tensile Properties of Plastics. ASTM International: West Conshohocken, PA, USA, 2014; Volume 1, p. 1.
28. *ASTM D695-15*; Standard Test Method for Compressive Properties of Rigid Plastics. ASTM International: West Conshohocken, PA, USA, 2015; Volume 1, p. 1.
29. *ASTM D7791-17*; Standard Test Method for Uniaxial Fatigue Properties of Plastics. ASTM International: West Conshohocken, PA, USA, 2017; Volume 1, p. 1.
30. *ASTM D790-17*; Standard Test Methods for Flexural Properties of Unreinforced and Reinforced Plastics and Electrical Insulating Materials. ASTM International: West Conshohocken, PA, USA, 2017; Volume 1, p. 1.
31. *ASTM D5279-21*; Standard Test Method for Plastics: Dynamic Mechanical Properties: In Torsion. ASTM International: West Conshohocken, PA, USA, 2021; Volume 1, p. 1.
32. Szwajka, K.; Zielińska-Szwajka, J.; Trzepieciński, T. The Use of a Radial Basis Function Neural Network and Fuzzy Modelling in the Assessment of Surface Roughness in the MDF Milling Process. *Materials* **2023**, *16*, 5292. [CrossRef]
33. Ibe, O.C. *Fundamentals of Applied Probability and Random Processes*, 2nd ed.; Elsevier: Amsterdam, The Netherlands, 2014.

Disclaimer/Publisher's Note: The statements, opinions and data contained in all publications are solely those of the individual author(s) and contributor(s) and not of MDPI and/or the editor(s). MDPI and/or the editor(s) disclaim responsibility for any injury to people or property resulting from any ideas, methods, instructions or products referred to in the content.

applied sciences

MDPI

Article

Selective Laser-Melted Alloy 625: Optimization of Stress-Relieving and Aging Treatments

Barbara Rivolta *, Riccardo Gerosa and Davide Panzeri

Department of Mechanical Engineering, Politecnico di Milano, via La Masa 1, 20133 Milan, Italy; riccardo.gerosa@polimi.it (R.G.); davide.panzeri@polimi.it (D.P.)
* Correspondence: barbara.rivolta@polimi.it

Abstract: Additive manufacturing is an innovative solution to produce components characterized by complex geometries. The use of such parts requires a deep knowledge of their behavior under different service conditions, especially from mechanical and corrosion resistance points of view. One of the most well-known and employed materials produced by selective laser melting is nickel alloy 625. It is already commonly used in its conventional form, but the additive manufacturing technology, despite its higher production costs and lower productivity, is becoming competitive because of its excellent mechanical strength. It is in fact significantly higher compared to the conventionally manufactured alloy whose properties are often limited by the difficulty in retaining a fine grain size during plastic deformation and heat treatment. Even though the as-built performance is already quite good, further strength improvement can be attained upon tailored single- and double-aging treatments that are optimized starting from the experimental results obtained in the conventional alloy and also considering the influence on corrosion resistance. In addition, considering that the stress-relieving treatment recommended for the conventional forged alloy at 870 °C is not suitable for the selective laser-melted material because of the more rapid precipitation response, this temperature is optimized to improve both the tensile deformability and the corrosion behavior.

Keywords: alloy 625; selective laser melting; aging treatment; stress-relieving treatment; corrosion resistance

1. Introduction

Nickel alloy 625 was patented in 1964 by H. L. Eiselstein and J. Gadbut. Its chemical composition is characterized by the presence of high amounts of chromium, molybdenum, and niobium, which provide excellent mechanical strength and corrosion resistance in several environments [1–11]. For such a reason, this alloy grade is adopted in many applications, such as aerospace, chemical, oil and gas extraction, power generation, and automotive [1,4,6,11]. The ASTM B446 standard [12] requires alloy 625 to be heat-treated following two processes: soft annealing and solution annealing. The former requires a minimum temperature of 870 °C, and it is recommended for applications below 600 °C, where good mechanical and corrosion properties are required [12]. The latter is instead suggested to improve the creep strength at temperatures above 600 °C, and it is performed at a minimum temperature of 1093 °C [12]. In the soft-annealed condition, this alloy is characterized by an austenitic microstructure with a heterogeneous distribution of primary Nb and Ti carbides and nitrides [8–11,13]. The thermal exposure above about 600 °C during processing, heat treatment, and service can activate complex precipitation phenomena that

are able to modify the mechanical and corrosion resistance significantly [1,10]. On the other hand, special heat treatments can be developed to obtain a hardening effect when required by the service conditions [12]. The time–temperature–precipitation (TTP) curves available in the literature are reported and adapted in Figure 1 for both the conventional alloy and that manufactured by SLM focusing the attention on the δ phase that is the most detrimental for the material's toughness. Metal carbides (MC, M_6C, and $M_{23}C_6$) and intermetallic (especially γ'' phase) and Laves phases can be present as well [10]. These compounds can decrease the corrosion resistance (especially when intergranular Cr- and Mo-rich carbides precipitate in the metal matrix), the ductility (especially when Cr- and Mo-rich carbides are created at the grain boundary), and the deformability of the alloy [1–4,10,14–16]. Finally, niobium, aluminum, and titanium promote the precipitation of the intermetallic hardening γ'' phase.

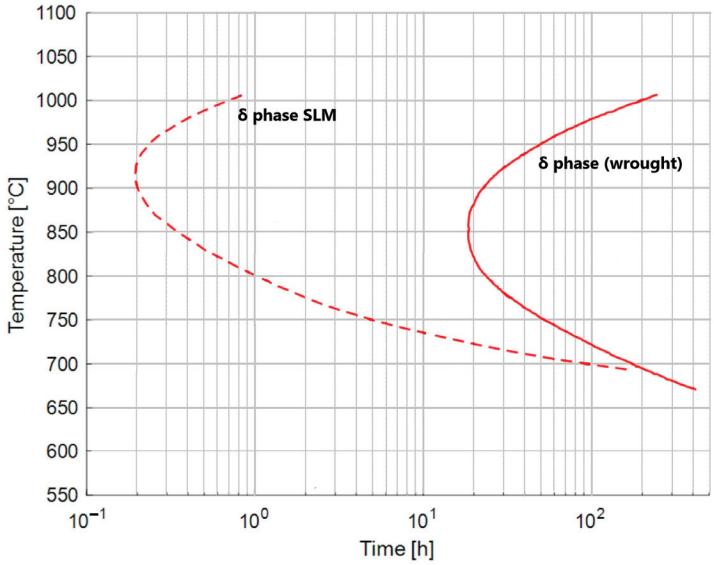


Figure 1. Experimental time–temperature–precipitation (TTP) curves for the delta phase of the SLMed 60 alloy 625 compared to those of the wrought (WR) alloy. Adapted from [10,17,18].

Nowadays, additive manufacturing is increasingly adopted for producing a variety of components especially when complex geometries are required. In fact, in these cases, the conventional manufacturing processes are typically not suitable because of technological limits and/or shape complexity. Among the wide range of additive technologies, this research work is focused on the selective laser melting (SLM) technique. Starting from a CAD model, this method allows us to generate parts layer by layer with a build direction perpendicular to the base plate. Each powder bed is selectively melted by a laser beam. Once the first layer is completed, the base plate is lowered, and the stacking process is continued. During the process, an inert gas (argon or nitrogen) is adopted to avoid powder oxidation within the chamber. Considering the huge growth in the adoption of additive manufacturing techniques in the last decade, this research work is also aimed at investigating the mechanical properties of the selective laser-melted alloy 625 in comparison with those of the conventionally manufactured one. This is extremely useful for designers in the transition from the conventional 625 alloy to the additive manufactured one with reliable data about the mechanical performance and strategies for further strength enhancement based on tailored heat treatments. The literature data about the mechanical properties of the selective laser-melted alloy 625 are reported in Table 1 and compared to those of the conventional wrought and centrifugally cast alloys. Table 2 provides a summary of the data reported in Table 1 with the range and the average values for each condition. According to these data, the as-built selective laser-melted alloy 625

shows outstanding mechanical properties compared to those of the conventional wrought and centrifugally cast alloys. Moreover, in the as-built condition, the mechanical strength is reduced by both soft- (1038 °C) and solution-annealing (1150 °C) treatments because of grain coarsening after recrystallization and the progressive removal of the original dendritic structure. However, because of the excellent fineness of the as-built microstructure, the mechanical strength upon annealing treatments remains higher than that observed in both the conventional wrought and centrifugally cast alloys. These excellent properties make selective laser melting a promising manufacturing process from the point of view of static mechanical strength.

Table 1. Literature data about the mechanical properties of the selective laser-melted alloy 625 compared to those of the conventional wrought and centrifugally cast alloys. A% is the percentage of elongation.

Condition	Hardness	YS [MPa]	UTS [MPa]	A%	Reference
As-built (SLM)	---	567–783	836–1041	10–57	[19]
As-built (SLM)	---	350–400	840–910	56–62	[20]
As-built (SLM)	285 HBW	618–783	891–1041	33–41	[21,22]
As-built (SLM)	---	770	1039	40	[23]
As-built (SLM)	---	709–859	1103–1242	27–30	[24]
As-built (SLM)	342 HV0.5	566	1087	29	[25]
As-built (SLM)	304 HV0.3	---	---	---	[26]
As-built (SLM)	332 HV0.5	676–767	964–1055	34–42	[27]
As-built (SLM)	273–303 HV2 300–320 HV0.1	630	827	---	[28]
As-built (SLM) + 1038 °C	---	523–577	841–854	---	[19]
As-built (SLM) + 1038 °C	253 HV0.5	598–633	955–1020	39–43	[27]
As-built (SLM) + 1150 °C	---	379	851	55	[22]
As-built (SLM) + 1150 °C	190 HBW	396	883	55	[21]
As-built (SLM) + 1150 °C	190 HBW	---	---	---	[29]
Wrought (solubilized)	---	413	914	70	[30]
Wrought (solubilized)	---	350	809	76	[23]
Wrought (solubilized)	169–275 HV30	317–460	751–910	47–70	[11,31]
Centrifugally cast	80–90 HRB 151–188 HV	290–310	580–595	46–57	[28,32]

Table 2. Summary of the data reported in Table 1 with range and average values for each condition.

Condition		YS [MPa]	UTS [MPa]	YS/UTS [-]	A%
As-built (SLM)	Range	350–859	827–1242	0.43–0.76	10–62
	Average	653	990	0.66	38
As-built (SLM) + 1038 °C	Range	523–633	841–1020	0.62–0.68	39–43
	Average	583	918	0.64	41
As-built (SLM) + 1150 °C	Range	379–396	851–883	0.45–0.45	55–55
	Average	388	867	0.45	55
Wrought (solubilized)	Range	317–460	751–914	0.43–0.47	47–76
	Average	384	851	0.45	68
Centrifugally cast	Range	290–310	580–595	0.50–0.52	46–57
	Average	300	588	0.51	53

The additive manufacturing technique permits a high customization level and design freedom in terms of shape and thicknesses. Such peculiarity is fundamental to efficiently exploit topological optimization at the design stage, with the aim of obtaining improved geometries in terms of weight and mechanical performance. However, low productivity and high manufacturing costs remain critical aspects for a broader application of these techniques. Moreover, in the as-built condition, additively manufactured parts are typically associated with poor surface finishing and process-induced defects which can detrimentally affect the fatigue resistance and lead to incompatibility with geometrical tolerances. For this reason, post-processing techniques, such as hot isostatic pressing, shot peening, sand blasting, electropolishing, and machining, can be adopted to improve the surface quality and the defect content. In the as-built condition, selective laser-melted (SLMed) components are characterized by the presence of textured tracks with their orientation dependent on the scanning strategy. Because the process involves high cooling rates, the microstructure is characterized by melt pools composed of very fine dendritic structures with both columnar and cellular morphology. The cellular morphology is induced by the modification of the columnar one due to high cooling rates [33]. The presence of high solidification rates and several local thermal cycles determines the formation of a very fine microstructure with a high level of micro-segregation [17]. Even though such high cooling rates are able to develop metallic glasses, alloy 625 solidifies as a crystalline solid with the possible formation of metastable phases sometimes with an amorphous structure. According to the literature [34,35], the dendrite cores are mainly enriched with nickel and chromium, while the interdendritic regions are rich in niobium and molybdenum and depleted in chromium. Such enrichment in niobium and molybdenum towards the interdendritic region promotes the formation of the δ and γ'' phases [17]. Therefore, the precipitation response in the selective laser-melted material is significantly enhanced. The comparison among the TTP curves of the conventional and selective laser-melted materials is reported in Figure 1. According to the literature [25], one of the main drawbacks of the SLM process is the formation of thermally induced residual stresses. This phenomenon can determine severe distortion and even failure caused by the accommodation of the residual stresses after the removal of the component from the build plate. Such behavior becomes more and more critical in the presence of thin components. This phenomenon is mainly provoked by the extremely high cooling rates (up to 10^6 K/s) achieved during the SLM process which determine strong thermal gradients between the layers [17]. For this reason, stress-relieving treatment performed before removing the components from the build plate is required to prevent such a detrimental phenomenon. According to the literature [5], the minimum stress-relieving temperature recommended for conventional alloy 625 is 870 °C (1 h per inch of section). In the selective laser-melted material, as observed by several authors [17,18,25], which is different from the wrought alloy, the formation of the detrimental δ, Ni_3Nb phase at 870 °C is obtained after very short exposure times (15 min). The precipitation of this phase provokes a significant decrease in toughness, tensile deformability, and corrosion resistance [25]. In fact, the low chromium content along the Ni_3Nb precipitates of both the γ'' and δ phases creates local anodic regions in the microstructures which are preferentially attacked, leading to an accelerated corrosion rate [36,37]. A further loss in corrosion resistance can be determined by the simultaneous precipitation of chromium-rich carbides that can be obtained at 870 °C after short exposure times, as demonstrated by the TTP diagram in Figure 1. The dramatic toughness loss in the presence of the δ phase is induced by its elongated and needle-shaped morphology. As reported in the literature [29], SLMed alloy 625 shows a faster kinetic of δ-phase precipitation in comparison to the conventional wrought alloy. In fact, in the alloy processed using SLM, at 870 °C, the formation of the δ phase starts after 15 min, while at least 20 h are required for the wrought alloy. Some studies also demonstrate that the presence of residual stresses promotes the precipitation response, but this

effect has a lower importance compared to micro-segregation [17]. Consequently, this research work investigates alternative stress-relieving temperatures that are able to relieve residual stresses, avoid the formation of δ phase, and maintain acceptable mechanical and corrosion properties. As reported by Martucci et al. [25], stress-relieving treatments performed at reduced temperatures in the range from 750 °C to 800 °C prevent the formation of the δ phase, but only a partial reduction (from 50% to 90%) in the residual stresses is obtained. Therefore, this research work investigates the feasibility of higher stress-relieving temperatures in terms of both mechanical and corrosion properties. Considering that the stabilization heat treatment is performed at 980 °C in the conventional wrought alloy [12], we decided to investigate the stress-relieving temperature of 980 °C to also permit a simultaneous improvement in the corrosion resistance, with a clear beneficial industrial effect related to the production of SLM parts with high mechanical resistance and superior corrosion properties.

Starting from the results published in prior research papers of the authors, the aging response of the as-built selective laser-melted material upon single- and double-aging treatments was analyzed in different time–temperature conditions among the most promising alloys by comparing the results against those obtained in the conventional alloy. The mechanical properties were measured using hardness and tensile tests, while corrosion resistance was analyzed in selected conditions in terms of susceptibility to intergranular corrosion in a solution of ferric sulfate and sulfuric acid for 120 h, according to the ASTM G28-A standard [38]. After the investigation of the aging treatment, the stress-relieving temperature was studied to improve the mechanical strength, tensile deformability, and corrosion resistance.

2. Materials and Method

The selective laser-melted alloy 625 was provided in the as-built condition in the form of bars printed horizontally, as shown in Figure 2. The dimensions of the transversal section were 12.5 mm × 12 mm, and the length was equal to 100 mm. The adopted bars were manufactured for each layer using the island scanning strategy, thus forming a chessboard pattern with a layer thickness of 30 μm, and the laser parameters are summarized in Table 3. The printing parameters were optimized by the producer aiming to minimize the residual porosity and improve the mechanical characteristics.

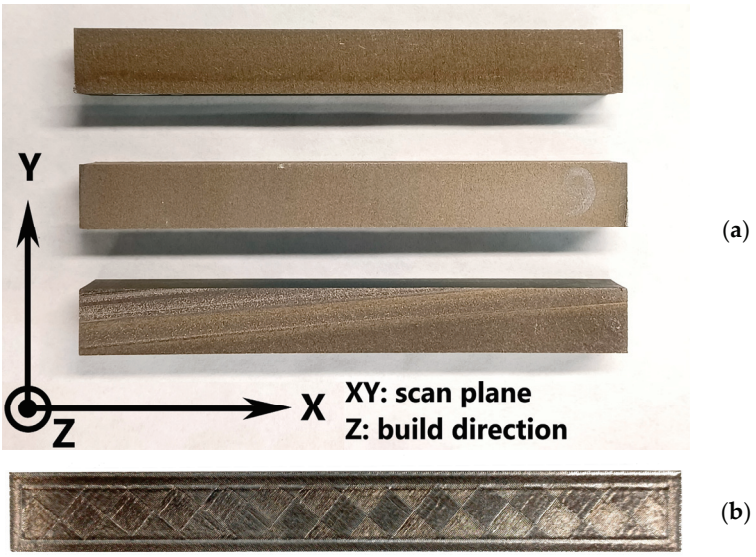


Figure 2. As-built selective laser-melted bars made of alloy 625 adopted in this work. (**a**) View of some of the printed rods; (**b**) details of the island scanning strategy adopted for the inner chessboard pattern.

Table 3. Laser parameters adopted for the contour and the inner area of the SLMed bars.

	Contour	Inner Area (Islands)
Power [W]	120	180
Speed [mm/s]	400	900
Spot size [μm]	50	150

The aging treatments were carried out in a laboratory furnace. The tensile specimens were machined along the longitudinal direction of the bars. The samples for microstructural analyses and hardness tests were prepared according to the conventional metallographic technique. In particular, cutting was performed using silicon carbide wheels with a Remet (model TR100 EV) cutting machine (Bologna, Italy). The mounting of the metallographic samples was performed in hot thermo-setting phenolic resin using a mounting machine. The grinding and polishing operations were performed using a Struers machine (Ballerup, Denmark). Chemical etching was carried out in five parts HCl diluted in one part 30% H_2O_2 for 10 s [5,39,40]. Microstructural analyses were carried out via a Leica light optical microscope (Wetzlar, Germany) and a Zeiss scanning electron microscope (Oberkochen, Germany). The HV30 Vickers hardness tests were conducted using a Wolpert Testor 930 hardness tester (Ludwigshafen am Rhein, Germany) according to the EN ISO 6507 standard [41]. The hardness tests of the selective laser-melted material were performed on the ZX plane. In each tested condition, five hardness measurements were carried out. Tensile tests were performed in selected conditions according to the EN ISO 6892 standard using round proportional specimens (6 mm gauge length and diameter) with an INSTRON 4507 testing machine (Norwood, MA, USA) [42]. The intergranular corrosion tests were carried out in a solution of ferric sulphate and sulfuric acid for 120 h, according to the ASTM G28—Method A standard [38]. The size of the corrosion specimens was 12 mm × 12.5 mm × 8 mm. They were cut along the longitudinal direction of the printed bars; then, they were prepared and polished according to the ASTM G28—Method A standard [38]. The mechanical strength requirements are reported in the ASTM B446 standard [12]. For corrosion resistance, a maximum corrosion rate of 1.20 mm/year was considered since it represents a typical prescription for most of the industrial applications of this grade.

The experimental data on the conventional forged and soft-annealed (1038 °C) alloy 625 were elaborated for comparison purposes from the literature data already published by Panzeri et al. [11,43,44]. In this case, the material was taken from an as-forged 60 mm diameter rod. All the soft-annealing and aging treatments were carried out on the metallographic samples and the tensile and corrosion specimens using a laboratory furnace. The samples for metallographic analyses and hardness tests were cut from the received rod with dimensions of 10 mm × 10 mm × 10 mm. The tensile specimens were machined from the longitudinal direction of the received rod. Hardness, tensile, and corrosion tests were carried out considering the same procedure and the reference standards adopted for the tests on the selective laser-melted material [38,41,42].

3. Results and Discussion

3.1. As-Built and Stress-Relieved Conditions

Figure 3 reports the micrographs of the selective laser-melted material in each plane obtained via light optical and scanning electron microscopy. XY is the scan plane, and it is perpendicular to the build direction Z. In the XY plane, the microstructural analysis showed the presence of elongated tracks of the melt pools with hatch angle rotation in the layer-stacking process equal to 60°, as shown in Figure 3b. The micrographs related

to the ZX and YZ planes report melt pools stacked in the build direction with uniform orientation and shape (Figure 3c,d). The solidified microstructure is represented in the SEM micrographs of Figure 3e,f. Both cellular-shaped structures and elongated dendrites are present with different orientations. The melt pool boundaries are clearly highlighted by the chemical etching process in Figure 3, and they are denoted by dashed yellow lines in the SEM micrographs. The average values of the melt pool width and depth were measured using the micrographs of the as-built material. They resulted equal to 115 μm and 220 μm, respectively.

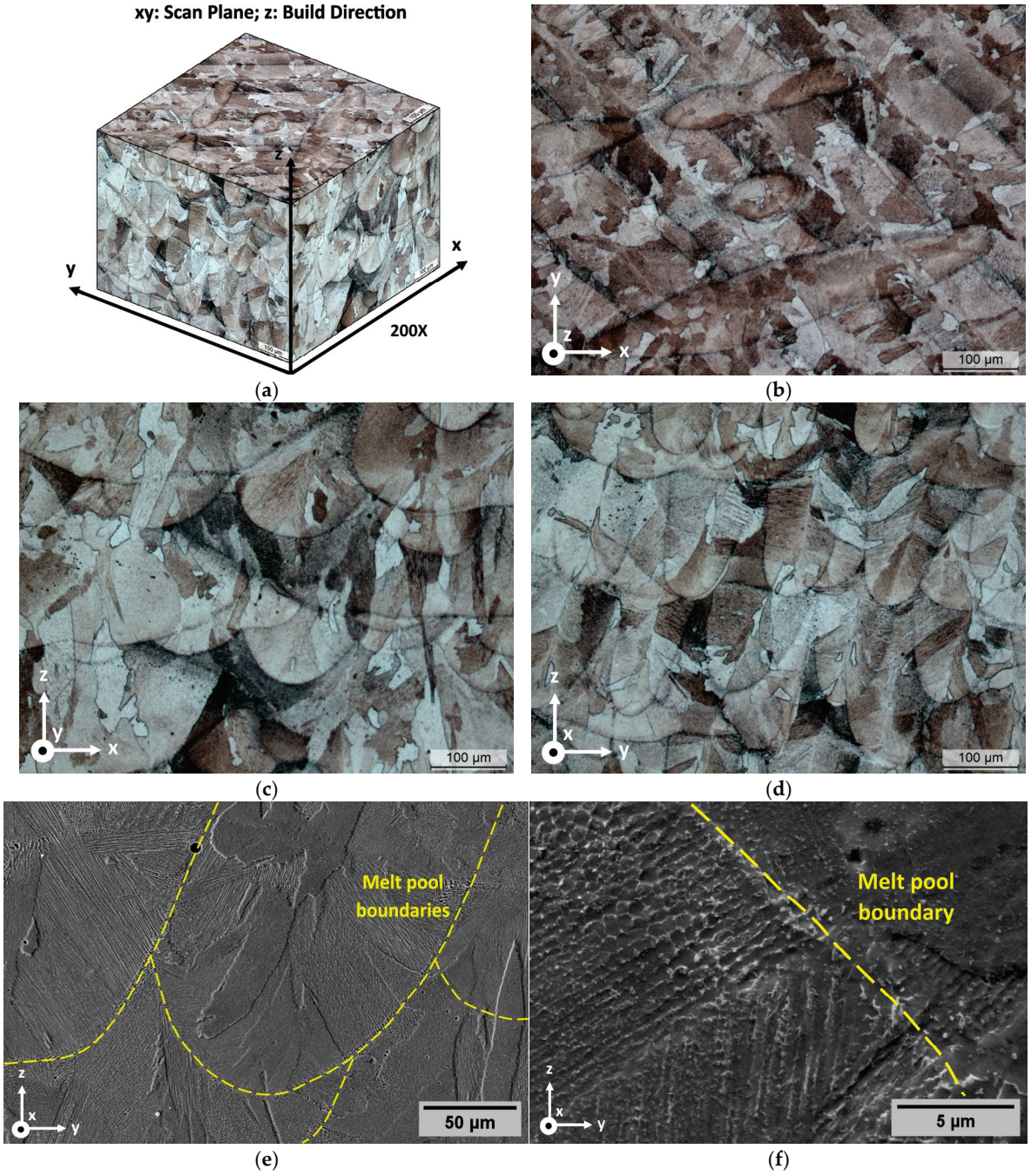


Figure 3. Micrographs of the selective laser-melted material in the as-built condition obtained via light optical and scanning electron microscopy. Figure (**a**) reports an overview of the microstructural features on three perpendicular planes. The melt pools on the three planes are shown in (**b**–**d**). SEM observation of the melt pools are reported in (**e**,**f**): dendrites with different orientations are visible in (**f**).

In SLMed alloy 625, the room-temperature mechanical properties obtained via the hardness and tensile tests in both the as-built and stress-relieved conditions are reported in Tables 4 and 5.

Table 4. Vickers hardness HV30 of the SLMed alloy 625 in both the as-built and stress-relieved conditions for each plane. The standard deviation values range from 1 to 3 HV30.

Plane	As-Built HV30	Stress-Relieved (875 °C 45 min) HV30
XY	312	314
YZ	306	307
ZX	310	311
Average	309	311

Table 5. Room-temperature mechanical properties of the SLMed alloy 625 in both the as-built and stress-relieved conditions. Tensile specimens were machined along the Y direction of the SLMed bars (longitudinal direction). Z% is the percentage reduction in area. The standard deviation values range from 1 to 2% for A% and Z% and from 2 to 10 MPa for YS and UTS.

	As-Built					Stress-Relieved (875 °C 45 min)				
	YS [MPa]	UTS [MPa]	YS/UTS	A%	Z%	YS [MPa]	UTS [MPa]	YS/UTS	A%	Z%
This work	732	1041	0.70	31.0	38	742	1078	0.69	28.0	30
Minimum ASTM B446	414	827	---	30.0	---	414	827	---	30.0	---

In both the as-built and the stress-relieved conditions, the selective laser-melted alloy 625 is characterized by outstanding mechanical strength. In fact, it is significantly higher compared not only with the average literature properties of the conventionally manufactured material reported in Table 2 (wrought and centrifugally cast) but also compared to the minimum requirements defined by the ASTM B446-19 standard [12]. This strength increase is obtained at the expense of tensile deformability, which is reduced when compared to that of the conventional material. Moreover, in the stress-relieved condition, the percentage of elongation after fracture A% is lower than the minimum standard of the prescription. The mechanical properties in the as-built condition are compatible with the literature ranges reported in Table 2 for SLMed alloy 625. The ratio between yield strength and ultimate tensile strength is appreciably increased in the selective laser-melted material (0.70) compared to the literature data of both the wrought (0.45) and centrifugally cast (0.51) counterparts reported in Table 2. In addition, the mechanical performance of the selective laser-melted material is significantly better than that of the centrifugally cast version, as shown by the comparison with the literature data in Table 2.

The susceptibility to intergranular corrosion was determined following the ASTM G-28 Method A standard [38] in both the as-built and stress-relieved conditions. The results were compared with those of the conventional wrought and soft-annealed material. In the as-built condition, the corrosion rate was equal to 0.38 mm/year after the 120 h corrosion test. Therefore, corrosion resistance in this condition is slightly higher than that measured by Panzeri et al. [43] on the conventional wrought and soft-annealed material (0.65 mm/year). Cabrini et al. [33] observed significantly higher corrosion resistance in the as-built condition (0.72 mm/year) compared to that of the conventional wrought and soft-annealed material (1.50 mm/year). They attributed this difference to the very fine dendritic structure of

the selective laser-melted alloy. In the stress-relieved condition, the corrosion rate was equal to 7.07 mm/year. As also reported in the literature [17,18,25,34,45], such a dramatic loss compared to the excellent behavior of the as-built material is mainly determined by the fast precipitation of carbides and the δ phase starting from the interdendritic regions. Consequently, this result confirms that the stress-relieving treatment at the temperature (875 °C) recommended for the conventional alloy is not feasible in the selective laser-melted material because of the significant loss in corrosion resistance induced by its faster precipitation response.

3.2. Single- and Double-Aging Treatments

The age-hardening response upon single-aging treatments was investigated in the selective laser-melted material at the same aging temperatures considered by Panzeri et al. [43,44] for the conventional wrought alloy, i.e., 732 °C and 621 °C. The experimental single-aging curves obtained using the hardness tests are reported in Figure 4 and were compared with those obtained by Panzeri et al. [43,44] on the conventional forged and soft-annealed material. The main difference is related to the initial hardness, which is significantly lower in the forged material (soft-annealed condition) compared to the selective laser-melted one (as-built condition). As previously described, this difference can be ascribed to the improved microstructural fineness in the selective laser-melted alloy. For such a reason, the conventional forged and soft-annealed alloy requires a single aging process at 621 °C for 600 h to attain a hardness value equal to that in the as-built condition for the selective laser-melted material. Regarding the hardness increment, the selective laser-melted material is characterized by a faster response in the early stage of precipitation, especially in the case of single aging at 621 °C. Then, the rate of hardness increase starts reducing compared to the behavior of the conventional material.

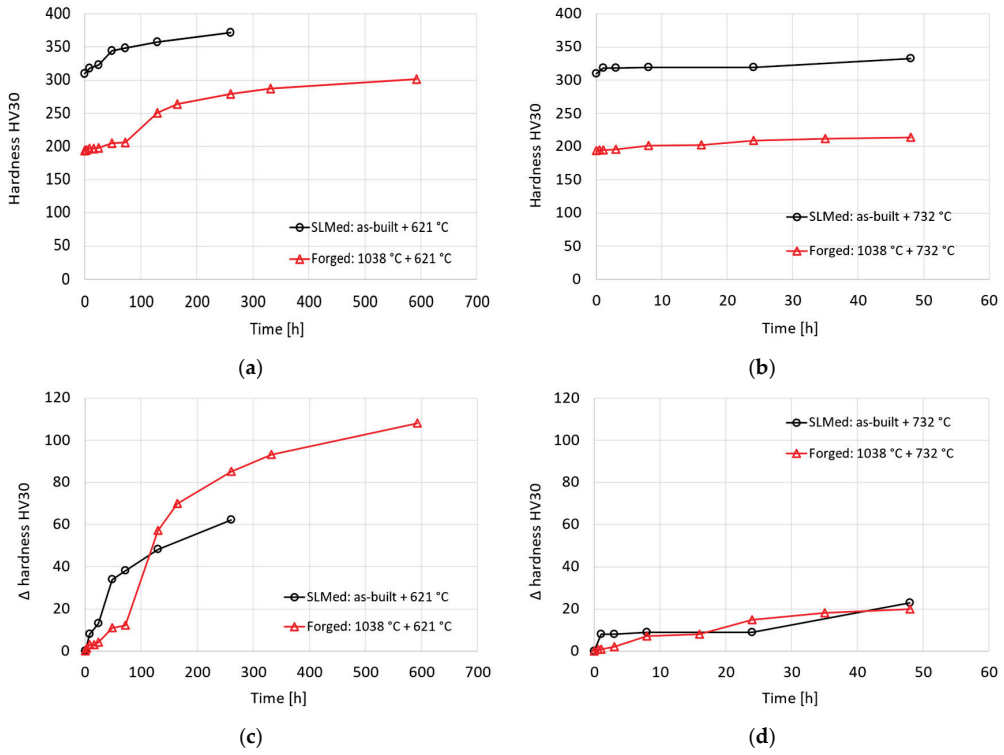
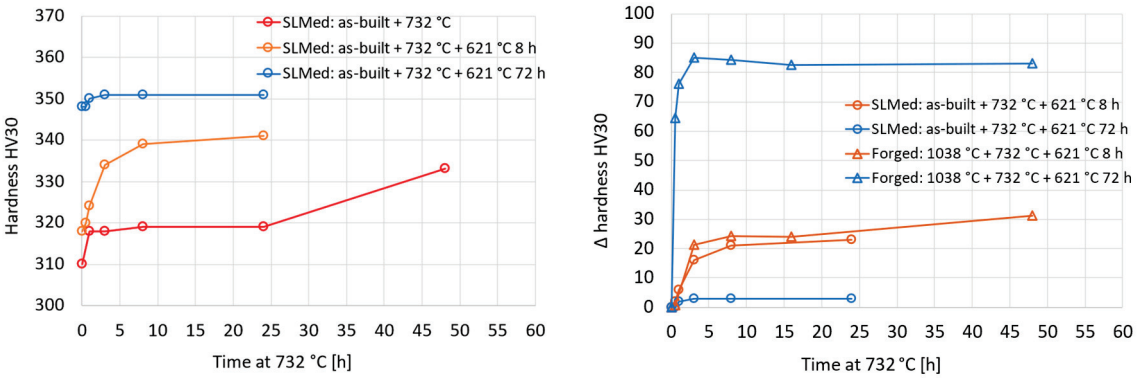


Figure 4. Hardness curves after single-aging treatments at 621 °C (**a**,**c**) and 732 °C (**b**,**d**) of the selective laser-melted alloy in comparison to the conventional forged one. The hardness increase induced by the aging treatment is significantly less for the SLMed specimens, even if their hardness always remains higher than that of the forged material. The standard deviation values range from 1 to 5 HV30.

Successively, starting from the results obtained by Panzeri et al. [43,44] on the double aging of the conventional forged alloy, the double-aging response with primary aging at 732 °C and secondary aging at 621 °C was also investigated in the selective laser-melted material by varying the exposure times at both the temperature levels. The results, reported in Figure 5, were compared to those obtained in the conventional material. Figure 5b shows that the hardness increase allowed for the addition of the primary aging step at 732 °C compared to single aging at 621 °C. According to the results reported in Figure 5b, the acceleration provided by the double-aging procedure is more significant in the conventional forged alloy compared to the selective laser-melted one. In fact, in the latter case, the hardness increment is largely reduced, and this behavior is even more evident when the duration of secondary aging is increased. Therefore, in the selective laser-melted material, the beneficial effects of double aging in terms of mechanical strengthening are appreciably lower than those experimented in the conventional alloy. Such different behavior is probably determined by the faster precipitation response of the additively manufactured material that does not need additional primary aging at higher temperatures to trigger and accelerate the age-hardening process, as is required for the conventional alloy [43,44].



(**a**) (**b**)

Figure 5. (**a**) Hardness curves upon double aging at 732 °C and 621 °C of the selective laser-melted alloy 625 in the as-built condition; (**b**) comparison of the hardness increments with double aging allowed for the addition of primary aging compared to single aging at 621 °C. The standard deviation values range from 1 to 3 HV30.

The influence of the single-aging treatments at 621 °C on room-temperature mechanical strength was investigated via tensile tests for both the selective laser-melted alloy and the conventional forged one. The results are reported and compared in Figure 6. In the conventional material, because of the presence of insufficient mechanical properties in the soft-annealed condition, the aging treatment is required to satisfy the minimum standard requirements [12]. In particular, in this case, single aging at 621 °C for 130 h is associated with acceptable tensile properties. Such strength improvement is obtained at the expense of tensile deformability, which is reduced, but it remains well above the minimum standard requirement (30%) [12]. The selective laser-melted alloy 625 is characterized by excellent mechanical strength in the as-built condition, but the percentage of elongation after fracture A% is very close to the minimum standard requirement [12]. In this case, the aging treatment can be exploited to further improve its mechanical strength. Nevertheless, such a strengthening effect is obtained at the expense of deformability. In fact, for the tested aging conditions, the values of the percentage of elongation after fracture A% are lower than the minimum prescription [12].

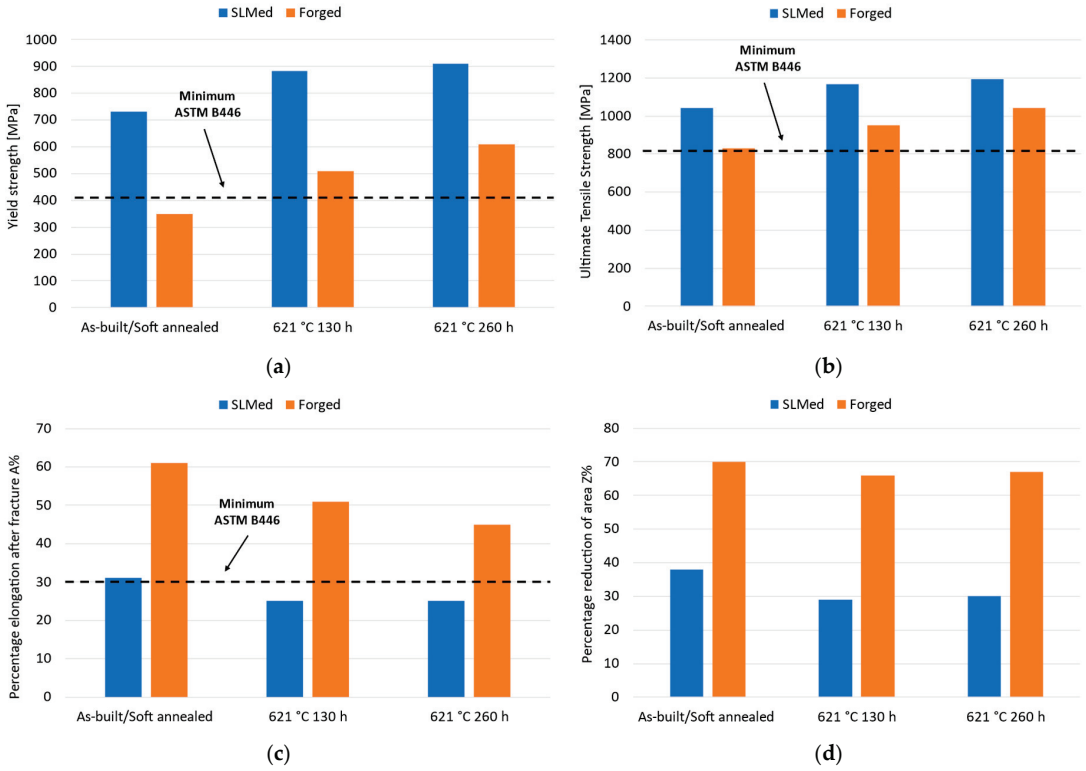


Figure 6. Room-temperature tensile properties after single-aging treatments at 621 °C of the conventional forged and soft-annealed alloy 625 [43,44] and the selective laser-melted one. Figures (**a**,**b**) report the yield strength (**a**) and the ultimate tensile strength (**b**) in selected conditions. The mechanical properties of the as-built material are significantly higher than those of the conventional forged alloy. Figures (**c**,**d**) report the percentage elongation after fracture A% (**c**) and the percentage reduction of area Z% (**d**). Tensile deformability is lower and even below the standard minimum requirement for the aged conditions. The standard deviation values for YS and UTS range from 2 to 13 MPa and from 1 to 2% for A% and Z%.

In the stress-relieved condition (875 °C 45 min), the mechanical properties of the selective laser-melted alloy 625 are similar to those in the as-built condition. However, tensile deformability is lower than the minimum prescription of the ASTM B446 standard [12]. In addition, the corrosion rate determined according to the ASTM G28-Method A standard is well above the limit value considered in this research work [38]. As reported in the literature [17,25,34,35,45], such dramatic degradation of properties is determined by the precipitation of carbides and the δ phase starting from the interdendritic regions and moving towards the dendrite center. Therefore, this behavior confirms that the stress-relieving temperature of 875 °C (recommended for the conventional alloy) is not feasible in the selective laser-melted material because of its faster precipitation response. Also in the conventionally manufactured alloy 625, the formation of the δ phase determines a severe loss of tensile deformability [2], but the precipitation of this embrittling phase requires at least 20 h at 875 °C, according to the time–temperature–precipitation diagram reported in Figure 1. Based on the literature TTP curve shown in Figure 1 for the selective laser-melted alloy 625, the onset of δ phase formation at 875 °C requires only 15 min due to the presence of faster precipitation [17,18]. According to the literature [25], the stress-relieving treatment at 875 °C is suitable to obtain a sufficient mitigation of residual stresses, but at the expense of a severe toughness loss due to δ phase formation. For this reason, it is required to optimize the stress-relieving temperature by avoiding the simultaneous precipitation of detrimental phases. Such microstructural modifications can be avoided with a sufficient reduction in the stress-relieving temperature, but the mitigation of residual stresses can become insufficient [25]. Another possibility is represented

by the adoption of temperatures above 875 °C. In this case, the reduction in residual stresses is ensured, but in order to not activate detrimental microstructural changes, it is necessary to select temperatures far enough from the nose of the TTP curves of the δ phase, which is located at about 920 °C. However, upon increasing the temperature, the loss of mechanical strength due to microstructural recrystallization and coarsening can become significant, and it should be carefully considered in order to identify the condition with the best combination of tensile strength, deformability, and corrosion resistance.

The influence of high-temperature annealing on the mechanical strength of the as-built material was investigated from 980 °C to 1100 °C. According to the results reported in Figure 7, thermal exposure above 875 °C determines a loss in mechanical strength compared to the as-built condition. In particular, at 980 °C and 1038 °C, the reduction in hardness is limited (10% and 15%, respectively), but this loss becomes more significant at 1100 °C (30 %). This reduction in mechanical strength upon high-temperature annealing was investigated via optical microscopy, as shown in Figure 8. By increasing the annealing temperature, the melt pool boundaries and the traces of the prior as-built microstructure become less visible, and they disappear almost completely at 1100 °C. In addition, the presence of recrystallized structures and annealing twins becomes more and more evident up to full recrystallization at 1100 °C, where the microstructural morphology is more similar to that of conventional forgings. This microstructural transformation and subsequent grain coarsening are associated with the loss in mechanical strength upon high-temperature annealing, as confirmed by the literature [19,46].

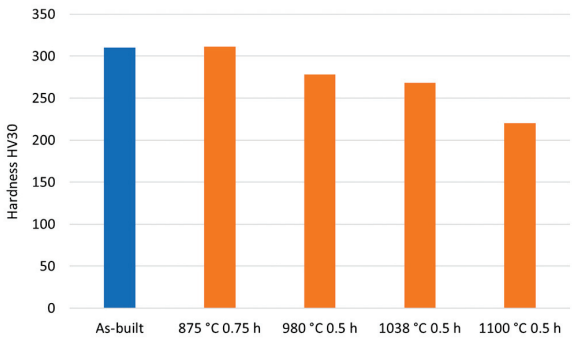


Figure 7. Hardness variation after high-temperature annealing from the as-built condition. It is due to the recrystallization phenomena occurring during the heat treatment. The standard deviation values range from 1 to 3 HV30.

According to the ASTM B446 standard [12], the corrosion resistance of the conventional alloy 625 can be improved by adopting a stabilization heat treatment at 980 °C after the solution-annealing treatment. For this reason and not to excessively reduce the mechanical strength of the as-built material, the temperature of 980 °C was selected as a potential alternative to the stress-relieving temperature of 875 °C. Moreover, according to the time–temperature–precipitation diagram reported in Figure 1, the onset of δ phase formation at 980 °C is delayed compared to that at 875 °C. The feasibility of this alternative temperature was assessed via tensile and corrosion tests. The tensile properties are reported in Figure 9. The selection of the alternative heat treatment at 980 °C for 0.5 h is associated with a slight reduction in tensile strength (15 % for yield strength and 3 % for ultimate tensile strength) compared to the as-built condition. However, the tensile properties remain well above the minimum prescriptions of the ASTM B446 standard [12]. An important advantage of this new temperature is represented by the moderate increase in tensile deformability. In fact, in this case, the percentage of elongation after fracture A% satisfies the minimum standard requirement, while the stress-relieving treatment at 875 °C was associated with insufficient A% values, as shown in Figure 9. In addition, tensile deformability is also slightly improved compared to the as-built condition.

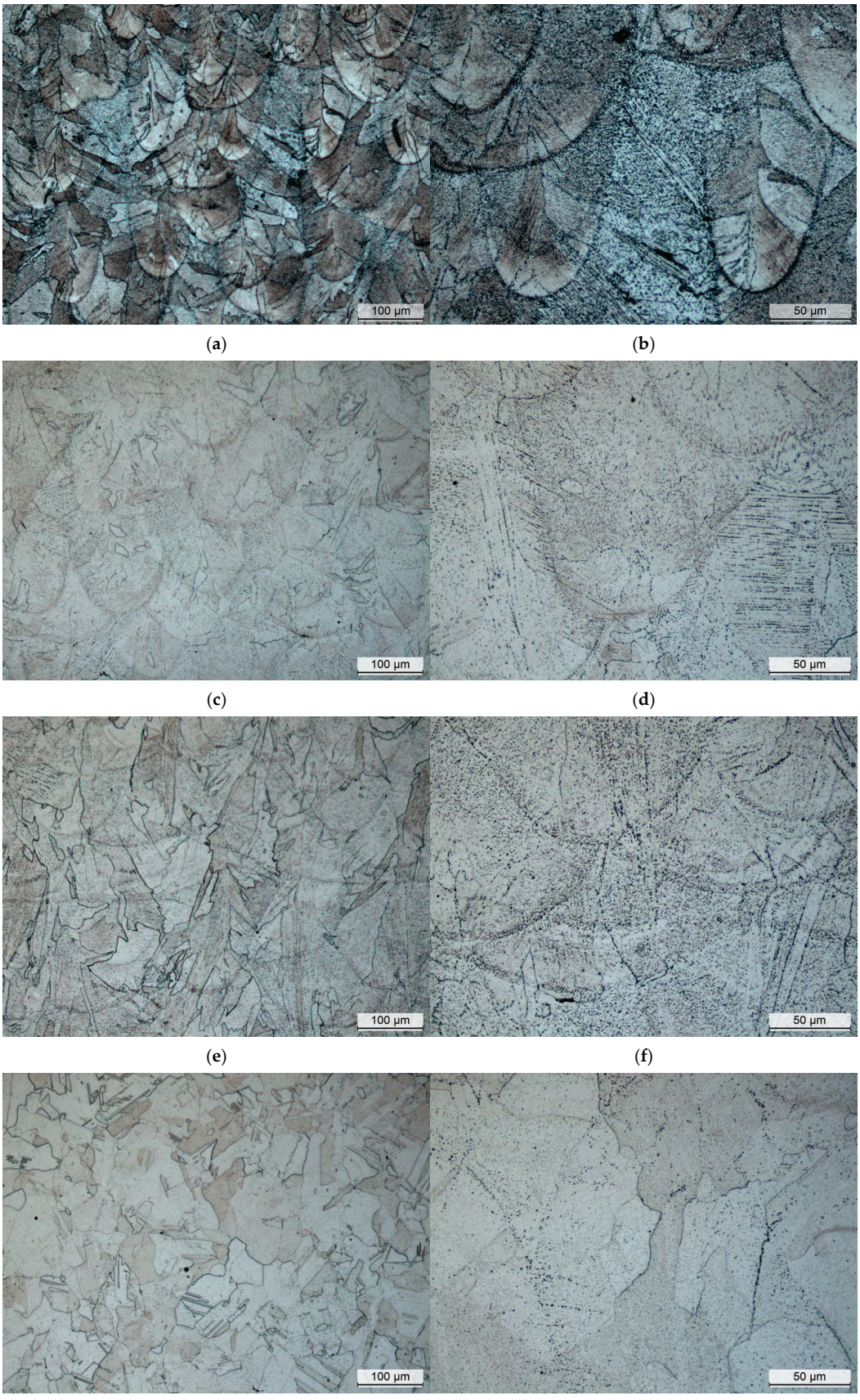


Figure 8. Optical micrographs on the ZY plane at 200X (**a**,**c**,**e**,**g**) and 500X (**b**,**d**,**f**,**h**) of the selective laser melted material after annealing at different temperatures from the as-built condition: (**a**,**b**) 875 °C 45 min; (**c**,**d**) 980 °C 0.5 h; (**e**,**f**) 1038 °C 0.5 h; (**g**,**h**) 1100 °C 0.5 h.

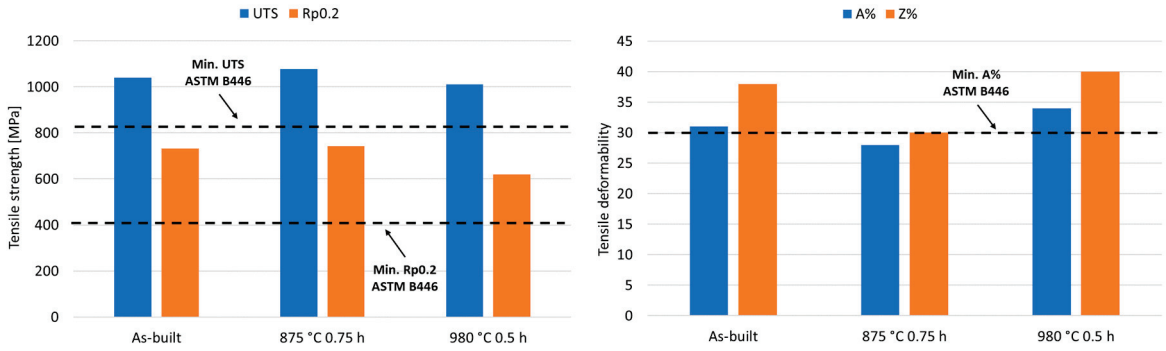


Figure 9. Room-temperature tensile strength (**a**) and tensile deformability (**b**) after heat treatment at 980 °C for 0.5 h compared to the as-built condition and to those obtained at the stress-relieving temperature recommended by the standard (875 °C). The mechanical resistance is slightly less than that of the as-built and 850 °C stress-relieved conditions, but the tensile deformability is improved and superior to the minimum standard requirement. The standard deviation values for YS and UTS range from 3 to 12 MPa and up to 1% for A% and Z%.

The susceptibility to intergranular corrosion was investigated following the ASTM G28—Method A standard [38]. The results obtained on the selective laser-melted material were compared with those obtained on the conventional forged alloy 625 published by Panzeri et al. in previous research studies [43,44]. All the experimental results were collected in the performance map reported in Figure 10 relating to the tensile and corrosion properties. In Figure 10, the green shaded area corresponds to the acceptability region with respect to the minimum standard requirements for the tensile properties [12]. Since the minimum yield strength requirement is more critical compared to the ultimate tensile strength one, the values associated with the latter property were not included in the performance map. The data labels report the corrosion rate in mm/year according to the ASTM G28—Method A standard. An acceptable limit for industrial applications of this grade is 1.2 mm/year (green label: acceptable; red label: not acceptable). Corrosion resistance and tensile deformability in the case of stress-relieving treatment at 875 °C are significantly improved after modifying the standard recommended temperature with a higher value, i.e., 980 °C, at the expense of a slight reduction in mechanical strength. Regarding the single-aging treatment at 621 °C, the strengthening effect is obtained with a detrimental reduction in corrosion resistance. Similarly, in conventional forged alloy 625, the increase in mechanical strength by aging treatment reduces both tensile deformability and corrosion resistance. In this case, full acceptability is obtained in a very narrow region, as also demonstrated by our previous research studies [43,44]. For this reason, considering the strict requirement for the corrosion resistance and rapid degradation of this property upon aging, the exploitation of aging treatments is significantly limited, and it requires a careful optimization of the aging time. Such limitation is even more critical in the selective laser-melted material because of its faster precipitation response. In this case, an additional obstacle to the adoption of aging treatments is represented by the rapid loss of the tensile deformability below the minimum standard requirement.

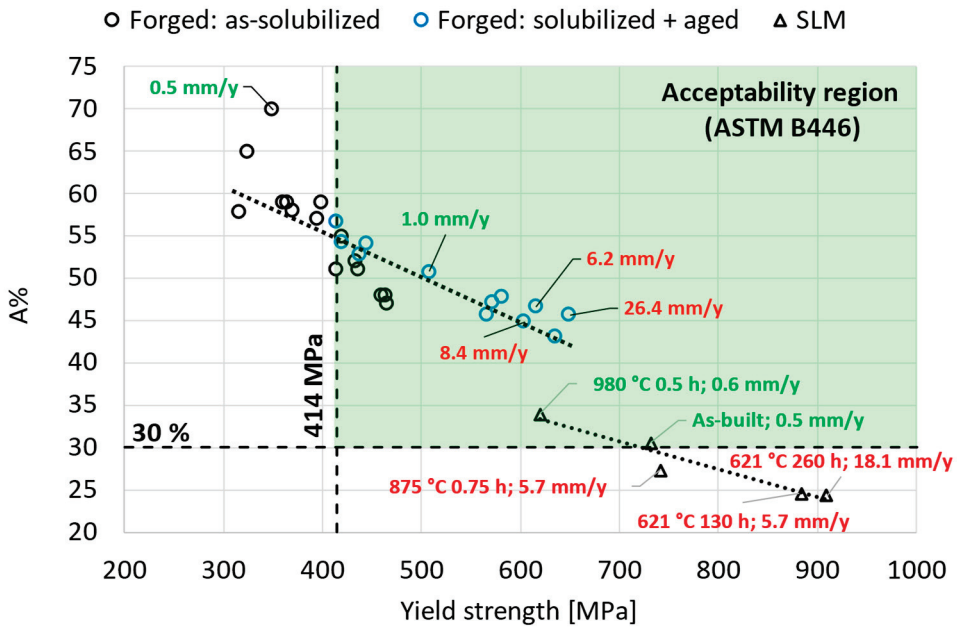


Figure 10. Performance map relating the tensile and corrosion properties of the conditions tested in this work for the selective laser-melted material and in our previously published papers [43,44] for conventional forged alloy 625. The green shaded area corresponds to the acceptability region with respect to the minimum standard requirements for the tensile properties (ASTM B446 [12]). The data labels report the corrosion rate in mm/year according to the ASTM G28—Method A standard [38] (green label: acceptable; red label: not acceptable). The standard deviation values range from 2 to 14 MPa for YS and from 1 to 2% for A%.

The corroded profiles were investigated in selected conditions for having a relationship with the corrosion rates and characterize the corrosion mechanism. The melt pool boundaries of the laser tracks are preferentially corroded compared to the inner regions. This behavior is confirmed by the literature data, which address such selective attack to the enhanced precipitation of sensitizing Ni_3Nb phases in these zones [33,36,47]. The corrosion rates are in good agreement with the observed corroded profiles.

Figure 11 shows some sections of the specimens subjected to the corrosion tests cut perpendicularly to the surfaces exposed to the corroding solution. Figure 11a,b represent the as-built condition. Some residual porosity is visible, but no corrosion damage characterizes the surface. The corresponding corrosion rate is in fact very low (0.5 mm/year). Pictures c and d are instead related to specimens aged at 621 °C for 130 h. Unlike the as-built condition, the surface clearly shows the effects of the corroding solution. The corrosion attack follows the laser tracks' borders preferentially, even if the damage includes the inner zones as well. Accordingly, the corrosion rate (5.7 mm/year) was much higher than of the as-built one. The effect of the standard stress-relieving temperature (850 °C) on corrosion resistance is clearly detrimental, as shown in Figure 11e,f. Similarly to the aged condition, the corrosion damage proceeds along the laser track direction and removes material both from the border and the inner part of the track. Also, in this case, the corrosion rate is quite high (5.7 mm/year). Finally, the new heat treatment at 980 °C resulted in a corrosion rate (0.6 mm/year) very similar to the as-built one. The corrosion pits reported in Figure 11g,h were in fact very small on all the corroded surface.

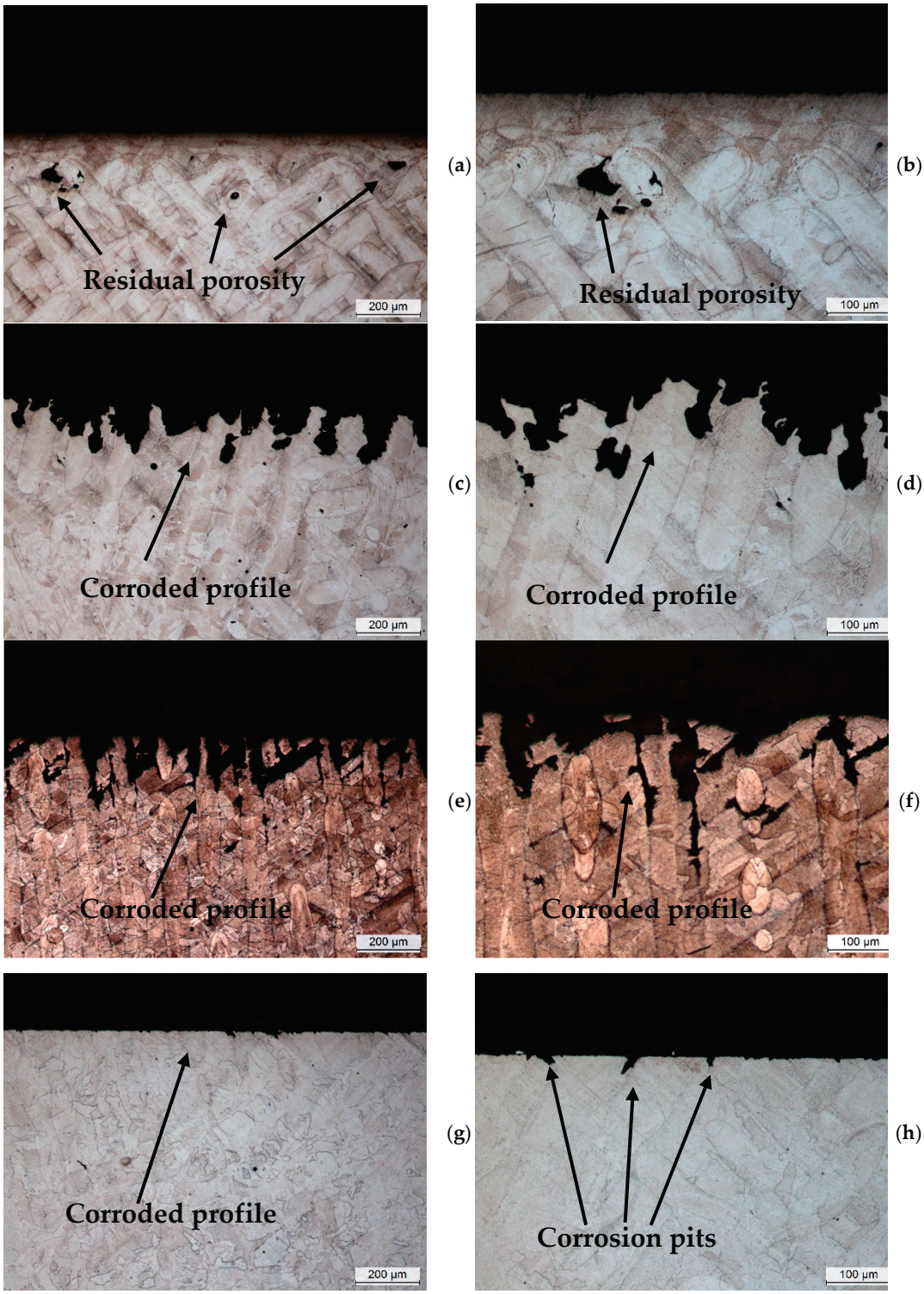


Figure 11. Metallographic sections of the scan plane of selected corrosion specimens. (**a**,**b**) As-built: 0.5 mm/year; (**c**,**d**) 621 °C 130 h: 5.7 mm/year; (**e**,**f**) 875 °C 0.75 h: 5.7 mm/year; (**g**,**h**) 980 °C 0.5 h: 0.6 mm/year.

4. Conclusions

The selective laser-melted alloy 625 shows outstanding mechanical and corrosion properties in the as-built condition. Compared to the conventional forged alloy, this difference is the most significant, and it can be ascribed to the improved microstructural fineness of the selective laser-melted material. However, because of the high local thermal gradients induced by the SLM process, residual stresses are present, and their mitigation by suitable

stress-relieving treatment is normally required to avoid distortions and failures when the component is removed from the build plate, especially in the presence of thin components. The conventional forged alloy 625 is stress-relieved at a minimum temperature of 870 °C. However, at this temperature, the selective laser-melted material is characterized by the very rapid precipitation of the δ phase which detrimentally degrades the deformability and corrosion resistance after short exposure times. Such different behavior depends on the fact that the aging response of the selective laser-melted alloy is significantly accelerated compared to that of the conventional material because of the higher micro-segregation level and the presence of residual stresses. Lower stress-relieving temperatures are not suitable for a satisfying mitigation of residual stresses. For this reason, in this research work, considering the TTP diagram of this alloy, higher stress-relieving temperatures were analyzed by investigating the influence on the mechanical and corrosion properties. In particular, the adoption of a higher temperature, i.e., 980 °C for 0.5 h, allows us to mitigate residual stresses while maintaining acceptable corrosion resistance. This alternative temperature also permits us to improve tensile deformability, which becomes even better than that in the as-built condition. This is one of the most important findings of this work, since the new stress-relieving treatment at 980 °C guarantees an optimal compromise among tensile properties, deformability, and corrosion resistance. This result is particularly important from a practical point of view, since it allows for the production of SLM parts with high mechanical properties that are superior to the minimum standard requirements even if slightly lower than those of the as-built condition and improved corrosion properties.

Even though the selective laser-melted material is characterized by excellent mechanical properties, this work investigates the possibility of a further strength improvement by single- and double-aging treatments starting from previous results obtained for the conventional forged alloy. Regarding the single-aging treatments at 732 °C and 621 °C, compared to the conventional material, a faster precipitation response is obtained in the early stages of formation. On the other hand, the acceleration provided by the double-aging procedure is much more significant in the conventional forged alloy. In fact, in the selective laser-melted material subjected to double-aging treatments, the hardness increments are largely reduced, and this behavior is even more evident when the duration of secondary aging is increased. Therefore, in the selective laser-melted alloy, the beneficial effects of double aging are appreciably lower than those in the conventional alloy. Furthermore, considering that the tensile deformability is already close to the minimum standard prescription in the as-built condition, the adoption of aging treatments encounters some limitations because of deformability loss which is typically associated with the strengthening effect of intermetallic precipitates. In fact, for the tested aging conditions, the values of the percentage of elongation after fracture A% are lower than the minimum standard requirement. In addition, as already observed in the conventional forged alloy 625, the reduction in corrosion resistance upon aging treatments is another critical aspect which is even more significant compared to the conventional material because of the faster precipitation response observed in the additively manufactured grade.

Author Contributions: Conceptualization, B.R., R.G. and D.P.; methodology, B.R., R.G. and D.P.; formal analysis, B.R., R.G. and D.P.; investigation, B.R., R.G. and D.P.; writing—original draft preparation, D.P.; writing—review and editing, B.R., R.G. and D.P.; supervision, B.R. and R.G. All authors have read and agreed to the published version of the manuscript.

Funding: This research received no external funding.

Institutional Review Board Statement: Not applicable.

Informed Consent Statement: Not applicable.

Data Availability Statement: The dataset is available upon request from the authors.

Conflicts of Interest: The authors declare no conflicts of interest.

References

1. Suave, L.M.; Cormier, J.; Villechaise, P.; Soula, A.; Hervier, Z.; Bertheau, D.; Laigo, J. Microstructural Evolutions During Thermal Aging of Alloy 625: Impact of Temperature and Forming Process. *Metall. Mater. Trans. A* **2014**, *45*, 2963–2982. [CrossRef]
2. Shankar, V.; Bhanu Sankara Rao, K.; Mannan, S.L. Microstructure and Mechanical Properties of Inconel 625 Superalloy. *J. Nucl. Mater.* **2001**, *288*, 222–232. [CrossRef]
3. Sukumaran, A.; Gupta, R.K.; Anil Kumar, V. Effect of Heat Treatment Parameters on the Microstructure and Properties of Inconel-625 Superalloy. *J. Mater. Eng. Perform.* **2017**, *26*, 3048–3057. [CrossRef]
4. Heubner, U.; Kloewer, J.; Alves, H.; Behrens, R.; Schindler, C.; Wahl, V.; Wolf, M. *Nickel Alloys and High-Alloyed Special Stainless Steels: Properties-Manufacturing-Applications*, 4th ed.; Expert-Verlag: Renningen, Germany; Stuttgart, Germany, 2012.
5. ASM International. *ASM Specialty Handbook: Nickel, Cobalt, and Their Alloys*; Davis, J., Ed.; ASM International: Materials Park, OH, USA, 2000.
6. Donachie, M.J.; Donachie, S.J. *Superalloys: A Technical Guide*, 2nd ed.; ASM International: Materials Park, OH, USA, 2002.
7. Eiselstein, H.L.; Tillack, D.J. The Invention and Definition of Alloy 625. In *Proceedings on Superalloys 718, 625, and Derivatives*; Loria, E.A., Ed.; The Minerals, Metals & Materials Society: Warrendale, PA, USA, 1991; pp. 1–14.
8. Durand-Charre, M. *The Microstructure of Superalloys*, 1st ed.; Routledge: London, UK, 1968.
9. Patel, S.J.; Smith, G.D. The Role of Niobium in Wrought Precipitation-Hardened Nickel-Base Alloys. In *Proceedings on Superalloys 718, 625, 706 and Derivatives*; Loria, E.A., Ed.; The Minerals, Metals & Materials Society: Warrendale, PA, USA, 2005; pp. 135–154.
10. Floreen, S.; Fuchs, G.E.; Yang, W.J. The Metallurgy of Alloy 625. In *Superalloys 718, 625, 706 and Derivatives*; The Minerals, Metals & Materials Society: Warrendale, PA, USA, 1994; pp. 13–37.
11. Rivolta, B.; Boniardi, M.V.; Gerosa, R.; Casaroli, A.; Panzeri, D.; Pizetta Zordão, L.H. Alloy 625 Forgings: Thermo-Metallurgical Model of Solution-Annealing Treatment. *J. Mater. Eng. Perform.* **2022**, *32*, 5785–5797. [CrossRef]
12. *ASTM B446-19*; Standard Specification for Nickel-Chromium-Molybdenum-Columbium Alloy (UNS N06625), Nickel-Chromium-Molybdenum-Silicon Alloy (UNS N06219), and Nickel-Chromium-Molybdenum-Tungsten Alloy (UNS N06650) Rod and Bar. ASTM International: West Conshohocken, PA, USA, 2019.
13. Reed, R.C.; Rae, C.M.F. Physical Metallurgy of the Nickel-Based Superalloys. In *Physical Metallurgy*; Elsevier: Amsterdam, The Netherlands, 2014; pp. 2215–2290. [CrossRef]
14. Vernot-Loier, C.; Cortial, F. Influence of Heat Treatments on Microstructure, Mechanical Properties and Corrosion Behaviour of Alloy 625 Forged Rod. In *Proceedings on Superalloys 718, 625, and Derivatives*; Loria, E.A., Ed.; The Minerals, Metals & Materials Society: Warrendale, PA, USA, 1991; pp. 409–422.
15. Heubner, U.; Köhler, M. Effect of Carbon Content and Other Variables on Yield Strength, Ductility, and Creep Properties of Alloy 625. In *Proceedings on Superalloys 718, 625, 706 and Derivatives*; Loria, E.A., Ed.; The Minerals, Metals & Materials Society: Warrendale, PA, USA, 1994; pp. 479–488.
16. Heubner, U.; Köhler, M. The Effect of Final Heat Treatment and Chemical Composition on Sensitization, Strength and Thermal Stability of Alloy 625. In *Superalloys 718, 625, 706 and Derivatives*; The Minerals, Metals & Materials Society: Warrendale, PA, USA, 1997; pp. 795–803.
17. Lindwall, G.; Campbell, C.E.; Lass, E.A.; Zhang, F.; Stoudt, M.R.; Allen, A.J.; Levine, L.E. Simulation of TTT Curves for Additively Manufactured Inconel 625. *Metall. Mater. Trans. A* **2019**, *50*, 457–467. [CrossRef] [PubMed]
18. Stoudt, M.R.; Lass, E.A.; Ng, D.S.; Williams, M.E.; Zhang, F.; Campbell, C.E.; Lindwall, G.; Levine, L.E. The Influence of Annealing Temperature and Time on the Formation of δ-Phase in Additively-Manufactured Inconel 625. *Metall. Mater. Trans. A* **2018**, *49*, 3028–3037. [CrossRef]
19. Sitek, R.; Ciftci, J.; Moszczyńska, D.; Maj, P.; Ura-Bińczyk, E.; Warzybok, P.; Cieślik, I.; Wiśniewski, P.; Mizera, J. Effect of Annealing on the Microstructure and Properties of IN 625 Specimens Manufactured by Selective Laser Melting. *Arch. Civil. Mech. Eng.* **2022**, *22*, 207. [CrossRef]
20. Gonzalez, J.A.; Mireles, J.; Stafford, S.W.; Perez, M.A.; Terrazas, C.A.; Wicker, R.B. Characterization of Inconel 625 Fabricated Using Powder-Bed-Based Additive Manufacturing Technologies. *J. Mater. Process Technol.* **2019**, *264*, 200–210. [CrossRef]
21. Marchese, G.; Lorusso, M.; Parizia, S.; Bassini, E.; Lee, J.-W.; Calignano, F.; Manfredi, D.; Terner, M.; Hong, H.-U.; Ugues, D.; et al. Influence of Heat Treatments on Microstructure Evolution and Mechanical Properties of Inconel 625 Processed by Laser Powder Bed Fusion. *Mater. Sci. Eng. A* **2018**, *729*, 64–75. [CrossRef]
22. Marchese, G.; Bassini, E.; Parizia, S.; Manfredi, D.; Ugues, D.; Lombardi, M.; Fino, P.; Biamino, S. Role of the Chemical Homogenization on the Microstructural and Mechanical Evolution of Prolonged Heat-Treated Laser Powder Bed Fused Inconel 625. *Mater. Sci. Eng. A* **2020**, *796*, 140007. [CrossRef]

23. Lee, J.; Terner, M.; Jun, S.; Hong, H.-U.; Copin, E.; Lours, P. Heat Treatments Design for Superior High-Temperature Tensile Properties of Alloy 625 Produced by Selective Laser Melting. *Mater. Sci. Eng. A* **2020**, *790*, 139720. [CrossRef]
24. Chen, F.; Wang, Q.; Zhang, C.; Huang, Z.; Jia, M.; Shen, Q. Microstructures and Mechanical Behaviors of Additive Manufactured Inconel 625 Alloys via Selective Laser Melting and Laser Engineered Net Shaping. *J. Alloys Compd.* **2022**, *917*, 165572. [CrossRef]
25. Martucci, A.; Marchese, G.; Bassini, E.; Lombardi, M. Effects of Stress-Relieving Temperature on Residual Stresses, Microstructure and Mechanical Behaviour of Inconel 625 Processed by PBF-LB/M. *Metals* **2023**, *13*, 796. [CrossRef]
26. Luna, V.; Trujillo, L.; Gamon, A.; Arrieta, E.; Murr, L.E.; Wicker, R.B.; Katsarelis, C.; Gradl, P.R.; Medina, F. Comprehensive and Comparative Heat Treatment of Additively Manufactured Inconel 625 Alloy and Corresponding Microstructures and Mechanical Properties. *J. Manuf. Mater. Process.* **2022**, *6*, 107. [CrossRef]
27. Renishaw. In625-0402 Powder for Additive Manufacturing: Data Sheet. September 2017. Available online: https://www.renishaw.com/media/pdf/en/674a7fa1d94b4da3907f9a2275b6f46d.pdf (accessed on 18 January 2023).
28. Concli, F.; Gerosa, R.; Panzeri, D.; Fraccaroli, L. High- and Low-Cycle-Fatigue Properties of Additively Manufactured Inconel 625. *Progress. Addit. Manuf.* **2024**, *9*, 1921–1940. [CrossRef]
29. Marinucci, F.; Marchese, G.; Bassini, E.; Aversa, A.; Fino, P.; Ugues, D.; Biamino, S. Hardness Evolution of Solution-Annealed LPBFed Inconel 625 Alloy under Prolonged Thermal Exposure. *Metals* **2022**, *12*, 1916. [CrossRef]
30. Kim, K.-S.; Kang, T.-H.; Kassner, M.E.; Son, K.-T.; Lee, K.-A. High-Temperature Tensile and High Cycle Fatigue Properties of Inconel 625 Alloy Manufactured by Laser Powder Bed Fusion. *Addit. Manuf.* **2020**, *35*, 101377. [CrossRef]
31. Rivolta, B.; Gerosa, R.; Tavasci, F.; Ori Belometti, L. Mechanical and Microstructural Characterization of Forged Inconel 625 Ring Gaskets for Oil and Gas Application. *Mater. Perform. Charact.* **2017**, *6*, 20170030. [CrossRef]
32. Rivolta, B.; Gerosa, R.; Tavasci, F.; Ori Belometti, L. Metallurgical Analysis of Inconel 625 Metallic Gaskets Produced by Centrifugal Casting. *Mater. Perform. Charact.* **2017**, *6*, 20170036. [CrossRef]
33. Cabrini, M.; Lorenzi, S.; Testa, C.; Brevi, F.; Biamino, S.; Fino, P.; Manfredi, D.; Marchese, G.; Calignano, F.; Pastore, T. Microstructure and Selective Corrosion of Alloy 625 Obtained by Means of Laser Powder Bed Fusion. *Materials* **2019**, *12*, 1742. [CrossRef]
34. Lass, E.A.; Stoudt, M.R.; Williams, M.E.; Katz, M.B.; Levine, L.E.; Phan, T.Q.; Gnaeupel-Herold, T.H.; Ng, D.S. Formation of the Ni3Nb δ-Phase in Stress-Relieved Inconel 625 Produced via Laser Powder-Bed Fusion Additive Manufacturing. *Metall. Mater. Trans. A* **2017**, *48*, 5547–5558. [CrossRef] [PubMed]
35. Dubiel, B.; Sieniawski, J. Precipitates in Additively Manufactured Inconel 625 Superalloy. *Materials* **2019**, *12*, 1144. [CrossRef]
36. Tawancy, H.M.; Allam, I.M.; Abbas, N.M. Effect of Ni3Nb Precipitation on the Corrosion Resistance of Inconel Alloy 625. *J. Mater. Sci. Lett.* **1990**, *9*, 343–347. [CrossRef]
37. Zhu, Z.; Sui, Y.; Dai, A.; Cai, Y.; Xu, L.-L.; Wang, Z.; Chen, H.; Shao, X.; Liu, W. Effect of Aging Treatment on Intergranular Corrosion Properties of Ultra-Low Iron 625 Alloy. *Int. J. Corros.* **2019**, *2019*, 9506401. [CrossRef]
38. *ASTM G28-02*; Standard Test Methods for Detecting Susceptibility to Intergranular Corrosion in Wrought, Nickel-Rich, Chromium-Bearing Alloys. ASTM International: West Conshohocken, PA, USA, 2015.
39. Carpenter Technology Corporation. CarTech® Custom Age 625 PLUS® Alloy: Technical Datasheet. Available online: www.carpentertechnology.com/alloy-finder/625-Plus (accessed on 25 August 2020).
40. Carpenter Technology Corporation. A Guide to Etching Specialty Alloys for Microstructural Evaluation. Available online: https://carpentertechnology.com/blog/a-guide-to-etching-specialty-alloys (accessed on 14 November 2023).
41. *ISO 6507-1:2018*; Metallic Materials—Vickers Hardness Test. BSI Standards: London, UK, 2018.
42. *BS EN ISO 6892-1:2019*; Metallic Materials—Tensile Testing. BSI Standards Limited: London, UK, 2020.
43. Rivolta, B.; Gerosa, R.; Panzeri, D.; Nazim, A. Optimization of the Mechanical and Corrosion Resistance of Alloy 625 through Aging Treatments. *Crystals* **2024**, *14*, 139. [CrossRef]
44. Rivolta, B.; Gerosa, R.; Panzeri, D. Influence of Single- and Double-Aging Treatments on the Mechanical and Corrosion Resistance of Alloy 625. *Metals* **2024**, *14*, 823. [CrossRef]
45. Lass, E.A.; Stoudt, M.R.; Katz, M.B.; Williams, M.E. Precipitation and Dissolution of δ and Γ″ during Heat Treatment of a Laser Powder-Bed Fusion Produced Ni-Based Superalloy. *Scr. Mater.* **2018**, *154*, 83–86. [CrossRef]
46. Li, C.; White, R.; Fang, X.Y.; Weaver, M.; Guo, Y.B. Microstructure Evolution Characteristics of Inconel 625 Alloy from Selective Laser Melting to Heat Treatment. *Mater. Sci. Eng. A* **2017**, *705*, 20–31. [CrossRef]
47. Dinda, G.P.; Dasgupta, A.K.; Mazumder, J. Laser Aided Direct Metal Deposition of Inconel 625 Superalloy: Microstructural Evolution and Thermal Stability. *Mater. Sci. Eng. A* **2009**, *509*, 98–104. [CrossRef]

Disclaimer/Publisher's Note: The statements, opinions and data contained in all publications are solely those of the individual author(s) and contributor(s) and not of MDPI and/or the editor(s). MDPI and/or the editor(s) disclaim responsibility for any injury to people or property resulting from any ideas, methods, instructions or products referred to in the content.

applied sciences

MDPI

Article

Simulation-Based Optimization of Material Supply in Automotive Production Using RTLS Data

Miriam Pekarčíková [1,*], Marek Kliment [1], Jana Kronová [1], Peter Trebuňa [1] and Anton Hovana [2]

[1] Faculty of Mechanical Engineering, Department of Industrial and Digital Engineering, Technical University of Košice, Park Komenského 9, 042 00 Košice, Slovakia; marek.kliment@tuke.sk (M.K.); jana.kronova@tuke.sk (J.K.); peter.trebuna@tuke.sk (P.T.)
[2] Faculty of Mechanical Engineering, Department of Applied Mathematics and Informatics, Technical University of Košice, Letná 9, 042 00 Košice, Slovakia; anton.hovana@tuke.sk
* Correspondence: miriam.pekarcikova@tuke.sk

Abstract

This study presents a comprehensive simulation-driven approach to identify and mitigate bottlenecks in the supply flows of an automotive manufacturing system. The supply process relies on a Kanban-based assembly line replenishment, supported by multiple material transports per shift using tugger trains. To analyze flow constraints, the research combines time–motion studies with data from a Real-Time Locating System (RTLS), enabling spatial-temporal mapping of material movements. Based on this data, digital-twin simulation models of the supply process were developed and validated. These models allowed testing of improvements aimed at increasing throughput and efficiency. The proposed methodology demonstrates effective bottleneck resolution and provides a structured framework for data collection and simulation integration. Unlike traditional observation-based approaches, the use of RTLS enables precise detection of routing deviations and operator behaviors. The simulation model was tested under real operating conditions and validated against ground-truth data. Results showed a reduction in collisions and delivery delays, as well as measurable productivity and financial gains. This approach offers a practical and transferable method for optimizing intralogistics in modern production environments.

Keywords: bottleneck; RTLS; simulation

1. Introduction

Efficient material supply is a critical factor in maintaining continuous production and minimizing operational disruptions in manufacturing systems [1,2]. In automotive environments, the timely replenishment of production lines using tugger trains is especially prone to delays and collisions due to space constraints, human error, and inadequate route planning [3,4]. If these inefficiencies are not addressed they can lead to frequent production stoppages, increased operational costs, and reduced competitiveness.

This challenge becomes increasingly relevant in the context of Industry 4.0 and 5.0, where expectations for lean, responsive, and data-driven logistics systems are growing. In this light, advanced monitoring and modeling tools are needed to address these inefficiencies in real time and to support agile decision-making.

Bottleneck detection and mitigation have been the subject of various studies across manufacturing and logistics. For example, Zhang et al. [5] developed a dynamic bottleneck prediction model based on throughput delays, while Kasemset and Kachitvichyanukul [6]

applied simulation methods for bottleneck mapping. Thürer and Stevenson [7] also explored simulation-based flow improvements. This paper builds upon and expands on several previously published studies. In 2023, a case study presented in [8] used simulation to optimize a blood plasma processing line. Similarly, Pekarčíková et al. [9] applied simulation tools to eliminate bottlenecks within logistics chains using Tecnomatix Plant Simulation. While these works demonstrated the potential of simulation, they typically relied on static or pre-processed data and did not integrate continuous real-time inputs into the optimization loop.

Recent advancements have focused on real-time and data-driven approaches to bottleneck analysis. West et al. [10] proposed a diagnostic method that dynamically identifies bottlenecks using live operational data, enabling rapid decision-making in serial manufacturing systems. Zhang et al. [11] introduced a cloud-based simulation approach employing Object-Oriented Colored Petri Nets to model and resolve flow constraints in discrete production environments. Marschall et al. [12] addressed the deployment of mobile robotic systems in reconfigurable production, using simulation to optimize layout and logistics flexibility. These studies illustrate the ongoing trend toward integrating simulation with real-time data to improve adaptability; however, most focus on either the data acquisition or the simulation phase, rather than their seamless integration.

While the above studies contributed valuable insights, many of them rely on simplified models or do not integrate real-time operational data. To address this gap, this paper proposes an integrated methodology that combines RTLS-based monitoring with digital simulation modeling to detect supply bottlenecks and test logistics improvements in a realistic, data-rich environment. This paper presents a case study on the supply process for production using tugger trains, which consist of a tractor and several wagons, depending on the volume of supply items. These trains are operated by workers who unload the necessary material items at designated stations for final product assembly and return empty containers to the warehouse [13,14].

In the studied system, frequent route deviations and tugger train collisions were observed, indicating critical weaknesses in logistics route planning and control [15]. These inefficiencies were quantified through combined observation and RTLS tracking methods [16,17]. The supply process uses the Kanban system, based on which production lines request the required material items from the warehouse according to consumption [18–20]. These materials are then loaded onto the two tugger train sets [21].

The key contribution of this paper is the integration of RTLS-based monitoring with digital simulation modeling, enabling the detection of supply bottlenecks and testing of logistics improvements in a realistic environment [22–24]. This combined approach supports the digital transformation of internal logistics in accordance with Industry 4.0 and 5.0 principles [25].

2. Materials and Methods

This section details the production and supply systems, the real-time monitoring technology based on RTLS, and the simulation methodology applied to logistics processes. The objective is to provide a comprehensive description of the methods, tools, and input data employed for the analysis and optimization of material flows within the examined production environment.

2.1. RTLS Monitoring Technology

The implementation of RTLS has become a pivotal technology for monitoring and improving internal logistics processes by providing accurate location data and movement tracking of material handling equipment and goods [26–28]. RTLS enables the identification

of critical delays, route deviations, and collisions, thus supporting data-driven decisions to optimize supply flows [29]. In the studied supply system, RTLS tracking combined with observational methods allowed the quantification of inefficiencies and bottlenecks in tugger train logistics, providing a solid data basis for simulation-based optimization.

Unloading time, loading time, scanning time, transport time, and the weight of individual deliveries served as input data for our study and implementation. Through measurement and observation methods, we regularly collected input data, where the average values showed minimal differences. These values were then used in both the analytical and design phases.

The RTLS UWB Wi-Fi Kit by Sewio Networks s.r.o. is an advanced real-time locating system that uses ultra-wideband (UWB) technology and the Time Difference of Arrival (TDoA) method to precisely determine the position of objects. This type of RTLS is designed primarily for industrial environments, where high accuracy, reliability, and scalability are essential. The kit consists of five Vista Omni anchors that provide the localization infrastructure, four tracking tags—two Leonardo Personal tags and two Leonardo Asset tags—and the RTLS Studio software version 3.5.

As illustrated in Figure 1, the layout of the production hall incorporates a monitoring method called the spaghetti spot. A spaghetti diagram is a visual representation that uses a continuous line to depict the movement of an item or activity through a process. This tool helps identify bottlenecks and critical points in the workflow, as well as opportunities to streamline the process. The spaghetti diagram highlights overlapping areas where multiple pathways intersect, causing delays. It is particularly useful in streamlining the movement of people, products, and tugger trains within the production unit.

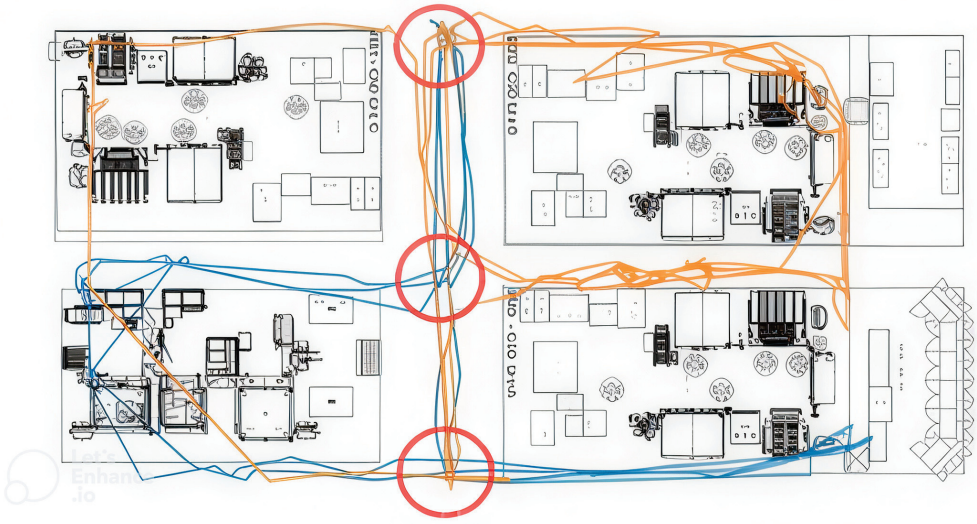


Figure 1. Spaghetti diagram with factory layout and bottleneck highlights.

The spaghetti diagram is one of the outputs of the RTLS monitoring technology. The layout in Figure 1 shows the arrangement of the four production lines, labeled as *CSD (CSD—Customer-Specific Demand) Line A*, *B*, *C*, and *D*.

The orange color represents the supplier operating the tugger (designated as JFG 77381), which is supposed to serve as the main supplier for CSD Line A and CSD Line B in terms of the logistics route. However, during the measurement and data collection period we observed multiple instances of this supplier being present in locations where they were not supposed to be, such as CSD Line C and CSD Line D.

The blue color represents the supplier and tugger 2 (designated as JFG 77382), responsible for supplying CSD Line C and CSD Line D. However, the measured operational behavior deviated significantly from the predefined logistics plan. The tugger train did not

adhere to its designated route and made unauthorized stops in areas outside its intended operation zones. This deviation was primarily caused by incorrect scanning performed by production workers handling Kanban cards. As a result, essential materials were not delivered on time, leading to material shortages and disruptions in the production cycle.

Due to these shortcomings, it was observed that input materials were at times retrieved manually by production line workers, bypassing standard logistics procedures. This practice subsequently led to another issue: incorrect scanning of materials. Under optimal conditions, material scanning should be performed exclusively by tugger train operators, while production line workers should interact only with designated storage bins rather than scanning materials directly from warehouse areas.

During data collection, several instances were recorded where the tugger train operator entered the production line area with full or empty material containers, disrupting the flow of operations and contributing to collisions and timing inconsistencies in material supply.

A critical issue identified was the occurrence of collisions between tugger trains, largely attributed to the absence of clearly defined routes and delivery paths in high-traffic areas. Inadequate logistics planning triggered cascading disruptions, negatively affecting not only the involved production lines but also downstream processes reliant on timely material deliveries.

The consequences of these inefficiencies manifested as production downtime, material shortages, time constraints, production stoppages, disruptions in meeting daily production plans, failure to fulfill customer orders, low machine efficiency, process blockages, increased movement between production lines, and other operational inefficiencies.

To validate these observations, a detailed quantitative analysis was conducted over a one-month period, during which the following irregularities were recorded:

These statistics demonstrate in Table 1. systemic process inconsistencies. For instance, 17 incidents were documented in which employees bypassed standard procedures and manually retrieved components—typically in response to delayed deliveries or miscommunication. Additionally, 11 instances of incorrect barcode scanning caused tugger trains to be misrouted, resulting in materials being delivered to incorrect locations or failing to reach critical unloading stations.

Table 1. Summary of observed process irregularities.

Observed Issue	Frequency (Per Month)
Collisions of tugger trains	9
Unauthorized employee interventions	17
Incorrect barcode scanning by operators	11

Although the recorded 9 collisions per month are not catastrophic, they highlight persistent weaknesses in logistics routing and coordination. These findings emphasize the necessity of implementing real-time tracking systems and well-defined logistics planning, supported by RTLS data, to enhance supply chain performance and reliability.

2.2. Simulation

The data collected through time studies and RTLS monitoring methods were analyzed and compared. Based on this data, we developed a simulation model of the supply chain within production. This simulation first confirmed the presence of bottlenecks and subsequently enabled us to explore various process improvement strategies in a digital environment.

The methodology for analyzing the supply process is illustrated in Figure 2.

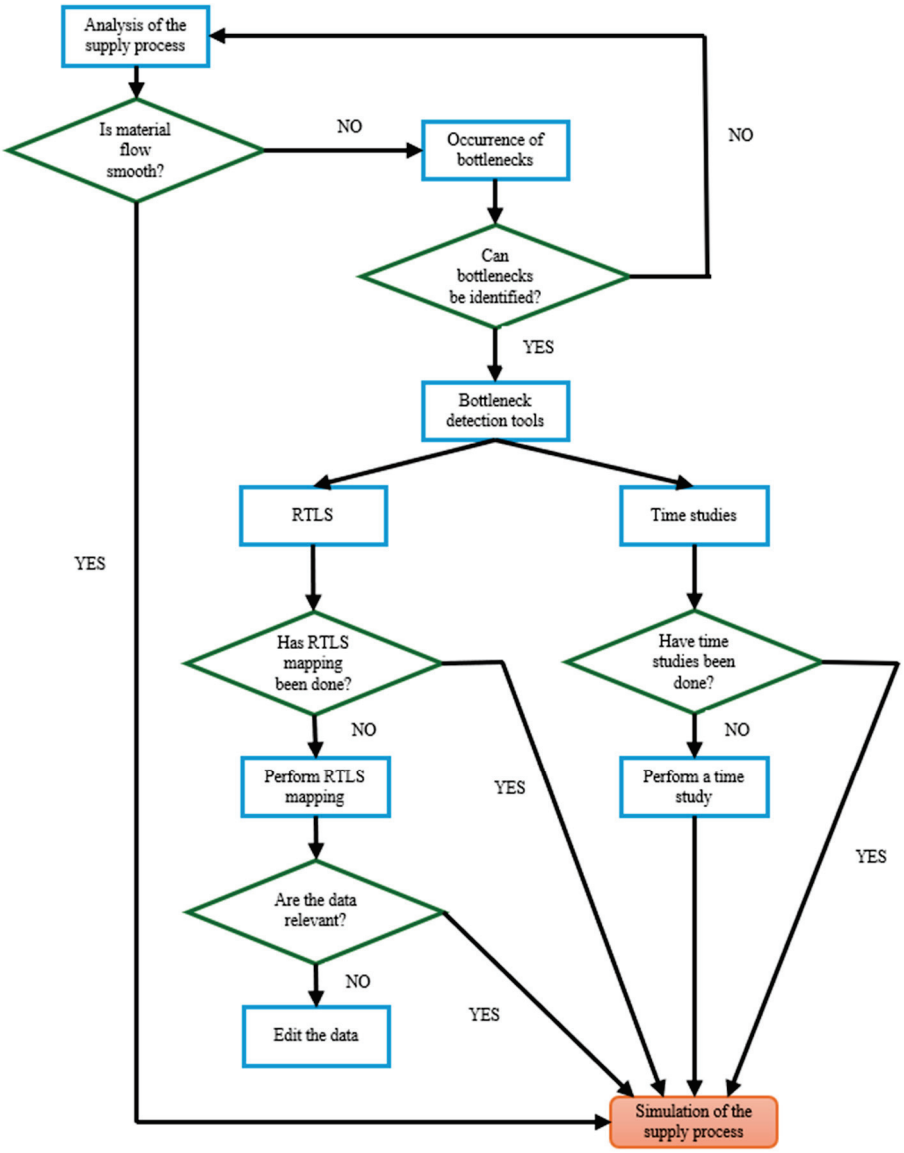


Figure 2. Algorithm for supply process simulation using tools for identifying bottlenecks.

This methodology is universal and can be applied to any operation—not only within the supply process, but generally to any production process regardless of the industrial sector or type of manufacturing.

According to the proposed methodology, data was collected using both observational and detection-based methods. The observational techniques were implemented over several daily shifts within the operation, during which the RTLS detection method was also active. The results obtained from time studies were compared with the output of the detection technology, which operated continuously over several days, including during shifts where no observational time–motion measurements were performed.

Based on the comparison of the datasets obtained through both methods, the results derived solely from the detection technology can be considered reliable. Therefore, these results were also used as input for the simulation model.

The significance of these data can be immediately observed in Figure 1, where the routes of two tugger train operators are visualized—Operator 1 in blue and Operator 2 in orange. The figure clearly illustrates multiple overlapping paths between the two operators, which ideally should not occur. Although both operators start from the same point, they

are expected to follow predefined routes; however, our investigation revealed that no such predefined routes were established by the company.

Thus, the figure also highlights the different paths taken and identifies bottlenecks within the supply workstation. These bottlenecks are defined as areas where a given operator must pass at least twice. Since the tugger train requires a minimum turning radius of three meters, it is not capable of turning on the spot. In the event of incomplete or delayed unloading of material at the designated location, the tugger is required to repeat the route to ensure proper delivery.

In Figure 3a, we can observe a photograph taken within the company's production hall, illustrating the actual locations where collisions occur during the material supply process. These are points where the routes of two tuggers undesirably overlap, which may lead to collisions or disruptions in the continuity of the supply process. This issue must be addressed in order to improve both the efficiency of the material supply process and the overall flow of all production lines being supplied.



(**a**) (**b**)

Figure 3. Real operation of the production hall (**a**) indication of areas where tugger train collisions occur and (**b**) supply tugger train system.

Figure 3b depicts the specific tugger train system responsible for performing the supply operations. Depending on the volume of material being transported, the train consists of two or three trailer cages. As can be seen in Figure 3a, the available space for tugger movement, in relation to the system's dimensions, is sufficient for the passage of only one such train—and only in a single direction. The area does not allow for bidirectional movement, nor does it provide space for two supply tugger trains to bypass or avoid each other.

A simulation of the original supply process was developed based on data collected during the production process analysis. Even within the simulation, collisions between tugger trains occurred, as illustrated in Figure 4.

Within the digital production model, various proposals were implemented and tested with the aim of minimizing the occurrence of potential collisions between the identified tugger trains. This approach focused on eliminating as many bottlenecks as possible in order to enhance the efficiency of both the supply process and the overall production workflow within the manufacturing hall.

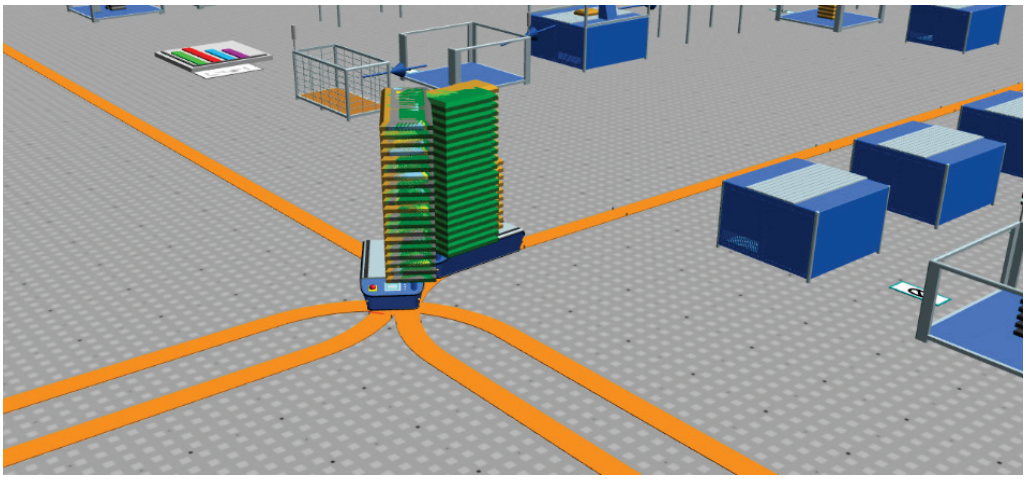


Figure 4. Simulation of tugger collision.

Although simplified tugger train models are used in the simulation, the operational conditions are accurately defined based on real-world parameters. The model attributes include realistic travel speeds and actual capacity, even though the digital representation does not visually display the cages for transporting components. The simulation portrays an ideal environment in which workers do not obstruct the tugger paths; however, a collision still occurs in one of the hall's predefined bottleneck areas. Therefore, it is necessary to propose corrective measures, including the design of optimized logistical routes for each tugger train, in order to avoid such undesired events.

The entire process—from the initiation of material supply to a potential collision—can be visualized using a flowchart of the current state in the enterprise. Figure 5 presents this flowchart, illustrating the sequence of events. The process begins with initiation and is monitored using selected observation methods. Special attention is paid to worker communication as well as their field of vision at pathway intersections.

The next step involves evaluating the potential for a collision, which is most likely to occur in the previously identified bottleneck zones. If no collision occurs, this represents the ideal scenario. In the event of a collision, a warning and response protocol is triggered. An acoustic signal indicates the collision, prompting immediate stoppage of the vehicles to ensure safety in the surrounding area.

Following this, a decision is made regarding whether a rescue operation is required, after which the process transitions into an investigation phase. Corrective measures are then proposed and implemented to improve both the production and supply processes.

Figure 5 schematically illustrates a simplified supply process using tugger train sets within the production unit. This basic methodology depicts the material flow and highlights the occurrence and resolution of collisions between two tugger trains within the supply chain. The primary causes of such collisions often include insufficient communication, deviations from planned routes, or unplanned delays at specific stops. To ensure uninterrupted production flow, immediate measures must be implemented to resolve collisions and enable continuous supply. Data on collision frequency and localization of critical zones are collected using two approaches: manual process mapping and digital localization via RTLS technology. However, merely identifying bottlenecks does not guarantee problem elimination; therefore, either prompt process interventions at collision points or route adjustments of tugger trains are necessary to prevent recurring collisions.

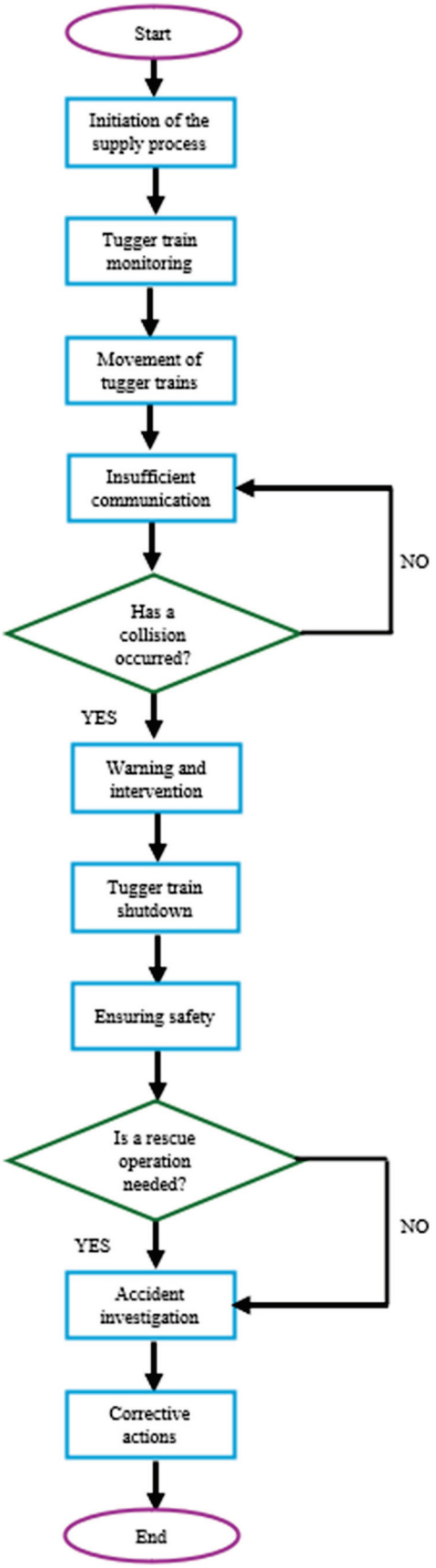


Figure 5. Flowchart of the material supply workflow and monitoring steps.

3. Results and Discussion

This chapter presents the case study, data acquisition, and simulation results aimed at optimizing material supply within the production process. It provides a comparative analysis between simulation outputs and empirical data, followed by a discussion on the implications for process efficiency improvement and bottleneck elimination.

3.1. Case Study Description

To implement changes to the current state, it was necessary to gather all relevant input data from the individual CSD lines, including the capacities of the Kanban storage bins, the capacities of the tugger trains, as well as the time required for the trains to be ready to deliver material to the Kanban containers. It was also essential to identify unloading times and locations that represent a high risk of negatively impacting the overall process.

For the development of simulation models, the software module Tecnomatix Plant Simulation was utilized. This tool enables the gradual design of the complete simulation environment, including the positioning of individual machines according to the real-world layout. The model can then be adjusted and optimized to ensure that the final configuration eliminates tugger train collisions within the production hall and improves overall operational efficiency.

The production process in this case study consists of four lines and focuses on manufacturing auxiliary dampers with electronic control. These parts are produced in multiple variants for different models of passenger and commercial vehicles. The production lines include Kanban storage bins, pressing machines, compression machines, milling machines, calibration machines, and inspection machines.

Each production line contains four high-capacity storage bins utilizing the Kanban method, which is one of the most widely used supply methods in the engineering industry. The applied Kanban method is supplied by two tugger train sets responsible for regularly delivering the necessary materials to individual Kanban storage bins. Each tugger train pulls 2–3 cages containing all required materials. The regularity of the delivery cycle is crucial, and the company aims to increase efficiency and design an optimized logistics route for individual high-capacity storage bins to ensure the continuity of the production process and eliminate downtime.

The primary goal of the simulation is to resolve the supply chain issue by ensuring uninterrupted material delivery to each production line without collisions. The proposed approach is illustrated in the flowchart in Figure 6.

Following this activity, a simplified schematic representation is provided in Figure 6, which focuses on the monitoring of the production and supply processes and the interventions to resolve collisions. It is essential to recognize that the production process is continuous; therefore, achieving at least a portion of the planned performance always requires making process decisions to mitigate the issue in some way. In this context, the human factor and the decision-making capacity of the workers at the given moment and location often play a critical role. The objective of this case study is to completely eliminate the human factor and fully eradicate the occurrence of the problem. To this end, monitoring is conducted at multiple levels of precision and relevance of the collected data. These data are then transferred into the simulation, which compares potential solutions to the problem. Consequently, the simulation provides recommendations that, once implemented, should relieve employees from the necessity of making interventions during supply collisions. Both schematics—Figures 5 and 6—represent the culmination of the methodology outlined and described in Figure 2, building upon it.

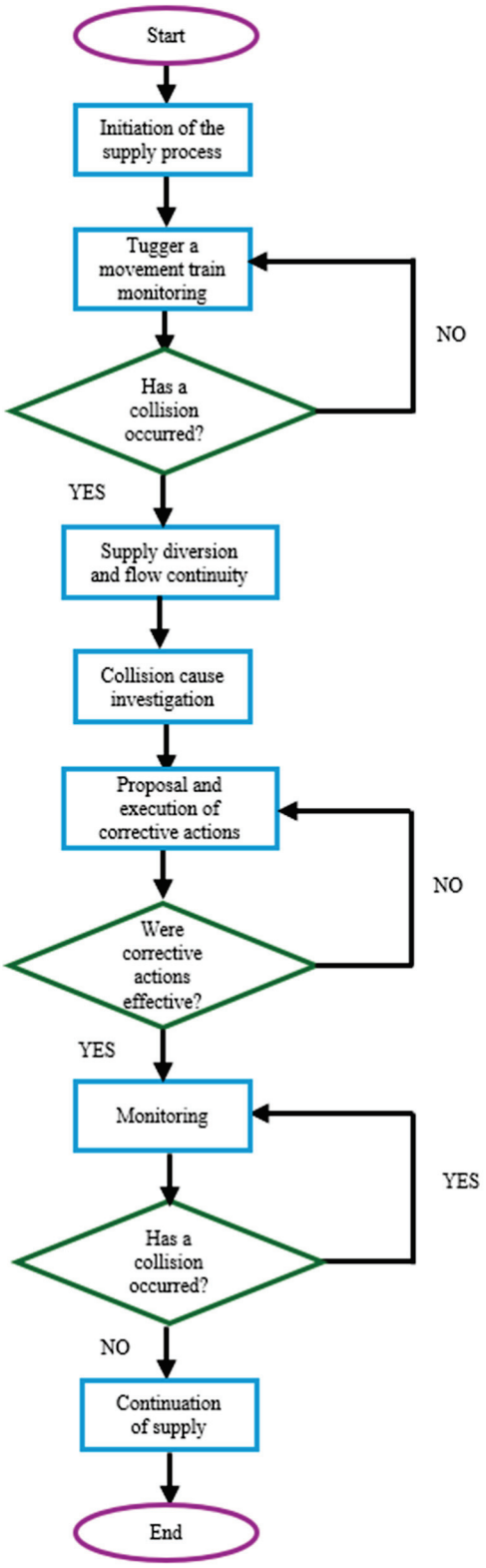


Figure 6. Flowchart of the simulation method to optimize material flow and avoid collisions.

Based on the collected data, it was necessary to gradually model the production unit, which—besides the pathways used by the tugger trains that represent the main focus of this case study—also includes the individual production and assembly workstations. Furthermore, the simulation must account for the staff operating each workstation.

The company operates a continuous two-shift system, which means production runs 24 h a day, 7 days a week. During each 12 h shift, the following personnel are present:

- Tugger train operators—2 employees;
- Production operators—20 employees;
- Line supervisors—4 employees;
- Maintenance service—2 employees;
- Security personnel—1 employee;
- Production and technical staff—3 employees;
- Data analysts—2 employees;
- Process engineers—3 employees;
- Shift supervisor—1 employee.

In total, 38 employees are involved in ensuring the smooth operation of production. For the purpose of our simulation, the focus is placed on the tugger train operators and the production operators. Figure 7 illustrates a simulation of the production line with workers, using Siemens Tecnomatix Plant Simulation software version 11.0.0.

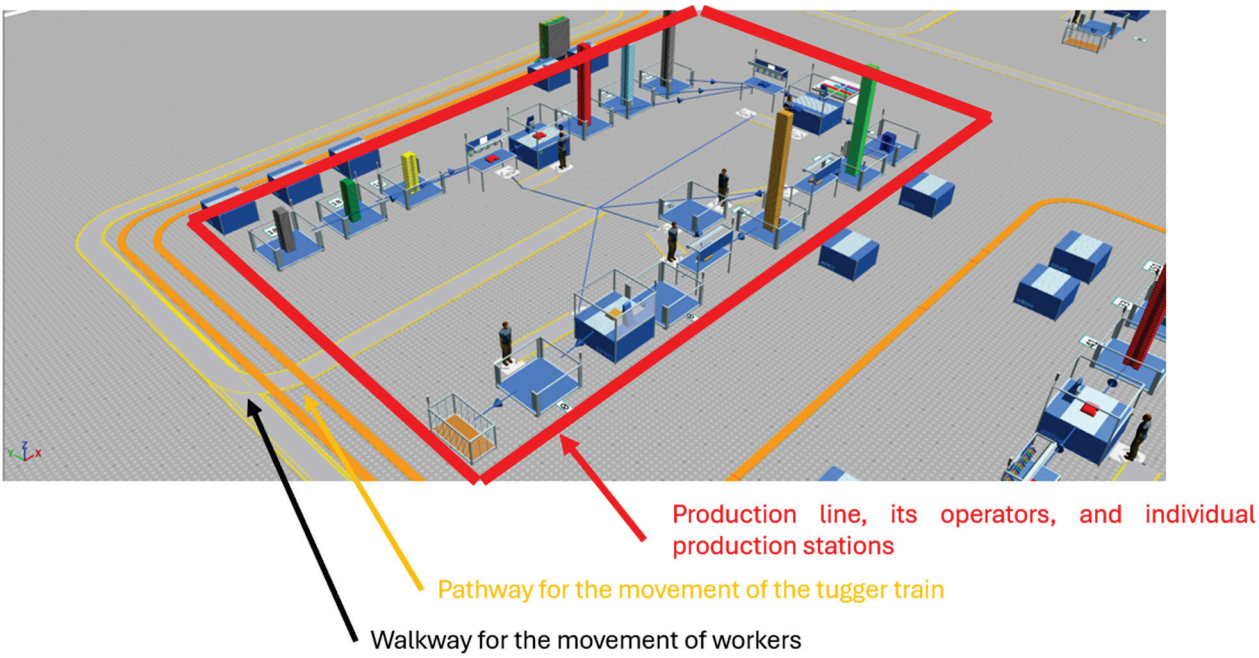


Figure 7. Simulation of production line.

Figure 7 depicts the various components of the simulation and the described production unit using color coding. It represents one of the four production lines included in the case study. The red zone indicates the individual workstations of the production line responsible for manufacturing the products. The orange color highlights the routes used by the material supply tugger trains. The yellow–gray areas represent sections of walkways utilized by employees when arriving at and leaving their workplaces.

As previously mentioned, the production unit in question includes four production lines which are very similar—or in some cases identical—in their operation, depending on the type of product that constitutes their final output. Within the simulation module, the entire production unit was gradually modeled, including both the production lines and the newly proposed routes for the movement of the material supply tugger trains.

The pathways for the tugger trains were designed in such a way that, in the event both tugger trains are operating in the production hall at the same time, the likelihood of their paths overlapping—particularly in areas previously identified as collision zones—would be minimized as much as possible.

The proposed routing of the material handling tugger trains can be seen in Figure 8, shown in 3D simulation models.

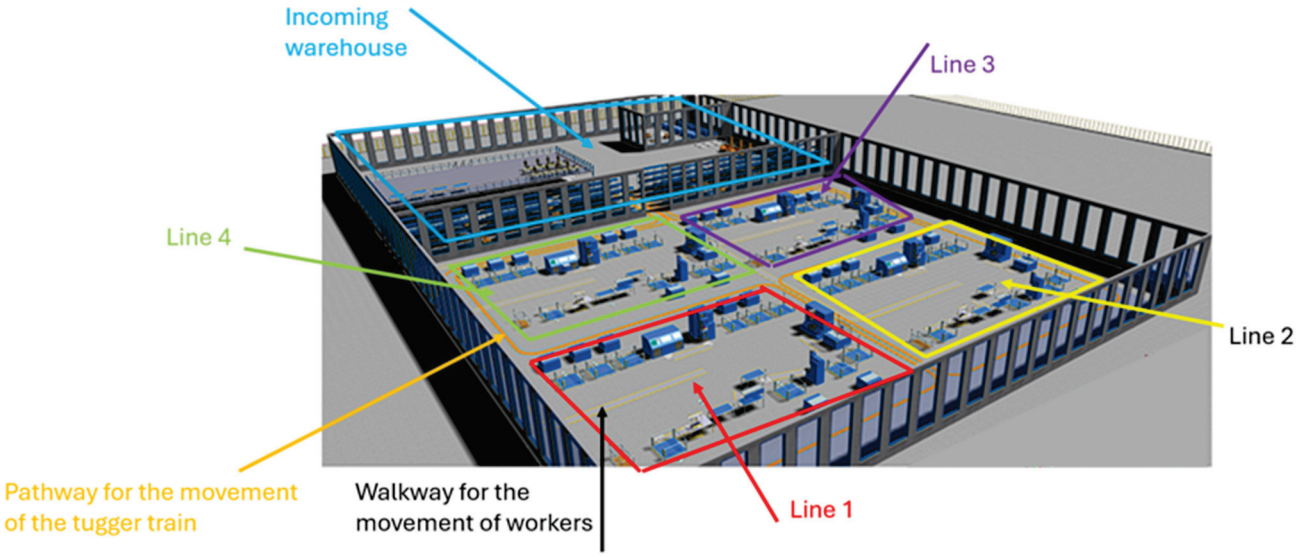


Figure 8. Model of the production unit with a tugger train sets.

Figure 8 presents a 3D simulation of the entire production process within the Tecnomatix Plant Simulation software environment. This figure highlights the key components of the production hall: the four production lines, the input warehouse from which the supply tugger trains originate, the proposed routes for the tugger trains, as well as the pathways designated for employee movement.

3.2. Data Collection and Input Parameters

With the proposed method of tugger train operation and its strict adherence, it is not possible to bypass any production line multiple times. It is essential to eliminate errors during the unloading of delivered materials, as well as the loading of empty containers after the consumed materials. When unloading and loading the delivered materials it is crucial that the barcode readers signal to the operator the exact number of containers to be unloaded at a given location to avoid the risk of a container being unloaded in the wrong place, which would result in the need to repeat the movement around the line. A similar process is necessary for the collection of empty containers after the consumed material.

A future vision for the optimal operation of such a system is the implementation of localization systems that would be integrated and networked with smart barcode readers. Operators would use these readers during loading and unloading processes. In this manner, the localization system would monitor the movement not only of operators and tugger trains but also of the containers holding the material. By tracking their precise locations, the barcode reader would automatically signal and validate the correct volume and location of the goods for the operator. By preventing errors during the loading and unloading processes, time losses on the production lines caused by supply errors would be significantly reduced.

The data acquired via the RTLS were processed and formatted into tables compatible with the Tecnomatix Plant Simulation software module. These tables were subsequently integrated into the simulation environment through programming methods implemented in the Simtalk language. Based on the programming commands within the simulation methods, the data were further edited and refined to ensure an accurate representation of the movements tracked by the RTLS devices within the digital simulation model. This

authentic digital portrayal of real-world material and personnel flows formed the basis for conducting experiments aimed at resolving the identified production issues.

Another proposal for maximizing the elimination of collisions between supply units in the production process is to ensure different initial material quantities for each production line, depending on which tugger train is assigned to supply them. This means the sizes of the Kanban bins would vary based on the route of the supplying tugger train. This approach would result in the tugger trains arriving at the production site at different times, further reducing the likelihood of collisions between them.

Both of these alternatives support the necessity of permanently implementing a localization system. This system would, in addition to continuous localization, enable the monitoring of material flows, workers, and logistical resources throughout the process. With ongoing data collection it would be possible to conduct retrospective validations of certain processes when necessary, and the collected data could be used for implementing innovations or for building new production units, whether of a similar or different nature.

Our expectation is summarized in the following table, see Table 2.

Table 2. Expected values.

	Planned Ideal State
Number of collisions per month	0
Production capacity (units/production line)	1200
Loading time of the tugger trains	90 min
Tugger train time in the production hall	<30 min
Kanban replenishment time	<3 min

3.3. Results and Comparison

We compare two methods of testing our suggested model, which are the simulation and classical approach, by collecting data. For normality testing we use the Shapiro–Wilk test, which says if $p > 0.05$ then our collected data confirms the normal distribution.

We start with a simulation where 950 scenarios occurred. When testing loading time, we obtain by the Shapiro–Wilk test that $p = 0.3571$ while the average is 102.44 min with a standard deviation of 6.73. For tugger train time, the Shapiro–Wilk test gives $p = 0.4436$ while the average is 17.54 min with a standard deviation of 4.12. The Shapiro–Wilk test takes a p-value of 0.4179 for the time of replenishment of Kanban, whereas the average is 1.74 min with a standard deviation of 0.581. It is worth mentioning that no collision occurs.

By classical data collecting we obtain 825 observed items. For the loading time, the p value of the Shapiro–Wilk test is equal to 0.2147 while the average is 118.54 min with a standard deviation of 11.38. For tugger train time, the Shapiro–Wilk test provides $p = 0.1723$ while the average is 42.17 min with a standard deviation of 4.72. Finally, the p-value for Kanban replenishment time is 0.2314 given by the Shapiro–Wilk test while the average is 1.31 with a standard deviation of 0.91.

Table 3 compares the planned ideal state, the state proposed and validated through simulation, and the actual state observed during data collection.

From a time perspective, every minute holds significant value for the company, with each minute of downtime associated with costs amounting to EUR 48. This estimate includes machine inactivity, labor idling, and other associated incidents. Based on our measurements, findings, and average data derived from Table 1, it is evident that collisions of tugger train sets result in an average downtime of 25 min. This, over the course of a month with 9 collisions, results in an average cost of EUR 10,800 per month.

Table 3. Comparison of processes.

	State Proposed and Verified Through Simulation	Actual State During Data Collection
Number of collisions per month	0	9
Production capacity (units/production line)	950	825
Loading time of the tugger trains	<105 min	<120 min
Tugger train time in the production hall	<20 min	<44 min
Kanban replenishment time	<2 min	<1.32 min

As shown in Table 3, the implementation of the proposed solution increases the number of products produced at the output by 125 units. The average price of products produced at this particular production unit, as established by the company, is EUR 67.55. This is an average value, as multiple types of finished products are produced on the individual lines. Through basic multiplication, the financial gain in output value of the production unit can be estimated at EUR 8443.75.

By eliminating downtime in the identified bottlenecks, with an average value of EUR 10,800, and with an average increase in the financial evaluation of production by EUR 8443.75, the benefits of this proposal can be quantified at nearly EUR 20,000 per month.

3.4. Discussion and Implications

With the implementation of a continuous improvement system based on further analyses, it is possible to shift the output parameters to the planned value, or even higher. As evident from the table, when addressing the specific problem some planned values have significantly improved compared to the original plan. The planned Kanban replenishment time has improved by an average of 1 min, and the planned time for the movement of tugger trains within the production hall has been reduced by an average of 10 min based on the proposed solution.

The primary objective of this study is the development and validation of an integrated approach combining data collection via RTLS with simulation-driven optimization. This approach captures the current state of the supply system while providing a predictive model for process planning and improvement.

The main contributions of this research include the design of a structured and repeatable methodology applicable across diverse industrial environments facing logistics and material flow challenges. Additionally, this work demonstrates that real-time data integration enhances simulation-based decision-making, enabling insights that cannot be obtained solely through observation or static simulation models.

The proposed methodology offers a framework for the digital transformation of logistics processes and holds significant potential for enterprises aiming to adopt Industry 4.0 and 5.0 principles.

4. Conclusions

Based on the analysis results using simulation, which were carried out and created based on data collected through observation and detection methods, possible improvement proposals for the efficiency and streamlining of the process have been developed and verified. The proposed improvements demonstrate clear enhancements in supply and logistics performance metrics, which are also reflected in the increase in final output. Based on the described methodologies, or their slight modification depending on the type of process in which we would like to apply them, it can be stated that they are universally applicable regardless of the type of process or industry sector. The results of such analyses can be compared in both homogeneous and heterogeneous processes.

Based on the statistical comparison of the results of the implemented proposals, the combination of multiple methods during data collection and their subsequent use demonstrates significant research potential, which should be further deepened. The proper combination of technologies in synergy with suitable industrial engineering methods needs to be utilized. Subsequently, it is crucial to correctly integrate the collected data in order to achieve the desired goals.

In relation to the focus of this paper and the results of the case study presented, the author collective sees several visions that could be supported through deepening technological advancements and research in this field. These visions are schematically illustrated in Figure 9. These future directions are illustrated schematically in Figure 9, using an example of the potential future functioning of the process presented in this paper. The integration and networking of certain technologies and research in this area could have the following impact, demonstrated through the example of the operational facility:

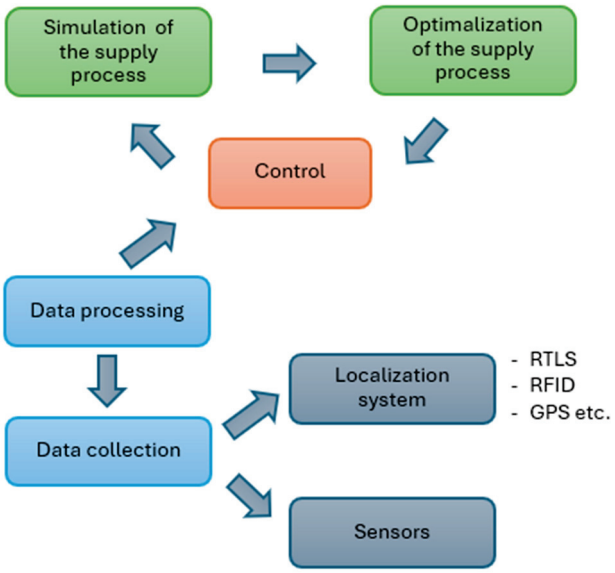


Figure 9. Cycle of utilizing simulations and data collection for streamlining the supply process.

The localization system would primarily track the location of the material stored on a specific supply unit. When the supply unit halts near the location where the material should be properly unloaded, the scanner used by the operator during material loading would dynamically process data about the material already in the correct location and that which is still in the tugger. If the operator fails to unload a container and tries to proceed to the next workstation, the scanner would alert the operator about the mistake. The system could be further improved; in the event of an error during loading or unloading, the tugger train, which would also be systemically recognized as a mobile entity within the process, could potentially be halted automatically until the operator completes the task correctly. The movement of the train would be unblocked only after each material container is properly localized.

Through the localization of materials, tugger trains, and possibly even operators, a multi-stage system control would ensure the accuracy of the supply process. This system would need to be wirelessly networked and operate smoothly in real time. Such a system would require wireless integration and seamless real-time operation as it would need to receive and send signals regarding the correctness of the location, notify the operator about the task's completion status, and inform the tugger train when it can proceed to the next station.

Such a system would implement not only the principles of Industry 4.0 but also, considering the preservation of operator positions, it would align with the principles of Industry 5.0, which integrates the human factor into the manufacturing process while minimizing both physical and cognitive workload wherever feasible. In case the elimination of the human factor is required, AGV (Automated Guided Vehicle) technology could be integrated into the process, utilizing machine learning techniques to autonomously perform certain operations. However, the goal of improving and implementing technological advancements should not be to eliminate human resources from manufacturing processes at all costs.

The implementation of digital-twin technology into this data-processing process would allow real-time verification of improvement possibilities for different states that may arise in the process, based on simulation procedures. Using a digital framework and the results of these simulations, continuous measures could be taken to improve the efficiency of the manufacturing process, maintaining it at an optimal level. The sensor technology within the context of the digital-twin would be complemented by localization devices, which would smoothly send collected data in real time for editing into a format suitable for simulation software. This editing could be performed with the help of artificial intelligence. The implementation of multi-stage analyses would accelerate continuous process improvement, as well as planning and modeling new processes based on data from existing operations.

Author Contributions: Conceptualization, M.K., J.K., M.P., P.T. and A.H.; methodology, M.K., J.K., M.P., P.T. and A.H.; software, M.K.; validation, M.K., J.K., M.P., P.T. and A.H.; formal analysis, J.K. and M.K.; investigation, M.K., J.K., M.P., P.T. and A.H.; resources, M.P. and J.K.; data curation, M.K., J.K., M.P., P.T. and A.H.; writing—original draft preparation, M.K., J.K., M.P., P.T. and A.H.; writing—review and editing, M.K., J.K., and A.H.; project administration, M.K. All authors have read and agreed to the published version of the manuscript.

Funding: This research received no external funding.

Data Availability Statement: No applicable.

Acknowledgments: This article was created by the implementation of the grant project APVV-17-0258: Digital engineering elements application in innovation and optimization of production flows, APVV-19-0418: Intelligent solutions to enhance business innovation capability in the process of transforming them into smart businesses, KEGA 020TUKE-4/2023: Systematic development of the competence profile of students of industrial and digital engineering in the process of higher education, VEGA 1/0508/22: Innovative and digital technologies in manufacturing and logistics processes and system, and VEGA 1/0383/25: Optimizing the activities of manufacturing enterprises and their digitization using advanced virtual means and tools.

Conflicts of Interest: The authors declare no conflicts of interest.

References

1. Ojstersek, R.; Javernik, A.; Buchmeister, B. The impact of the collaborative workplace on the production system capacity: Simulation modelling vs. real-world application approach. *Adv. Prod. Eng. Manag.* **2021**, *16*, 431–442. [CrossRef]
2. Glova, J.; Sabol, T.; Vajda, V. Business Models for the Internet of Things Environment. *Emerg. Mark. Queries Financ. Bus.* **2013**, *15*, 1122–1129. [CrossRef]
3. Krajcovic, M.; Gabajová, G.; Matys, M.; Grznár, P.; Dulina, Ľ.; Kohár, R. 3D Interactive Learning Environment as a Tool for Knowledge Transfer and Retention. *Sustainability* **2021**, *13*, 7916. [CrossRef]
4. Marschall, M.; Gregor, M.; Durica, L.; Vavrík, V.; Bielik, T.; Grznár, P.; Mozol, Š. Defining the Number of Mobile Robotic Systems Needed for Reconfiguration of Modular Manufacturing Systems via Simulation. *Machines* **2022**, *10*, 316. [CrossRef]
5. Gola, A.; Plinta, D.; Grznar, P. Modelling and simulation of reconfigurable manufacturing system for machining of casing-class parts. In Proceedings of the 20th International Scientific Conference Engineering for Rural Development, Jelgava, Latvia, 26–28 May 2021; pp. 1563–1568. [CrossRef]

6. Wicher, P.; Stas, D.; Karkula, M.; Lenort, R.; Besta, P. A Computer Simulation-Based Analysis of Supply Chains Resilience in Industrial Environment. *Metalurgija* **2015**, *54*, 703–706, ISSN 0543-5846, eISSN 1334-2576.
7. Tsai, J.F.; Wang, P.C.; Tsai, W.L. Competence Set Expansion for Production Process Planning. *NTU Manag. Rev.* **2013**, *23*, 263–296. [CrossRef]
8. Holtewert, P.; Bauernhansl, T. Interchangeable Product Designs for the Increase of Capacity Flexibility in Production Systems. *Procedia CIRP* **2016**, *50*, 252–257. [CrossRef]
9. Sarjono, H.; Kusuma, V.; Hamali, S.; Mulyono. Planning Production Capacity Optimisation with Rough Cut Capacity Planning. *Pertanika J. Soc. Sci. Humanit.* **2016**, *24*, 33–45, ISSN 0128-7702, eISSN 2231-8534.
10. Huang, D.; Lin, Z.K.; Wei, W. Optimal production planning with capacity reservation and convex capacity costs. *Adv. Prod. Eng. Manag.* **2018**, *13*, 31–43. [CrossRef]
11. Schwarz, J.A.; Tan, B. Optimal sales and production rollover strategies under capacity constraints. *Eur. J. Oper. Res.* **2021**, *294*, 507–524. [CrossRef]
12. Creutznacher, T.; Berger, U.; Lepratti, R.; Lamparter, S. The Transformable Factory: Adapting Automotive Production Capacities, Research and Innovation in Manufacturing: Key Enabling Technologies for the Factories of the Future. In Proceedings of the 48th Cirp Conference on Manufacturing Systems, Ischia, Italy, 24–26 June 2015; Volume 41, pp. 171–176. [CrossRef]
13. Saderova, J.; Poplawski, L.M.B., Jr.; Michalkova, S.; Cvoliga, M. Layout Design Options for Warehouse Management. *Pol. J. Manag. Stud.* **2020**, *22*, 443–455. [CrossRef]
14. Paska, M.; Malkus, T.; Rosova, A.; Trebuna, P.; Kacmary, P.; Behun, M. International Commercial Terms and Their Necessity for the Logistics. In Proceedings of the 8th Carpathian Logistics Congress 2018, Prague, Czech Republic, 3–5 December 2018; pp. 688–696, ISBN 978-80-87294-88-8.
15. Balzer, R.; Užík, M.; Glova, J. Managing Growth Opportunities in The Digital Era—An Empiric Perspective of Value Creation. *Pol. J. Manag. Stud.* **2020**, *21*, 87–100. [CrossRef]
16. Saniuk, S.; Grabowska, S.; Straka, M. Identification of Social and Economic Expectations: Contextual Reasons for the Transformation Process of Industry 4.0 into the Industry 5.0 Concept. *Sustainability* **2022**, *14*, 1391. [CrossRef]
17. Matisková, D.; Balog, M.; Husár, J. Criteria for the Optimization of Production Processes in Machining of Metallic Materials. *Manag. Syst. Prod. Eng.* **2018**, *26*, 227–230. [CrossRef]
18. Sujova, A.; Marcinekova, K.; Hittmar, S. Sustainable Optimization of Manufacturing Process Effectiveness in Furniture Production. *Sustainability* **2017**, *9*, 923. [CrossRef]
19. Laciak, M.; Raskayova, D.; Flegner, P.; Kacur, J.; Durdan, M. Automated system for optimizing input parameters of the UCG process. In Proceedings of the 20th International Carpathian Control Conference, Krakow-Wieliczka, Poland, 26–29 May 2019; pp. 311–315. [CrossRef]
20. Chu, J.F.; Xu, F.; Zhu, Q.Y.; Fukuyama, H. Production scale expansion and congestion in two-stage network systems. *Comput. Ind. Eng.* **2024**, *193*, 110317. [CrossRef]
21. Lin, M.H.; Tsai, J.F.; Wang, P.C.; Ho, Y.T. A coordinated production planning model with capacity expansion for supply chain networks. *Eur. J. Ind. Eng.* **2019**, *13*, 435–460. [CrossRef]
22. Min, Z.; Nie, G.H.; Ming, Z.; Lihm, H. Capacity improvement of an LCM production line. In Proceedings of the 3rd International Conference on Innovation & Management, Vols 1 and 2, Wuhan, China, 2–3 December 2006; pp. 1028–1031, ISBN 978-7-5629-2471-5.
23. Radatz, H.; Kühne, K.; Bramsiepe, C.; Schembecker, G. Comparison of capacity expansion strategies for chemical production plants. *Chem. Eng. Res. Des.* **2019**, *143*, 56–78. [CrossRef]
24. West, N.; Schwenken, J.; Deuse, J. Data-Driven Approach for Diagnostic Analysis of Dynamic Bottlenecks in Serial Manufacturing Systems. *arXiv* **2023**, arXiv:2306.16120. [CrossRef]
25. Zhang, Y.; Peng, E.; Luo, Z. Bottleneck Detection for Discrete Manufacturing System Based on Object-Oriented Colored Petri Nets and Cloud Simulation. *EDP Sci.* **2022**, *45*, 01015. [CrossRef]
26. Pekarciková, M.; Trebuna, P.; Kliment, M.; Edl, M.; Rosocha, L. Transformation the Logistics to Digital Logistics: Theoretical Approach. *Acta Logist.* **2020**, *7*, 217–223. [CrossRef]
27. Kábele, P.; Edl, M. Increasing the Efficiency of the Production Process Due to Using Methods of Industrial Engineering. In *Advances in Design, Simulation and Manufacturing II, Proceedings of the 2nd International Conference on Design, Simulation, Manufacturing II 2019, Lutsk, Ukraine, 11–14 June 2019*; Springer: Berlin/Heidelberg, Germany, 2019; pp. 126–137. [CrossRef]

28. Sasiadek, M.; Kielec, R.; Wozniak, W. The Application of the Dependency Structure Matrix in the Planning of Production Processes, Vision 2025: Education Excellence and Management of Innovations Through Sustainable Economic Competitive Advantage. In Proceedings of the 36th IBIMA Conference, Madrid, Spain, 13–14 November 2019; pp. 6148–6155, ISBN 978-0-9998551-3-3.
29. Manlig, F.; Slaichova, E.; Koblasa, F.; Vavruska, J. Innovation of business processes by means of computer-aided simulation. *Nov. Trends Prod. Devices Syst.* **2014**, *474*, 67–72. [CrossRef]

Disclaimer/Publisher's Note: The statements, opinions and data contained in all publications are solely those of the individual author(s) and contributor(s) and not of MDPI and/or the editor(s). MDPI and/or the editor(s) disclaim responsibility for any injury to people or property resulting from any ideas, methods, instructions or products referred to in the content.

applied sciences

MDPI

Article

An Attempt to Establish a Mathematical Model for an Unconventional Worm Gear with Bearings

Simion Haragâș [1], Roland Ninacs [1], Ovidiu Buiga [1,*], Lucian Tudose [1], Alexandru Haragâș [2], Ioana Monica Sas-Boca [3,*] and Felicia Aurora Cristea [1]

[1] Mechanical Systems Engineering Department, Faculty of Industrial Engineering, Robotics and Production Management, Technical University of Cluj-Napoca, 28 Memorandumului Street, 400114 Cluj-Napoca, Romania; simion.haragas@omt.utcluj.ro (S.H.); ninacs_roland@yahoo.com (R.N.); felicia.cristea@mep.utcluj.ro (F.A.C.)
[2] Computer Department, Technical University of Cluj-Napoca, 28 Memorandumului Street, 400114 Cluj-Napoca, Romania; haragas.si.alexandru@student.utcluj.ro
[3] Materials Science and Engineering Department, Faculty of Materials and Environmental Engineering, Technical University of Cluj-Napoca, 28 Memorandumului Street, 400114 Cluj-Napoca, Romania
* Correspondence: ovidiu.buiga@omt.utcluj.ro (O.B.); monica.sas.boca@ipm.utcluj.ro (I.M.S.-B.)

Abstract: The aim of this paper is to develop a mathematical model for an unconventional worm gear consisting of a globoid worm and a worm wheel where the teeth are bearings. Using rolling elements such the teeth of the worm wheel (ball bearings) transforms the sliding friction to rolling friction during the process of worm gear meshing, improving power. The geometry of the component elements of the gear is analyzed in correlation with its kinematics. After the creation of the mathematical model, it is validated both analytically (through complex graphic representations) and experimentally (by creating, for a particular case, the 3D model and the concrete physical model (prototype) of the gear through 3D printing).

Keywords: mathematical model; globoid worm; rolling friction; analytical validation; experimental validation; graphical simulation; additive manufacturing

1. Introduction

To fulfill the increasing demands for a high gear transmission ratio using a single stage (up to 80) with compact gear dimensions, high load-carrying capacity, and smoothness in operation, etc.—needed for lifting-and-shifting machines in the aerospace industry and modern manufacturing processes—various worm drive types are used. These space-saving gearings, depending on the external surface shape of the worm and wheel, can be cylindrical (with a cylindrical worm known as a single-enveloping worm being the most commonly used [1]); globoid, known as the TA or Hindley worm drive or double-enveloping worm (DEW) (in this case, either the worm is globoid [2] or both the worm and wheel are globoid); or special (where the worm has a conical shape, called a spiroid [1], and the other element is a face-type gear) [3].

Until now, worm drives have been the subject of many researchers' studies. In the technical literature, there are significant publications about mathematical modeling methods, various surface analyses, research regarding new types of worm gears, and manufacturing processes.

A summary of the development phases of these worm gearings is presented in [4]. Litvin and Fuentes [5] described a study on the theory of gearing. Ninacs, Cristea, and Haragâș [6] presented a detailed kinematic and functional analysis of a double-envelope worm gear. Practical design aspects are detailed [7]. Zhao, Huai, and Zhang [8] proposed a new meshing theory for a globoid worm gear considering some modifications regarding the following parameters: center distance, transmitting ratio, and the height of the cutter frame.

Xu, Qin, and Shi [9] suggested new research on worm gear drives based on the practical manufacturing process known as the direct digital modeling method (DDMM). They presented a detailed discussion on the misalignment errors and contact deformations in the contact zone and concluded that the proposed design solution is characterized by reduced misalignment and transmission errors. Polowniak, Sobolak, and Marciniec [10] created an algorithm for generating the helix of a double-enveloping worm gear. They generated CAD models, which were used for FEM analysis to manufacture real prototypes employing additive manufacturing processes. Zhao and Zang [11] presented a study regarding the curvature analysis for the helicoidal surface of a modified TA worm. However, the author of this study did not investigate the meshing process. A meshing theory for the TA worm gearing is described [12]. The performance of the studied worm gear set is considerably favorable over the other types of conical worm drive. A discussion about a new type of spiroid gear set is detailed [12]. Regarding the manufacturing process, the following studies were conducted. Andrianto, Wu, and Arifin [13] developed a new method for machining double-enveloping worms (DEWs). Firstly, they carried out a virtual simulation of the cutting process, followed by an experimental test of a worm gear set. In their research, Rui et al. [14] presented a land surface cutting Hob's design for increasing the machining tool's service life. Lei et al. [15] proposed a five-axis tool path for worm gear flank milling. This machining process is then compared to the conventional end milling processes. The method studied offers high process efficiency and surface quality. Dong et al. [16] described a method of rough turning for the toroidal worm that permits higher-efficiency manufacturing. Chen Y. et al. [17] introduced a new type of worm drive consisting of a planar internal gear and a crown worm. The components were machined and then the obtained prototype was assembled and subject to a running test, in which the efficiency and the oil temperature were checked.

Double-enveloping worm drives, as previously mentioned, have applications in various domains considering their advantages (as compared to the other worm gear types) such as higher efficiency (because of more favorable functioning conditions [10]), smoothness, and silence in operation, high load capacity due to a higher contact ratio, etc. However, this type of worm gear is sensitive to tolerance, needs accurate alignment, and is characterized by high wear and a tendency to seize [1]. Another significant aspect is the backlash, which has a major impact on smooth operation and over-transmission errors.

To overcome these disadvantages of the globoid worm gear drive, a new roller enveloping toroidal worm gear was proposed. This design solution consists of a worm wheel in which the teeth are replaced with deep groove ball bearings. Using rolling elements turns the sliding friction into rolling friction during the process of worm gear meshing, which eliminates the backlash [18] (when they are used custom-designed bearings) and conducts higher gear efficiency. In [18], Deng et al. investigated a new single-roller enveloping hourglass worm gear. They proposed a design to eliminate the backlash in mating gear transmission. A parametric study was conducted to analyze the influence of some design variables, i.e., the center distance, roller radius, transmission ratio, and radius of the base circle over the gear set characteristics. An analysis of the dynamic behavior of these gears was carried out in [19–21]. The 3D-generated CAD model was then compared with the calculated one. A very good match was found. Another interesting study about these new gearings is described in [9]. It presented a methodology for thermal power calculation.

What we pursue as a priority in this paper is to obtain a general mathematical model of the non-conventional worm gear with bearings that is clear, coherent, demonstrable, and easy to apply for particular situations, an essential aspect for the realization of both 3D and physical models. The objective of the paper is to reduce the friction force in the worm-roller gear using the rolling force of the bearing (tooth) on the surface of a helical worm. In this paper, a mathematical model of a double-deep groove ball-bearing enveloping worm gear drive is presented. A total of 36 bearings were used (each new worm wheel tooth was composed of two bearings), replacing the worm wheel teeth. Here, a mathematical model

is first formulated, followed by graphical validation of the globoid helix. The Wolfram 14.1, online version [22] program was utilized to generate globoid helices.

2. Materials and Methods

The "classic" globoid worm gear (Figure 1) consists of a globoid worm and a similar globoid worm wheel [4]. The globoid worm is one in which the helix coils around a toroidal reference surface. Kinematic and functional analyzes of this type of gear are carried out in works [1,10,13,16,23–25]. Constructive design aspects are presented in [4]. The materials used include hardened steels (generally case-hardening steels) for the worm and an anti-friction material (tin bronze or aluminum, nodular graphite cast iron or gray) for the worm wheel.

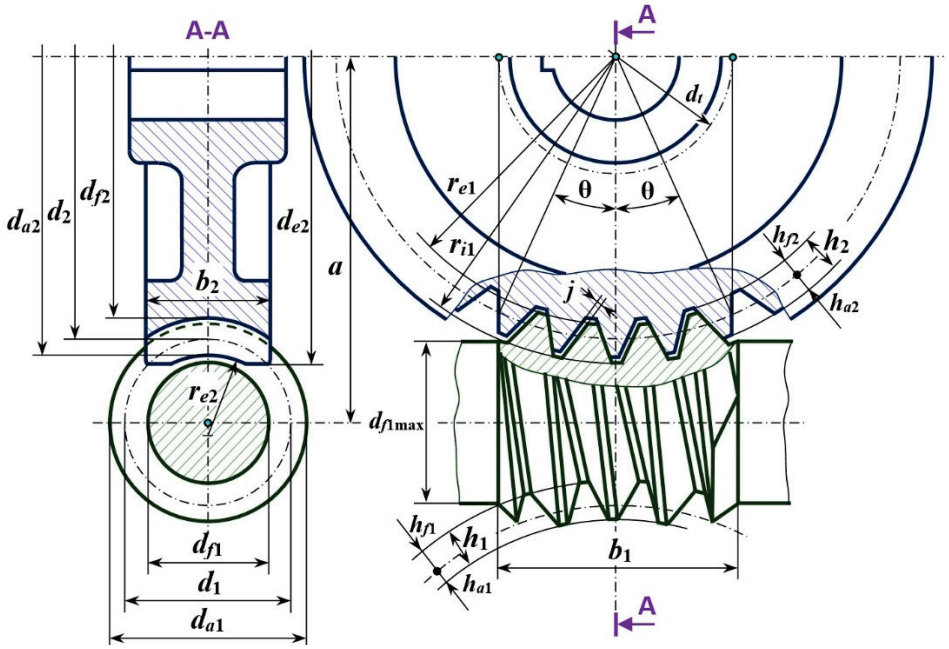


Figure 1. Globoid worm gear.

The advantages of this gear include its quiet operation, high degree of coverage, and high bearing capacity (smaller gauge at the same power to be transmitted).

The main disadvantage is that of frictional losses (due to the sliding friction between the worm turn and the worm gear teeth). As the friction is intense, there is a significant release of heat and, implicitly, the transmission efficiency will be reduced.

Another disadvantage is that of positioning accuracy because there is quite a large interplay (denoted *j* in Figure 1) between the elements in contact.

To reduce the effects of these disadvantages, several variants of "unconventional" gears have been proposed in which the sliding friction is replaced by rolling friction (the rolling friction coefficient is about ten times lower than the sliding friction coefficient). Also, the play in the gear can be precisely controlled; even pre-tensioning can be achieved.

Such a construction is the worm gear with bearings (Figure 2), which is the subject of study in this paper.

In this gear, the shape of the worm does not change, but the driven wheel will have radial bearings instead of teeth. The contact between the worm coil and the bearings is a linear contact (Hertz contact theory). The bearings will rotate around their own axis during operation. By changing the pitch of the spiral of the auger, the contact between its flanks and the bearings will be in different directions (Figure 2), which leads to the cancellation of the play between the elements of the gear components.

Various studies on specific aspects of this gear can be found in works [2–6,18,19,26–41]. In these articles, theoretical and experimental research, 3D modeling, finite element analysis, and research on concrete physical models are presented.

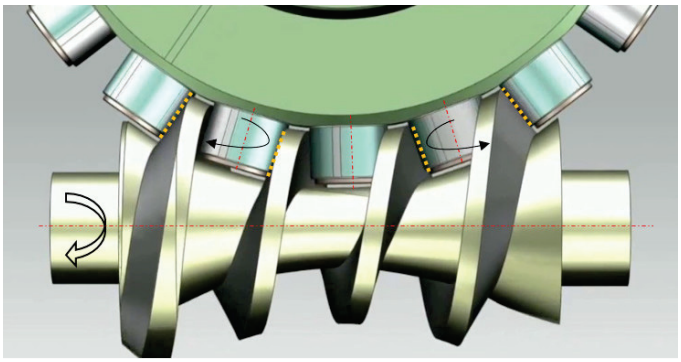


Figure 2. Worm gear with a single row of bearings per roller.

The mathematical model of this type of gear, however, is treated in a cursory manner. Rather, the defining equations seem to be obtained after the model generation and not the other way around, as would normally be the case.

2.1. Geometry of the Unconventional Worm Gear with Bearings, Kinematic Analysis, and Mathematical Model Formulation

The main geometric elements of the gear are shown in Figure 3. In the axial section, the flanks of the spiral of the worm are rectilinear and tangent to the profiling circle (with the center in O_2 and diameter d, equal to the outer diameter of the bearing), which is concentric with the worm wheel. The inclination of the helix profile will be equal to the angular pitch θ between the rollers of the worm wheel.

Consider point M positioned in the center of the roller (bearing) and points A, B, D and E at its ends. The displacement of the lines AB and DE in the O_{1xvz} system (related to the worm gear) results in the generation of the flanks of the spiral (Figure 3).

The equations of point M related to the worm wheel (system O_{1xyz}) are:

$$\begin{cases} x = \frac{d_2}{2} \cdot \sin\varphi_2 \\ y = \left(a - \frac{d_2}{2}\right) + \frac{d_2}{2} \cdot (1 - \cos\varphi_2) \\ z = 0 \end{cases} \begin{cases} x = \frac{d_2}{2} \cdot \sin\varphi_2 \\ y = a - \frac{d_2}{2} \cdot \cos\varphi_2 \\ z = 0 \end{cases} \quad (1)$$

Relative to the driven wheel, the trajectory of point M is an arc of a circle. The position equations of point M related to the worm (system O_{1xyz}) are:

$$\begin{cases} x = \frac{d_2}{2} \cdot \sin\varphi_2 \\ y = \left[\left(a - \frac{d_2}{2}\right) + \frac{d_2}{2} \cdot (1 - \cos\varphi_2)\right] \cdot \cos\varphi_1 \\ z = -\left[\left(a - \frac{d_2}{2}\right) + \frac{d_2}{2} \cdot (1 - \cos\varphi_2)\right] \cdot \sin\varphi_1 \end{cases} \begin{cases} x = \frac{d_2}{2} \cdot \sin\varphi_2 \\ y = \left(a - \frac{d_2}{2} \cdot \cos\varphi_2\right) \cdot \cos\varphi_1 \\ z = -\left(a - \frac{d_2}{2} \cdot \cos\varphi_2\right) \cdot \sin\varphi_1 \end{cases} \quad (2)$$

where

d_2 is the worm wheel pitch diameter, mm;
a represents the center distance, mm;
φ_1 is the angle of the position for the worm wheel, ° (degrees);
φ_2 is the angle of the position for the worm wheel, ° (degrees).

$$\varphi_1 = u_{12} \cdot \varphi_2 \quad (3)$$

where

u_{12} represents the gear ratio

$$u_{12} = \frac{z_2}{z_1} = \frac{n_1}{n_2} \quad (4)$$

where

z_2 is the worm wheel number of radial ball bearings, i.e., the number of teeth (in a classic worm gearing);
z_1 represents the thread number of the worm;
n_1 and n_2 represent the rotational speed of the worm and wheel, respectively.

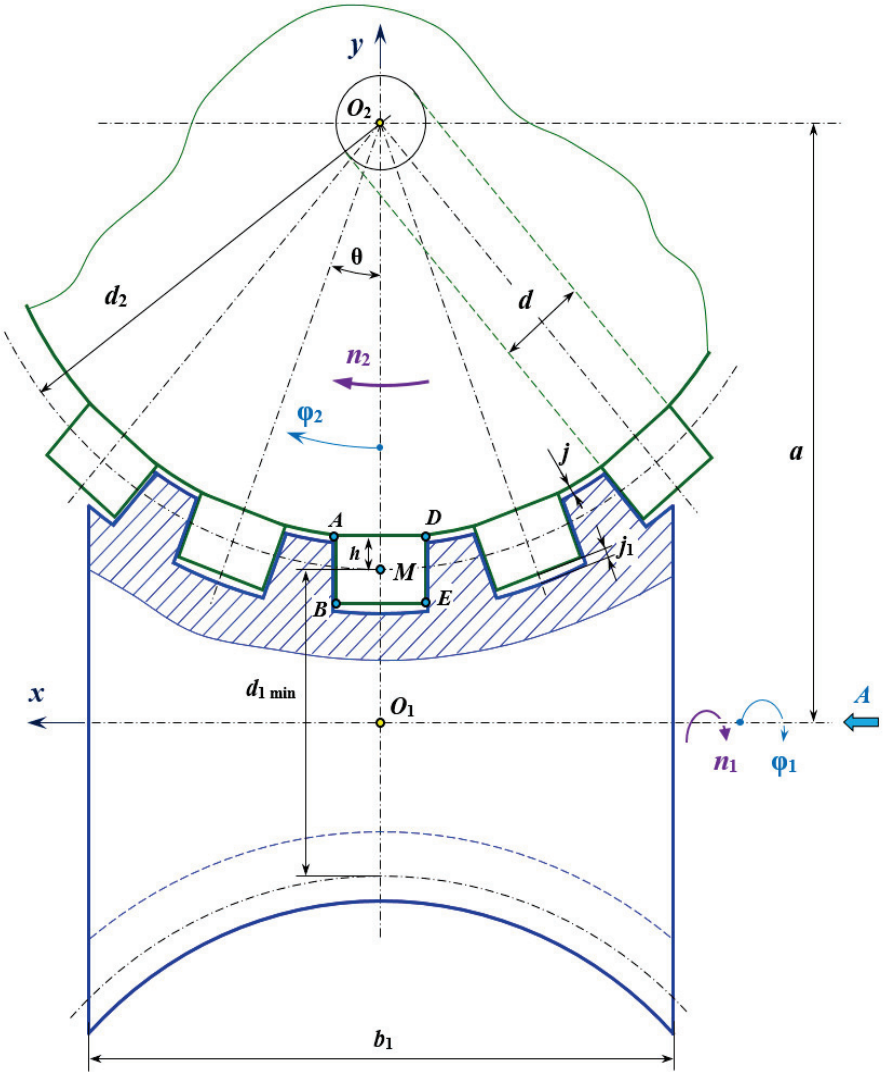


Figure 3. The geometry of the worm gear with bearings.

Relative to the worm, the trajectory of the M point is a helix wound on a toroidal surface (an inner circular torus).

Starting from Equation (2) of point M, the position equations of characteristic points A, B, D, and E (related to the coordinate system O_1xyz) are shown:

Equations of point A (system O_{1xyz}) are as follows:

$$\begin{cases} x = \frac{d}{2} \cdot \cos\varphi_2 + \left(\frac{d_2}{2} - h\right) \cdot \sin\varphi_2 \\ y = \left[a + \frac{d}{2} \cdot \sin\varphi_2 - \left(\frac{d_2}{2} - h\right) \cdot \cos\varphi_2\right] \cdot \cos\varphi_1 \\ z = -\left[a + \frac{d}{2} \cdot \sin\varphi_2 - \left(\frac{d_2}{2} - h\right) \cdot \cos\varphi_2\right] \cdot \sin\varphi_1 \end{cases} \quad (5)$$

where

d is the outer diameter of the bearing.

$$h = \frac{B_r}{2} \tag{6}$$

where

B_r is the bearing width.

Equations of point B (system O_{1xyz}) are as follows:

$$\begin{cases} x = \frac{d}{2} \cdot \cos\varphi_2 + \left(\frac{d_2}{2} + h\right) \cdot \sin\varphi_2 \\ y = \left[a + \frac{d}{2} \cdot \sin\varphi_2 - \left(\frac{d_2}{2} + h\right) \cdot \cos\varphi_2\right] \cdot \cos\varphi_1 \\ z = -\left[a + \frac{d}{2} \cdot \sin\varphi_2 - \left(\frac{d_2}{2} + h\right) \cdot \cos\varphi_2\right] \cdot \sin\varphi_1 \end{cases} \tag{7}$$

The parametric equations of the line AB (O_{1xyz} system) are as follows:

$$\begin{cases} x \cdot \cos\varphi_2 \cos\varphi_1 + y \cdot \sin\varphi_2 - \left[a \cdot \sin\varphi_2 + \frac{d}{2}\right] \cdot \cos\varphi_1 = 0 \\ y \cdot \sin\varphi_1 + z \cdot \cos\varphi_1 = 0 \end{cases} \tag{8}$$

For point D, the equations are:

$$\begin{cases} x = -\frac{d}{2} \cdot \cos\varphi_2 + \left(\frac{d_2}{2} - h\right) \cdot \sin\varphi_2 \\ y = \left[a - \frac{d}{2} \cdot \sin\varphi_2 - \left(\frac{d_2}{2} - h\right) \cdot \cos\varphi_2\right] \cdot \cos\varphi_1 \\ z = -\left[a - \frac{d}{2} \cdot \sin\varphi_2 - \left(\frac{d_2}{2} - h\right) \cdot \cos\varphi_2\right] \cdot \sin\varphi_1 \end{cases} \tag{9}$$

For point E, the equations are:

$$\begin{cases} x = -\frac{d}{2} \cdot \cos\varphi_2 + \left(\frac{d_2}{2} + h\right) \cdot \sin\varphi_2 \\ y = \left[a - \frac{d}{2} \cdot \sin\varphi_2 - \left(\frac{d_2}{2} + h\right) \cdot \cos\varphi_2\right] \cdot \cos\varphi_1 \\ z = -\left[a - \frac{d}{2} \cdot \sin\varphi_2 - \left(\frac{d_2}{2} + h\right) \cdot \cos\varphi_2\right] \cdot \sin\varphi_1 \end{cases} \tag{10}$$

The parametric equations of the line DE (O_{1xyz} system) are as follows:

$$\begin{cases} x \cdot \cos\varphi_2 \cos\varphi_1 + y \cdot \sin\varphi_2 - \left[a \cdot \sin\varphi_2 - \frac{d}{2}\right] \cdot \cos\varphi_1 = 0 \\ y \cdot \sin\varphi_1 + z \cdot \cos\varphi_1 = 0 \end{cases} \tag{11}$$

The surfaces described by lines AB and DE in the O_1xyz system (parametric Equations (8) and (11)) materialize the surfaces of the flanks of the spiral of the worm (as will be explained in the next subsection).

The profile of the worm's spiral in its axial plane will be linear. The inclination of the profile of the spiral will be equal to the angular pitch θ between the driven wheel rollers (Figure 4).

$$\theta = \frac{2 \cdot \pi}{z_2} \text{ [rad]} \tag{12}$$

The inclination of the flank of the worm is as follows:

$$\alpha = \frac{\theta}{2} \text{ [rad]} \tag{13}$$

The contact between the flank of the auger spiral and the rollers (bearings) is shown in Figure 5. The plane in which the point of contact is located makes an angle β, equal to the angle of inclination of the spiral helix on the splitting diameter, with the frontal median plane of the wheel (which also contains the axis of the auger). This angle is variable with a maximum value for d1min and smaller values towards the ends.

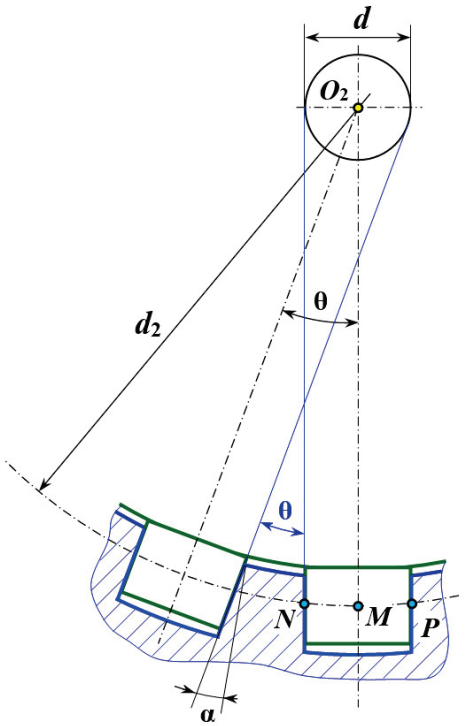


Figure 4. The profile of the worm wheel.

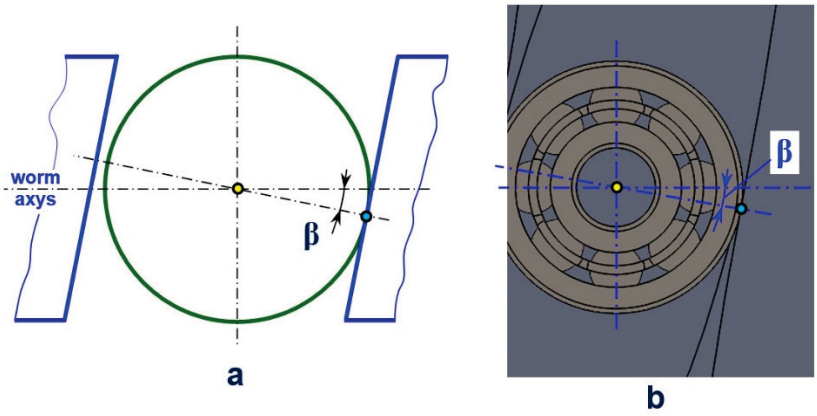


Figure 5. The worm–bearing contact: (**a**) 2D worm–bearing contact, (**b**) 3D worm–bearing contact.

In the axial section of the worm, the distance between the flanks is:

$$d_s = \frac{d}{\cos \beta} \tag{14}$$

This must be taken into account when machining the worm. Thus, the diameter of the machining tool (finger cutter) must be larger than ds calculated with the minimum value of β.

The angle β can be calculated from the velocity plane (Figure 6).

$$\tan \beta = \frac{v_2}{v_1} \Rightarrow \beta = \arctan\left(\frac{v_2}{v_1}\right) \tag{15}$$

where

v_2 is the peripheral speed of the driven wheel (constant).
v_1 is the peripheral speed of the worm (variable).

$$v_1 = \frac{\pi \cdot d_1 \cdot n_1}{60 \cdot 1000} \text{ [m/s]} \tag{16}$$

$$v_2 = \frac{\pi \cdot d_2 \cdot n_2}{60 \cdot 1000} \text{ [m/s]} \tag{17}$$

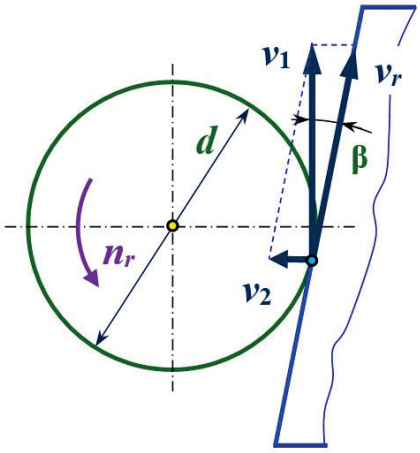


Figure 6. The velocity plane.

Substituting relations (16) and (17) into relation (15) and taking into account relation (4) gives:

$$\beta = \arctan\left(\frac{d_2}{u_{12} \cdot d_1}\right) \tag{18}$$

The worm splitting diameter d_1 is variable, its minimum value being $d_{1\min}$.

$$d_1 = d_{1\min} + d_2 \cdot (1 - \cos \varphi_2) \tag{19}$$

$$d_{1\min} = 2 \cdot a - d_2 \tag{20}$$

Finally:

$$\beta = \arctan\left[\frac{d_2}{u_{12} \cdot (2 \cdot a - d_2 \cdot \cos \varphi_2)}\right] \tag{21}$$

Rolling speed of the bearings (rollers):

$$v_r = \frac{v_1}{\cos \beta} \text{ [m/s]} \tag{22}$$

Speed of the bearings (rollers):

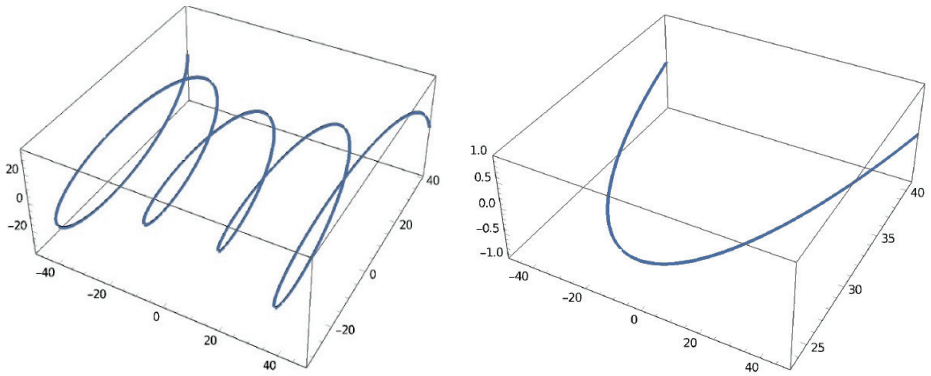
$$n_r = \frac{60000 \cdot v_r}{\pi \cdot d} \text{ [rpm]} \tag{23}$$

The common point of the rolling surfaces is the common normal line, where the displacement occurs in a perpendicular tangent plane. The bearings move in the direction of the tangent of the reference helix line, which means that the generatrix of the bearing is in contact with the helicoid surface in front of the axis section of the worm. The contact generatrix of the bearing is a straight line that skews from the worm axis, so they are not coplanar.

2.2. Analytic Validation of the 3D Model

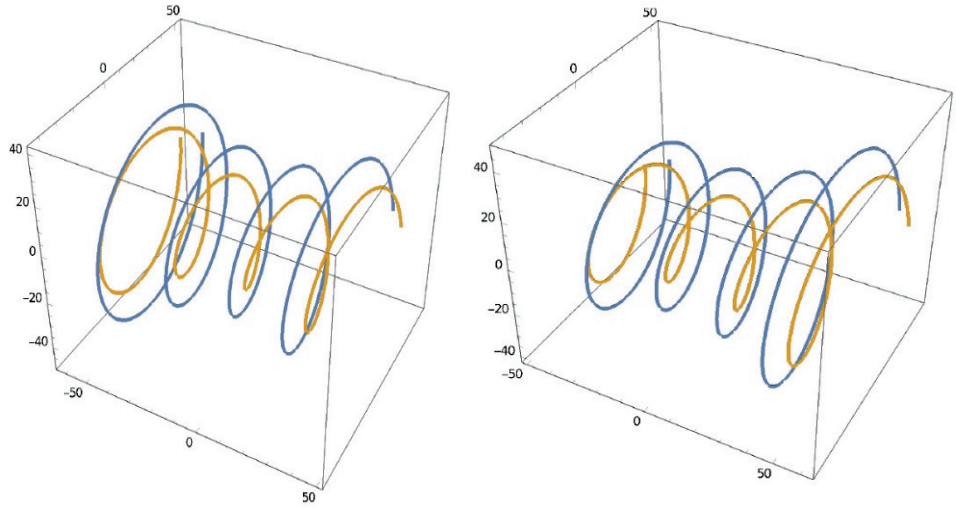
For the graphic representation of the previously determined equations, a particular case was considered, for which the following values were selected: a = 100 mm; d_2 = 154 mm; $\varphi_2 = -40 \ldots +40°$; z_1 = 1; z_2 = 18; d = 16 mm; B_r = 10 mm. The Wol-

fram [20] program was used to plot the graphs and validate the above equations. The obtained results are presented in Figures 7–11.



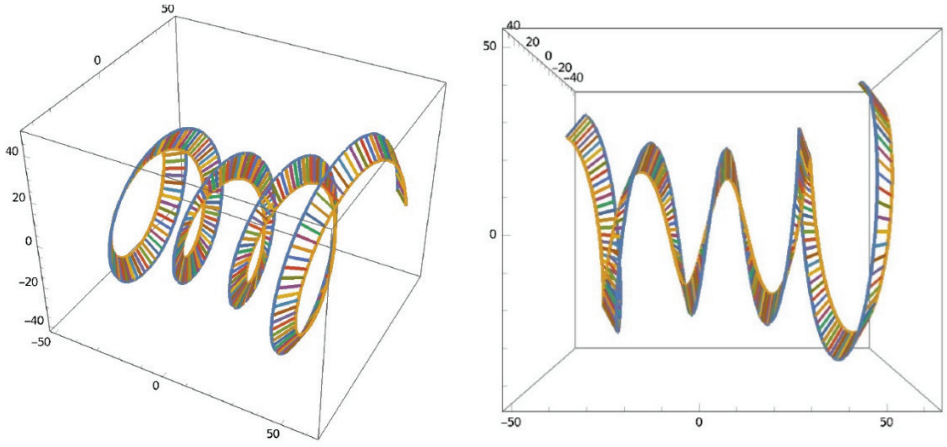
(**a**) (**b**)

Figure 7. The trajectory of point *M*. (**a**)—related to the worm; (**b**)—related to the worm wheel.



(**a**) (**b**)

Figure 8. The trajectories of *A*, *B*, *C*, and *D* points. (**a**)—*A* and *B* points; (**b**)—*D* and *E* points.



(**a**) (**b**)

Figure 9. The worm flank surface generated by sweeping the *AB* segment along the globoid-guided curve. (**a**)—isometric position; (**b**)—frontal position.

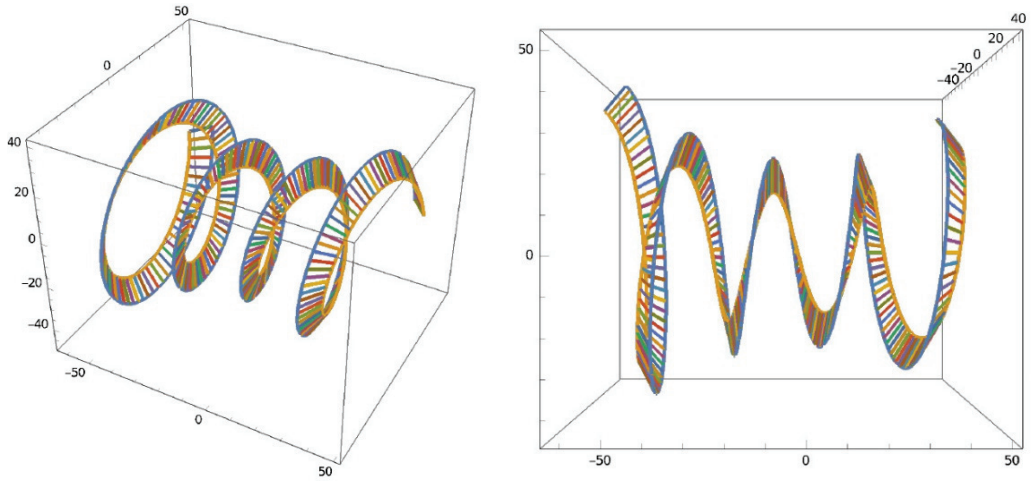


Figure 10. The worm flank surface generated by sweeping the *DE* segment along the globoid-guided curve. (**a**)—isometric position; (**b**)—frontal position.

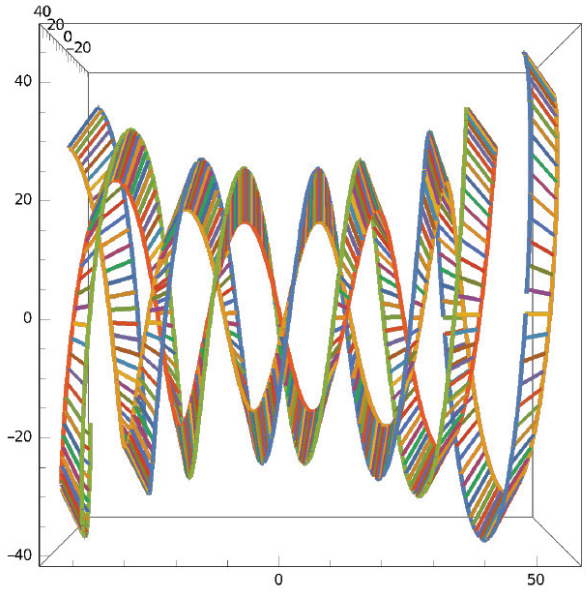


Figure 11. An overlap image of the surfaces of the globoid worm generated by sweeping segments *AB* and *DE* through the globoid-guided curves.

The trajectory of point *M* relative to the worm (O_{1xyz} system) is obviously a helix wound on a toroidal surface and relative to the driven wheel is an arc of a circle (which appears distorted due to perspective) (Figure 5).

The graphs of points *A*, *B*, *D*, and *E* follow the same pattern, with the gap due to the positioning of the points in relation to point *M*. The fact that their trajectories are correct is confirmed by the practical realization of the 3D model of the worm (Figure 6).

Lines *AB* and *DE* each generate one flank of the worm spiral (Figures 9 and 10), their combination leading to the realization of the functional surfaces of the globoid spiral (Figure 11). The obtained results resemble that of a worm.

To create the 3D model of the worm, Equations (8) and (11) were used to generate the helices along which the profile of the worm's spiral is generated (Figure 12). It can be seen that the propellers are tangent to the edges of the wheel rollers (bearings), which confirms that the mathematical model is correct. A 3D model of the worm (made in Solid Works) is presented in Figure 13, and that of the gear is shown in Figure 14.

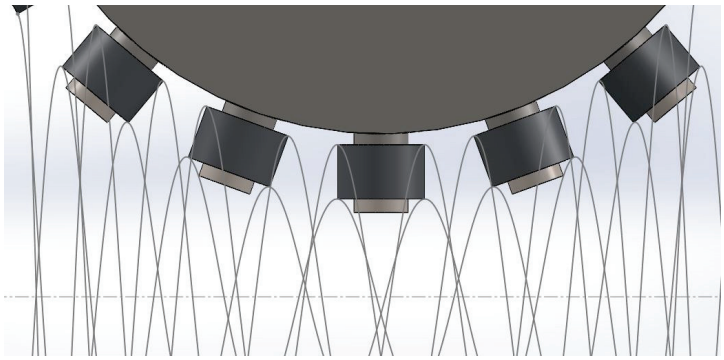


Figure 12. Generation of helices of the spiral.

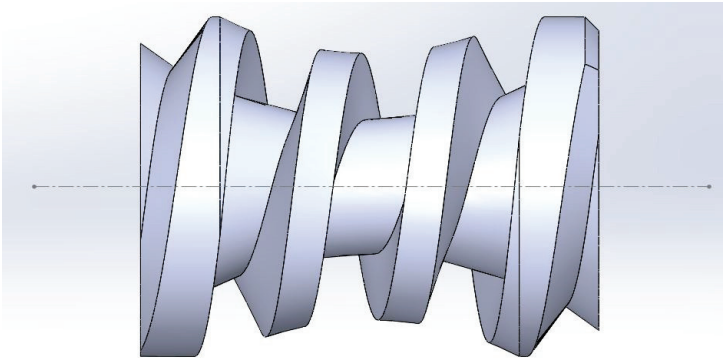


Figure 13. Three-dimensional model of the worm.

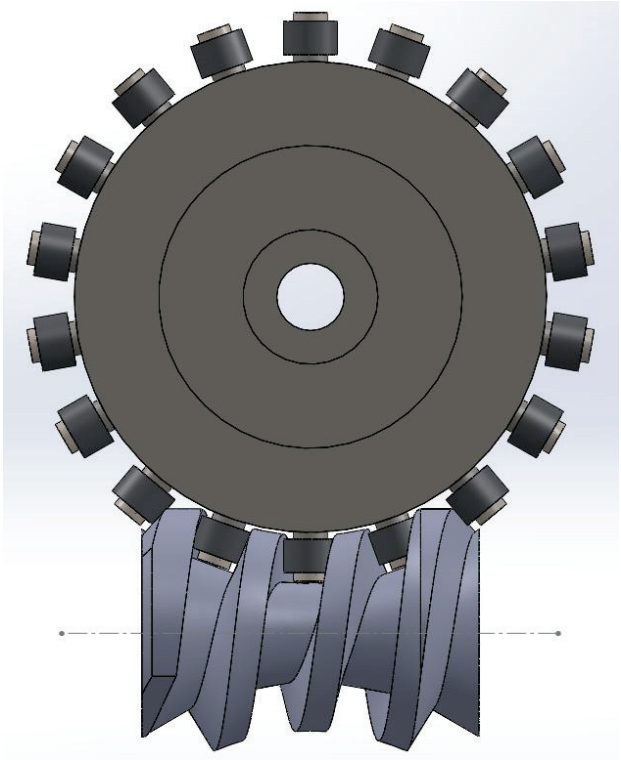


Figure 14. Three-dimensional model of the gear.

At this moment, when the mathematical model of the worm gearing's geometry is validated, the authors generate 3D models of the worm and worm wheel in SolidWorks

to obtain .stl files necessary for achieving a 3D prototype of the worm gearing. Figure 12 shows the prototype of the globoid worm gear obtained employing 3D printing additive manufacturing.

3. Results

Experimental Validation of the Physical Model

For the experimental validation of the mathematical model, the physical model of the mechanism was made. The worm (Figure 15), driven wheel body, and worm bearings were made from PLA on a Creatbot DX Plus 3D printer. Two 625 series bearings were used for each "tooth" of the driven wheel. The dimensions of the gear elements are those used in the creation of the 3D model. Even if the dimensional accuracy is not at the same level as a machined part, it is sufficient for preliminary checks.

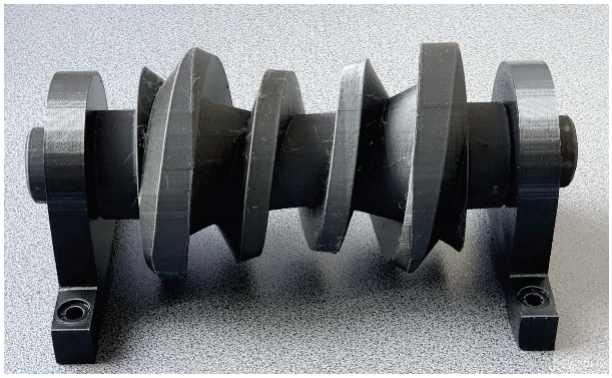


Figure 15. Three-dimensional prototype worm and bearings obtained through additive manufacturing.

The physical model (Figure 16) works, and the gearing is correct.

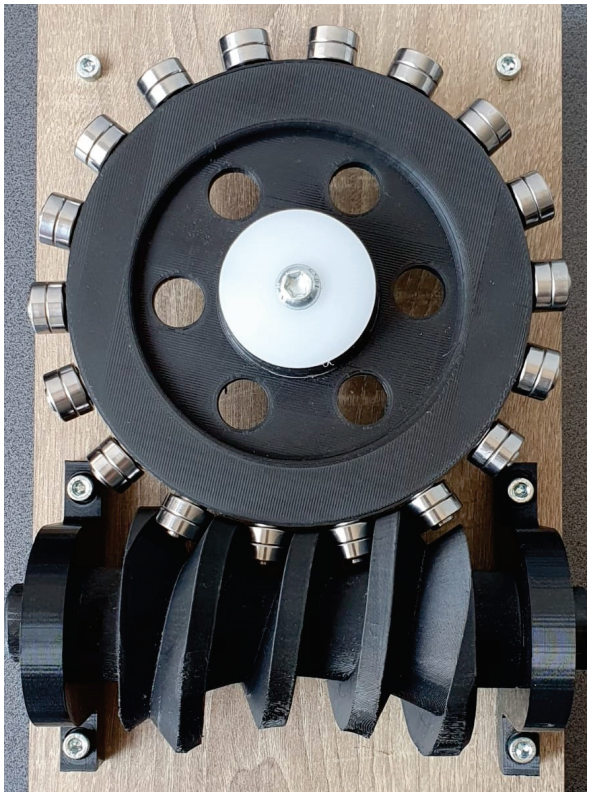


Figure 16. Prototype of the unconventional worm gear with bearings.

Other constructive, kinematic, and even dynamic aspects can be studied on it, and various tests and trials can be carried out.

The accuracy of the presented theoretical model as well as the numerical analysis is therefore verified by making the 3D model and assembling it in a perfectly functional worm gear.

4. Conclusions

A mathematical model consisting of a non-conventional worm gear is presented in this study. The main aim of the paper was to develop a mathematical model for the non-conventional worm gear that is simple and easy to implement in practice but, at the same time, correct. The main problem was given by the globoid shape of the worm and the fact that the profile of the gap between the turns are rectangular, and this profile was found in the median frontal plane of the wheel, a plane that also contains the axis of the worm. Any machine on a CNC machine can be easily programmed taking these aspects into account.

The contact between the worm coil and the rollers is a linear Hertzian contact, and the relative motion is a rolling one. Due to this fact, the efficiency of such a transmission is obviously much higher than that of classic globoid gear: the friction force caused by the rolling of the bearing on the surface of the worm is lower.

The contact generatrix of the bearing is a straight line that skews from the worm axis, so they are not coplanar.

A finite element analysis of the stresses to which the active elements of the gear (the spiral of the worm and the rollers) are subjected can be performed based on its 3D model.

The presented mathematical model is viable, having been validated both theoretically and experimentally. It can be applied for different transmission ratios and component sizes.

A dynamic analysis of the studied mechanism can be carried out, including a calculation of the transmission efficiency. For example, the stresses to which the bolts on which the bearings are fixed are subjected can be analyzed.

Mechanical transmissions with gears of this type have applications in various technical fields, ranging from robotics and precision industrial transmissions to the field of micro air vehicles.

Author Contributions: Conceptualization, S.H. and L.T.; methodology, S.H., R.N. and O.B.; software, S.H., A.H. and I.M.S.-B.; validation, S.H., F.A.C., O.B. and I.M.S.-B.; formal analysis, L.T. and F.A.C.; investigation, R.N. and A.H.; resources, S.H. and I.M.S.-B.; data curation, S.H.; writing—original draft preparation, S.H.; writing—review and editing, S.H., O.B. and I.M.S.-B.; visualization, S.H., R.N., O.B., L.T., A.H., F.A.C. and I.M.S.-B.; supervision, S.H. and I.M.S.-B. All authors have read and agreed to the published version of the manuscript.

Funding: This research received no external funding.

Institutional Review Board Statement: Not applicable.

Informed Consent Statement: Not applicable.

Data Availability Statement: Data is contained within the article.

Conflicts of Interest: The authors declare no conflicts of interest.

References

1. Dudás, I. *The Theory and Practice of Worm Gear Drives*; Penton Press: London, UK, 2000.
2. Grote, K.H.; Antonsson, E.K. *Springer Handbook of Mechanical Engineering*; Springer: Berlin/Heidelberg, Germany, 2009.
3. Zhao, Y.; Kong, X. Meshing principle of conical surface enveloping spiroid drive. *Mech. Mach. Theory* **2018**, *123*, 1–26. [CrossRef]
4. Crosher, W.P. *Design and Application of the Worm Gear*; ASME Press: New York, NY, USA, 2002.
5. Litvin, F.L.; Fuentes, A. *Gear Geometry and Applied Theory*; Cambridge University Press: Cambridge, UK, 2004.
6. Ninacs, R.; Cristea, A.F.; Haragâș, S. Study regarding the kinematic and functional aspects of globoidal worm gear. *Acta Tech. Napoc. Ser. Appl. Math. Mech. Eng.* **2022**, *65*, 499–504.
7. Cristea, A.F.; Ninacs, R.; Haragâș, S. Study regarding the kinematic and functional aspects of unconventional worm gear. *Acta Tech. Napoc. Ser. Appl. Math. Mech. Eng.* **2022**, *65*, 437–442.

8. Zhao, Y.; Huai, C.; Zhang, Y. Compound modification of globoidal worm drive with variable parameters. *Appl. Math. Model.* **2017**, *50*, 17–38. [CrossRef]
9. Xu, W.; Qin, D.; Shi, W. Direct digital design and simulation of meshing in worm-gear drive. *Chin. J. Mech. Eng.* **2006**, *19*, 428–433. [CrossRef]
10. Polowniak, P.; Sobolak, M.; Marciniec, A. Double enveloping worm gear modeling using CAD environment. *Bull. Pol. Acad. Sci. Tech. Sci.* **2021**, *69*, e136736.
11. Zhao, Y.; Zhang, Y. Novel methods for curvature analysis and their application to TA worm. *Mech. Mach. Theory* **2016**, *97*, 155–170. [CrossRef]
12. Zhao, Y. Meshing analysis for TA worm. *Mech. Mach. Sci.* **2016**, *43*, 13–20. [CrossRef]
13. Andrianto, M.; Wu, Y.R.; Arifin, A. A novel manufacturing method for double-enveloping worms using a whirl-machining process. *Mech. Mach. Theory* **2023**, *179*, 105099. [CrossRef]
14. Rui, C.; Li, H.; Yang, J.; Wei, W. Research on a method for designing land surfaces of a dual-cone double enveloping hourglass worm wheel hob. *J. Adv. Mech. Des. Syst. Manuf.* **2018**, *12*, JAMDSM0090. [CrossRef]
15. Lei, Z.; Bi, Q.; Wang, Y.; Ding, H. Five-Axis Flank Milling Method of Plane Double Enveloping Hourglass Worm. *Adv. Mater. Res.* **2011**, *314–316*, 1523–1532.
16. Dong, L.; Wang, J.; Liu, P.; Wei, W.; Li, H. An NC rough turning method of an enveloping toroidal worm. *Prod. Eng.* **2012**, *6*, 129–135. [CrossRef]
17. Chen, Y.; Zhang, G.; Chen, B.; Luo, W.; Li, F.; Chen, Y. A novel enveloping worm pair via employing the conjugating planar internal gear as counterpart. *Mech. Mach. Theory* **2013**, *67*, 17–31. [CrossRef]
18. Deng, X.; Wang, J.; Wang, S.; Wang, S.; Wang, J.; Li, S.; Liu, Y.; He, G. Investigation on the Backlash of Roller Enveloping Hourglass Worm Gear: Theoretical Analysis and Experiment. *J. Mech. Des.* **2018**, *141*, 053302. [CrossRef]
19. Wang, S.; Wang, S.; Wang, J.; Deng, X. Temperature Field Simulation and Experimental Study of Anti-backlash Single-Roller Enveloping Hourglass Worm Gear. *Chin. J. Mech. Eng.* **2020**, *33*, 59. [CrossRef]
20. Gao, S.; Wang, X. Theoretical modeling and transmission characteristics analysis of a novel double-roller hourglass worm drive based on enveloping principle. *Discov. Mech. Eng.* **2023**, *2*, 20. [CrossRef]
21. Zhang, H.; Wang, J.; Wang, S.; Wang, S.; He, G. A comparative investigation of meshing characteristics of antibacklash single-and double-roller enveloping hourglass worm gears. *J. Adv. Mech. Des. Syst. Manuf.* **2019**, *13*, JAMDSM0064. [CrossRef]
22. Available online: https://www.wolframalpha.com/ (accessed on 10 May 2024).
23. Polowniak, P.; Sobolak, M.; Marciniec, A. Mathematical model of the worm wheel tooth flank of a double-enveloping worm gear. *Alex. Eng. J.* **2021**, *60*, 3037–3046. [CrossRef]
24. Polowniak, P.; Sobolak, M. Mathematical description of tooth flank surface of globoidal worm gear with straight axial tooth profile. *Open Eng.* **2017**, *7*, 407–415. [CrossRef]
25. Dudás, L. New technology for manufacturing quasi-globoid worm gearings. *IOP Conf. Ser. Mater. Sci. Eng.* **2018**, *448*, 012035. [CrossRef]
26. Chen, Y.; Chen, Y.; Luo, W.; Zhang, G. Development and Classification of Worm Drive. In Proceedings of the 14th IFToMM World Congress, Taipei, Taiwan, 25–30 October 2015. [CrossRef]
27. Chen, Y.; Wang, W.; Ma, H.; Pu, Y.; Chen, Y. A Novel Precision Grinding Method for Roller Enveloping Hourglass Worm. *Int. J. Precis. Eng. Manuf.* **2024**, *25*, 2223–2234. [CrossRef]
28. Deng, X.; Wang, J.; Horstemeyer, M.F. Modification design method for an enveloping hourglass worm gear with consideration of machining and misalignment errors. *Chin. J. Mech. Eng.* **2013**, *26*, 948–956. [CrossRef]
29. Deng, X.; Liu, Y.; He, G. Design and Assessment of an Antibacklash Single Roller Enveloping Hourglass Worm Gear. *SAE Tech. Pap.* **2019**, 2019-01-1071. [CrossRef]
30. Deng, X.; Wang, J.; Wang, S.; Wang, S.; Liu, Y.; He, G. An optimal process of machining complex surfaces of anti-backlash roller enveloping hourglass worms. *J. Manuf. Process.* **2020**, *49*, 472–480. [CrossRef]
31. Pop, D.; Haragâş, S.; Buiga, O. *Organe de Maşini*; Editura Risoprint: Cluj-Napoca, Romania, 2024; Volume 3.
32. Haragâș, S.; Ninacs, R.; Cristea, A.F. Contributions on the Kinematics of Unconventional Worm Gears. In Proceedings of the 14th International Conference on Mechanical and Aerospace Engineering (ICMAE), Porto, Portugal, 18–21 July 2023; pp. 89–94, ISBN 979-8-3503-4031-0.
33. Jiang, Y.; Deng, X. Parametric study on the cylindrical roller enveloping end-face internal engagement worm gear. *J. Adv. Mech. Des. Syst. Manuf.* **2017**, *11*, JAMDSM0024. [CrossRef]
34. Kacalak, W.; Majewski, M.; Budniak, Z.; Ponomarenkow, J. Worm Gear Drives with Improved Kinematic Accuracy. *Materials* **2021**, *14*, 7825. [CrossRef] [PubMed]
35. Maros, D. *Angrenaje Melcate*; Editura Tehnică: București, Romania, 1966.
36. Ninacs, R.; Haragâș, S. Design and optimal modeling of unconventional worm gear with bearings. In Proceedings of the 27th Edition of Innovative Manufacturing Engineering & Energy Conference, (IMANEE), Chișinău, Republic of Moldova, 12–14 October 2023.
37. Ninacs, R.; Haragâș, S. Contributions on mathematical determination of surfaces in unconventional worm gear. In Proceedings of the 12th International Conference on Machine and Industrial Design in Mechanical Engineering (KOD 2024), Balatonfùred, Hungary, 23–26 May 2024.

38. Sohn, J.; Park, N. Modified worm gear hobbing for symmetric longitudinal crowning in high lead cylindrical worm gear drives. *Mech. Mach. Theory* **2017**, *117*, 133–147. [CrossRef]
39. Vyathin, A. Analysis of the geometry and contact density of globoid gearing. In *MATEC Web of Conferences ICMTMTE 2020*; EDP Sciences: Les Ulis, France, 2020; Volume 329, p. 03008. [CrossRef]
40. Zhao, T.; Li, K.; Ma, H. Study on dynamic characteristics of a rotating cylindrical shell with uncertain parameters. *Anal. Math. Phys.* **2022**, *12*, 97. [CrossRef]
41. Chen, L.; Cheng, C.; Zhou, C.; Zhang, Y.; Wu, J. Flapping rotary wing: A novel low-Reynolds number layout merging bionic features into micro rotors. *Prog. Aerosp. Sci.* **2024**, *146*, 100984. [CrossRef]

Disclaimer/Publisher's Note: The statements, opinions and data contained in all publications are solely those of the individual author(s) and contributor(s) and not of MDPI and/or the editor(s). MDPI and/or the editor(s) disclaim responsibility for any injury to people or property resulting from any ideas, methods, instructions or products referred to in the content.

MDPI AG
Grosspeteranlage 5
4052 Basel
Switzerland
Tel.: +41 61 683 77 34

Applied Sciences Editorial Office
E-mail: applsci@mdpi.com
www.mdpi.com/journal/applsci



Disclaimer/Publisher's Note: The title and front matter of this reprint are at the discretion of the Guest Editors. The publisher is not responsible for their content or any associated concerns. The statements, opinions and data contained in all individual articles are solely those of the individual Editors and contributors and not of MDPI. MDPI disclaims responsibility for any injury to people or property resulting from any ideas, methods, instructions or products referred to in the content.





Academic Open
Access Publishing

mdpi.com

ISBN 978-3-7258-8604-3